UNIVERSITY OF LEICESTER

Development of small field of view gamma cameras for medical imaging

A thesis submitted for the degree of

Doctor of Philosophy

By

LAYAL KHALID JAMBI

Space Research Centre

Department of Physics and Astronomy

October 2018

Development of small field of view gamma cameras for medical imaging

Layal Khalid Jambi

Abstract

Over recent years, in the field of nuclear medicine, advances in the development of small field of view (SFOV) gamma cameras have been increased. High resolution compact gamma cameras are designed to be used in intraoperative medical imaging procedures such as in head and neck sentinel node biopsies or for small organ imaging such as thyroid investigations. SFOV imaging can offer advantages over large field of view (LFOV) cameras in spatial resolution and sensitivity although, there is a trade-off between spatial resolution and sensitivity. Also SFOV cameras are highly favourable in terms of reduced size and weight in comparison to the standard gamma camera. Over the last two decades, advances in semiconductor detector technology have now reached the point where they are sufficiently sensitive to be the basis of SFOV cameras for nuclear medicine imaging systems.

A new concept for a medical imaging system is presented, the Hybrid Gamma Camera (HGC). The performance characteristics of the HGC are evaluated following modified quality assurance protocols.

The Cadmium-Telluride (CdTe) XRI-UNO and the HEXITEC semiconductor (CdTe) detector are also investigated. Their performance is compared to that of the scintillator-based Hybrid Gamma Camera (HGC).

A novel dual gamma near infrared (NIR) fluorescence camera has been developed and is described. Preliminary in vivo and in vitro studies were undertaken to demonstrate the suitability of the system for fluorescent imaging. This dual modality gamma-NIR system has been proposed as one possibility for improving surgical utility.

Acknowledgments

First and foremost, I would like to thank and praise Allah for blessing me with the ability and perseverance to accomplish this thesis. I would not have made it this far without him.

I would like to express my sincere gratitude to my supervisor Professor John E. Lees who helped me throughout my PhD journey with his continuous support and encouragement. Without his advice and guidance this thesis would not have been completed. I am very grateful to him for giving me the opportunity and assistance to publish most of the results obtained in this thesis. He is immensely organised and very professional and I have been amazingly fortunate to be a PhD student under his supervision and a team member of his Bioimaging group.

I would also like to express my deepest thanks to my second supervisor Professor Alan C. Perkins for his advice and guidance, which was invaluable.

I would especially like to thank Dr Sarah L. Bugby for her valuable suggestions for improving my research. Her insightful advice, helpful guidance, inspirational criticism, and patient encouragement assisted the writing of this thesis in numerous ways.

I would like to extend my sincerest thanks and appreciation to the Physics and Astronomy Department, especially the staff in Space Research Centre (SRC).

I acknowledge the Advanced Microscopy Facility, University of Leicester for generating the Scanning Electron Microscope (SEM) images.

I would like to thank the staff at the Leicester Royal Infirmary particularly Sharon McMahon and the nuclear medicine team and William McKnight, SRC, University of Leicester for their technical support. I am also grateful to Elaine Blackshaw, Nottingham University Hospitals NHS Trust, who has been invaluable in patient recruitment.

I also acknowledge Marieke Stammes and Hein Handgraaf from Leiden University Medical Centre, The Netherlands for their support during preclinical imaging.

I also thank Matt Wilson from Science and Technology Facilities Council (STFC), Rutherford Appleton Laboratory (RAL), The UK for providing the HEXITEC detector.

I also appreciate the scientific and personal support from my colleague Mohammed S. Alqahtani throughout our postgraduate studies in the UK since 2012.

I am extremely grateful to the colleagues I've worked alongside whether in the project or sharing room 105 at Michael Atiyah The Annexe, Awad Almarhaby, Bahadar Bhatia, Numan Dawood, Dr Simon Lindsay, Jane Macarthur, Kjell Koch-Mehrin, Aik Ng, Jack Piercy, Sion Richard and Sean Tipper.

I am also grateful to my colleagues Rehab Baghadood and Saeed Kabrah from Umm Al- Qura University, Makkah, Saudi Arabia, for providing me with both clear and black 96-well plate.

I acknowledge the financial support from King Saud University, Riyadh, Saudi Arabia for granting me a full funded scholarship to pursue this study and the Saudi Cultural Bureau, London, United Kingdom for its generous support. It has also supported me to attend many conferences in my research area.

I would like to acknowledge a debt of gratitude that can never be repaid to my parents, Saadia Aljawi and Khalid Jambi, for their constant prayers for me to be safe, happy and successful. May Allah bestow them with health. I am incredibly thankful to my family, my sisters, my brothers and my friends for their continuous motivations.

Giant steps into Medical Imaging

Table of Contents

Abstract i

Acknowledgments ii

Table of Contents v

List of publications x

List of conferences xii

Chapter 1 1

Introduction 1

1.1 Pre-surgical mapping 2

1.1.1 Standard gamma camera 3

1.1.2 SPECT/CT 3

1.2 Intra-operative SLN imaging 4

1.2.1 Gamma probes 4

1.2.2 Portable gamma cameras 5

1.2.3 Handheld small field of view gamma camera 6

1.3 Radiation detectors 10

1.3.1 Hybrid Gamma Camera 10

1.3.2 CdTe X-ray and gamma ray detectors for imaging system 11

1.4 Optical imaging 12

1.5 Gamma and optical imaging modality systems 12

1.6 Thesis aim 13

1.7 Thesis outline 14

1.8 Personal contribution to this work 14

Chapter 2 16

Radiation detection using scintillators and semiconductor detectors 16

2.1 Gamma ray attenuation 17

2.1.1 Attenuation coefficients 17

2.1.2 Absorber mass thickness 18

2.2 Interaction of radiation with matter 18

2.2.1 Gamma rays 18

2.2.2 The photoelectric effect 19

2.2.3 Compton scattering 20

2.2.4 Pair production 22

2.3 Scintillation detector principles 22

2.3.1 Scintillator materials 24

2.3.2 Properties of Caesium iodide (CsI:TI) 25
2.3.3 Properties of Gadolinium Oxysulfide (Gd_2O_2S) 28
2.3.4 Properties of Cadmium Tungstate ($CdWO_4$) 29
2.4 Photomultiplier tube 31
2.5 Charged coupled device 33
2.6 Semiconductor detector principles 36
2.6.1 Properties of Cadmium Telluride (CdTe) 37
2.7 Summary 39
Chapter 3 40
Small Field of View (SFOV) Hybrid Gamma Camera (HGC): its design and application 40
3.1 Materials and methods 41
3.1.1 Hybrid gamma camera design 41
3.1.2 Optical gamma image alignment 43
3.1.3 Simulation of lymphatic imaging 43
3.1.4 Phantoms 44
3.1.5 Clinical patient imaging 50
3.2 Clinical imaging of lacrimal drainage 51
3.3 Research team roles 53
3.4 Conclusion 53
Chapter 4 55
Protocols for assessing the performance characteristics of small field of view (SFOV) gamma cameras 55
4.1 Planar imaging 56
4.1.1 Intrinsic spatial resolution 56
4.1.2 Extrinsic spatial resolution 59
4.1.3 Intrinsic spatial uniformity 60
4.1.4 Intrinsic spatial sensitivity 61
4.1.5 Extrinsic spatial sensitivity 62
4.1.6 Count rate capability 62
4.2 HGC methods 64
4.2.1 Intrinsic spatial resolution 64
4.2.2 Extrinsic spatial resolution 65
4.2.3 Intrinsic spatial uniformity 68
4.2.4 Intrinsic spatial sensitivity 69
4.2.5 Extrinsic spatial sensitivity 69
4.2.6 Count rate capability 69

4.3 Summary and conclusion 70

Chapter 5 72

Comparison of the performance characterisation of a scintillator-CCD based detector using CsI:TI, GOS and $CdWO_4$ scintillators for nuclear medical imaging 72

5.1 Materials and methods 73

5.1.1 Scintillators 73

A. Columnar CsI:TI scintillator 73

B. Pixelated GOS scintillator 74

C. Transparent inorganic $CdWO_4$ scintillator 74

5.1.2 Coupling method 76

5.1.3 Imaging process 76

i. Gamma reconstruction for CsI:TI 77

ii. Gamma reconstruction for GOS 77

iii. Gamma reconstruction for $CdWO_4$ 78

5.1.4 Experimental setup 78

I. Intrinsic spatial resolution 79

II. Extrinsic spatial resolution 80

III. Intrinsic spatial uniformity 80

IV. Intrinsic spatial sensitivity 81

V. Extrinsic spatial sensitivity 81

VI. Count rate capability 81

5.2 Results 82

5.2.1 CsI:TI scintillator 82

i. Intrinsic spatial resolution 82

ii. Extrinsic spatial resolution 85

iii. Intrinsic spatial uniformity 88

iv. Intrinsic spatial sensitivity 89

v. Extrinsic spatial sensitivity 90

vi. Count rate capability 92

5.2.2 GOS scintillator 93

i. Intrinsic spatial resolution 94

ii. Extrinsic spatial resolution 97

iii. Intrinsic spatial uniformity 100

iv. Intrinsic spatial sensitivity 101

v. Extrinsic spatial sensitivity 101

vi. Count rate capability 103

5.2.3 $CdWO_4$ scintillator 105
I. Intrinsic spatial resolution 105
II. Extrinsic spatial resolution 107
III. Intrinsic spatial uniformity 109
IV. Intrinsic spatial sensitivity 110
V. Extrinsic spatial sensitivity 110
VI. Count rate capability 111
5.3 Discussion 113
5.4 Conclusion 115
Chapter 6 117
Evaluation of a semiconductor CdTe detector for medical imaging 117
6.1 Materials and methods 119
A. XRI-UNO system 119
B. HEXITEC ASIC detector 121
6.1.1 Imaging procedures 122
A. XRI-UNO system 122
Initial investigation 122
B. HEXITEC ASIC detector 123
6.1.2 Performance specifications 124
i. Intrinsic spatial resolution 124
ii. Extrinsic spatial resolution 128
iii. Intrinsic spatial uniformity 134
iv. Intrinsic spatial sensitivity 135
v. Extrinsic spatial sensitivity 138
vi. Count rate capability 141
vii. Contrast to noise ratio 143
6.2 Results and discussion 145
6.3 Conclusion 149
Chapter 7 151
A hybrid gamma and near infrared fluorescence imaging camera 151
7.1 Near-Infrared (NIR) fluorescence imaging system 152
7.1.1 Principles of operation 152
7.1.2 Filters, light source and camera 153
I. Filters 153
II. Excitation light source 154
III. Fluorescence camera 155

7.1.3 NIR fluorescent contrast agents 155
I. Indocyanine green (ICG) 156
II. IRDye 800CW Infrared Dye 157
7.2 Materials and methods 158
7.2.1 Fluorescence imaging camera 158
I. NIR CP camera 158
II. XS camera 158
7.2.2 LED 740 nm ring 159
7.2.3 Filters 160
7.2.4 Initial investigation 162
7.2.5 Quantitative performance of the fluorescence imaging 165
7.2.6 Performance of the fluorescence imaging using 96-well plate 168
I. Clear 96-well plate 170
II. Black 96-well plate 172
7.3 Dual radio-NIR fluorescent tracers 174
7.4 Dual radio-NIR fluorescent camera 174
7.5 Dual radio-NIR fluorescent imaging 176
7.5.1 In vitro 176
7.5.2 In vivo 177
7.6 Results and discussion 179
7.6.1 In vitro imaging 179
7.6.2 In vivo imaging 179
7.7 Conclusion 180
Chapter 8 182
Summary, conclusion and future work 182
8.1 Summary and conclusion 182
8.2 Future work 185
8.2.1 HGC system: further development 185
I. Depth estimation 185
II. Clinical applications 186
8.2.2 HEXITEC detectors 186
8.2.3 Fluorescence development 187
8.2.4 Small animal imaging 188
Appendix A 189
Bibliography 191

List of publications

1. **Layal K. Jambi**, John E. Lees, Sarah L. Bugby, Bahadar S. Bhatia, Mohammed S. Alqahtani, Numan S. Dawood, Aik H. Ng, Alan C. Perkins. Comparison of columnar and pixelated scintillators for small field of view hybrid gamma camera imaging. IEEE Xplore. 2016 IEEE Nuclear Science Symposium, Medical Imaging Conference and Room-Temperature Semiconductor Detector Workshop (NSS/MIC/RTSD), Strasbourg, France, 2017, p.1-4.

2. Aik H. Ng, Patricia E. Blackshaw, Mohammed S. Alqahtani, **Layal K. Jambi**, Sarah L. Bugby, John E. Lees and Alan C. Perkins. A novel compact small field of view hybrid gamma camera: first clinical results. Nuclear Medicine Communications, 2017. 38(9).

3. **LK Jambi**, JE Lees, SL Bugby, MS Alqahtani, BS Bhatia, WR McKnight, NS Dawood, AH Ng and AC Perkins. A hand-held hybrid gamma-near-infrared fluorescence imaging camera. Soc. Nuclear Med. 58(Supplement 1): 220, 2017.

4. MS Alqahtani, JE Lees, SL Bugby, **LK Jambi**, BS Bhatia, WR McKnight, NS Dawood, AH Ng and AC Perkins. Capability of a novel small field of view hybrid gamma camera (HGC) for sentinel lymph node and small organ imaging. Soc. Nuclear Med. 58(Supplement 1): 157, 2017.

5. Lees, J.E., S.L. Bugby, M.S. Alqahtani, **L.K. Jambi**, N.S. Dawood, W.R. McKnight, A.H. Ng, and A.C. Perkins, A Multimodality Hybrid Gamma-Optical Camera for Intraoperative Imaging. Sensors (Basel), 2017. 17(3).

6. S.L. Bugby, **L.K. Jambi**, J.E. Lees. A comparison of CsI:TI and GOS in a scintillator-CCD detector for nuclear medicine imaging. J. Inst. 11(9):P09009, 2016.

7. M.S. Alqahtani, J.E. Lees, S.L. Bugby, **L.K. Jambi**, A.C. Perkins. Quantitative investigation of a novel small field of view hybrid gamma camera (HGC) capability for sentinel lymph node detection. The British Journal of Radiology, 2016(89): p. 20160435.

8. MS Alqahtani, JE Lees, SL Bugby, **LK Jambi**, BS Bhatia, WR McKnight, NS Dawood, AH Ng, AC Perkins. Quantitative analysis of sentinel node detection using a novel small field of view hybrid gamma camera (HGC). Soc. Physica Medica. 32(Supplement 3): 256-257, 2016.

9. AC Perkins, AH Ng, SL Bugby, PE Blackshaw, MS Alqahtani, **LK Jambi**, JE Lees. A novel compact hybrid optical gamma camera: First clinical results. Soc. Nuclear Med. 57(Supplement 2):531, 2016.

10. MS Alqahtani, JE Lees, SL Bugby, **LK Jambi**, BS Bhatia, WR McKnight, NS Dawood, AH Ng, AC Perkins. Investigation of a novel small field of view hybrid compact gamma camera (HCGC) for scintigraphic imaging. Insights Imaging 7(Supplement 1):162, 2016.

11. M.S. Alqahtani, J.E. Lees, S.L. Bugby, **L.K. Jambi**, A.C. Perkins. Lymphoscintigraphic imaging study for quantitative evaluation of a small field of view (SFOV) gamma camera. J. Inst. 10(7):P07011, 2015.

12. **L.K. Jambi**, J.E. Lees, S.L. Bugby, S. Tipper, M.S. Alqahtani, A.C. Perkins. Evaluation of XRI-UNO detector for nuclear medical imaging. J. Inst. 10(6):P06012, 2015.

13. J.E. Lees, S.L. Bugby, B.S. Bhatia, **L.K. Jambi**, M.S. Alqahtani, W.R. McKnight, A.H.Ng, A.C. Perkins. A small field of view camera for hybrid gamma and optical imaging. J. Inst. 9(12):C12020, 2014.

List of conferences

1. Aik H. Ng, Mohammed S. Alqahtani, **Layal K. Jambi**, Sarah L. Bugby, John E. Lees and Alan C. Perkins. Characterization of a small field of view hybrid gamma camera. The 18th Asia-Oceania Congress of Medical Physics (AOCMP) in conjunction with the 16th South-East Asia Congress of Medical Physics (SEACOMP), Kuala Lumpur, Malaysia, 2018.

2. Awad M. Almarhaby, John E. Lees, Sarah L. Bugby, Mohammed S. Alqahtani, **Layal K. Jambi**, Numan S. Dawood, William R. McKnight, Bahadar S. Bhatia and Alan C. Perkins. A multimodality hybrid gamma-near infrared (NIR) fluorescence camera for intraoperative cancer surgery. Photon 2018, Birmingham, United Kingdom, 2018.

3. Alexandra Mackenzie, Sarah L. Bugby, **Layal K. Jambi**, Mohammed S. Alqahtani, Alan C. Perkins and John E. Lees. Investigating the utility of a small field of view gamma camera for radioiodine dosimetry. The UK Radiological Congress and Radiation Oncology Congress, Liverpool, United Kingdom, 2018.

4. Aik H. Ng, Mohammed S. Alqahtani, **Layal K. Jambi**, Sarah L. Bugby, John E. Lees and Alan C. Perkins. Assessing a small field of view hybrid gamma camera for perioperative radioactive seed localisation. World Congress on Medical Physics and Biomedical Engineering, Prague, Czech Republic, 2018.

5. Mohammed S. Alqahtani, John E. Lees, Sarah L. Bugby, **Layal K. Jambi**, Aik H. Ng, Bahadar S. Bhatia, Numan S. Dawood, Awad M. Almarhaby, William R. McKnight and Alan C. Perkins. A novel small field of view hybrid gamma camera for scintigraphic imaging. SPIE Medical Imaging 2018: Image-Guided Procedures, Robotic Interventions, and Modeling. DOI: 10.1117/12.2293792

6. **LK Jambi**, JE Lees, SL Bugby, MS Alqahtani, BS Bhatia, NS Dawood, AM Almarhaby, WR McKnight, AH Ng and AC Perkins. Development of small field of view hybrid gamma camera for intra-operative imaging. The 5th International Conference on Radiation Medicine, Riyadh, Saudi Arabia, 2018.

7. JE Lees, SL Bugby, MS Alqahtani, **LK Jambi**, NS Dawood, WR McKnight, BS Bhatia, AH Ng and AC Perkins. Hybrid gamma camera for medical applications. PSD11: 11th International Conference on Position Sensitive Detectors, Milton Keynes, UK, 2017.

8. JE Lees, SL Bugby, **LK Jambi** and M D. Wilson. Characterisation of a CdTe detector for medical imaging applications. PSD11: 11th International Conference on Position Sensitive Detectors, Milton Keynes, UK, 2017.

9. JE Lees, SL Bugby, MS Alqahtani, **LK Jambi**, NS Dawood, WR McKnight, BS Bhatia, AH Ng and AC Perkins. A multimodality camera for intraoperative imaging. Cancer Imaging Conference. London, UK, 2017.

10. NS Dawood, JE Lees, SL Bugby, MS Alqahtani, **LK Jambi**, WR McKnight, AH Ng and AC Perkins. Radionuclide depth estimation using a novel SFOV hybrid gamma-optical camera with an anthropomorphic breast phantom. The 45th Annual Spring BNMS Meeting. Birmingham, UK, 2017.

11. AH Ng, MS Alqahtani, **LK Jambi**, SL Bugby, JE Lees and AC Perkins. Use of a novel small field of view hybrid gamma camera (HGC) for Iodine-125 seed localisation. The 45th Annual Spring BNMS Meeting. Birmingham, UK, 2017.

12. SL Bugby, JE Lees, AH Ng, MS Alqahtani, **LK Jambi**, MA Stammes, HJM Handgraaf, AC Perkins. Portable hybrid gamma-near-infrared fluorescence imaging. European Association of Nuclear Medicine (EANM) Annual Congress. Barcelona, Spain, 2016. DOI: 10.1007/s00259-016-3484-4

13. JE Lees, SL Bugby, MS Alqahtani, **LK Jambi**, AH Ng, NS Dawood, AC Perkins. A high-resolution hybrid gamma-optical camera for intraoperative imaging. European Association of Nuclear Medicine (EANM) Annual Congress. Barcelona, Spain, 2016. DOI: 10.1007/s00259-016-3484-4

14. **LK Jambi**, JE Lees, SL Bugby, MS Alqahtani, BS Bhatia, WR McKnight, NS Dawood, AH Ng, AC Perkins. Development of a small field of view gamma camera for medical imaging. European Congress of Radiology (ECR), Vienna, Austria, 2016. Abstract available in: http://dx.doi.org/10.1594/ecr2016/C-2206

15. MS Alqahtani, JE Lees, SL Bugby, **LK Jambi**, BS Bhatia, WR McKnight, NS Dawood, AH Ng, AC Perkins. Investigation of a novel small field of view hybrid compact gamma camera (HCGC) for scintigraphic imaging. European Congress of Radiology (ECR), Vienna, Austria, 2016. Abstract available in: http://dx.doi.org/10.1594/ecr2016/B-0033

16. AH Ng, SL Bugby, **LK Jambi**, MS Alqahtani, PE Blackshaw, PS Morgan, JE Lees, AC Perkins. Development of a hybrid optical-gamma camera: A new innovation in bedside molecular imaging. World Congress on Medical Physics and Biomedical Engineering, Toronto, Canada, 2015.

17. NS Dawood, JE Lees, SL Bugby, **LK Jambi**, MS Alqahtani, WR McKnight, AC Perkins. A method of source-depth estimation using a Hybrid Gamma Camera. British

Institute of Radiology (BIR) Annual Congress, London, UK, 2015. Abstract available in: http://www.eposters.net/poster/a-method-for-source-depth-estimation-using-a-hybrid-gamma-camera-

18. MS Alqahtani, JE Lees, SL Bugby, **LK Jambi**, AC Perkins. Assessment of a novel hybrid optical-gamma camera for nuclear scintigraphic imaging, UK Radiological Congress (UKRC), Liverpool, UK, 2015.

19. JE Lees, AC Perkins, SL Bugby, BS Bhatia, **LK Jambi**, MS Alqahtani, WR McKnight, NS Dawood, AH Ng. A high-resolution handheld hybrid camera for gamma and optical imaging. British Nuclear Medicine Society (BNMS) Autumn Meeting, London, UK, 2015.

20. **LK Jambi**, JE Lees, SL Bugby, MS Alqahtani, BS Bhatia, WR McKnight, AH Ng, AC Perkins. A high-resolution gamma-optical hybrid camera for medical imaging, KFMC Conference on Medical Physics and Engineering in Medicine, Riyadh, Kingdom of Saudi Arabia, 2015.

21. MS Alqahtani, JE Lees, SL Bugby, **LK Jambi**, AC Perkins. Assessment of a novel hybrid optical-gamma camera for nuclear scintigraphic imaging, KFMC Conference on Medical Physics and Engineering in Medicine, Riyadh, Kingdom of Saudi Arabia, 2015.

22. AH Ng, SL Bugby, **LK Jambi**, MS Alqhatani, D Clay, PE Blackshaw, PS Morgan, JE Lees, AC Perkins. Hybrid optical-gamma camera for intraoperative imaging: A flexible phantom to assess system performances for sentinel node detection. International Conference on Clinical PET-CT and Molecular Imaging (IPET), Vienna, Austria, 2015.

23. **LK Jambi**, JE Lees, SL Bugby, BS Bhatia, MS Alqahtani, WR McKnight, AH Ng, AC Perkins. Performance of a hybrid gamma-optical camera for improved utility in diagnostic imaging. British Institute of Radiology (BIR) Annual Congress, London, UK, 2014. Abstract available in: http://www.eposters.net/poster/performance-of-a-hybrid-gamma-optical-camera-for-improved-utility-in-diagnostic-imaging

24. MS Alqahtani, JE Lees, SL Bugby, BS Bhatia, **LK Jambi**, AH Ng, AC Perkins. A lymphoscintigraphic phantom study using a novel hybrid optical-gamma camera. British Institute of Radiology (BIR) Annual Congress, London, UK, 2014. Abstract available in: http://www.eposters.net/poster/a-lymphoscintigraphic-phantom-study-using-a-novel-hybrid-optical-gamma-camera

25. JE Lees, SL Bugby, BS Bhatia, **LK Jambi**, MS Alqhatani, AH Ng, AC Perkins. A small field of view camera for hybrid gamma and optical imaging. PSD10: 10th International Conference on Position Sensitive Detectors, Guildford, UK, 2012.

Chapter 1

Introduction

In the 1950s the gamma camera which now is used in Nuclear Medicine departments to scan patients following the injection of a radioactive material called a radiopharmaceutical was developed by Hal Anger. Once the radiopharmaceutical is administered to the patient, it can concentrate and localise to a specific organ within the body. This property has advantages for nuclear medicine as it enables imaging of the physiological function of disease processes in the body rather than imaging the anatomical tissue. Conventional gamma cameras are large devices requiring large spaces and usually the patient walks in to the nuclear medicine department to be scanned (1). There are two types of nuclear medicine procedures; diagnostic procedures and therapeutic procedures. Diagnostic nuclear medicine procedures are mainly focused in the diagnosis of diseases using a gamma camera following the administration of the radioactive material. Therapeutic nuclear medicine procedures are used mainly to treat cancers using high energy radioactive material emitting alpha or beta particles to the targeted tumours. For the purpose of this thesis, the main focus will be for the diagnostic, pre-, intra-, and post- operative imaging procedures.

Nowadays, medical imaging technologies are being combined together to perform what is called hybrid imaging. Single Photon Emission Computed Tomography (SPECT)

combined with X-ray Computed Tomography (CT) is called SPECT/CT and is one of the modern modalities in nuclear medicine, this provides X-ray mapping, and detection of gamma rays released from the radiopharmaceutical (2). SPECT/CT has a particular property that is able to provide both functional and anatomical information from a single study. Although multi-modality systems have a long heritage in nuclear medicine, Single Photon Emission Computed Tomography (SPECT/CT) and Positron Emission Tomography-Computed Tomography (PET/CT), rarely have gamma and optical imaging been available in one system.

1.1 Pre-surgical mapping

The fundamental phase of diagnosing the breast tumour is the assessment of the presence of the sentinel lymph node (SLN) and/or metastasis around the node. The preoperative stage for breast cancer treatment is the localisation of sentinel lymph nodes (SLNs). That can be achieved by lymphoscintigraphy. Lymphoscintigraphy is a nuclear medicine imaging procedure using gamma cameras, which is used to assess the lymphatic system. The common indications of lymphoscintigraphy are: it is used for sentinel lymph node mapping in breast cancer or to identify the initial node that receives the lymph drainage from a tumour such as malignant melanoma. It can be used in oncology as a cancer treatment plan by biopsy, and for investigation of lymphedema to assess the blockage points in the lymphatic system. A radioactive material called ^{99m}Tc labelled nanocolloid is the preferred radiopharmaceutical used. During surgical theatre a gamma probe is used for counting the radioactivity of SLNs. Imaging small nodes requires high spatial resolution which means these clinical and surgical applications are making the new generation of hybrid gamma camera system in demand. If these small cameras can be constructed to be truly portable devices they have the potential to be used as hand-held cameras, to replace or augment the hand held probes currently used for pre-surgical and intra-operative applications, such as tumour localisation and the identification of sentinel lymph nodes.

1.1.1 Standard gamma camera

Preoperative SLN mapping and localisation is one of the most important phases for surgeons to improve the detection accuracy of identifying of lymph nodes. Morton and his colleagues (Morton et al. 1992 (3)) were the first who applied SLN biopsy in melanoma patients. Afterwards, Giuliano (Giuliano et al. 1997 (4)) used this technique in order to assess the stage of the disease in breast cancer patients.

The concept of the SLN mapping is relied on the ability of the LFOV gamma camera to detect the lymph nodes that drain from the injection site immediately after the administration of a radioactive material called ^{99m}Tc labelled nanocolloid which is the preferred radiopharmaceutical used in lymphoscintigraphy. Figure 1.1 shows a picture of the standard LFOV gamma camera. Image acquisition is dependent on the clinical cases, in some cases where the fast drainage is expected such as melanoma and head and neck cancer a dynamic study is required. Currently, imaging protocols are based on early and late acquisitions. Early acquisition preformed within the first 30 min following the injection while late acquisition after nearly 2 hours. The purpose of this protocol is to differentiate early draining SLNs from other nodes (5).

1.1.2 SPECT/CT

In some applications such as head and neck and intra-abdominal region, the standard LFOV gamma camera unable to define exactly the anatomical location of the SLNs. This is mainly due to the complexity of the anatomical structure and the presence of the soft tissues. To overcome this problem SPECT/CT camera is used instead. SPECT provides tomographic image with better contras and resolution. When SPECT fused with CT then SPECT/CT image provides an accurate anatomical information that aid the pre-surgical planning.

Figure 1.1: The e.cam® dual headed gamma camera system. (Taken from Southern Scientific Limited, Retrieved 3 September 2018, http://www.southernscientific.co.uk. With permission.)

1.2 Intra-operative SLN imaging

1.2.1 Gamma probes

During the last ten years, the SLN biopsy procedures held in the operating theatre has been undergone using sound signals by using gamma probes. Gamma probes offer real time detection of the radioactive material that accumulated within the SLNs using acoustic signals. In 1942, a hand held Geiger-Muller (GM) tube was used by Marinelli and Goldschmidt (6) aiming to make an uptake comparison of phosphorus-32 sodium phosphate in different skin diseases. Sequentially, in 1946, Low-Beer and his colleagues (7) used the GM tube pre-surgical in order to discriminate between benign and malignant breast tumours. Later, in 1949, the first intra-operative use of a gamma probe was with patients who have brain tumours (8). As the GM tubes were low sensitive to gamma radiations, scintillation gamma probes have developed. In 1956, Harris and co-workers (9) discussed the use of a thallium activated caesium iodide (CsI:TI) scintillation detector and Iodine-131 (^{131}I) with patients who have thyroid cancers. Then during

1970s, semiconductor probes have been introduced. Thereafter, various surgical probes have been developed. Figure 1.2 shows an example of a basic gamma probe system.

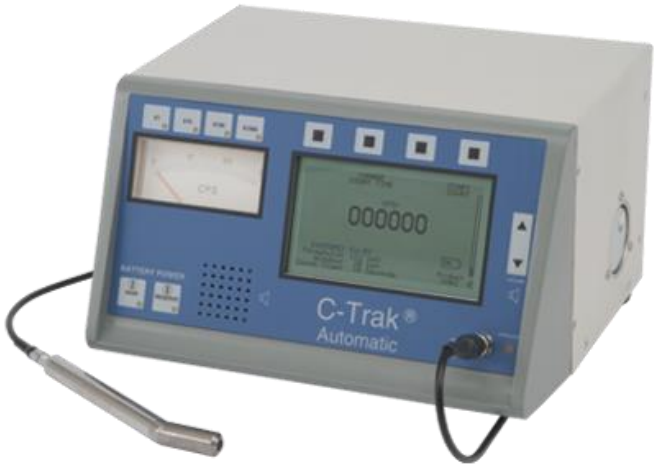

Figure 1.2: A basic gamma probe system (Taken from Southern Scientific Limited, Retrieved 3 September 2018, http://www.southernscientific.co.uk. With permission.)

There are two types of surgical gamma probes; scintillation detector and semiconductor detector probes. Scintillation detectors are high sensitive probes while semiconductor detectors are better in energy resolution but low sensitive probes. The selection of the gamma probe is dependent on the type of the surgical procedure (10) for example, high sensitive scintillation detector probes are the most appropriate probes to be used with sentinel lymph node studies to detect the exact location of small lymph nodes during surgery.

1.2.2 Portable gamma cameras

The advances in technology make the availability of mobile or portable gamma cameras possible. They enable the patient to be imaged either bedside and/or inside the operating theatre. The initial experience with a portable scintillation camera was used in 1973 by Hurwitz and his colleagues (11). Figure 1.3 shows one example of the commercially available solid state gamma camera. It is a LFOV gamma camera that designed for various patient studies such as cardiac studies, bone scan, lymphoscintigraphy, lung, liver, gastric emptying, renal and thyroid scans at patient

bedside. The camera head is attached to a rotatable parallel and slant-hole collimator (12).

Figure 1.3: ERGO – solid state gamma camera (Taken from Southern Scientific Limited, Retrieved 3 September 2018, http://www.southernscientific.co.uk. With permission.)

1.2.3 Handheld small field of view gamma camera

Converging multi-hole collimators have been used with large field of view (LFOV) gamma cameras to improve sensitivity and spatial resolution (13). As a larger area of the detector is used, the photon efficiency is also improved. Recently, a pinhole collimator has been used with small field of view (SFOV) to give similar detection efficiency and offer high spatial resolution (14). The introduction and development of the concept of the handheld gamma imaging system was performed in 1984 by Barber and co-workers (15). Barber et al., have developed a small prototype gamma ray imaging device capable to be inserted into the upper or lower gastrointestinal tract (GIT) to image the accumulation of radioactive material within tumour.

In medical imaging, SFOV cameras have been used as small-organ dedicated systems particularly for intraoperative imaging, such as for the breast to assess sentinel lymph node mapping/ biopsy, the thyroid in parathyroid gland surgery, malignant melanoma

and radiopharmaceutical guided surgery (16). The design of the SFOV gamma cameras is similar to conventional LFOV gamma cameras. It consists of imaging detector, collimator, shielding, readout and control electronics system and gamma image acquisition and processing software. The most essential characteristics of a SFOV gamma cameras that it have a small and compact size and light weight to be easily carried and flexible to move closely around the patient. The second main characteristics of the camera are small field of view with superior resolution of less than 1 mm, as opposed to a few millimetres in the conventional large gamma cameras.

From the literature it has been found that the appropriate weight of SFOV gamma camera heads to be used for clinical procedures were ranging between 320 g (17) and 2490 g (18). However, the size of the imaging detector varied from 8.192 mm x 8.192 mm (19) up to 127 mm x 127 mm (20). Researcher from all over the world have encouraged to explore and develop this new technology of SFOV handheld gamma cameras. Examples of the currently available SFOV gamma cameras are illustrated in Figure 1.4. Figure 1.4A is an example of the IP Guardian2 portable SFOV gamma camera with a CsI:TI scintillator detector coupled to position sensitive photomultiplier tube manufactured by Li-Tech SpA, Italy. Figure 1.4B is an example of an imaging gamma probe produced by Crystal Photonics known as the CrystalCam which is designed to have an interchangeable tungsten collimators to be used with various range of energy radionuclides. Figure 1.4C illustrates an example of a SFOV gamma camera integrated with pinhole collimator and CsI:Na scintillator detector coupled to position sensitive photomultiplier tube, this gamma imaging device known as Sentinella. Figure 1.4D shows a mini gamma camera 500 (MGC500) which has a parallel hole collimator, Produced by Acrorad Co. Ltd.

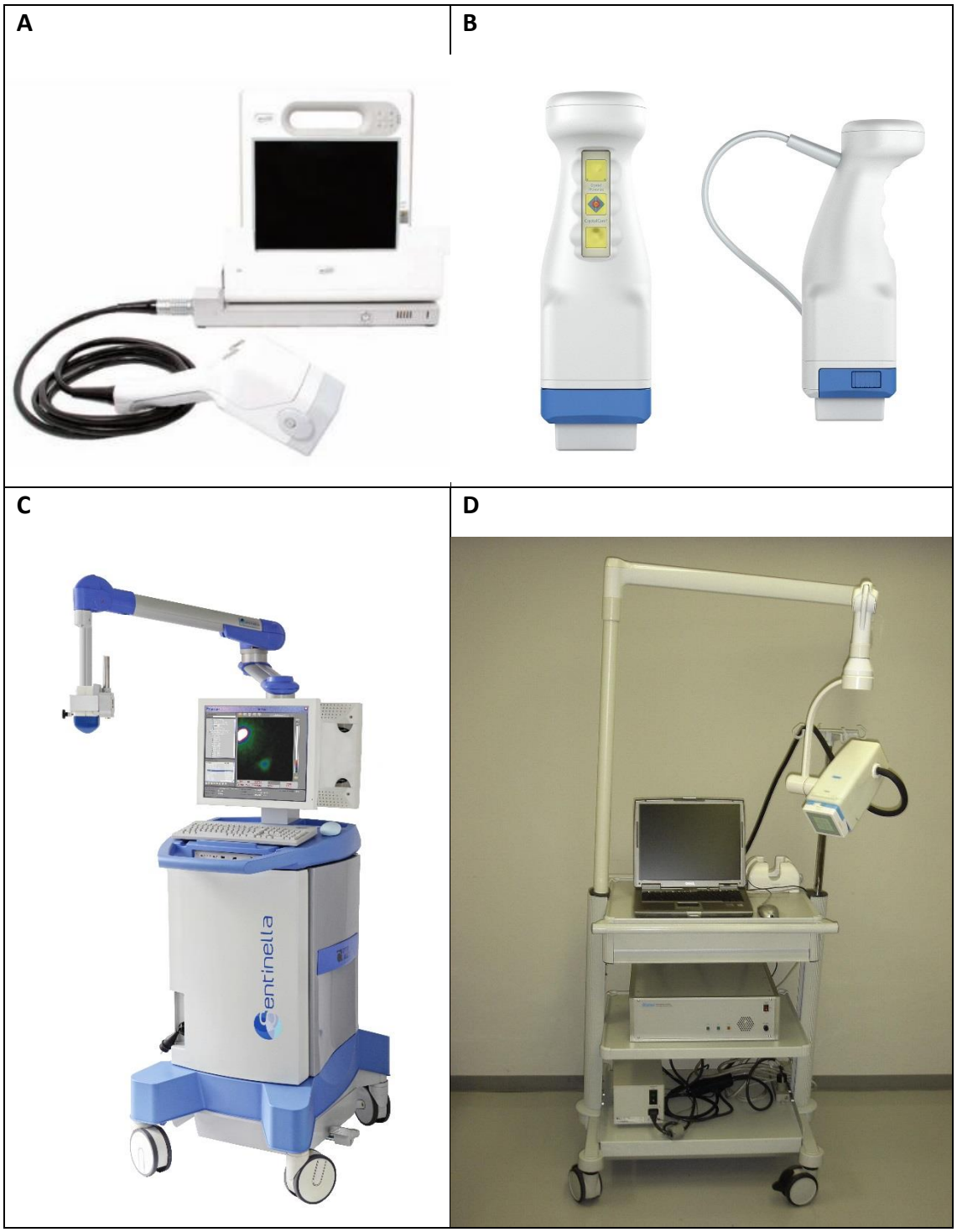

Figure 1.4: Examples of SFOV handheld gamma cameras. A) The IP Guardian2 portable gamma imaging system with a CsI:TI scintillator detector. B) The CrystalCam imaging probe with CdZnTe semiconductor. (Images courtesy of crystal photonics, Berlin). C) Sentinella 102 SFOV gamma camera with pinhole collimator. D) The small CdTe gamma camera system with parallel hole collimator mounted on the articulating arm. Taken from Perkins, A. C., Ng, A. H., & Lees, J. E. (2016). Small field of view gamma cameras and intraoperative applications, *Gamma cameras for interventional and intraoperative imaging*, Retrieved 4 September 2018. With permission from CRC Press.)

Table 1.1 summarises the characteristics of the currently available SFOV gamma cameras either as novel prototypes or in clinical use (21-23).

Table 1.1: Characteristics of SFOV intraoperative gamma cameras. Table retrieved 4 September 2018 from Perkins, A. C., Ng, A. H., & Lees, J. E. (2016). Small field of view gamma cameras and intraoperative applications, *Gamma cameras for interventional and intraoperative imaging*. With permission from CRC Press.

Camera	Detector			Detector head		Collimator	
	Type/ Material	FOV (mm)	Matrix size	Size (mm)	Weight (g)	Type	Material
IOGC	Hg_2I, electrodes	23.75x 23.75x1	16x16	43x45	NA	Parallel hole	Tungsten
POCI2	CsI:Na, IPSD	Ø 40x3	50x50	Ø95x90	1200	Parallel hole	Lead
TreCam	$LaBr_3$:Ce, MAPMT	49x49x 5	16x16	NA	2200	Parallel hole	Lead
Mediprobe	CdTe:Cl	14.08x 14.08x1	256x 256	200x70 X30	1500[a]	Pinhole	Tungsten
eZ Scope	CZT	32x32x 5	16x16	74x72 X210	820	Parallel hole	NA
MGC500	CdTe	44.8x 44.8	32x32	82x86 X205	1400[a]	Parallel hole	Tungsten
IHGC	NaI:Tl, PSPMT	50x50 X6	29x29	64x64 X76	1100	Parallel hole	Lead
IP	CsI:Tl, PSPMT	44.1x 44.1x5	18x18	NA	1200	Parallel hole	Tungsten
GE	CZT	40x40	16x16	150(L)	1200	Parallel hole	NA
Sentinella 102	CsI:Na, PSPMT	40x40	300x 300	80x90 X1500	1000*	Pinhole	Lead
GCOI	CsI:Tl, PSPMT	38.4x 38.4x4	24x24	NA	NA	Parallel hole	NA
Crystal Cam	CZT	40x40	16x16	65x65 X180	800	Parallel hole	Tungsten
Minicam2	CdTe	40x40	16x16	250x170 X70	700	Parallel hole	Tantalum
MRG15	CsI:Tl, SiPM	13.2x 13.2x5	4x4	114x32 X26	320	Parallel hole	NA
CarollRes	GSO:Ce, MAPMT	50x50	8x8	78x78 X275	2490	Parallel hole	Lead
Medica GammaCam/ OR	NaI:Tl, PSPMT	127x 127x6	56x56	NA	NA	Parallel hole	NA

1.3 Radiation detectors

Radiation detectors are the sensing element in nuclear measurement systems and are commonly devices that convert radiation energy into an electronic signal. Detection of the radiation is related to the absorption of radiation and how it interacts with matter (24). There are several types of radiation detectors which are categorised according to the general mode of interaction mechanisms and process of recording the acquired data. Scintillation detectors and semiconductor detectors are typically used in medical imaging. The main purpose of scintillation in detectors is that the scintillator material converts higher energy incident photons into several lower energy photons. For traditional gamma imaging, the scintillating material is coupled to photomultiplier tubes or photodiodes which amplify and convert the lower energy photons into electronic signals which can then be read out (25). On the other hand, instead of converting high energy particles into lower energy photons and then into an electronic signal, semiconductors are based on a more direct approach which converts photons directly into an electronic signal.

1.3.1 Hybrid Gamma Camera

The Hybrid Gamma Camera (HGC) is an example of a scintillation based camera. It is a new portable gamma camera with a small field of view. This new technology has been originally developed at Space Research Centre (SRC), University of Leicester in collaboration with Queen's Medical Centre, Nottingham. The work described in this thesis characterises the performance of the HGC using different scintillator materials. Also, described is a novel development dual radio near infrared (NIR) fluorescence imaging camera.

1.3.2 CdTe X-ray and gamma ray detectors for imaging system

Cadmium Telluride (CdTe) based semiconductor detectors have been used in imaging systems with the potential to take the place of the most commonly used scintillating materials such as CsI:TI and NaI:TI in gamma cameras (26). Although the use of CdTe detectors in medical imaging systems is limited, there are some applications of the detector in diagnostic imaging. Conventional mammography offers the potential for screening of breast cancer. Hybrid CdTe pixel detector arrays have been developed to convert the incident X-ray photons directly into charge signals. According to Yin et al. (27), good quality images can be obtained using CdTe detectors which means that this is a promising material for radiation detection. But there are some limitations which need to be considered such as a redesign of the readout chip to produce a digital mammography system having a sufficient efficiency and high resolution.

Also, a novel high-resolution spiral breast CT technology has been developed by Kalender et.al (28, 29) this new dedicated breast CT technology based on using a direct conversion CdTe material and photon counting electronics which contain 100 µm detector element size. The provided information from the acquired CT images are useful in diagnosing the presence of microcalcifications in the breast and assessing the soft tissue structures at very low dose comparing to conventional mammography.

Furthermore, a new technology of an imaging probe based on semiconductor detectors has been developed. According to Russo et al. (30), the CdTe probe prototype localise all of the SLNs precisely and effectively but the reduction in sensitivity is a limitation.

All of the above examples of CdTe semiconductor based on X-ray and gamma-ray detectors in imaging system, may indicate that the development of semiconductor detectors have the potential to be highly competitive for high imaging performance with the existing imaging devices based on scintillators.

1.4 Optical imaging

Optical imaging is a standard imaging technique which has been used for centuries. Unlike nuclear medical imaging, optical imaging generates images using non-ionising radiation it requires photon interaction with biological system to provide images of soft tissues with high resolution. Thus, images are produced depending on the cell properties when electrons are excited in order to capture absorption, emission, reflection, scattering and fluorescence of visible and infrared light. Endoscopy is one example of optical imaging which is used to detect gastrointestinal problems. Optical imaging technology is highly efficient, compact, portable and low-cost. The main drawback of optical imaging is that it has poor depth penetration in tissue. Therefore the large dimensions associated with human tissue and organs will lead to high absorption and scattering of light comparing to that of X-rays and gamma rays (31).

In biomedical research, fluorescence based optical imaging is an emerging technique for functional imaging of biological tissue. The use of near infrared (NIR) light gives the imaging system the ability to increase the penetration of the human tissue to greater depths. However, the maximum penetration that the system can achieve cannot exceed 25 mm (32). The fundamental process of fluorescence imaging is the generation of light which is either generated internally by releasing energy from a chemical reaction (i.e. bioluminescence), or by an external light source. Therefore, the fluorescence image is dependent on the absorption and emission characteristics of the spectrum at certain wavelengths. A typical fluorescence imaging system consists of an imaging system to acquire the fluorescence images, light sources to produce the desired signal, optical filters to allow transmission of fluorescence emission and to reject unwanted light signals and detectors and photon detectors to collect signals (33).

1.5 Gamma and optical imaging modality systems

Positron emission tomography (PET) is a molecular imaging modality which allows the physicians to visualise the metabolic processes in human's body. The main concept of

PET imaging technology relies on the detection of pairs of gamma rays which are emitted indirectly by a positron-emitting radiopharmaceuticals. In recent years, Parout and his research group at the University of California, Los Angeles (UCLA) crump Institute for Molecular Imaging (CIMI) have designed and developed a small animal imaging system called optical PET (OPET) (34). This novel technology has the ability to detect both high energy coming from gamma rays in addition to optical wavelength photons. Optical imaging technology alone is limited in humans as it has poor penetration of visible light photons into living tissues. So, the introduction of optical imaging to be combined with PET imaging will permit simultaneous optical and PET imaging of small animal using the same imaging detector (34, 35).

Another hybrid imaging system is the integrated PET and three dimensional (3D) fluorescence optical tomography (FOT) PET-FOT for small animal imaging, which have been designed and built by Changqing Li and co-workers at the University of California, Los Angeles (UCLA) (36) aiming to characterise both temporal and spatial distribution simultaneously using combined optical and PET signals. Small animal imaging using PET alone can produce an image with spatial resolution of ~ 1mm. While 3D FOT can record an image with spatial resolution around several millimetres at depth. However, the optical image acquired from combining those two modalities PET-FOT has improved spatial resolution to around 1 mm (37, 38).

1.6 Thesis aim

The three main aims of this thesis are firstly, to fully characterise the Hybrid gamma camera (HGC) developed at the Space Research Centre (SRC), University of Leicester in collaboration with Queen's Medical Centre, University of Nottingham to determine the suitable choice of scintillator materials to be used for diagnostics nuclear medical imaging. Secondly, to evaluate the performance characteristics of Cadmium Telluride (CdTe) semiconductor detectors in nuclear medical imaging specifically on intraoperative imaging applications. Thirdly, to investigate the capability of the HGC system to be integrated to the modified near infrared (NIR) fluorescence camera to be

used as a dual imaging system known as dual radio near infrared (NIR) fluorescence camera.

1.7 Thesis outline

Chapter 2 presents a theoretical background of the interaction of gamma radiation with matter, also provides a brief explanation of the commonly used radiation detectors using scintillators and semiconductor detectors in nuclear medical imaging. Chapter 3 describes the design of the Hybrid gamma camera (HGC), the anthropomorphic phantoms developed for the performance characterisation of the HGC and clinical patients imaging conducting at Queen's Medical Centre, Nottingham. Chapter 4 provides a full details of the protocols for assessing the performance of small field of view (SFOV) gamma cameras. Chapter 5 compares the performance characteristics of the HGC using different scintillator materials such as: Thallium doped caesium iodide (CsI:TI) scintillator, Gadolinium oxysulfide (GOS) scintillator and Cadmium Tungstate $CdWO_4$ scintillator. Chapter 6 investigates the characteristics of the Cadmium Telluride (CdTe) semiconductor detectors (i.e. XRI-UNO system and HEXITEC detector) in nuclear medical imaging and aims to determine if semiconductor detectors can replace the scintillator-based detectors in the HGC. Chapter 7 evaluates the performance of the HGC for near infrared fluorescence imaging. Finally, Chapter 8 summarises the work done in the thesis and further future work is suggested.

1.8 Personal contribution to this work

The HGC system described in this work were fully designed and developed by my supervisors at Space Research Centre, University of Leicester in collaboration with Queen's Medical Centre, University of Nottingham before I have joined the research group. Then, the HGC system continues to develop over the course of my PhD studies in collaboration with my colleagues at both University of Leicester and University of

Nottingham. I fully performed the characterisation of the HGC using three different scintillator materials; CsI:TI, GOS and $CdWO_4$ scintillators which are fully described in Chapter 5 in this thesis. I have also fully characterised the CdTe detectors; XRI-UNO system and HEXITECH in Chapter 6. Finally, in Chapter 7 in vitro imaging work for fluorescence imaging was fully carried out by me. However, the in vivo work was carried out in corporation with the research group at Leiden University Medical Centre (LUMC), Leiden, The Netherlands.

Chapter 2

Radiation detection using scintillators and semiconductor detectors

Radiation detectors are the sensing element in nuclear measurement systems that convert radiation energy into an electronic signal. Detection of radiation is related to the absorption of radiation and how it interacts with matter (24). Therefore, the interaction mechanisms depend on the energy transfer to matter when it passes through it. The energy transfer mechanisms could cause either ionisation and/or excitation of atoms and molecules. Furthermore, the radiation that is emitted during radioactive decay is so called ionising radiation.

There are several types of radiation detectors which are categorised according to the general mode of interaction mechanisms and process of recording the acquired data. Scintillation detectors and semiconductor detectors are typically used in medical imaging.

In order to understand the effects on the performance of the radiation detector for the small field of view (SFOV) hybrid gamma camera (HGC) a good understanding of how scintillator and semiconductor detectors work is essential.

2.1 Gamma ray attenuation

2.1.1 Attenuation coefficients

When an X or gamma ray pass through a material, the photon may either be absorbed, scattered or travel through the material without interaction. If the gamma photon is absorbed or scattered, in this case it has been attenuated. In the absorption process, the energy of the photon beam is transferred to atoms of the targeted material while in the scattering process, the travel direction of the photon beam is diverted during one or more interactions (39).

So, a simple exponential attenuation of the primary energetic photon beam will result when a γ-ray passes into a material (25). The possibility of occurrence per unit path length in the absorber is known as the probable interaction process. The total probability per unit length that the photon is removed from the beam can be found by taking the sum of all the possibilities. This is called the linear attenuation coefficient, μ and has units of inverse length (cm^{-1}). In other words, the linear attenuation coefficient known as the fraction of a photon beam of X or gamma rays that is absorbed or scattered per unit thickness of the absorber. The intensity of photons transmitted through a thickness *t* is given by the Beer-Lambert law:

$$I_{trans} = I_0 \, e^{-\mu t} \tag{2.1}$$

where, I_0 is the initial intensity of photons, t thickness of the attenuator, μ linear attenuation coefficient. As seen from equation 2.1, the Beer-Lamber law describes the attenuation of light to the properties of the material through which the light is travelling.

However, the intensity of photons absorbed by the material can be calculated by:

$$I_{Abs} = I_0 \, [1 - e^{-\mu t}] \tag{2.2}$$

As the photon interaction mechanisms are energy dependent, the linear attenuation coefficient depends mainly on energy. The attenuation is usually expressed using the mass attenuation coefficient $\mu_m = \mu/\rho$ where ρ is the density of the medium (gcm^{-3}). Thus, the mass attenuation coefficient unit is (cm^2g^{-1}).

2.1.2 Absorber mass thickness

In regard to mass attenuation coefficient μ_m, the attenuation equation for γ-rays could be:

$$\frac{I}{I_0} = e^{-(\mu/\rho)\rho t} \quad (2.3)$$

where ρt is the mass thickness of the absorber, which has unit of (gcm^{-2}). Thus, the degree of attenuation can be determined by the mass thickness of the absorber.

2.2 Interaction of radiation with matter

There are two significant types of radiation which are emitted during radioactive decay process. Those general types are charged-particles such as alpha (α) particles and beta (β) particles and electromagnetic radiation (high energy photons) such as γ rays and X- rays.

2.2.1 Gamma rays

High energy gamma (γ) rays interact with matter in complicated interactions mechanisms with the constituent atoms, nuclei and electrons. There are three primary different ways by which γ rays interact with matter. These are Photoelectric effect, Compton scattering and Pair production. Figure 2.1 illustrates the photon interaction mechanisms for lead as an example as a function of photon energy (MeV) and the mass attenuation coefficient (cm^2g^{-1}).

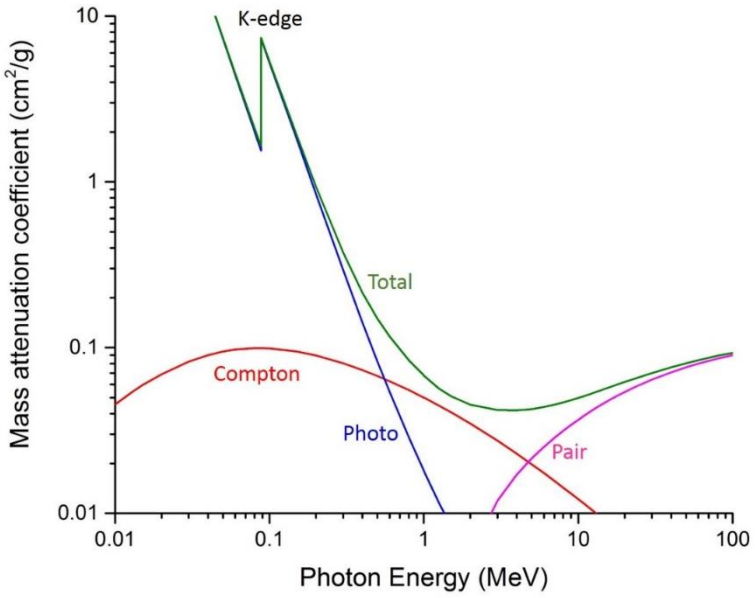

Figure 2.1: Photon mass attenuation coefficient (cm^2g^{-1}) for lead as a function of photon energy (MeV). (Blue line) shows the photoelectric effect, (red line) shows the Compton scattering and (pink line) shows the pair production. This plot was derived from mass attenuation values taken from XCOM (40).

2.2.2 The photoelectric effect

Also called photoelectric absorption, which occurs when the energy of the incident photon is completely absorbed by an electron in an inner atomic shell. The incident photon will disappear and the energy absorbed by the electron when is ejected from the atom. The ejected electron is called a photoelectron, Figure 2.2 shows the process of the photoelectric absorption. The photoelectron will have a kinetic energy E_e which is given by:

$$E_e = hv - E_b \qquad (2.4)$$

where E_b is the binding energy of the photoelectron in its original shell from which it was ejected. h is Plank's constant and v is the frequency of the incident radiation.

The photoelectric interaction occurs only with bound electrons as the entire atom is essential to conserve momentum.

Once, a vacancy is left behind in one of the bound shells of the absorber atom it is now, ionised and in an excited state. The vacancy created by the photoelectron is filled

immediately by a free electron from a higher shell of the atom or from an adjacent atom. Therefore, characteristics X-ray may also be emitted. However, some of the generated X-rays may be reabsorbed due to photoelectric absorption by the outer shell orbital electrons. When this occur and the characteristic X-ray interacts with an electron from a farther shell then it will eject it from the atom. Thus, known as Auger electrons (41).

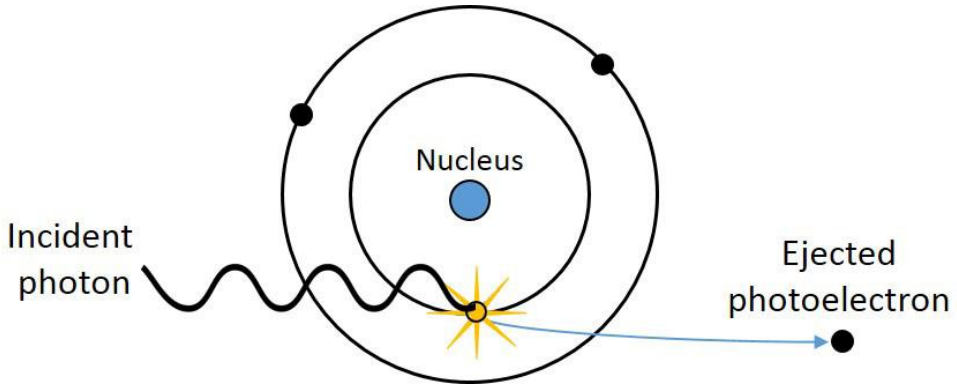

Figure 2.2: Schematic illustration of the photoelectric absorption. The energy of the incident photon is absorbed and an amount is transferred to the ejected photoelectron.

2.2.3 Compton scattering

In Compton scattering interactions, the interaction occurs between an incident photon with a high energy and a loosely bound electron which is located in an outer shell of an atom. The incident photon is scattered from its original direction through an angle θ from a valance electron which is essentially regarded as being free. This electron is known as a recoil electron. Therefore, the incident photon dissipates a portion of its energy to eject the recoil electron by an angle Ø from its original direction. This ejected recoil electron will have kinetic energy equal to that of the energy absorbed from the incident photon. Figure 2.3 illustrates the Compton scattering mechanism. Both energy and momentum are conserved in the collision.

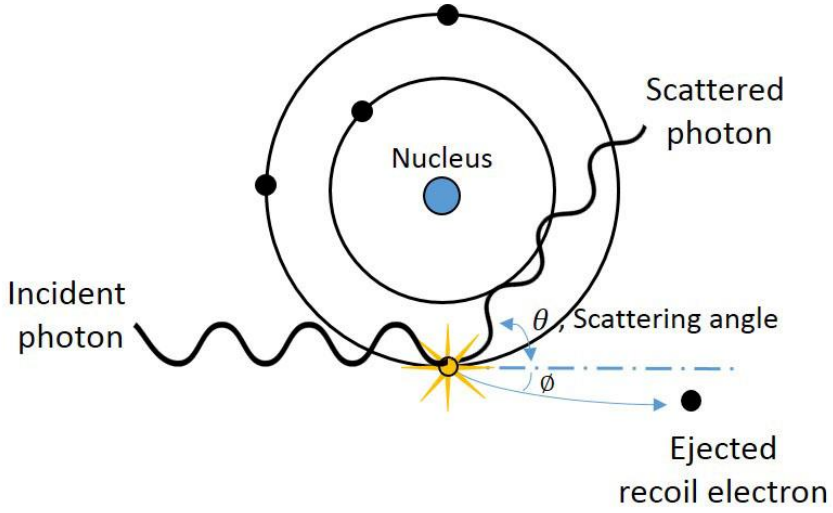

Figure 2.3: Schematic representation of Compton scattering. The incident photon dissipates a portion of its energy to the recoil electron and is scattered from its original direction by scattering angle θ.

The Compton scattered photon released from the collision travels in new direction with decreased energy and increased wavelength. Thus the Compton shift which is the change in wavelength of a Compton scattered photon is given by (41):

$$\lambda - \lambda_0 = \frac{h}{m_0 c}(1 - \cos\theta) \qquad (2.5)$$

Where $\lambda - \lambda_0$ is the Compton shift, λ is the photon wavelength after scattering, λ_0 is the photon wavelength before scattering, h is Plank's constant (h = 6.626 x 10^{-34} Js), m_0 the mass of an electron (m_0 = 9.1 x 10^{-31} Kg), c is the speed of light (c = 3 x 10^{-8} ms^{-1}), and θ is the scattering angle of the photon. The term $\frac{h}{m_0 c}$ is often called the Compton wavelength.

Based on equation 2.5, the energy of a scattered photon can be calculated by (42):

$$E_{sc} = \frac{E_0}{1 + \frac{E_0}{m_0 c^2}(1 - \cos\theta)} \qquad (2.6)$$

Where E_{sc} energy of the scattered photon, E_0 incident photon energy. The amount of scattered photon energy does not rely on the density, atomic number, or any other property of the absorbing material. Thus, Compton scattering is mainly a photon-electron interaction.

2.2.4 Pair production

Pair production occurs when the γ-ray has an energy above 1.022 MeV, thus during interactions the incident photon disappears and all of its energy is used to produce an electron-positron pair. The kinetic energy transferred to the electron-positron pair goes to each component equally, as both of the electron and positron have an equivalent rest mass of 0.511 MeV. The kinetic energy of the electron and positron dissipated in ionisation and excitation interactions. Figure 2.4 represents the Pair production process.

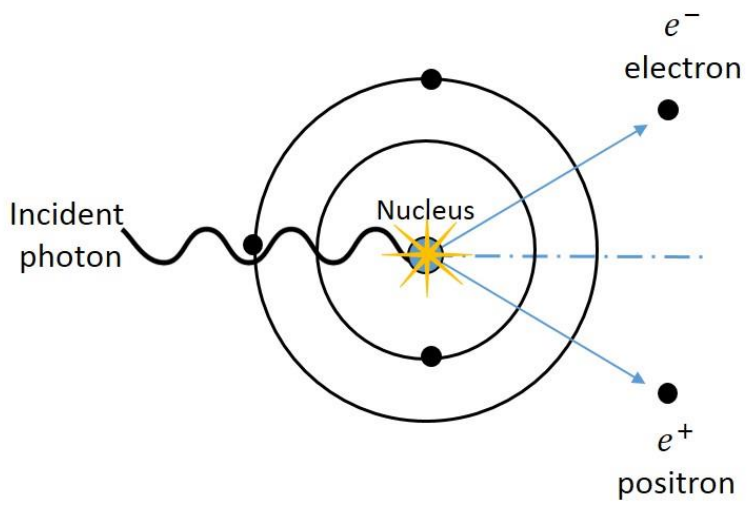

Figure 2.4: Schematic illustration of Pair production. The energy of the incident photon used to produce an electron-positron pair.

2.3 Scintillation detector principles

As discussed in the first section of this chapter, radiation from radioactive materials releases energy when interacting with matter. Most of that energy is dissipated as thermal energy. However, in some materials the energy is released as visible light. This process is called scintillation and these materials are known as scintillators and the radiation detectors made from them are called scintillation detectors (43). The main purpose of scintillation in detectors is that the scintillator material converts higher energy incident photons into many lower energy photons. For traditional gamma imaging the scintillating material is coupled to photomultiplier tubes (PMTs) or

photodiodes that amplify and convert the lower energy photons into electronic signals which can then be read out (25).

There are two types of scintillation material that are used in nuclear medical imaging; inorganic scintillators and organic scintillators. Inorganic scintillators are solid crystals made of alkali-halides such as NaI and CsI. Thallium is used as activator to shift scintillation emission into the visible range of the spectrum. (NaI:TI) is the most frequently used scintillation crystal. Organic scintillators on the other hand are either plastics or liquid composed of aromatic hydrocarbons (24). The scintillation processes for inorganic and organic scintillator are different in their behavior. In a simple way, the scintillation light in inorganic scintillator produced by the crystal lattice itself. However, in organic scintillator the scintillation light arises from transitions in the energy levels of a single molecule. For the purpose of this thesis, the mechanism of the inorganic scintillator will be described briefly.

The scintillation process for the inorganic scintillator occur in the electronic band structure in inorganic scintillator material. The incident γ or X-rays excite weakly bound electrons of their individual atoms or molecules from the valance band into the conduction band. On return back to the valence band a photon is emitted in the band gap which may not be the visible light frequency range. Therefore, those emitted photons can only be absorbed by crystals themselves without converting signals. In order for the scintillators to produce more visible photons an activator like thallium needs to be added to the crystal. This activator will provide states within the crystal which allows emission of photons having lower energy. The performance of the scintillator detector will improve by collecting more visible light at the readout (44). Figure 2.5 illustrates the scintillation mechanism in inorganic crystals.

The common characteristic for all scintillator materials is that the total amount of the visible light produced is proportional to the energy deposited in the scintillator. The amount of visible light produced ranges between a few hundreds to few thousands photons for photons with energy in the 70 - 511 keV range (45).

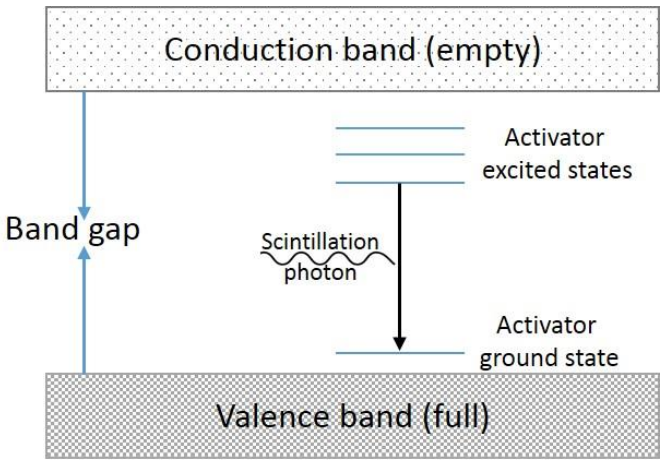

Figure 2.5: Energy band structure in inorganic scintillator material.

2.3.1 Scintillator materials

The choice of a particular scintillator material for a specific nuclear medical application is determined by several factors. The scintillator materials should have high absorption efficiency for the incident photons to convert the absorbed photons to scintillation photons, high light yield (i.e. proportional to the absorbed energy) and low afterglow. Another two factors are peak emission wavelength and refractive index which is should be comparable to that refractive index of glass (i.e. ~ 1.5) in order to be capable of obtaining a good coupling efficiency to detection optics those factors have an influence on the overall efficiency of the incident photon detected (46). For the experimental research of this thesis three scintillator materials were considered and will be discussed in detail. Those scintillator materials are: Thallium doped Caesium iodide (CsI:TI), Gadolinium oxysulfide (GOS) and Cadmium tungstate ($CdWO_4$). Table 2.1 summarises and compares the properties of these scintillator materials for the photons from ^{99m}Tc at 140.5 keV which is the most commonly used radioactive source in nuclear medicine investigations.

On the Anger-type gamma camera, the NaI:TI scintillator has been chosen for nuclear medical imaging because it is relatively low cost and it is easy to grow into the large crystals. However, on small field of view gamma cameras NaI:TI scintillator is also used in addition to CsI:TI scintillator. As various studies prove its suitability and efficiency in

multiple applications (47). The CsI:TI scintillator possess several properties which make it a good scintillator to be used which will be discussed in the next section.

Table 2.1: Comparison of some properties of CsI:TI, GOS and $CdWO_4$ scintillators. NaI:TI scintillator has been mentioned as it is the common scintillator used with large field of view (LFOV) gamma cameras. Theoretical sensitivity has been calculated using (Equation 2.2). Table reproduced from Bugby et al (48).

Parameter	**NaI:TI**	**CsI:TI**	**GOS**	**$CdWO_4$**
Density (gcm^{-3})	3.67	4.51	7.32	7.9
Attenuation coefficient at 140.5 keV (cm^2g^{-1})	0.713	0.855	1.101	1.180
Photon yield (per keV)	38	52-66	35-50	27
Peak emission wavelength (nm)	415	550	512	495
Refractive index at peak emission	1.85	1.79	2.2	2.2-2.3
Theoretical absorption for 140.5 keV photons (1500 μm thickness)	32.5%	43.9%	70.1%	75.3%

Some studies mention that the use of pixelated scintillator is usually improve the image contrast and provide higher image resolution (49). According to that, pixelated scintillator have been chosen to be tested in this thesis. Both of GOS and $CdWO_4$ scintillators have been tested due to their availability in the University of Leicester laboratory.

2.3.2 Properties of Caesium iodide (CsI:TI)

Caesium iodide (CsI:TI) scintillator is one of the most common scintillators used in nuclear medical imaging. It has a high gamma ray stopping power due to its relative high density 4.51 gcm^{-3} and high atomic number of 54. Its emission spectrum is in the visible range with a broad peak at 550 nm. It is one of the brightest scintillators as it has a light output of 54 photons/keV (50). In order to activate the scintillation emission, Thallium (TI) is doped into CsI scintillator. Columnar CsI:TI scintillator can be formed of needle-like micro-columnar material that preserves spatial resolution by allowing scintillation light to exit the surface through internal reflection within the scintillator and minimising the spread of the optical photons, as shown in Figure 2.6. The thickness of the

scintillators has an effect on the probability of stopping gamma rays emitted by the radioactive material and thus can affect the sensitivity of the system.

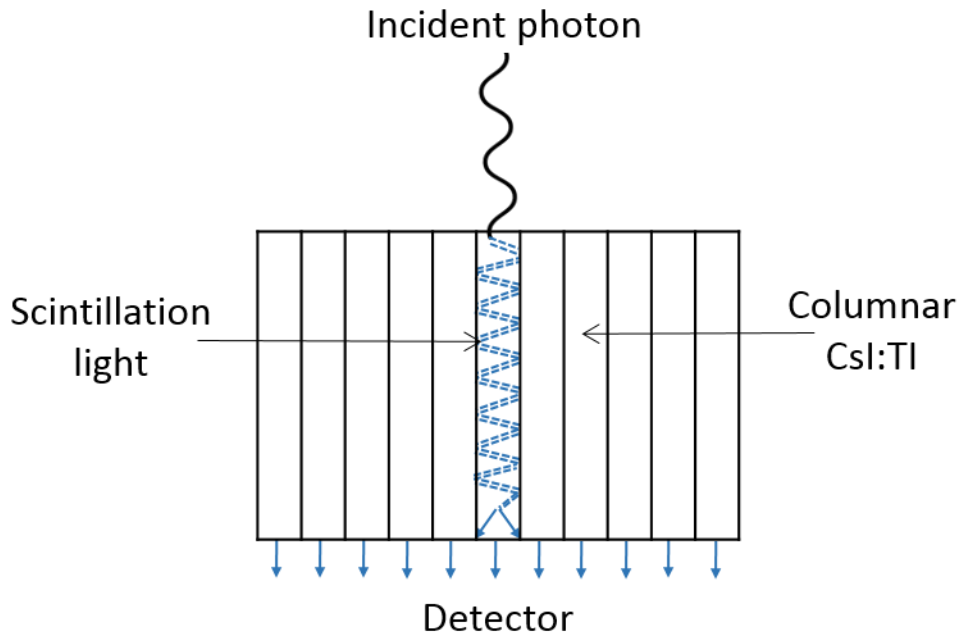

Figure 2.6: Schematic diagram of the columnar CsI:Tl scintillator illustrating the effect of the columnar crystal on improving spatial resolution by preventing lateral spreading of light.

For CsI the mass attenuation coefficient is 0.855 cm^2g^{-1} at a photon energy of 140.5 keV and its density is 4.51 gcm^{-3}, therefore the linear attenuation coefficient μ is 3.85 cm^{-1} at 140.5 keV. A mass attenuation coefficient curve for the CsI:TI is plotted (by using IDL software (51)) as a function of photon energy, (see Figure 2.7).

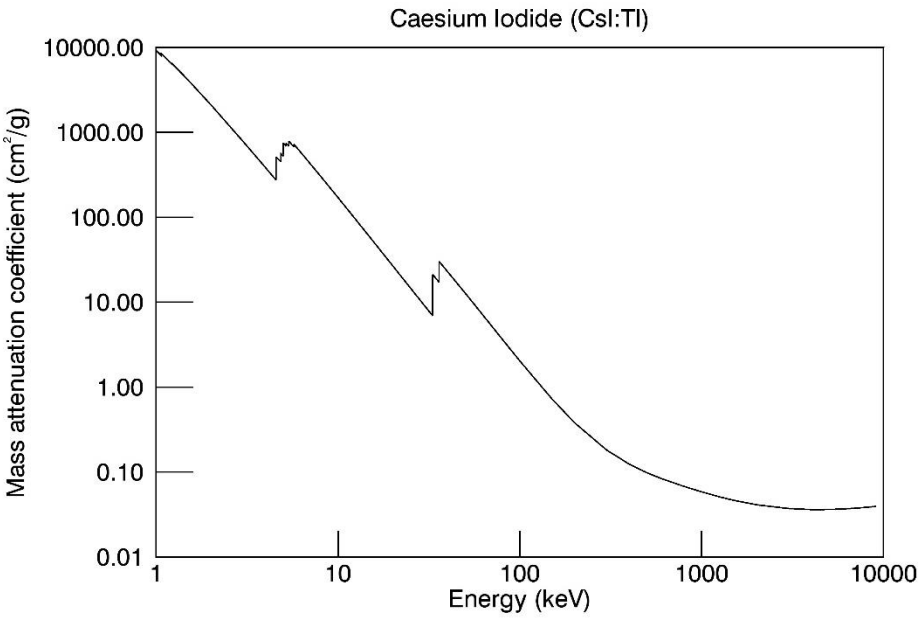

Figure 2.7: Mass attenuation coefficient (cm^2g^{-1}) curve of the CsI:Tl versus photon energy (keV).

The absorption curves for two thicknesses of CsI:Tl scintillator (i.e. 600 µm and 1500 µm) are shown in Figure 2.8 as a function of the photon energy (keV). The mass attenuation coefficients μ/ρ have been derived from the NIST database (40).

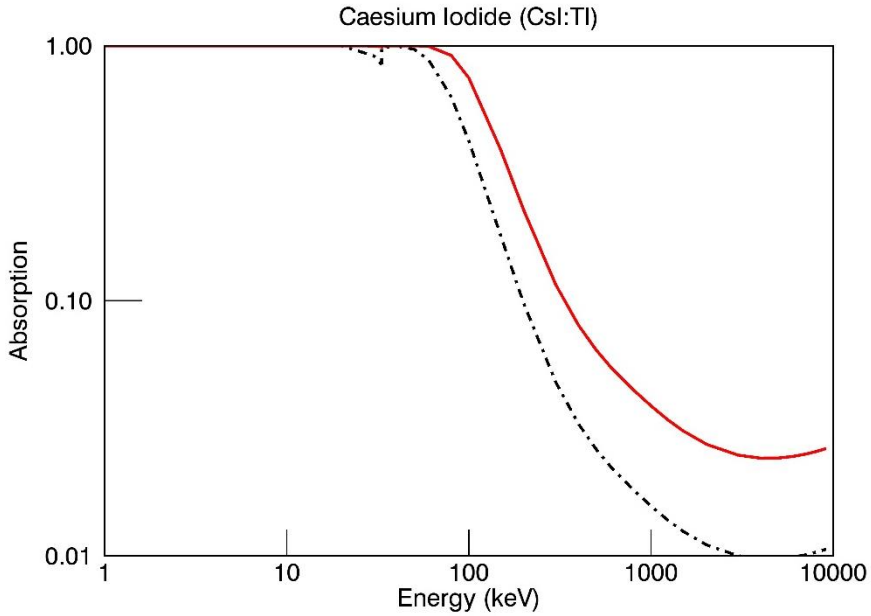

Figure 2.8: Caesium Iodide absorption curve for differing CsI:Tl thickness; 600 µm (black dash-dotted line), 1500 µm (red line).

It is worth to mention that at the early development of the hybrid gamma camera the 600 µm thick CsI:TI scintillator was first applied that is the reason behind using this thickness specifically. On the other hand, the 1500 µm thick CsI:TI scintillator then was chosen for comparison in this thesis as it is agreed that in literatures (52) increasing the thickness of a scintillator provide a good level of detectability, however, a poorer spatial resolution as increasing the thickness will increase the absorption percentage of the incident photons. To prove that the 1500 µm thick CsI:TI scintillator was used.

2.3.3 Properties of Gadolinium Oxysulfide (Gd_2O_2S)

Gadolinium Oxysulfide (GOS) is a translucent ceramic scintillator which is currently considered as an efficient scintillation material to be used for nuclear medical imaging. For GOS the mass attenuation coefficient is 1.101 cm^2g^{-1} at a photon energy of 140.5 keV and its density is 7.32 gcm^{-3}, therefore the linear attenuation coefficient μ is 8.06 cm^{-1} at 140.5 keV. A mass attenuation coefficient curve of the GOS is plotted as a function of photon energy, (see Figure 2.9).

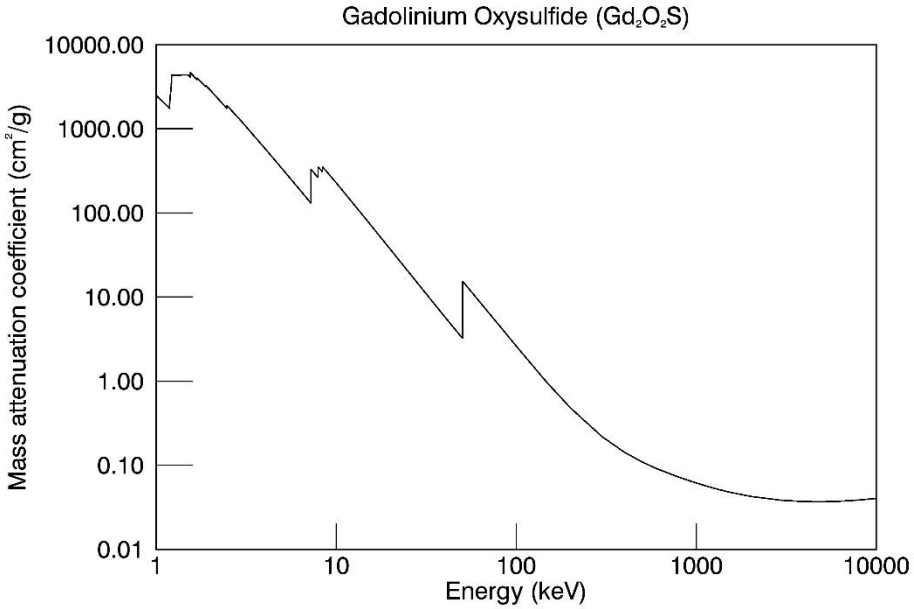

Figure 2.9: Mass attenuation coefficient (cm^2g^{-1}) curve of the GOS versus photon energy (keV).

The absorption curves for two thicknesses of GOS scintillator (i.e. 600 µm and 1500 µm) are shown in Figure 2.10 as a function of the photon energy (keV). The mass attenuation coefficients μ/ρ have been derived from the NIST database (40).

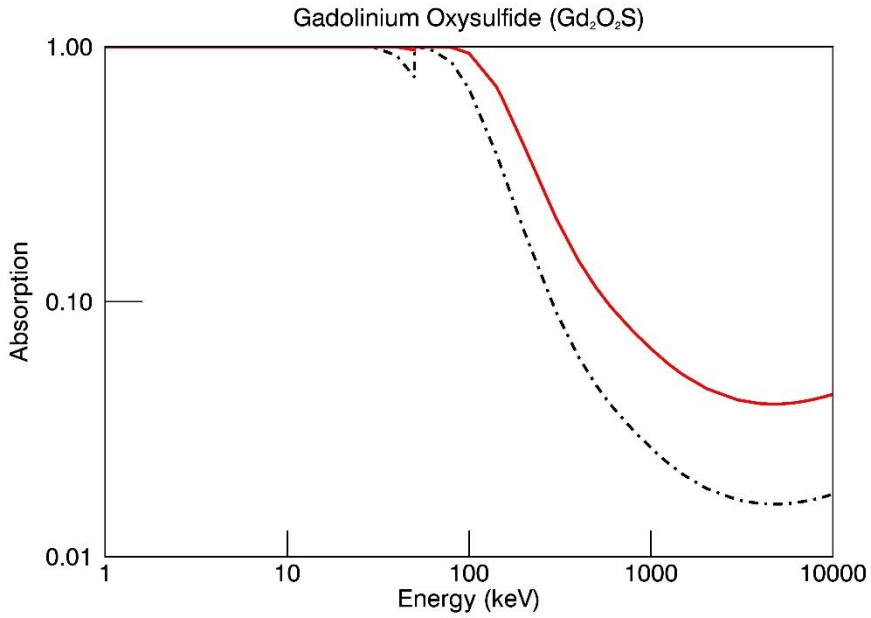

Figure 2.10: Gadolinium Oxysulfide absorption curve for differing GOS thickness; 600 µm (black dash-dotted line), 1500 µm (red line).

2.3.4 Properties of Cadmium Tungstate ($CdWO_4$)

Cadmium Tungstate ($CdWO_4$) scintillator is a transparent ceramic scintillator. Although it has been reported by Greskovich and Duclos (53) that when a radiation detector was coupled with a $CdWO_4$ scintillator, the resultant image was low quality and low contrast to noise ratio. This is mainly because that the $CdWO_4$ crystal is monoclinic which makes fabrication into scintillator material very difficult. Also it has low light output (i.e. 30 % less than that of CsI:TI). A $CdWO_4$ scintillator has been tested and compared to CsI and GOS scintillators.

For $CdWO_4$ the mass attenuation coefficient is 1.180 cm^2g^{-1} at a photon energy of 140.5 keV and its density is 7.9 gcm^{-3}, therefore the linear attenuation coefficient μ is 9.32 cm^{-1} at 140.5 keV. A mass attenuation coefficient curve of the $CdWO_4$ is plotted as a function of photon energy, (see Figure 2.11).

The absorption curves for two thicknesses of $CdWO_4$ scintillator (i.e. 600 µm and 1500 µm) are shown in Figure 2.12 as a function of the photon energy (keV). The mass attenuation coefficients μ/ρ have been derived from the NIST database (40).

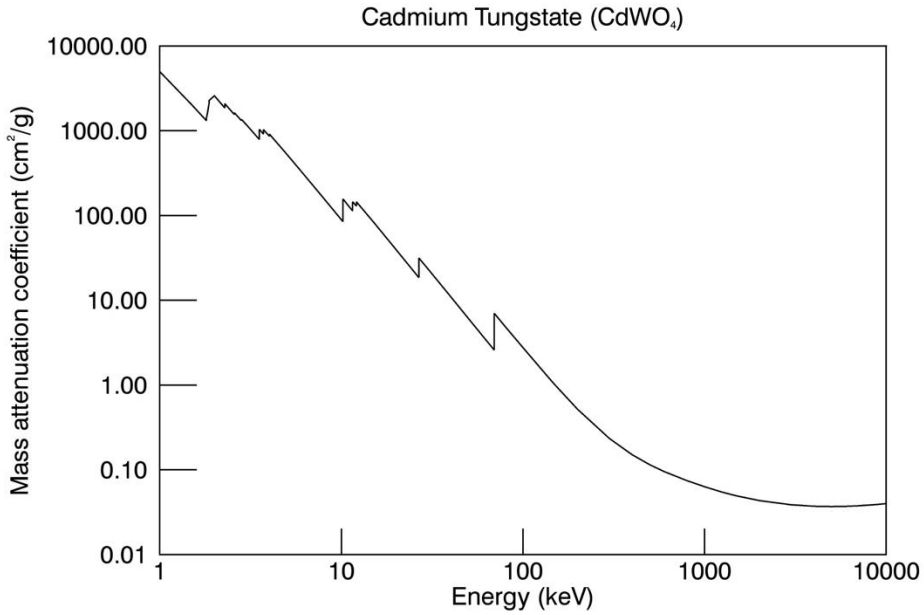

Figure 2.11: Mass attenuation coefficient (cm^2/g) curve of the $CdWO_4$ versus photon energy (keV).

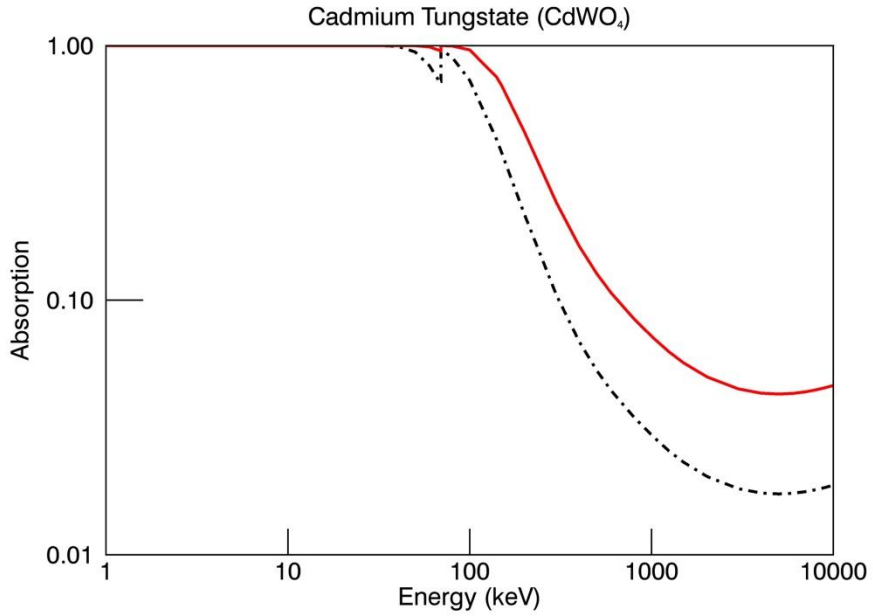

Figure 2.12: Cadmium Tungstate absorption curve for differing $CdWO_4$ thickness; 600 µm (black dash-dotted line), 1500 µm (red line).

The absorption curves for a range of CsI:TI, GOS and $CdWO_4$ scintillators having thickness of 1500 µm are combined and shown in Figure 2.13 as a function of the photon energy (keV).

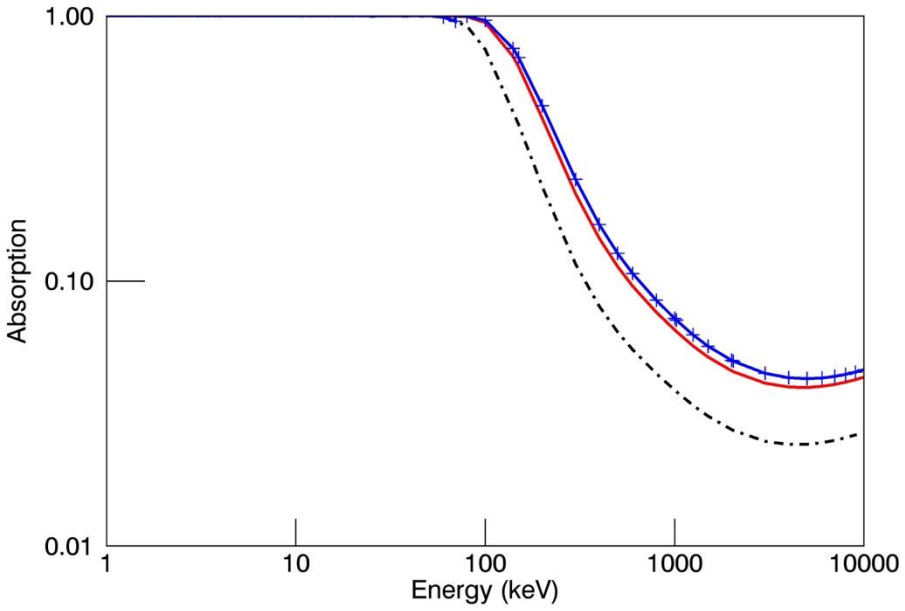

Figure 2.13: Absorption curve of 1500 µm thick for all scintillator materials; CsI:TI scintillator (black dash-dotted line), GOS scintillator (red line) and $CdWO_4$ scintillator (blue line with plus sign).

2.4 Photomultiplier tube

The incident scintillation photons from a standard large field of view (LFOV) gamma camera can be detected using photomultiplier tubes (PMTs). PMTs can convert the visible light into an electronic signal that is proportional to the incident photon energy. Figure 2.14 shows a schematic diagram of a scintillator detector coupled to a PMT. As shown in Figure 2. PMT is enclosed in a vacuum glass tube and composed of several parts; photocathodes which is a light sensitive material that transfer the incident photons into photoelectrons. A focusing electrode which directs the photoelectrons toward the dynode. The dynodes or electron multiplier that accelerate and amplify the photoelectrons at a positive bias within the PMT. The dynode is coated or made of a material that has the characteristics of ejecting multiple secondary electrons when a

high-speed photoelectron striking its surface. The process of acceleration and multiplication of those multiple secondary electrons is continued and repeated through many additional dynodes (usually 9 to 12), until it reach the final dynode, which is called the anode. The anode collects and receives the large output current of electrons and sends them to an external circuit (43). The electron multiplication factor depends on the energy of the photoelectron, which is determined by the voltage difference between the dynode and the photocathode. The PMT is coupled to the scintillator with an optical coupling material thus to reduce reflection losses.

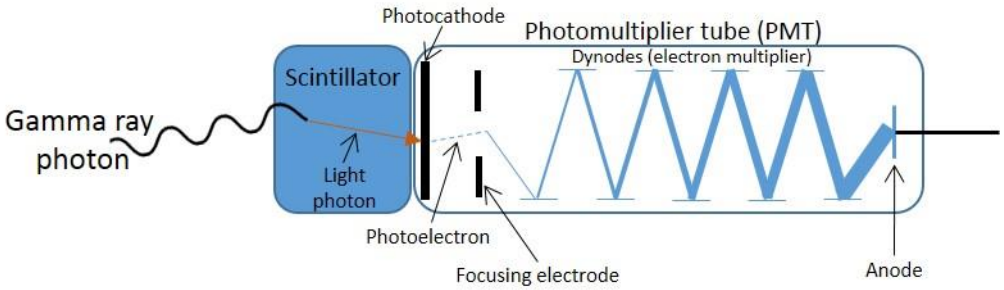

Figure 2.14: Schematic diagram showing the basic principles of the photomultiplier tube (PMT) in a scintillation detector.

The standard PMT can usually detect the gamma photon that enters the tube anywhere across its face, but it is not designed to determine the exact location from where the gamma photon entered. However, the new developed position sensitive photomultiplier tube (PSPMT) is able to detect exactly where the original gamma photon was received across the tube face. In a PSPMT, the dynodes are arranged in parallel layers. Each dynode is consisting of several separate channel. Several anodes are segmented into a corresponding channel. Thus provide an exact information and location at which the gamma photon is received and interacted. The design of the PSPMT is short which makes it possible to be used with a compact gamma cameras (54).

2.5 Charged coupled device

Charge coupled devices (CCDs) were invented over forty years ago by Willard Boyle and George Smith (1969). The CCD is a silicon (Si) based pixel array of metal oxide semiconductor (MOS) diodes that converts optical photons to electrical signals. In fact, the CCD started out as a memory device before it was discovered that it has the ability to be used as an image sensor. However, it was recognised by the researchers that the CCD could be able to be used as an image recording sensor through the photoelectric effect (55).

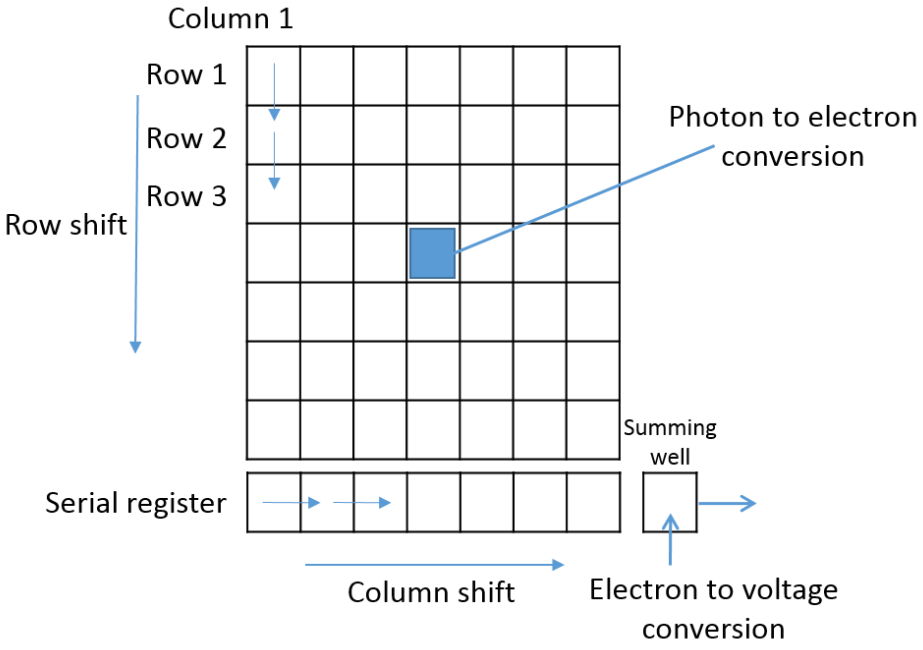

Figure 2.15: Schematic diagram showing the basic principles of the charge coupled device (CCD).

The CCD consists of number of light sensor elements known as photodiodes and potential well which can be considered as a bucket for photoelectrons, (see Figure 2.15). These elements are aligned in a two dimensional array on a thin layer of silicon substrate. When those photoelectrons are accumulated in each bucket and photon charge carriers are induced, the CCD is able to trap and hold them under suitable electrical bias conditions. Once all of the photoelectrons are shifted from one bucket down to the next row, then a time variable sequence is applied therefore the charges

will be physically shifted (i.e. serially pixel by pixel) toward a readout capacitance that acts as a charge to voltage converter (56).The output sequence of voltages are converted by external readout electronics (usually a computer) into a two-dimensional 2D digital image.

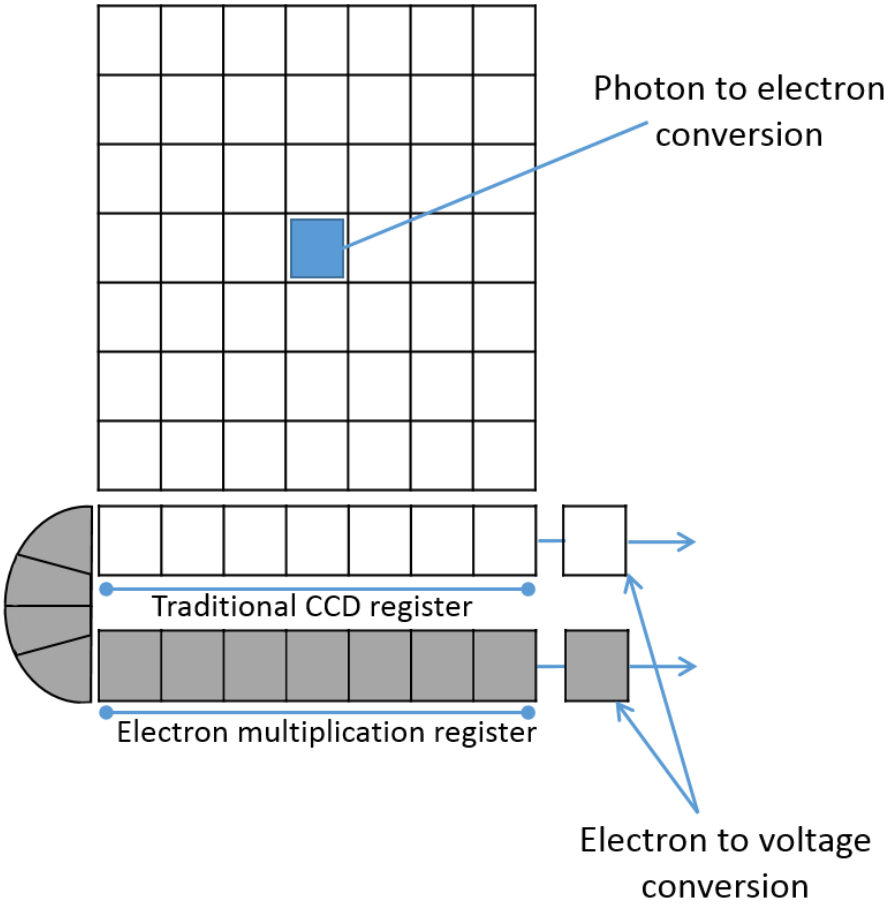

Figure 2.16: Schematic diagram showing the basic principles of the electron multiplication (EMCCD).

The EMCCDs have the same basic structure as normal CCDs, with additional feature of internal multiplication gain register, (see Figure 2.16). The addition of this gain will amplify the signal in CCD and make it less sensitive to read-out noise. Furthermore, CCDs are often categorised according to their illumination mode; either front illuminated CCDs or back illuminated CCDs. The illumination mode indicates whether photons incident on the front side of the detector or on the back side. Figure 2.17 illustrates the difference. For the purpose of this thesis the focus will be on the back illuminated CCDs.

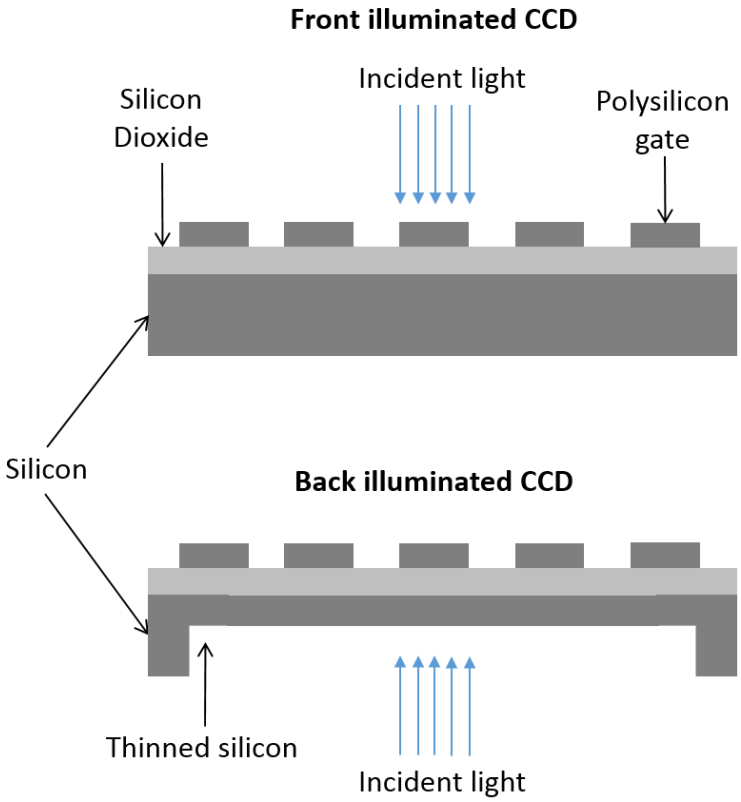

Figure 2.17: Schematic diagram illustrating the CCD illumination modes. Top: front illuminated CCD. Bottom: back illuminated CCD.

Back illuminated EMCCDs are devices having an extra post fabrication called thinning. This feature enables the photoelectrons to be diffused into the front side pixel well also it allows collection of the photoelectrons under the sites where they were generated. BI-EMCCDs have high quantum efficiency (QE), which is the percentage of the actual collected incident photons when striking the CCD that makes it more efficient device in detecting light. Also, BI-EMCCDs have small pixel size which increases the image resolution and sensitivity. For medical imaging applications the most effective design for CCDs is that the one which have very small pixel dimensions, to ensure that the output image has an excellent spatial resolution. The dynamic range describes the relationship between the pixel size of the CCD and the spatial resolution of the detector. Sometimes there is a change in the voltage timing pattern, so charge from multiple pixels is combined together during transfer to the serial register or during transfer to the output amplifier. This creates high charge capacity and allows for larger dynamic range which in turn reduces the image resolution.

2.6 Semiconductor detector principles

Instead of converting high energy particles into lower energy photons and then into an electronic signal, semiconductors are based on a more direct approach which converts photons directly into an electronic signal. The basic principle of semiconductors is that when a high energy photon hitting the semiconductor it will excite electrons from valance band to conduction band. This will produce pairs of conduction electrons and electrons vacancies (i.e. called hole), the combination of those two is called an electron-hole pair. If an electrical field is applied, the electrons in the conduction band tend to move as well as the hole which represent a net positive charge can be moved under the influence of the applied electrical field, but in an opposite direction of the electron. The movement of those two charges will contribute to the observed conductivity of the material. Figure 2.18 illustrates a schematic diagram of a semiconductor detector.

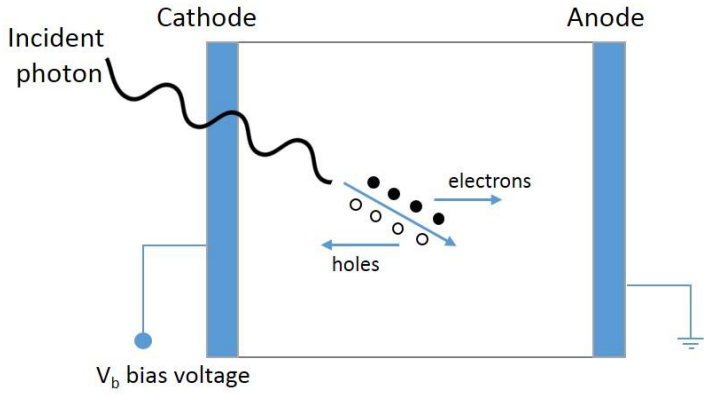

Figure 2.18: Schematic diagram of a semiconductor detector

In recent years, Cadmium Telluride (CdTe) or Cadmium Zinc Telluride (CZT) semiconductor detectors have been used in both standard and SFOV gamma camera system. Table 2.2 summarises some relevant properties of these semiconductor detectors used for medical gamma imaging.

Table 2.2: Comparison of some properties of CdTe, CZT and Silicon (Si) semiconductor detectors used in medical gamma cameras

Parameter	CdTe	CZT	Si
Density (gcm^{-3})	5.85	5.78	2.33
Effective atomic number (Z)	48-52	30-52	14
Attenuation coefficient at 140.5 keV (cm^2g^{-1})	0.705	0.680	0.149
Ionisation energy (eV)	4.43	4.46	3.62
Fano factor	0.1	0.089	0.16
Bandgap (eV)	1.50	1.57	1.12

The biggest advantage of semiconductors is that some are able to operate at room temperature and which allows for smaller more compact detectors, as they are not required to house a cooling device. Some of the main advantages of semiconductors over scintillators are the relatively better energy resolutions obtained, variable thickness without loss of spatial resolution and compact sizes (25). Semiconductors can also measure higher count rates, which when coupled with faster timing capabilities, greatly reduces the pile-up effects seen in scintillators (57). The intrinsic spatial resolution of semiconductors is independent of the energy of the incident photons, and only depends on the size of the detector and the imaging collimator used (57).

However, some of the technical challenges that semiconductors faced are limitation of the detector thickness due to incomplete charge collection. Also, limitation of charge collection and useful detector size due to lack of material uniformity. Limitation of the yield of good detectors with high costs because of poor reproducibility (58).

2.6.1 Properties of Cadmium Telluride (CdTe)

Cadmium Telluride (CdTe) is an example of a semiconductor that can be used for high energy photon detection due to its high absorption properties. For CdTe the mass attenuation coefficient is 0.7091 cm^2g^{-1} at a photon energy of 140.5 keV and its density is 5.85 gcm^{-3}, therefore the linear attenuation coefficient μ is 4.15 cm^{-1} at 140.5 keV. A mass attenuation coefficient curve of the CdTe is plotted as a function of photon energy, (see Figure 2.19).

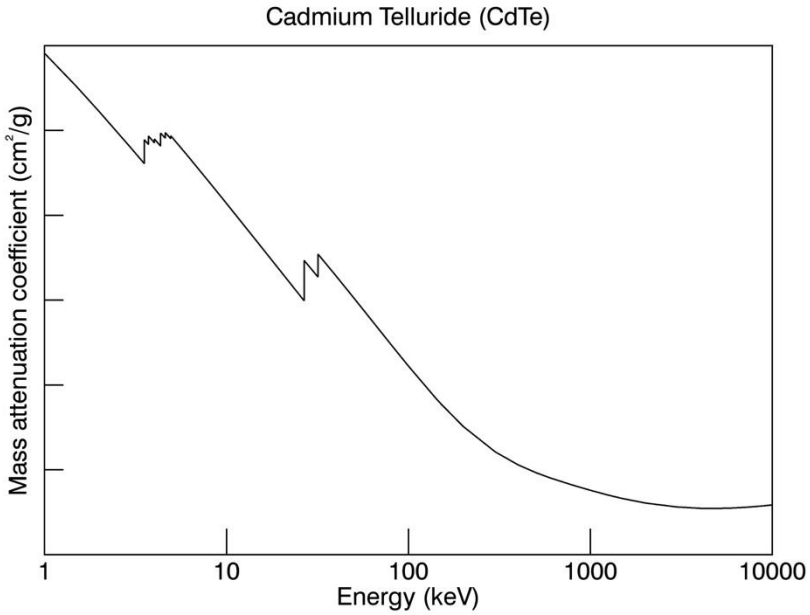

Figure 2.19: Mass attenuation coefficient (cm^2g^{-1}) curve of the CdTe versus photon energy (keV).

The absorption curves for a range of CdTe thicknesses of 600 µm and 1500 µm are shown in Figure 2.20 as a function of the photon energy (keV). The mass attenuation coefficients μ/ρ have been derived from the NIST database (40).

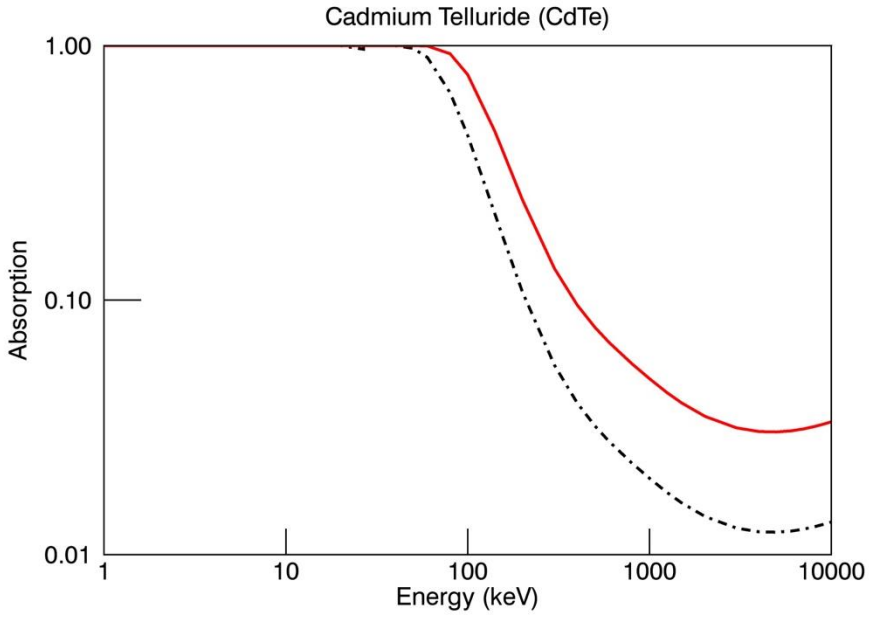

Figure 2.20: Cadmium Telluride absorption curves for differing CdTe thickness; 600 µm (black dash-dotted line), 1500 µm (red line).

2.7 Summary

Medical imaging procedures techniques and applications are the key role in the diagnosis of abnormalities and treatment of diseases. A conventional large field of view (LFOV) gamma cameras use NaI:TI scintillators coupled to photomultiplier tubes (PMTs). A new approach for medical gamma cameras is to use a small field of view (SFOV) camera with different scintillator materials such as CsI:TI scintillator. Also, the use of the newly developed scintillator-CCD based portable gamma camera is possible. Furthermore, the use of semiconductor detectors to provide direct gamma rays imaging have been introduced clinically. CdZnTe detector is one example of these semiconductor detectors. The performance characteristics of SFOV hybrid gamma camera (HGC) using different scintillator materials like CsI:TI, GOS and $CdWO_4$ scintillators will be discussed in more detail in Chapter 5. In general, scintillation based gamma cameras could provide high imaging sensitivity. However, the performance of CdTe semiconductor detectors in medical imaging will be discussed in Chapter 6. CdTe semiconductor detectors will be investigated as they have some advantages such as their superior energy resolution, this is due to that the CdTe detectors have a large bandgap energy of E_g= 1.5 eV which allows direct conversion of the absorbed gamma energy into charge, thus will lead to much better energy resolution in comparison to scintillator-based gamma cameras (59).

Chapter 3

Small Field of View (SFOV) Hybrid Gamma Camera (HGC): its design and application

A number of diagnostic clinical applications have had an impact on motivating the development of new compact gamma camera systems. An example of these clinical procedures is lymphoscintigraphy. Lymphoscintigraphy is a nuclear medicine imaging procedure, which is used to assess the lymphatic system. Lymphoscintigraphy is used for sentinel lymph node mapping in breast cancer or to identify the initial node that receives the lymph drainage from a tumour such as malignant melanoma. It can, also, be used in oncology as a cancer treatment plan by biopsy, and for investigation of lymphedema to assess the blockage points in the lymphatic system.

A new generation of compact gamma camera systems are now in demand. Some of those compact gamma cameras are small and can be used as a hand held gamma camera. Imaging small nodes during intraoperative procedures requires high spatial resolution cameras. Compact gamma cameras should have particular specifications to be suitable for these clinical and surgical applications.

The main aim of this chapter is to introduce the design of a novel small field of view (SFOV) hybrid gamma camera (HGC). Images were acquired in laboratory simulations using a range of anthropomorphic bespoke phantoms. Clinical scintigraphic images,

from patients attending the nuclear medicine clinic, acquired using the hybrid gamma camera were also evaluated.

3.1 Materials and methods

3.1.1 Hybrid gamma camera design

The Hybrid Gamma Camera (HGC) is a novel hand-held, small field of view (SFOV) camera. This new innovation has been developed at the Space Research Centre (SRC), University of Leicester, in collaboration with the University of Nottingham. The HGC combines an optical and a gamma camera in a co-aligned configuration which could provide high spatial resolution intraoperative imaging and may enhance the physical localisation of radiopharmaceutical uptake during critical surgical procedures such as in breast and head and neck sentinel node biopsies (60).

The HGC uses a scintillator-based detector, Figure 3.1 shows a schematic of the HGC. The HGC consists of a back illuminated electron multiplying charge coupled device (EM-CCD) (e2v CCD97 BI, e2v Technologies Ltd., Chelmsford, UK. (61)) with 16 µm x 16 µm pixels which have been binned 4 x 4 to produce 64 µm x 64 µm square pixels. The main scintillator used is thallium-doped caesium iodide (CsI:TI) either 600 µm or 1500 µm thick, coupled to the CCD. A simple collimator design based on 6 mm thick Tungsten, 45 mm in diameter with a single pinhole having an acceptance angle of 60 degree. Either a 0.5 mm or a 1.0 mm diameter pinhole was chosen to be used for imaging. This is mainly to make the construction of the system simple and to expand the imaging field of view. The distance between the CCD and the pinhole collimator was fixed at 10 mm. The distance between the pinhole collimator and the source being imaged will determine the magnification factor on the CCD (62). A thin front surface mirror, 1 mm thick, is positioned directly in front of the pinhole collimator at an angle of 45 degrees. The purpose of the mirror was to act as a reflector to reflect the optical photons towards the optical camera. Figure 3.2 represents a photograph of the HGC head to show the position of the optical camera and the mirror. The system used to cool down the CCD is known as a Thermo-Electric Cooler (TEC) device or Peltier cooler. This brings the

operating temperature of the CCD down to - 10°C. Three mm thick tungsten shielding surrounds the head of the hybrid camera. Both the gamma and optical cameras are connected to the readout and control electronics system, all are managed by a standard PC or laptop. The HGC head is also sealed in a non-toxic plastic enclosure thus providing both thermal and electrical isolation for the camera. Full details of the design and construction of the HGC were explained previously (19, 60, 62, 63). The performance of the HGC characterised following protocols based on those of the Institute of Physics and Engineering in Medicine (IPEM) has been described previously (63-65).

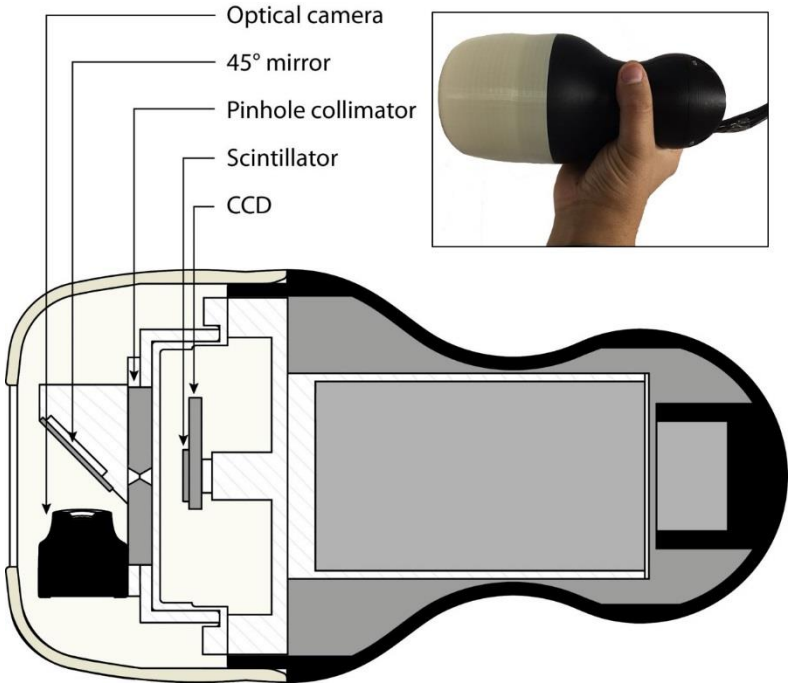

Figure 3.1: Main: Schematic of Hybrid Gamma Camera (HGC). Inset: image of HGC with the protective cover.

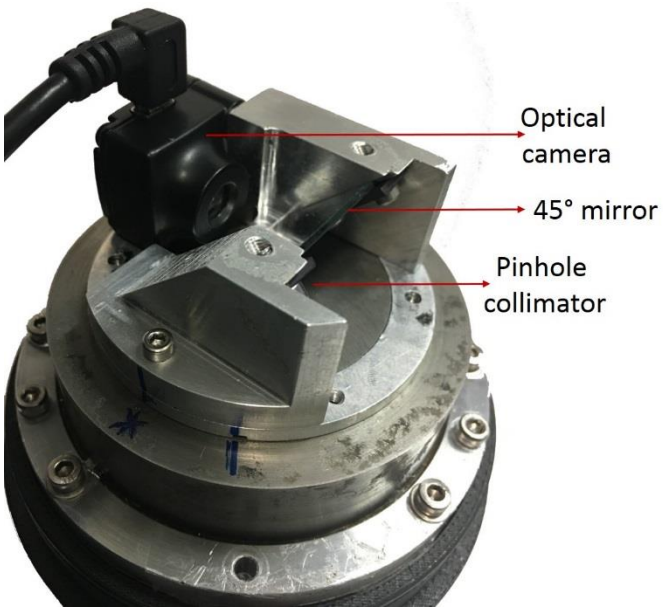

Figure 3.2: Photograph of the HGC without the protective cover to show the optical camera and the mirror.

3.1.2 Optical gamma image alignment

The assessment of the alignment accuracy is known as optical gamma image alignment test. The accuracy of alignment of both gamma and optical modalities depends mainly on the position of the optical camera, mirror and the pinhole collimator. The aim is to achieve the closest alignment of the two cameras, which is depend on the design of the imaging system. Software corrections were applied in order to superimpose the gamma image with the optical image accurately. The alignment accuracy test is based on the measurement of deviation of the centre of landmark position between both gamma and optical images.

3.1.3 Simulation of lymphatic imaging

At an early stage of development of the HGC an investigation of images of simulated lymphatic vessels using a 0.55 mm diameter cannula filled with 10 MBq of ^{99m}Tc solution were taken, see Figure 3.3. This was done to evaluate the efficacy of the HGC in detecting both gamma and optical images. Images were acquired with the HGC using a

600 µm thick CsI:TI scintillator and a 0.5 mm diameter pinhole collimator at 100 mm collimator to source distance. Total number of frames was 2000, thus the acquisition time was approximately 3 min.

The fused images (Figure 3.3C) show good alignment of the two modalities (gamma and optical) allowing accurate localisation of the activity.

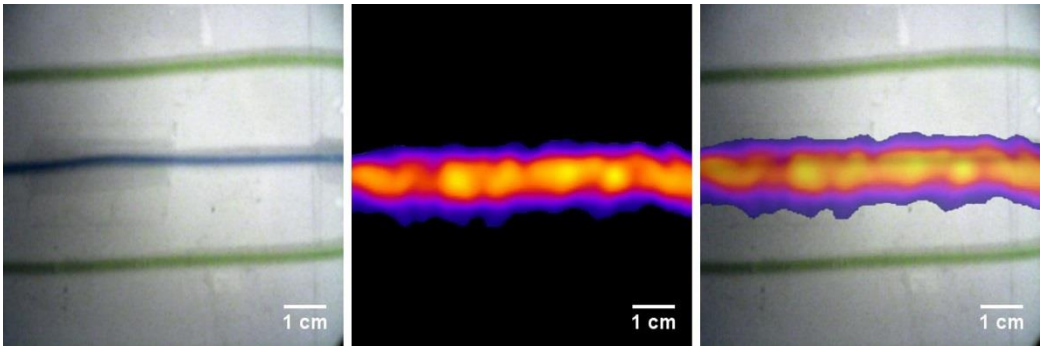

(A) **(B)** **(C)**

Figure 3.3: Optical and gamma images acquired by the HGC. A 0.55 mm diameter cannula was filled with 10 MBq of ^{99m}Tc solution mixed with blue dye (middle cannula), the upper and lower one filled with green dye only. A) Optical image, B) gamma image and C) fused gamma optical images.

3.1.4 Phantoms

In addition to the previous phantom test, a range of anthropomorphic bespoke phantoms were designed and manufactured at the SRC laboratory and at the University of Nottingham for further HGC capability evaluation in SFOV gamma imaging. The main aim of constructing those phantoms is to investigate the response and the behaviour of the HGC system to a variety of different phantoms having similar shapes and configurations of the anatomical human body. Thus simulating the clinical diagnostic nuclear imaging scenarios.

To give an example, a novel SLN phantom was designed and constructed at University of Nottingham, simulating the sentinel lymph node with the existence of a high dose of the radioactive material at the injection site, this study was explained fully by Ng et al (66). Figure 3.4 shows the design of the sentinel lymph node phantom where two syringes filled with ^{99m}Tc radioactive source were used, the big syringe simulates the

injection site while the small syringe simulates the node. Layers of Perspex plates were used to simulate the node depth. Nine Perspex bars were used to simulate the node separation from the injection site. Gamma images have been taken with HGC to assess the contrast to noise ratio and to evaluate the performance of the HGC in sentinel lymph node (SLN) imaging.

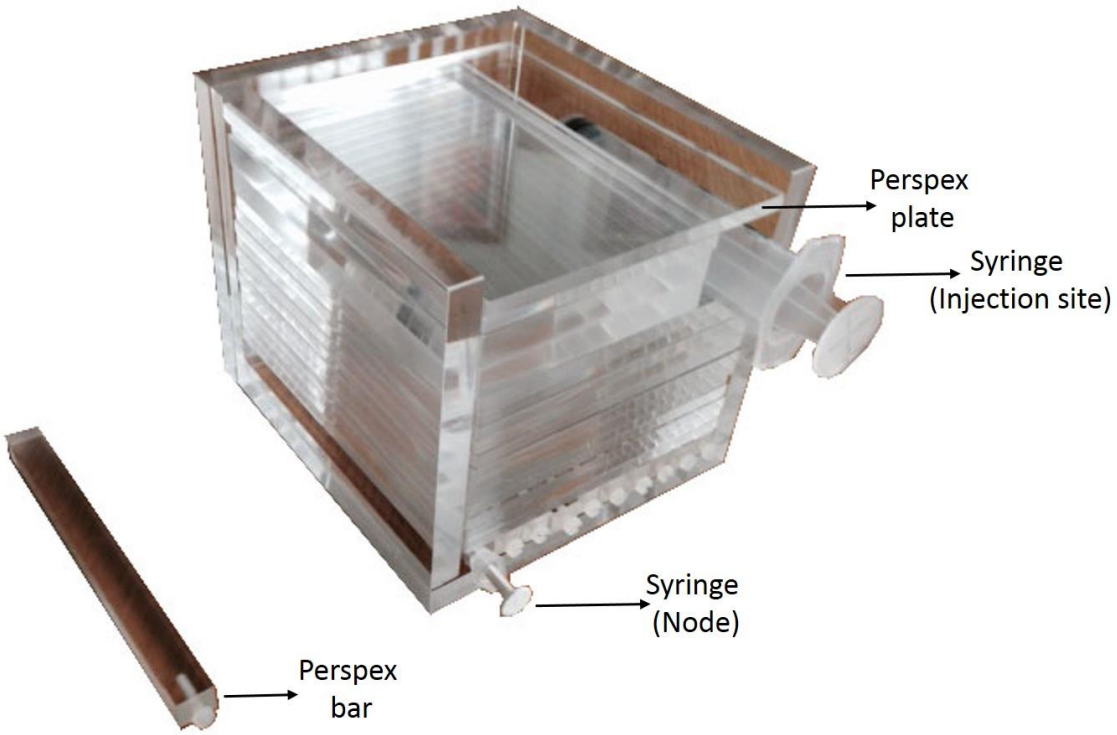

Figure 3.4: A photograph of sentinel lymph node (SLN) phantom. Sixteen Perspex plates were used to simulate node depth. Nine Perspex bars were used to simulate the node separation. Big syringe was used to simulate the injection site. Small syringe was used to simulate the node.

Another lymphoscintigraphic phantom was designed and built at the University of Leicester, to simulate the lymphatic vessels and the sentinel lymph nodes aiming to evaluate the performance of the HGC quantitatively in lymphoscintigraphic imaging, full details were discussed by Alqahtani et al (67, 68). Figure 3.5 illustrates a photograph of the lymph node contrast (LNC) phantom where two plates of Perspex used to design the phantom. Circular wells were filled with ^{99m}Tc radioactive source ranging between 2.5 mm to 10 mm diameter were used to simulate the sentinel lymph nodes. The

second Perspex plate were filled with ^{99m}Tc radioactive source to simulate the tissue background. Gamma images have been acquired using the HGC to assess the capability of the small field of view HGC system in detecting various sizes of SLNs with various radioactivity concentrations.

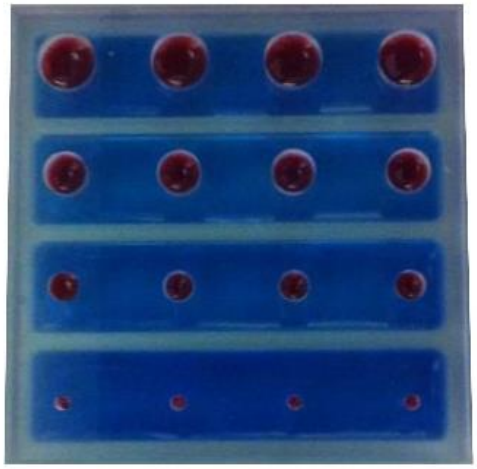

Figure 3.5: An image of the lymph node contrast (LNC) phantom showing two Perspex plates. (Bottom): Four rectangular wells simulating the background activity of the tissues surrounding the SLNs. (Top): Sixteen circular wells ranging from 10 mm to 2.5 mm diameters simulating the SLNs.

In addition, a commercially available thyroid phantom was used to investigate the capability of the HGC in imaging the thyroid gland. The phantom imaged was a Picker thyroid phantom (Picker Nuclear phantom, part no. 3602, Cleveland, OH), (see Figure 3.6). The performance of the HGC using this phantom was reported by Bugby et al (48). A clinical simulation of thyroid imaging had been performed by filling the thyroid phantom with 15 MBq ^{99m}Tc radioactive solution and images have been taken using HGC fitted with 1.0 mm diameter pinhole collimator. The phantom was placed at 105 mm distance from the camera. Figure 3.6 illustrates an example of the gamma image acquired, the acquisition time was approximately 15 min. Contrast to noise ratio have been calculated too to investigate the suitability of HGC for thyroid imaging.

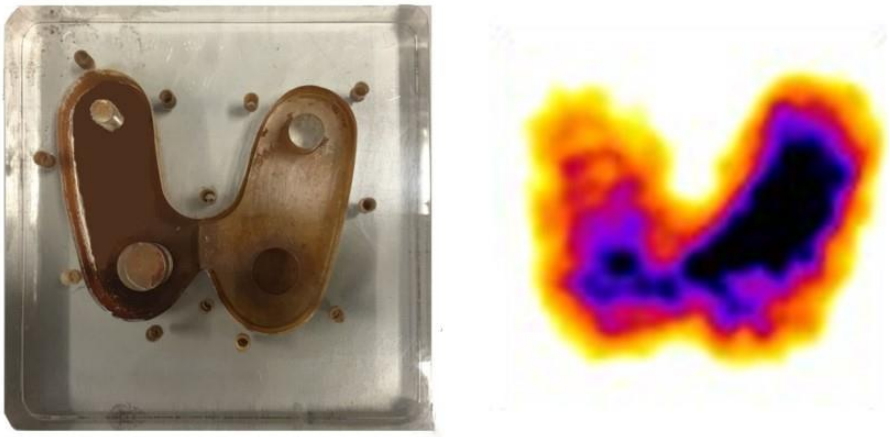

Figure 3.6: (Left): A photograph of the Picker thyroid phantom. (Right): A gamma image of the thyroid phantom filled with 15 MBq of ^{99m}Tc solution at 105 mm distance using a 1.0 mm pinhole collimator.

Moving on to another stage of assessing the HGC for nuclear medical applications, two additional new phantoms were designed and developed at University of Leicester, those phantoms are breast and head and neck phantoms. The breast phantom was built aiming to evaluate the ability of the HGC system in breast imaging to detect the tumours and sentinel lymph nodes. The breast phantom was manufactured in two main separate parts; the dome and the base. The base simulates the bone and/or the muscle of the breast. It has six holes to secure and seal the dome into it. The dome simulates the skin on top of the breast. Both of the base and the dome were made from Perspex, however, the dome were made using a 3-D rapid prototyping processes. Figure 3.7 shows a photograph of the breast phantom and an example of fused optical and gamma image using 90 MBq of ^{57}Co source (~ 8 mm in diameter) placed inside the breast phantom at 70 mm distance below the apex.

Figure 3.7: (Left): An image of the breast phantom designed at Space Research Centre, University of Leicester. (Right): a fused gamma and optical image of a 90 MBq of ^{57}Co source placed inside the breast phantom at 70 mm distance below the apex of the dome.

The head and neck phantom was designed to mimic the adult head and neck anatomy. Figure 3.8 illustrates the design of the phantom. The external casing of the phantom was obtained from The Phantom Laboratory. The inner anatomical jig was designed at University of Leicester and it contains the simulated three dimensional (3D) printed thyroid gland, trachea, cervical spine and lymph nodes at different locations and injection site. Hybrid gamma images have been taken to assess the HGC for imaging the head and neck region. Also, to evaluate the ability of the HGC system in imaging small body organs such as thyroid imaging. Figure 3.8 shows an example of the fused optical and gamma image of the simulated thyroid gland filled with 15 MBq of ^{99m}Tc radioactive material, image was taken at 100 mm distance from the phantom surface using 0.5 mm diameter pinhole collimator.

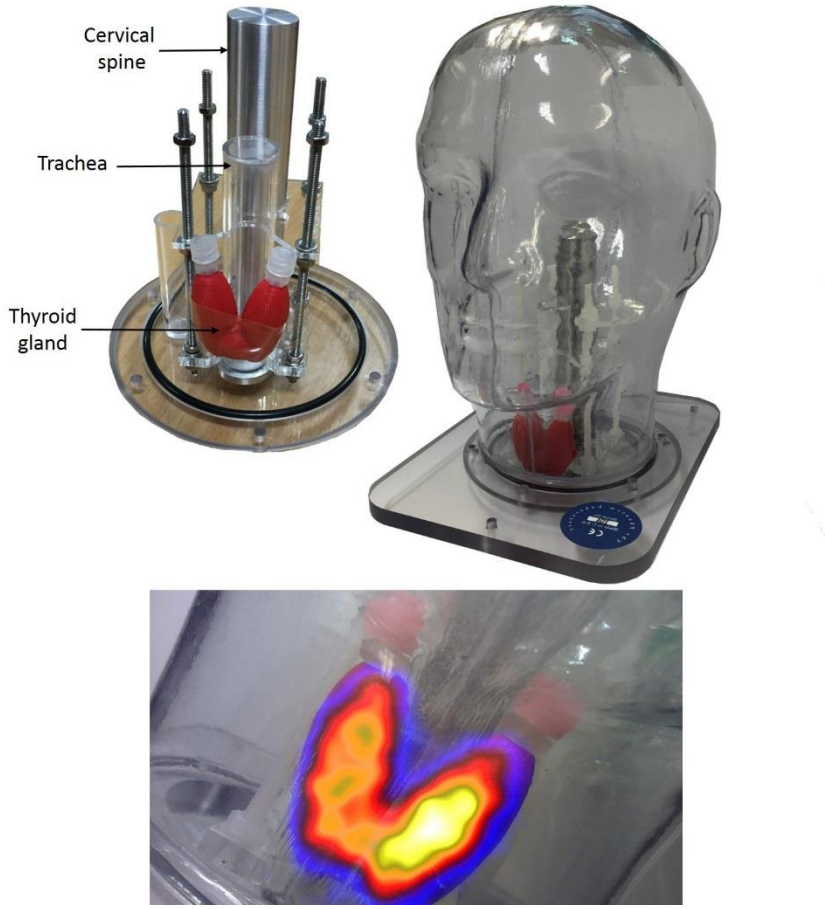

Figure 3.8: (Top): A photograph of the head and neck phantom. (Top right): The external casing. (Top left): The inner anatomical jig compromising; 3D printed thyroid gland, trachea and cervical spine. (Bottom): A fused gamma and optical image of the simulated thyroid gland at 100 mm distance from the phantom surface.

Further details about the design and the construction of breast and head and neck phantoms were reported by Lees et al (69) and Alqahtani et al (70).

From all the previous anthropomorphic phantom studies it was concluded that the HGC is suitable to be used in small organ nuclear medical imaging. Also, the spatial resolution of the HGC has been investigated and the contrast to noise ratio (CNR) has been calculated. The novel sentinel lymph node phantom along with the lymph node contrast phantom were proved that the HGC system is capable of detecting low accumulation of ^{99m}Tc activity in small sentinel lymph nodes. Indicating that the HGC is a useful imaging system in intraoperative SLNs procedures. Imaging both the commercially available thyroid phantom and the 3D printed thyroid gland within the head and neck phantom using the HGC demonstrated that the system has the ability to define the feature of the

thyroid gland and it is a promising utility in thyroid imaging. Also, those results are encouraging to investigate the HGC at clinic with patients having thyroid scan. The breast phantom was used mainly to assess and estimate the depth and the precise position of the radioactive material within a patient. Aiming to help the surgeons to localise the exact depth of the targeted tissues.

3.1.5 Clinical patient imaging

During the development of the HGC, a number of clinical patients were investigated and imaged using our hybrid camera. The main aim was to assess the capability of the HGC to be used as an alternative investigational tool in nuclear medicine clinics. Another aim was to test the ability and the performance of the hybrid camera for the appropriate small body organ imaging for future clinical procedures.

The patient study was carried out in the Nuclear Medicine Department at Queen's Medical Centre, Nottingham University Hospitals NHS Trust, during the period from February 2013 until November 2015. The ethical approval of this patient study was agreed by the UK National Research Ethics Committee (Reference Number: 12/EM/0201) and the Research and Innovation, Nottingham University Hospitals NHS Trust. The outcomes from this pilot study was published by Ng et al (71).

Patients who had a diagnostic nuclear medicine scan, were asked to participate in the study. Once they agreed to take part in the research study, they were asked to sign a formal written consent. Patients were administrated with the standard amount of radionuclides activity for their routine studies. Gamma images were acquired in the Nuclear Medicine Department with a standard large field of view (LFOV) gamma camera. LFOV gamma images were taken by either a Philips Brightview XCT (Philips Healthcare, Milpitas, California, USA) or General Electric Discovery NM/CT 67 (GE Healthcare, Waukesha, Wisconsin, USA). Following the main procedure, patients were then imaged with the HGC. Both optical and gamma images were acquired.

There were 24 patients in this study, the age range of the patients was between 30 and 83 years. Images of 18 cases were successfully assessed subjectively. The clinical studies

included were: lymphoscintigraphy scans, lacrimal drainage scans, thyroid and bone imaging, leucocyte scan and DaT scans. Full details of the nuclear clinical studies were discussed in Ng et al (71). In this chapter one of the clinical cases will be discussed briefly as an example of one of the clinical procedure adopted for imaging patients using the HGC.

3.2 Clinical imaging of lacrimal drainage

A lacrimal drainage scan is a nuclear medicine procedure where the function of the nasolacrimal drainage system - specifically the tear duct – is investigated non-invasively using a very low amount of radiation dose (i.e. 2 – 4 MBq of ^{99m}Tc) delivered to the eye. The significant importance of this study is to evaluate the patency of the nasolacrimal duct and to localise the area of the obstructed ducts. Surgeons can use this study pre and or post operation (72, 73).

During the lacrimal scan, the patient was administered with 1 MBq of ^{99m}Tc isotope in each eye. At 10 min post administration the patient's eyes were imaged using a LFOV gamma camera, (see Figure 3.9A). Twenty five min post administration the patient's eyes were imaged again using LFOV gamma camera, (see Figure 3.9B).

After that the patient was imaged using the HGC, approximately 40 min post administration. Figure 3.10 shows the optical, gamma and hybrid images obtained from the patient. Images were acquired with the HGC using a 600 µm thick CsI:TI scintillator and a 0.5 mm diameter pinhole collimator at a 100 mm distance away from the hybrid camera. Acquisition time was approximately 3 min.

As shown in (Figure 3.10B), the gamma image produced from the HGC can provide a good visualisation of the distribution of ^{99m}Tc activity at both eyes. The fused gamma-optical image (Figure 3.10C), shows good physiological and anatomical localisation of the activity. Comparing the gamma image acquired by the HGC (Figure 3.10B) with the clinical gamma image obtained from the LFOV gamma camera (Figure 3.9), shows that the right (RT) nasolacrimal duct clearance can be identified clearly.

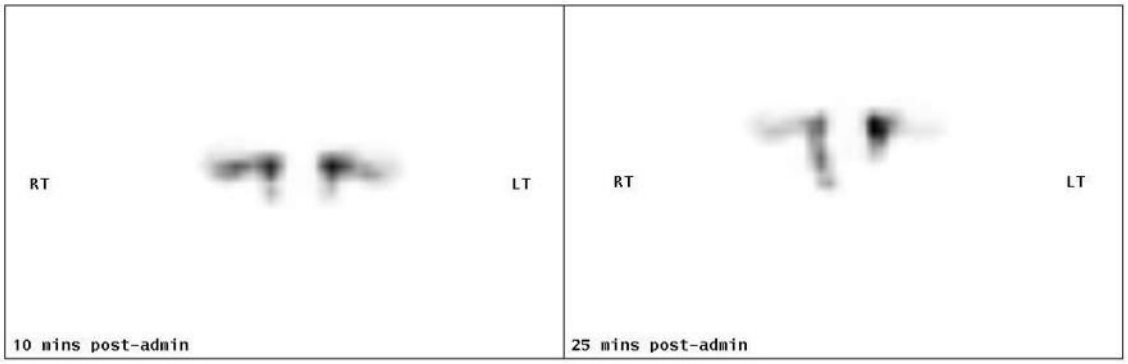

(A) **(B)**

Figure 3.9: The standard clinical gamma image for the above lacrimal drainage case recorded by using the standard large field of view (LFOV) gamma camera at the Nuclear Medicine Department at (A) 10 min post administration and (B) 25 min post administration.

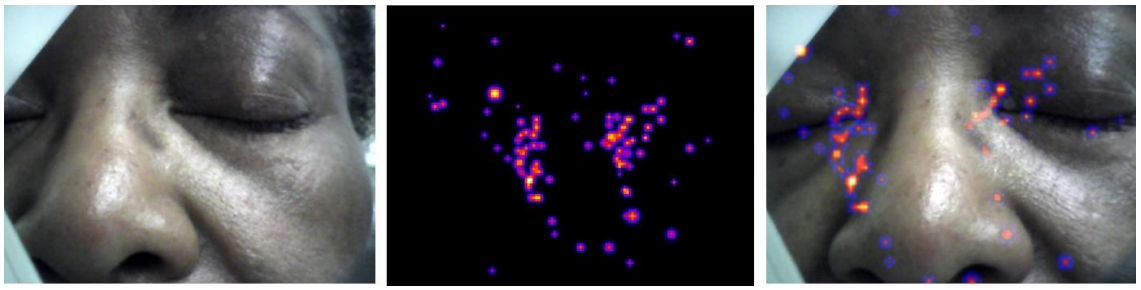

(A) **(B)** **(C)**

Figure 3.10: Images acquired by the HGC A) Optical B) gamma C) fused gamma-optical images of both right and left eyes and right nasolacrimal duct. The gamma image was acquired at approximately 40 min following an administration of 1 MBq of ^{99m}Tc to the surface of each eye. Total no. of frames was 2000 with the acquisition time of approximately 3 min.

3.3 Research team roles

The HGC was initially designed and developed by Lees et al. (19, 60, 62, 74, 75) at Space Research Centre, University of Leicester in collaboration with Queen's Medical Centre, University of Nottingham. Following that the characterisation of the HGC was performed by Bugby et al. (64) using 600 µm CsI:TI scintillator. Then a full scheme for assessing the performance characteristics of SFOV gamma cameras was outlined and described fully by Bhatia et al. (65). Once I have started my PhD studies a range of anthropomorphic bespoke phantoms were designed and manufactured to assess the performance of the HGC for sentinel node imaging which was done by Ng et al. (66) at University of Nottingham. Also, another lymphoscintigraphic phantoms were constructed at SRC laboratory by Alqahtani et al. (67, 68) my contribution here was performing the experiment and acquiring the gamma and optical images using ^{99m}Tc radioactive source. Furthermore, both breast and head and neck phantoms were designed and built at University of Leicester. I have contributed with by Lees et al. (69) in performing the experiment of the breast phantom while Alqahtani et al. (70) implement the whole work with the head and neck phantom.

However, for the clinical patient study the roles were distributed equally between the research team. I was one of the principal investigators and my role was to be present in the research room either in Queen's Medical Centre or Nottingham City Hospital to assist with the operation of the HGC and the equipment and help work on the data that we collected.

3.4 Conclusion

The initial gamma and fused gamma-optical images demonstrate that the HGC has a good visual alignment of the two modalities allowing accurate localisation of activity. Design and development of the anthropomorphic bespoke phantoms aid the evaluation of the performance characteristics of the HGC. The hybrid images obtained from these phantom studies demonstrate that the hybrid camera is well suited for small body organ imaging such as sentinel lymph node (SLN) imaging and thyroid imaging. The simulated

lymphatic vessels was detected by the HGC with a spatial resolution values ranging between 4.4 mm and 6.3 mm at 100 mm source to collimator distance. Furthermore, the simulated SLN having various radioactivity concentrations was detected by the HGC with high contrast to noise ratios ranging between 11.6 and 110.8, when 5mm to 30 mm Perspex thicknesses placed in between. These studies encourage us to carry out further evaluation in preparation for its use in a surgical theatre setting. The capability of the HGC to employ either 0.5 mm or 1.0 mm diameter pinhole collimators enhances its practicality and significantly improves its capability to be flexible for all the needs of different small organ nuclear medical imaging. The 0.5 mm diameter pinhole collimator can increase the resolution of the image by about 50 %. However, the 1.0 mm diameter pinhole collimator improves the image sensitivity but degrades the spatial resolution. First clinical patients imaging results show that, the new system i.e. small field of view (SFOV) hybrid gamma camera (HGC), will have many practical benefits for a number of clinical procedures including; diagnosis, surgical investigations and the visualisation of drug delivery. An example of these procedures are thyroid, lymphatic and lacrimal drainage imaging where the radiopharmaceutical uptake could be clearly seen. However, some limited data were produced from bone scan and leucocyte labelling studies and this was due to the presence of a high background noise in the acquired gamma images. This is caused by insufficient detector shielding from the emitted gamma radiation throughout the patient. The clinical advantages of fusing the gamma image to the optical image are clear and should be ideally suited for intraoperative imaging and bedside small organ nuclear imaging such as lacrimal drainage studies.

In the next following chapters, further characterisation of the HGC will be performed using different types of scintillators (i.e. CsI:TI, GOS and $CdWO_4$ scintillators) to decide which scintillator to use for particular nuclear medical imaging applications (Chapter 5). Furthermore, modifying of the HGC will be discussed describing a novel hand-held hybrid near infrared NIR-gamma small field of view camera (Chapter 7). In the near future, more in-depth evaluation for the HGC will be carried out aiming to obtain a stereoscopic imaging for both optical and gamma photons, which can help surgeons to get a more accurate information and precise estimation of the position (i.e. depth) of radiopharmaceuticals within patient's body.

Chapter 4

Protocols for assessing the performance characteristics of small field of view (SFOV) gamma cameras

The performance characteristics of nuclear medical imaging cameras are highly important to ensure that the final clinical diagnostic gamma images are clinically suitable. Any artefacts in the gamma images can lead to incorrect interpretation of the clinical diagnostic images and thus can alter the patient's diagnosis by the radiologists. Therefore, acceptance and quality control (QC) tests of gamma camera systems have been designed to ensure an optimal gamma camera performance. An acceptance test is normally performed during gamma camera installation to verify that the system agrees with the performance specification provided by the manufacturers. QC tests are then performed on a regular basis after the camera has been used over a period of clinical diagnosis. Some of the QC tests are carried out daily or weekly, others monthly, or yearly. The purpose of these QC tests is to check the gamma camera performance day to day and to detect any changes to the system performance from baseline values. Furthermore, QC tests can sometimes be performed to allow a comparison between different systems characteristics and to optimise the quality of the clinical studies (76).

The National Electrical Manufacturers Association (NEMA) has published guidelines to standardise the QC tests for medical gamma cameras (77). The results of the QC tests,

measured according to NEMA standards, can be used to check the quality of the gamma camera, report its performance and compare the performance of different systems (78). The specification parameters established by NEMA are as follows: intrinsic spatial resolution, intrinsic energy resolution, flood field uniformity, spatial linearity, count rate capability, system spatial resolution and system sensitivity. For each measured parameter, NEMA advises manufacturers to specify the standard expected value to make it easy for the physicists and/or hospital technicians to ensure that the specifications are met (79).

The main purpose of this chapter is to outline the standard performance characteristics of the standard large field of view (LFOV) gamma cameras to be applicable to be used with small field of view (SFOV) Hybrid Gamma Camera (HGC) (19) following the protocols based on the Institute of Physics and Engineering in Medicine (IPEM) (65). The performance characteristics measured are: intrinsic and extrinsic spatial resolution, intrinsic spatial uniformity, intrinsic and extrinsic spatial sensitivity and count rate capability. These tests are then performed to fully characterise the HGC system, in Chapter 5, and to fully characterise the Cadmium Telluride (CdTe) detectors, in Chapter 6, to test their suitability for medical imaging.

4.1 Planar imaging

4.1.1 Intrinsic spatial resolution

In medical imaging, spatial resolution is one of the most important factors when considering a new device, as it is the accuracy at which the detector is able to distinguish the position of a discrete source.

The intrinsic spatial resolution is defined as the full width at half maximum (FWHM) of a line spread function (LSF) or of a point spread function (PSF) without an imaging collimator in place. According to Rayleigh's criterion, this parameter corresponds to the minimum separation needed between two sources to distinguish them. The FWHM is

expressed as the width at 50 % of the height of the LSF/PSF peak. The narrower the peak, the better the intrinsic spatial resolution (80). The full width at tenth maximum (FWTM) should also be stated as the PSF and LSF may deviate from a Gaussian profile (81).

For large field of view (LFOV) gamma cameras, the intrinsic spatial resolution is measured by using a 0.5 mm diameter cannula as a line source and filled with approximately 40 MBq ^{99m}Tc radioactive source. Typically the intrinsic spatial resolution of the LFOV gamma cameras at 140.5 keV ^{99m}Tc is of the order 3 mm FWHM (82, 83).

This method is unsuitable for smaller detectors such as SFOV gamma cameras, as the expected intrinsic spatial resolution can be as low as 100 µm (84). According to the protocol standards for LFOV cameras, a line source with a diameter of less than 80 µm would be required. At these widths it is difficult to manufacture and fill those kinds of phantoms without specialist equipment (85, 86). So, IPEM has been suggested an alternative method for SFOV measurements.

The modified methodology for SFOV gamma cameras is to use a machined edge mask made from material that has low transmission for the incident gamma energies. The edge should be perpendicular to the surface of the mask and straight to an accuracy of at least 10 % of the expected spatial resolution. The minimum thickness of the mask should be sufficient to attenuate 99 % of the incident gamma photons. A thicker mask is preferred to eliminate divergent photons.

The mask should be installed as close as possible to the scintillator material. A point source should be placed at a distance of at least 100 times its diameter to ensure uniformity.

The intrinsic spatial resolution measure can be calculated using the edge response function (ERF) method which excludes the necessity for imaging very small sources. An example of the ideal analysis of the ERF of a simulated edge mask image is shown in Figure 4.1 (87).

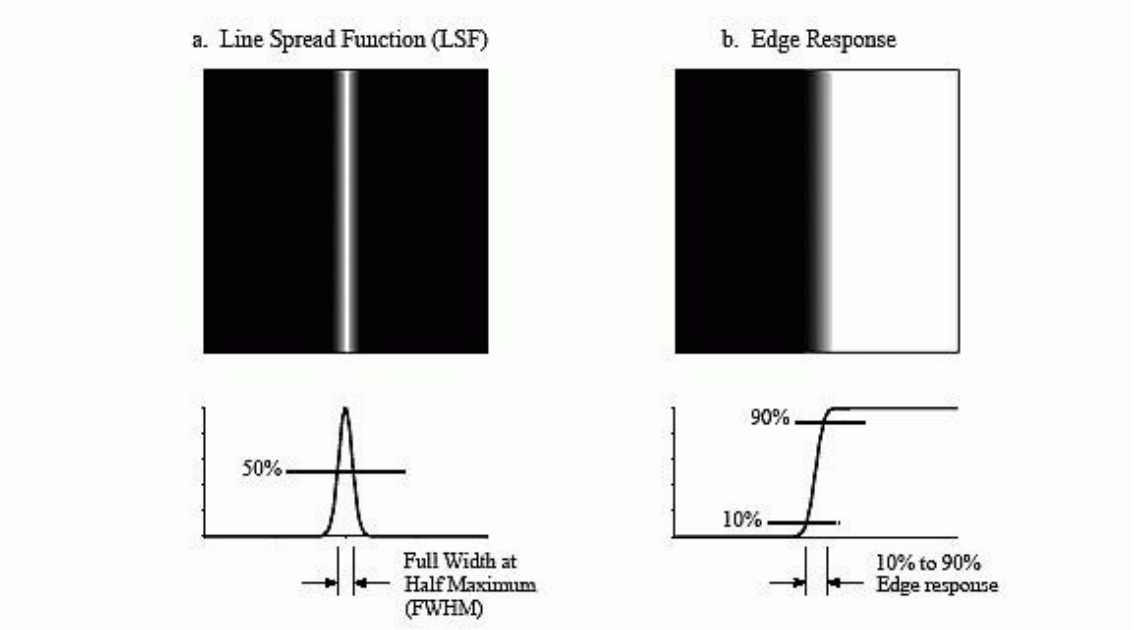

Figure 4.1: Graphs of the line spread function (LSF) and edge response function (ERF) calculated from a simulated edge mask image. (Taken from Steven W. Smith (2002). Special imaging technique, *The Scientist and Engineer's Guide to Digital Signal Processing*, Retrieved 12 September 2018. With permission from the author.)

From the simulated image Figure 4.1 a high count region can be seen which is due to the uncover area in the detector by the mask while the low count region, where the mask covered the detector. The variety in counts between them are often associated to the spatial resolution of the detector.

An example of the required image processing is shown in Figure 4.2. The edge response function (ERF) is first calculated (Figure 4.2B) by plotting the position on the image plane (i.e. in perpendicular direction to the mask edge). The ERF is then differentiated to give a LSF (Figure 4.2C). Then the modulus of LSF is fitted with a Gaussian curve/distribution (Figure 4.2D). The intrinsic spatial resolution is reported as the mean FWHM and the mean FWTM of the LSF.

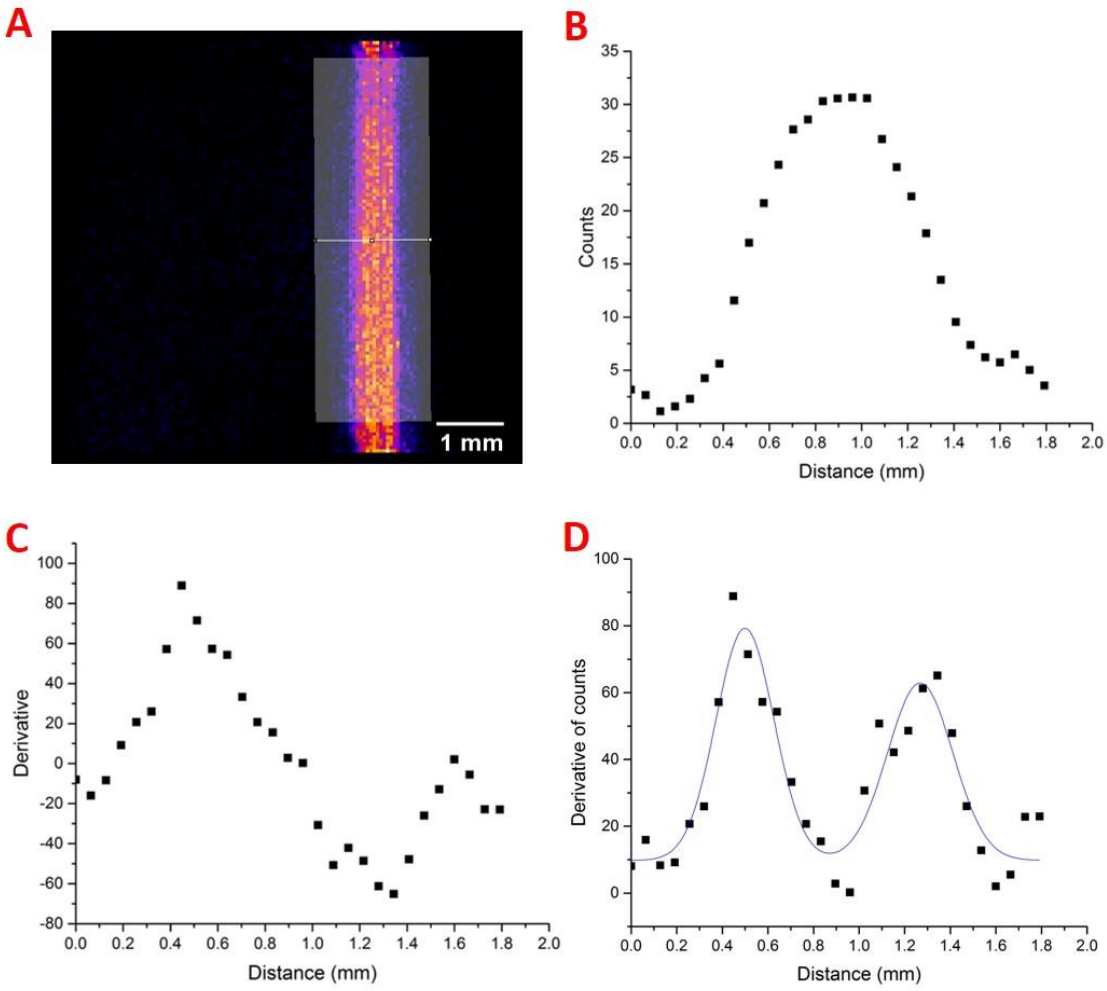

Figure 4.2: Graphs showing the intrinsic spatial resolution measurement process for the 1500 µm thick CsI:TI scintillator using 20 MBq ^{99m}Tc source. A) Final image of ^{99m}Tc at 250 mm distance from the 2 mm width slit. Total no. of frames was 10000. The acquisition time was 1200 sec. B) Edge response function (ERF) for ^{99m}Tc source. C) Line spread function (LSF) i.e. derivative of ERF. D) Modulus of LSF with fitted Gaussians.

4.1.2 Extrinsic spatial resolution

The extrinsic or system spatial resolution is defined as the FWHM of a LSF or of a PSF with the imaging collimator in place (81).

The standard protocol for LFOV gamma cameras is again to use a 0.5 mm diameter cannula as a line source with an imaging collimator installed in. The FWHM and FWTM can be calculated to measure the extrinsic spatial resolution of the gamma camera by

placing the line source at different distances (typically 0 mm (i.e. on the collimator face) and/or 100 mm distance). The extrinsic spatial resolution can be stated with and without scattering material such as PMMA poly methyl methacrylate (i.e. Perspex) placed between the line source and the collimator surface to simulate different depths inside the human body as Perspex has an acceptable level of similarity with human tissue (88).

To measure the extrinsic spatial resolution of SFOV systems, a point source or line source of diameter no greater than 0.5 mm should be used. Parallel hole collimators or pinhole collimators can be used for imaging. Images should be carried out at least five distances to cover the range of distances expected during operation. For each imaging distance, the FWHM and FWTM of the source should be calculated and these values plotted on a graph.

4.1.3 Intrinsic spatial uniformity

The intrinsic spatial uniformity is defined as the response of the camera to a uniform flux of radiation using a point source without a collimator in place (89). The ideal response would be a perfectly uniform image. The radiation flux is defined as the rate at which the radiation can pass through or is incident on the detector (90). The uniformity of the gamma camera is one of the most significant indicators of the performance of the system which is performed to check the homogeneity of the gamma image produced.

Two types of quantitative measures can be made to assess changes in uniformity; integral uniformity (IU) and differential uniformity (DU). Integral uniformity can be defined as the difference between the maximum (C_{max}) and minimum (C_{min}) counts per pixel in the image:

$$IU = \frac{C_{max} - C_{min}}{C_{max} + C_{min}} \times 100\ \% \qquad (4.1)$$

This measure gives an idea of the overall pixel count within the whole field of view. However, differential uniformity can be used to look at local variations by using

Equation 4.1 but only for small groups of neighbouring pixels. IPEM standards report 86 (91) suggests calculating 10 differential uniformity values for each pixel by using the adjacent 5 pixels in a row and a column across an entire image, and then calculating the spread of these values.

The IU for any detector is 100 % if there is a minimum count value of 0. Therefore, IPEM report 86 suggests a more effective measure to calculate the global changes in uniformity the coefficient of variation (CoV) (Equation 4.2)

$$\text{CoV} = \frac{\sigma}{m} \text{ x } 100\ \% \qquad (4.2)$$

The coefficient of variation (CoV) is the ratio of σ the standard deviation of counts per pixel to m the mean counts across the image.

For LFOV gamma cameras, a radioactive point source placed ideally at a distance of approximately five times the detector's useful field of view (UFOV) away from the face of the un-collimated gamma camera. Thus ensuring a delivery of a uniform illumination on the detector (92).

The same method can be applied directly to SFOV systems. A point source placed at a sufficient distance from the detector to ensure the incident gamma photons can be considered uniform.

4.1.4 Intrinsic spatial sensitivity

Intrinsic spatial sensitivity is the ability of the gamma detector to detect the gamma rays emitted from a radionuclide source (89).

For LFOV gamma cameras a point source of a radioactive material is imaged at a known distance away from the un-collimated camera face. The intrinsic sensitivity can be reported as a ratio of the recorded counts on the detector to the actual incident counts at the detector.

This procedure can be applied directly to SFOV gamma cameras. A point source of known activity is used. Images are taken over a known period of time and the total number of counts in the image is recorded.

The sensitivity can then be found by dividing the total recorded counts by the incident counts. The incident counts on a rectangular detector can be calculated using a solid angle formula:

$$\Omega = 4\tan^{-1}\frac{ab}{2h\sqrt{4h^2+a^2+b^2}} \qquad (4.3)$$

The solid angle (Ω) depends on the dimension of the rectangular detector (ab) (i.e. length and width), the distance from source to detector (h) and the source activity. The incident counts on the detector can then be found by ($\frac{\Omega}{4\pi}$), which is the proportion of the incident gamma photons emitted from the radioactive point source on the detector.

4.1.5 Extrinsic spatial sensitivity

System or extrinsic spatial sensitivity of a gamma camera is measured with an imaging collimator in place.

The extrinsic spatial sensitivity can be calculated using the same images that were obtained for the extrinsic spatial resolution. This means that the extrinsic spatial sensitivity measurements should be performed with and without scattering materials between the detector and the source being imaged.

The extrinsic spatial sensitivity can be calculated by dividing the recorded count rate by the activity of the source to give sensitivity in cps/MBq.

4.1.6 Count rate capability

Count rate capability is expressed by a count rate response curve. Ideally the recorded counts should increase linearly with incident count rates for an increasing activity of a radioactive source (93). However, as the incident counts are accumulated over a sufficient long duration, there is a possibility of rerecording two events at the same time

which causes count rate losses. So IPEM suggested that the count rate capability measure should be reported in term of the input count rate in cps units at which there is a 20 % difference between the recorded and input count rate.

For LFOV gamma camera systems, a radioactive source is placed at sufficient distance from the un-collimated detector. Then the count rate is recorded at intervals as the source decays.

For SFOV gamma camera systems, a point source of known activity is placed at a distance of at least 100 times its diameter from the un-collimated detector. The radioactive source is imaged at regular intervals (i.e. every hour) until the source has decayed to an undetectable level. Incident counts can then be plotted versus recorded counts, producing a count rate capability curve. A straight line can be fitted to the linearly proportional section of the curve. An example of a fitted graph is shown in Figure 4.3.

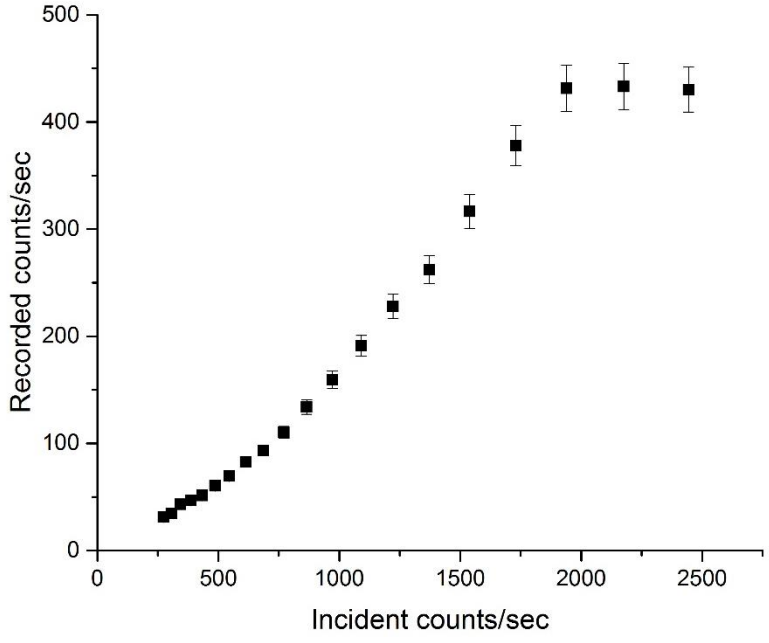

Figure 4.3: Recorded count rate capability for HGC with 1500 µm CsI:TI scintillator by using 10 mm diameter point source filled with 30 MBq ^{99m}Tc placed 250 mm away from the un-collimated camera. Images were taken over the course of 24 hrs at regular intervals (i.e. every hour). For each measurement no. of frames was 2000 and the acquisition time was ~ 240 s.

4.2 HGC methods

4.2.1 Intrinsic spatial resolution

For the purpose of this thesis, a 10 mm thick lead block with a slit of 3 mm width and 20 mm length was positioned on top of the un-collimated camera. A 2 mm diameter ^{99m}Tc source was placed at a distance of 200 mm above the surface of the slit, Figure 4.4.

After acquiring the slit image, the line profile was found by placing a line segment horizontally across the source image. Origin Lab software (94) was used to analyse the resulting values. The Edge Response Function (ERF) curve was plotted then the derivative of the ERF was used to produce the Line Spread Function (LSF). After that the modulus of the LSF was taken. After analysing the image the FWHM and the FWTM were calculated. A full example of the performance characterisation of HGC using a 600 µm CsI:TI scintillator has been previously described by Bugby et al. (64).

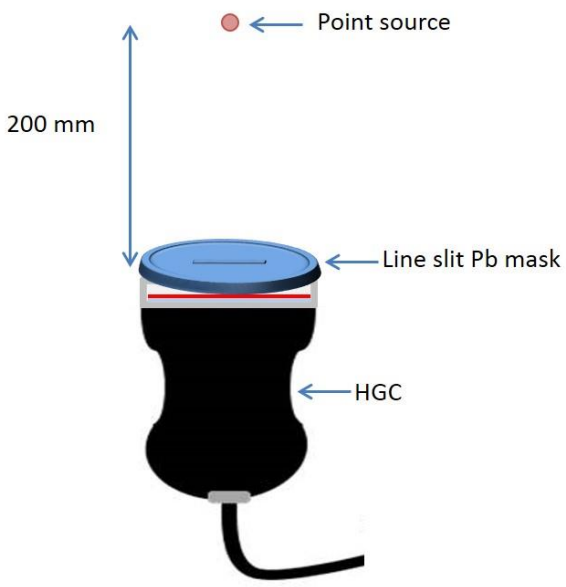

Figure 4.4: Schematic diagram illustrates the experimental setup of the intrinsic spatial resolution using the HGC. A 2 mm diameter ^{99m}Tc source was placed at a distance of 200 mm above the surface of the slit.

4.2.2 Extrinsic spatial resolution

To measure the extrinsic spatial resolution of the HGC system, a 2 mm diameter point source was filled with ^{99m}Tc. The source was then imaged with either a 0.5 mm or a 1.0 mm diameter pinhole collimator. Layers of Perspex starting from 20 mm thickness up to 80 mm were placed between the collimator and the source. Figure 4.5 shows the experimental setup.

When using the pinhole collimator, images can be magnified or de-magnified depending on the imaging configuration used. The extrinsic spatial resolution (i.e. the true FWHM and FWTM values) must be corrected first for the magnification of the pinhole. The magnification factor of each source distance was calculated (Equation 4.4):

$$M = \frac{DD}{SD} \tag{4.4}$$

The magnification factor *M* is the ratio between *DD* the detector to the centre of pinhole collimator distance and SD the source to collimator distance. This magnification gives gamma cameras with pinhole collimators a variable field of view (FOV), which can be larger than the detector size and can be adjusted by changing the distance between the detector and the source being imaged.

After acquiring the images, the resulting images of the ^{99m}Tc point source were fitted with a Gaussian curve to calculate the extrinsic spatial resolution. Then a straight line was fitted for FWHM data and FWTM data using 0.5 mm or 1.0 mm diameter pinhole collimator. A slope-intercept formula (Equation 4.5) is used to calculate the FWHM resolution value as the relationship between the extrinsic spatial resolution and the source distance is expected to be linear (64).

$$\text{FWHM} = c + (bH) \tag{4.5}$$

where *H* is 10 mm which is the distance from the source to the centre of the pinhole collimator, the source is said to be at the non-magnifying position, *b* is the gradient and *c* is the intercept obtained from the fit to experimental data.

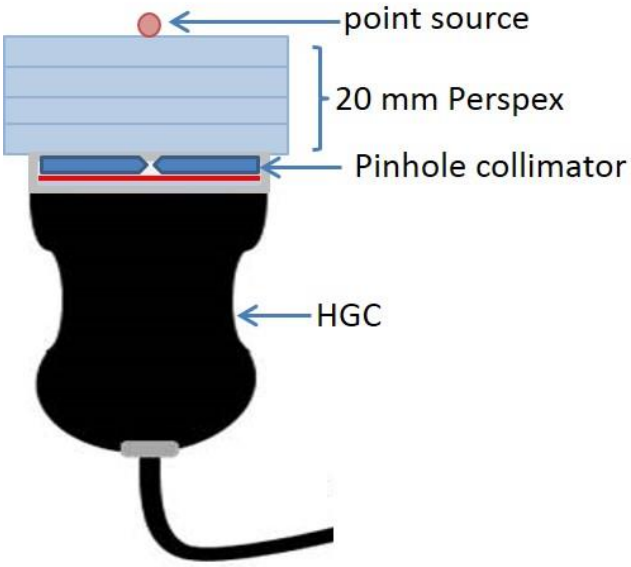

Figure 4.5: Schematic diagram illustrates the experimental setup of the extrinsic spatial resolution using the HGC. A 2 mm diameter point source is filled with ^{99m}Tc solution. Layers of Perspex starting from 20 mm thickness up to 80 mm were placed between the pinhole collimator and the source.

When calculating the extrinsic spatial resolution it is important to compare the results with the theoretical geometric resolution R_{geom} of the pinhole collimator which is given by (95):

$$R_{geom} = d\,(\frac{1}{M} + 1) \qquad (4.6)$$

where *d* is the diameter of the pinhole collimator, *M* magnification factor. The theoretical geometric resolution degrades with decreasing in magnification (Table 4.1).

Table 4.1: Geometric resolution (R_{geom}) for two different pinhole diameters at different source to collimator distances used by the HGC. The collimator to detector distance has been fixed at 10 mm in all cases.

Source to collimator distance (mm)	**M**	**Geometric resolution (mm)**	
		0.5 mm diameter pinhole collimator	1.0 mm diameter pinhole collimator
10	1	1	2
50	$^1/_5$	3	6
100	$^1/_{10}$	5.5	11

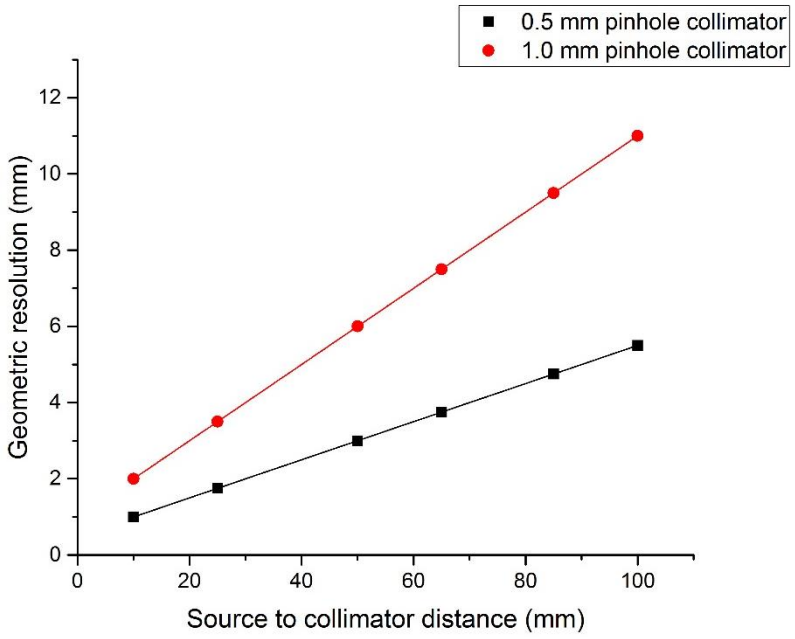

Figure 4.6: Graphs showing the theoretical geometric resolution vs source to collimator distance when 0.5 mm pinhole collimator (black square) and 1.0 mm pinhole collimator (red dots) installed.

Equation 4.6 calculates the geometric resolution without considering the possibility of the penetration of the incident photons through the collimating material. So Equation 4.6 could be modified to account for gamma ray penetration through the collimator. This modification could be done using an effective diameter d_{eff} (by Piax, 1976)(96):

$$d_{eff} = \sqrt{d\left(d + \frac{2\tan\frac{\alpha}{2}}{\mu}\right) + \frac{2\tan^2\frac{\alpha}{2}}{\mu^2}} \qquad (4.7)$$

Where α is the acceptance angle of the pinhole collimator, μ is the linear attenuation coefficient of the material of the pinhole collimator.

Also, there is an alternative equation (i.e. resolution effective diameter by Accorsi and Metzler, 2004 (97)) which take into account the source to collimator angle ψ:

$$d_{\mathrm{re}/\!/} = d + \Delta L_k \left(\tan^2\frac{\alpha}{2} - \cot^2\psi\right)\cot\frac{\alpha}{2}\sin\psi, \qquad (4.8)$$

$$d_{re\perp} = \sqrt{\left(d + \Delta L_k \tan\frac{\alpha}{2}\sin\psi\right)^2 - \Delta L_k^2\cos^2\psi} \qquad (4.9)$$

Where $d_{\mathrm{re}/\!/}$ is the effective diameter parallel to the plane having the point source and pinhole collimator normal, while $d_{re\perp}$ is the effective diameter in perpendicular direction. ΔL_k is the path length through the attenuating collimator material which gives attenuation by a factor of *k* that means ($k = \exp(-\mu\Delta L_k)$) (97, 98).

4.2.3 Intrinsic spatial uniformity

A flood image from a ^{99m}Tc source was produced by placing a 2 mm diameter point source of ^{99m}Tc solution at a distance of 200 mm away from the un-collimated camera, (see Figure 4.7).

The reporting parameter for intrinsic spatial uniformity was the CoV – the ratio of standard deviation in counts to mean counts. The CoV is considered an integral uniformity measure of the SFOV gamma camera as it covers the entire image.

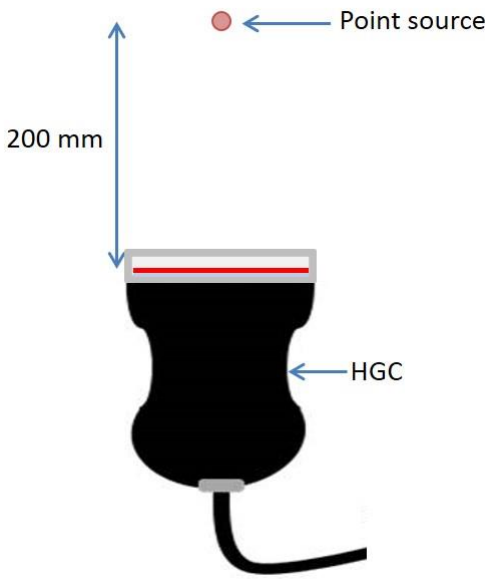

Figure 4.7: Schematic diagram shows the experimental setup of the intrinsic spatial uniformity, intrinsic spatial sensitivity and count rate capability using HGC. A 2 mm diameter point source is filled with ^{99m}Tc solution and placed at a distance of 200 mm away from the un-collimated camera.

4.2.4 Intrinsic spatial sensitivity

A flood image from a ^{99m}Tc source can be produced by placing a 2 mm diameter point source of ^{99m}Tc solution at a distance of 200 mm away from the un-collimated camera. Figure 4.5 illustrates the experimental setup.

The theoretical sensitivity of the detector for a known source energy should also be calculated, to allow a comparison between both the theoretical and experimental sensitivities of the detector. This can be done using the photon efficiency formula (Equation 4.10):

$$I/I_0 = 1 - e^{-\mu t} \qquad (4.10)$$

where μ is the linear attenuation coefficient which has unit of inverse length (cm^{-1}), t is the thickness of the scintillator.

4.2.5 Extrinsic spatial sensitivity

Extrinsic spatial sensitivity is reported at a nominal distance of 50 mm from the 0.5 mm and/or 1.0 mm diameter pinhole collimator, both with and without Perspex.. To report the extrinsic spatial sensitivity, a graph showing the relationship between extrinsic sensitivity and distance can be plotted. Extrinsic spatial sensitivity is expressed as cps/MBq.

4.2.6 Count rate capability

A 2 mm diameter point source was filled with ^{99m}Tc and placed at a distance of 200 mm away from the un-collimated camera, (see Figure 4.5).

To report the count rate capability, solid angle formulae (Equation 4.3) was used to calculate the incident count rate, taking into account the activity of the source being imaged during each acquisition time. Recorded counts can be plotted against incident counts and a straight line fitted for the linear section. Count rate capability is expressed as the maximum recorded counts, along with the incident count rate at which the

recorded count is 20 % less than that would be expected from the linear fitting from the plotted graph.

4.3 Summary and conclusion

Nuclear medical imaging systems are strongly dependent on the accuracy of the imaging instrumentation to produce an accurate clinical diagnostic images. Quality control (QC) tests are the most significant measurements and the most critical routine tests to ensure that the performance of the gamma camera systems is within a predefined acceptable range. The most commonly evaluated performance parameters include: spatial resolution (both intrinsic and extrinsic), intrinsic spatial uniformity, spatial sensitivity (both intrinsic and extrinsic) and count rate capability. Several number of institutes and organisations have developed schematic protocols for reference tests, such as; the National Electrical Manufacturers Association (NEMA) and the Institute of Physics and Engineering in Medicine (IPEM).

Over recent years, in the field of nuclear medicine, there have been significant advances in the development of SFOV gamma cameras. High resolution compact gamma cameras have been designed to be used in intraoperative medical imaging procedures such as in sentinel node biopsies in breast and head and neck cancer or for small organ imaging such as thyroid investigations. SFOV imaging can offer advantages over LFOV cameras in spatial resolution and sensitivity although, there is a trade-off between high spatial resolution and sensitivity. In addition SFOV cameras have the advantage of small size, low weight and portability.

These recent advances of the compact SFOV gamma cameras in the clinical applications has increased the demand for the most accurate and appropriate quality assurance testing. The variation of detectors of the SFOV gamma cameras, the design of the collimators used, the FOV produced and clinical procedures performed make the standard performance characterisation difficult to apply for all systems. Therefore, the modified protocols outlined in this chapter aim to be an introductory method that are applied when characterising the HGC with different scintillators and characterising other

imaging systems such as the semiconductor cadmium telluride CdTe detectors (later in the thesis). Also, it is envisaged that these protocols can be used as a guideline when comparing between different systems.

A full assessment of the HGC has been undertaken previously by Bugby et al. (64), following the performance characteristics protocols of SFOV gamma cameras that has been modified by Bhatia et al. (65). A comparison has been made between the SFOV hybrid gamma camera and for an example LFOV gamma camera (Nucline^{TM} Cardio-C) (99) from literature which are shown in Table 4.2.

Table 4.2: Comparative results for the evaluated SFOV hybrid gamma camera and for an example LFOV gamma camera. Table reproduced from Bugby et al. (64)

	LFOV (Nucline^{TM} Cardio-C) (Alsótőrőkvész u, 2004)	**SFOV (Hybrid gamma camera) (Bugby et al., 2014)**
Field of view	370 x 210 mm	40 x 40 mm
Intrinsic spatial resolution	2.8 mm FWHM	0.63 mm FWHM
Extrinsic spatial resolution	7.1 mm FWHM	1.28 mm FWHM
Intrinsic spatial uniformity	Integral uniformity 2.4 % Differential uniformity 1.9 %	Integral uniformity 8.5 % Differential uniformity 0.60 %
Sensitivity	144 cps/MBq	214 cps/MBq
Count rate capability	200 kBq	>1.2 kBq

As SFOV systems are still a growing field in nuclear medicine, future protocols need to be developed to provide more accurate and convenient protocols for the SFOV gamma cameras in specific clinical applications.

So these protocols were used in this thesis to characterise the HGC in Chapter 5, and the CdTe semiconductor detectors in Chapter 6.

Chapter 5

Comparison of the performance characterisation of a scintillator-CCD based detector using CsI:Tl, GOS and $CdWO_4$ scintillators for nuclear medical imaging

Over recent years, in the field of nuclear medicine, there have been important advances in the development of small field of view (SFOV) gamma cameras. High resolution compact gamma cameras have been designed to be used in intraoperative medical imaging procedures such as in sentinel node biopsies in breast and head and neck cancer, or for small organ imaging such as thyroid investigations (100). SFOV imaging can offer advantages over large field of view (LFOV) cameras in terms of spatial resolution and sensitivity although there is a trade-off between high spatial resolution and sensitivity. In addition SFOV cameras have the advantage of small size, low weight and portability in comparison to the standard gamma camera.

Scintillator-based SFOV gamma cameras may use position sensitive photo multiplier tubes (PSPMTs), photodiodes, or an electron multiplying charge coupled devices (EM-CCDs) (101).

There are several aspects that could affect the choice for a suitable scintillator for a particular medical imaging application: the absorption of an incident photon is directly

proportional to the density and the attenuation coefficient of the material, the number of scintillation photons are proportionally dependant on the light yield, peak emission wavelength and refractive index could affect the efficiency of the photon scintillations detected. Those aspects have been compared previously in (Chapter 2, section 2.3.1) for CsI:TI, GOS and $CdWO_4$ at 140.5 keV, which is the photo-peak of a commonly used radioactive isotope in nuclear medical imaging ^{99m}Tc.

The main purpose of this chapter is to compare the performance of the Hybrid Gamma Camera (HGC) (19) following the modified protocols (discussed in Chapter 4) based on the Institute of Physics and Engineering in Medicine (IPEM) (65) using a columnar CsI:TI scintillator, a pixelated GOS scintillator and a transparent inorganic $CdWO_4$ scintillator. The performance characteristics measured were: intrinsic and extrinsic spatial resolution, intrinsic spatial uniformity, intrinsic and extrinsic spatial sensitivity and count rate capability.

5.1 Materials and methods

5.1.1 Scintillators

A. Columnar CsI:TI scintillator

In this study both a 600 µm and a 1500 µm thick Hamamatsu CsI:TI scintillators, on a 500 µm thick amorphous carbon substrate (102) were investigated. The substrate supports the relatively fragile scintillator. It also has a reflecting layer which redirects the light back towards the CCD to increase the light collection. The CsI:TI scintillator is grown in a columnar structure. Figure 5.1 shows the features of the scintillator imaged using a scanning electron microscope (SEM). The columns act as a guide to channel the light to the CCD and so reduce the light spread within the scintillator. More details of the properties of CsI:TI have been discussed in Chapter 2, section 2.3.2.

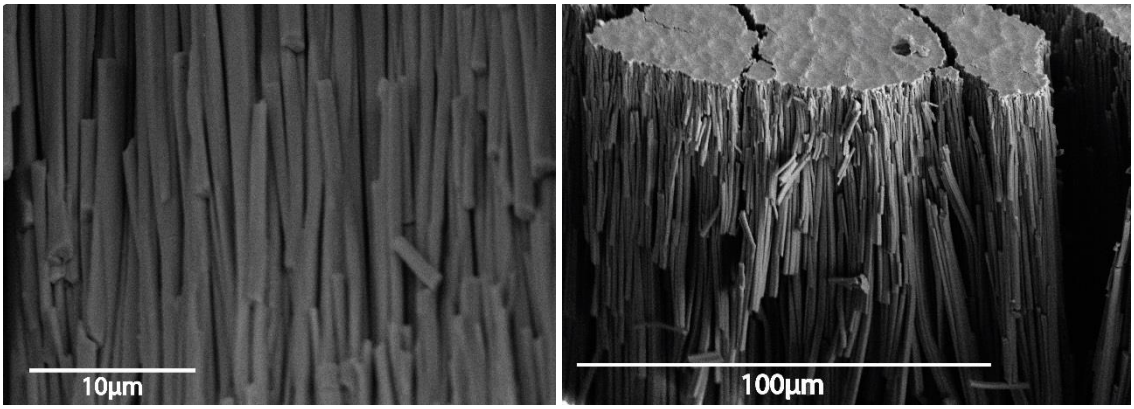

Figure 5.1: An example of the columnar CsI:TI scintillator imaged using a scanning electron microscope (SEM) showing that the columns are tightly packed and extended vertically through the thickness of the scintillator. Each column is approximately 1 µm in diameter.

B. Pixelated GOS scintillator

The 1500 µm thick Gadolinium oxysulfide (GOS) scintillator was provided by Toshiba specifically for this study (103). GOS is a relatively new efficient pixelated scintillator in medical imaging applications. Figure 5.2 shows a subsection of the scintillator which is 8 mm x 8 mm in total. There are 18 x 18 pixels in the full scintillator and each pixel is 400 µm x 400 µm, individually separated by 40 µm thick material covered with TiO_2. The TiO_2 was used to make it easier for the scintillation photons to be constrained within each pixel. Further details of the GOS properties have been discussed in Chapter 2, section 2.3.3.

C. Transparent inorganic $CdWO_4$ scintillator

A prototype $CdWO_4$ scintillator (104) was created using femtosecond pulsed ablation from a Thales Bright Laser. Figure 5.3 illustrates the features of a 5200 µm thick $CdWO_4$ scintillator which is 12 mm x 11 mm in dimension and consists of 25 x 24 segments of $CdWO_4$. For more details of the laser micromachining of $CdWO_4$ scintillator refer to Richards's doctoral thesis, 2015 (104). The properties of $CdWO_4$ have been discussed in Chapter 2, section 2.3.4.

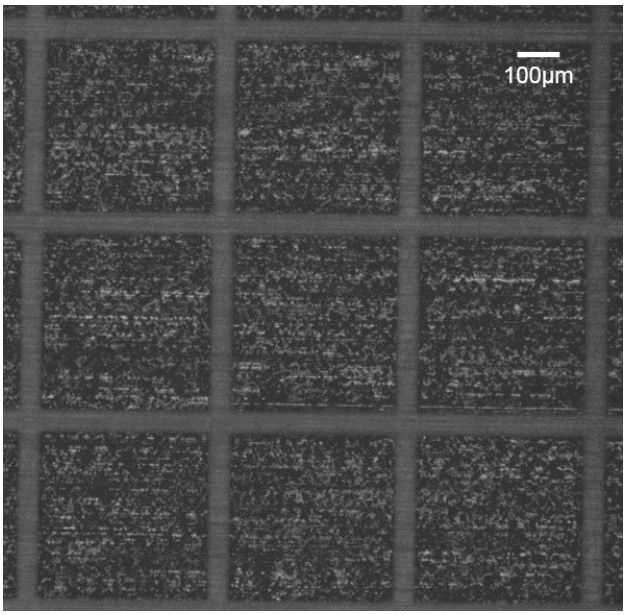

Figure 5.2: Scanning electron microscope (SEM) image of a 3 x 3 section of a 1500 µm thick pixelated GOS scintillator. Each pixel is 400 µm x 400 µm, separated individually by 40 µm wide material coated with TiO_2.

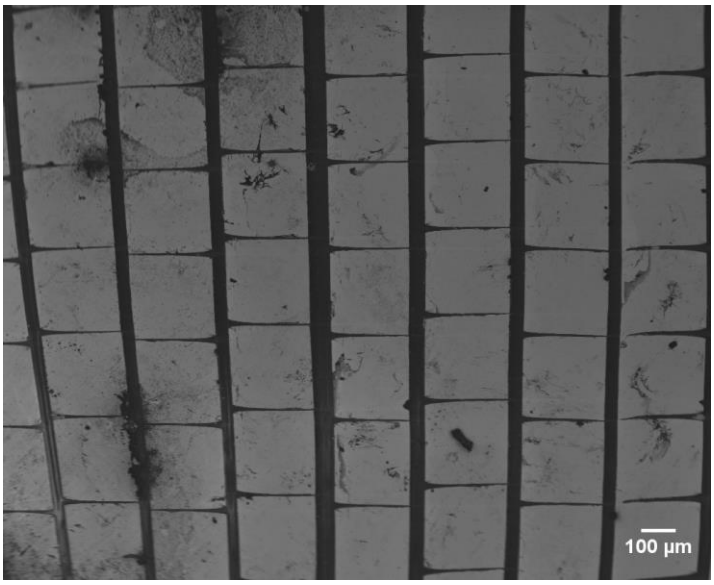

Figure 5.3: Scanning electron microscope (SEM) image of a 7 x 7 section of the femtosecond prototype $CdWO_4$ scintillator. The image shows some damage occurred from the polishing process due to the absence of the inter segment filler material that was used to add strength to the scintillator structure.

According to literatures (58), the advantages of the pixelated scintillators that they have fewer edge effects than the columnar scintillators and the images acquired using the pixelated scintillators have high intrinsic spatial resolution. However, the cost and the complexity of designing the gamma camera system using pixelated scintillators will be increased. Also, the detection sensitivity will be decreased and this is because of the presence of the dead area between the pixelated scintillators.

5.1.2 Coupling method

A flexible Kapton window was used to hold the scintillator in place on the active area of the CCD. In the case of both thicknesses of CsI:TI scintillator and the $CdWO_4$ scintillator no optical grease was used. However, the 1500 μm thick GOS scintillator was installed in the HGC twice; with and without optical grease coupling.

5.1.3 Imaging process

Imaging software programme which is called CCD control and acquisition was written on IDL software by a member of our research group using a special algorithm named "blob detection" with automatic scale selection (62). This software is based on determining the location of each gamma interaction within the scintillator crystal along with the energy of the detected photon.

A full gamma image can consists of any number of frames, typically ranging from 100 – 10000 frames. Each frame took approximately 0.1 s to acquire. Images were stored in a proprietary event record format, which separates each image frame to allow for image processing. The format of the acquired gamma image detected by the HGC records the x-position, y-position and signal level for each pixel in the frame which exceeds a pre-set threshold value.

In some situations, counts can be recorded above the expected thermal noise in more than 5 % of frames in a dark image. Those recorded counts are called hot pixels.

Therefore, hot pixel mapping was used to remove those hot pixels from each frame during the acquisition processes.

During image processing, the pixel signals on the CCD were converted to an image which displays the magnitude and position of deposited energy throughout the acquisition time. The type of post image processing used depended on the type of scintillator installed.

i. Gamma reconstruction for CsI:TI

If the columnar CsI:TI scintillator is installed in the HGC, then each gamma photon interaction within the crystal will produce an approximately Gaussian light splash on the CCD (105, 106), with a typical width between two and ten pixels. Each light splash has a signal higher than the detector noise thus during acquisition excluding both thermal and readout noise can be possible by setting a threshold equal to the mean of the noise peak plus 5σ.

Blob detection with an automatic scale selection algorithm is used to calculate the intensity of each light splash as well as the energy of the incident gamma photon (105, 106). This algorithm determines each light splash and calculates a representative Gaussian distribution with a peak amplitude A and standard deviation σ. The incident gamma photon energy is derived from the total signal within each light splash which is given by $2\pi A\sigma^2$ and a single gamma event is placed at the centroid of the light splash (105, 106).

ii. Gamma reconstruction for GOS

When the pixelated GOS scintillator is installed in the HGC, each gamma photon interaction within the crystal will produce a number of scintillator photons that are constrained within each GOS pixel where the interaction occurs. Each 400 µm square GOS pixels could cover approximately 49 CCD pixels. Threshold setting is not applied during acquisition as the signal levels within each CCD pixel are not higher than the background noise. This is due to the lower scintillation photon yield of GOS in

comparison to CsI:TI along with the larger area over which the light is typically spread (106).

The area of the CCD corresponding to each GOS pixel is determined after installation of the GOS to the HGC. Then during gamma reconstruction, the CCD image was binned into an 18 x 18 pixel image corresponding to the GOS array. In the case of the CsI:TI acquisition only events above a threshold are recorded, however, in the GOS acquisition this method records a signal in each pixel in every frame but many of these will not be due to a gamma event (106).

iii. Gamma reconstruction for $CdWO_4$

With the pixelated $CdWO_4$ scintillator installed in the HGC, each gamma photon interaction within the scintillator produces a number of scintillator photons which are constrained within each $CdWO_4$ pixel in which the interaction occurs same as the GOS scintillator. However, the significant difference with the $CdWO_4$ analysis that the $CdWO_4$ pixels are not well defined and delineated. So, improvements to the analysis code has been made by squaring the blank pixels off to record accurately a signal in each pixel in every frame.

5.1.4 Experimental setup

The performance characteristics measured were: intrinsic and extrinsic spatial resolution, intrinsic spatial uniformity, intrinsic and extrinsic sensitivity and count rate capability. Full description of the protocols for assessing the performance characteristics of small field of view (SFOV) gamma cameras have been discussed previously in Chapter 4.

Test images for characterisation were acquired using the medical radionuclide ^{99m}Tc radioactive isotope, which is widely used in nuclear medical imaging. It has a relatively low gamma ray energy of about 140.5 keV, which can be easily detected by all medical gamma cameras. It has a short physical half-life for gamma emission of 6 hours which

allows for acquiring data promptly and minimises radiation exposure to patients. The ^{99m}Tc solution used in this study was provided by the Nuclear Medicine Department, Leicester Royal Infirmary (LRI). A small amount of ^{99m}Tc solution was added to a well 2 mm in diameter and 5 mm in depth. The amount of activity was measured by using a radionuclide activity calibrator from Capintec, Inc (107). The activity used for each measured parameter is illustrated in (Table 5.1). The starting activity in each parameter has been given, then for long and multiple gamma acquisitions the reduction in the activity during the performance of the experiment was calculated and taken into account.

Table 5.1: Activity used in the experiment.

Scintillators	**Activity (MBq)**				
	CsI:TI		GOS		$CdWO_4$
Parameters	600 µm	1500 µm	without optical grease	with optical grease	4350 µm
Intrinsic spatial resolution	20	1.35	14.0	1.55	138.8
Extrinsic spatial resolution and extrinsic sensitivity	30	1.35	1.70	1.55	110.6
Intrinsic spatial uniformity and intrinsic sensitivity	25	1.35	14.0	1.55	5.45
Count rate capability	20	72.0	72.60	70.0	59.4

I. Intrinsic spatial resolution

A 10 mm thick lead block with a slit of 3 mm width and 20 mm length was positioned on top of the un-collimated camera. A 2 mm diameter ^{99m}Tc source was placed at a distance of 200 mm above the surface of the slit. This distance was chosen in order to ensure a uniform gamma image. This can be achieved by placing the point source at least 100

times its diameter size (65). A slit image was obtained with 5000 frames (acquisition time of ~ 510 s) by the HGC.

A line profile was then produced by placing a line segment horizontally across the image of the source. The resulting values were analysed using Origin software (94) to obtain the Edge Response Function (ERF). The derivative of the ERF was then taken to produce the Line Spread Function (LSF). The modulus of the LSF was fitted with a Gaussian distribution from which the FWHM and the FWTM were calculated.

II. Extrinsic spatial resolution

To measure the extrinsic spatial resolution, a 2 mm diameter source was filled with ^{99m}Tc solution. This was imaged with a 1.0 mm diameter tungsten pinhole collimator. It is agreed that the extrinsic spatial resolution can be improved by reducing the pinhole's diameter size (108-110). However, for the majority of clinical uses, the 1.0 mm diameter pinhole is the appropriate choice despite the sensitivity is improved at the cost of degraded spatial resolution. During intraoperative surgical procedures, the need for acquiring gamma images quickly is most important (68). For this reason the 1.0 mm diameter pinhole collimator was chosen for this study rather than a 0.5 mm diameter pinhole collimator. Layers of PMMA poly methyl methacrylate (i.e. Perspex) starting from 20 mm thickness up to 77.5 mm were placed between the collimator and the source to simulate different tissue depths within the human body. Perspex has similar attenuation properties to those of human tissue (88). Images were recorded both with and without Perspex at 10 different distances starting from 20 mm to 200 mm over 2000 frames (acquisition time of ~ 204 s).

III. Intrinsic spatial uniformity

A flood image was produced by placing a 2 mm diameter source of ^{99m}Tc solution at a 200 mm distance away from the un-collimated camera and imaged over 20,000 frames with an acquisition time of ~ 2040 s.

IV. Intrinsic spatial sensitivity

Intrinsic spatial sensitivity was calculated with the same flood image acquired for intrinsic spatial uniformity measurements.

V. Extrinsic spatial sensitivity

Extrinsic spatial sensitivity was calculated from the same images that were recorded for the extrinsic spatial resolution measurements.

VI. Count rate capability

A 2 mm diameter source of ^{99m}Tc solution was placed at 250 mm distance from the un-collimated camera. The point source was left in place for several days and images were taken over that period at regular intervals (i.e. every 60 minutes). Each image was formed from 2000 frames and the acquisition time was 204 s.

5.2 Results

The performance characteristics of the HGC fitted with each scintillator have been evaluated and the results are described in the following section.

5.2.1 CsI:TI scintillator

i. Intrinsic spatial resolution

Figures 5.4 and 5.5 show the analysed resultant images. Detailed and full process of analysing the resultant images have been discussed in Chapter 4. Results obtained from analysing the images are tabulated in (Table 5.2).

Comparing the intrinsic spatial resolution results of the HGC with 600 µm and 1500 µm thick CsI:TI scintillators show that the thinner scintillator operates with lower intrinsic spatial resolution (i.e. 170 µm) compared to the thicker scintillator (i.e. 230 µm). Therefore the HGC fitted with 600 µm thick CsI:TI would offer better spatial resolution. Due to more Compton scattering and lateral spread of the optical photon, that is because of the needle structure of the CsI:TI scintillator, the thicker scintillator i.e. 1500 µm would have slightly poor spatial resolution by about 50 % (52, 68). In this experiment the use of 1500 µm thick CsI:TI scintillator degraded the resolution only by 26 %, this relatively small change of resolution was due to the light guiding effect from the columnar features of the CsI:TI scintillation layer.

600 µm thickness

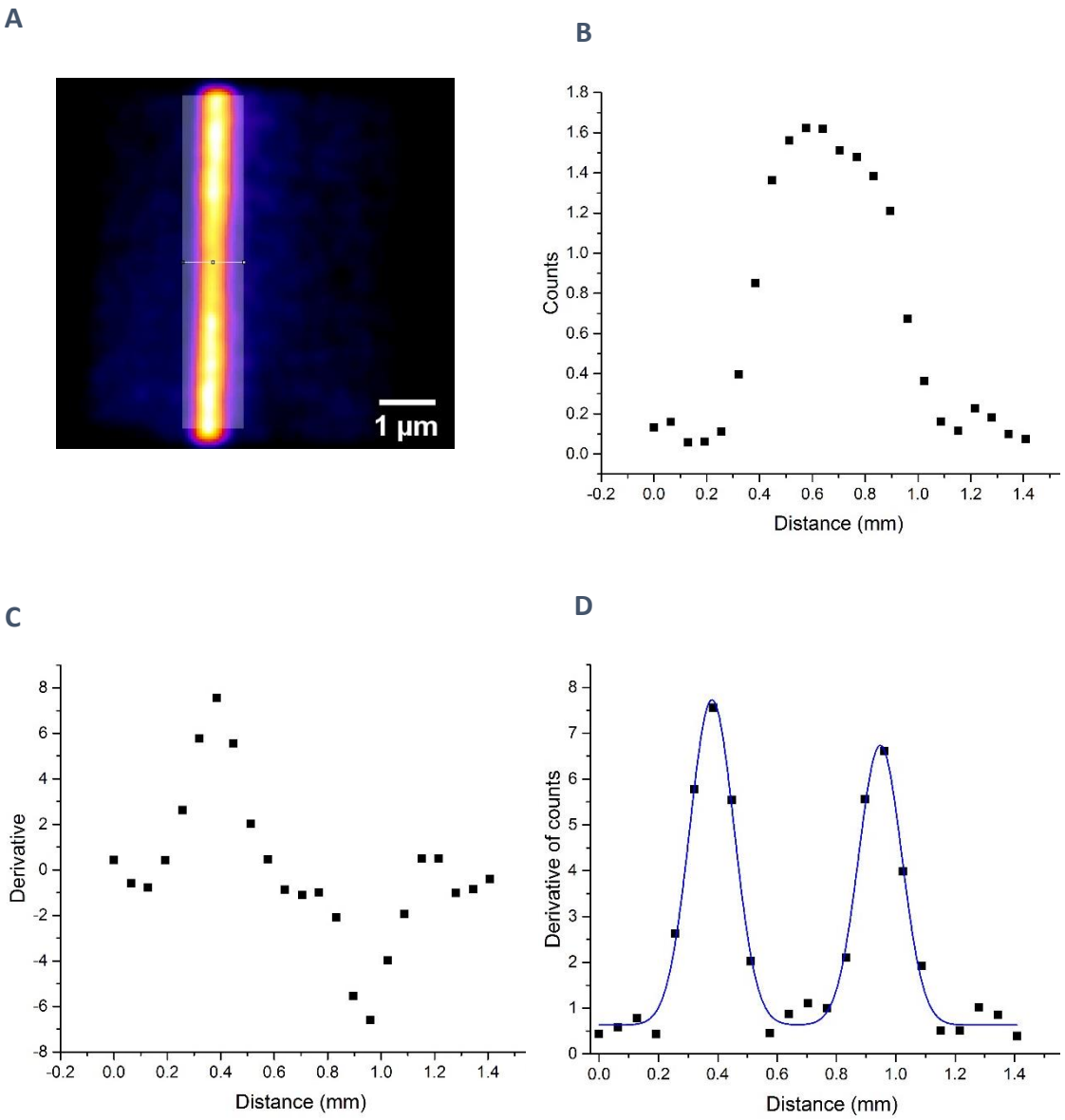

Figure 5.4: Graphs showing the intrinsic spatial resolution measurement process for the 600 µm thick CsI:TI scintillator using 20 MBq ^{99m}Tc source. A) Final image of ^{99m}Tc at 200 mm distance from the 3 mm width slit. Total no. of frames was 5000. The acquisition time was 510 sec. B) Edge response function (ERF) for ^{99m}Tc source. C) Line spread function (LSF) i.e. derivative of ERF. D) Modulus of LSF with fitted Gaussians.

1500 µm thickness

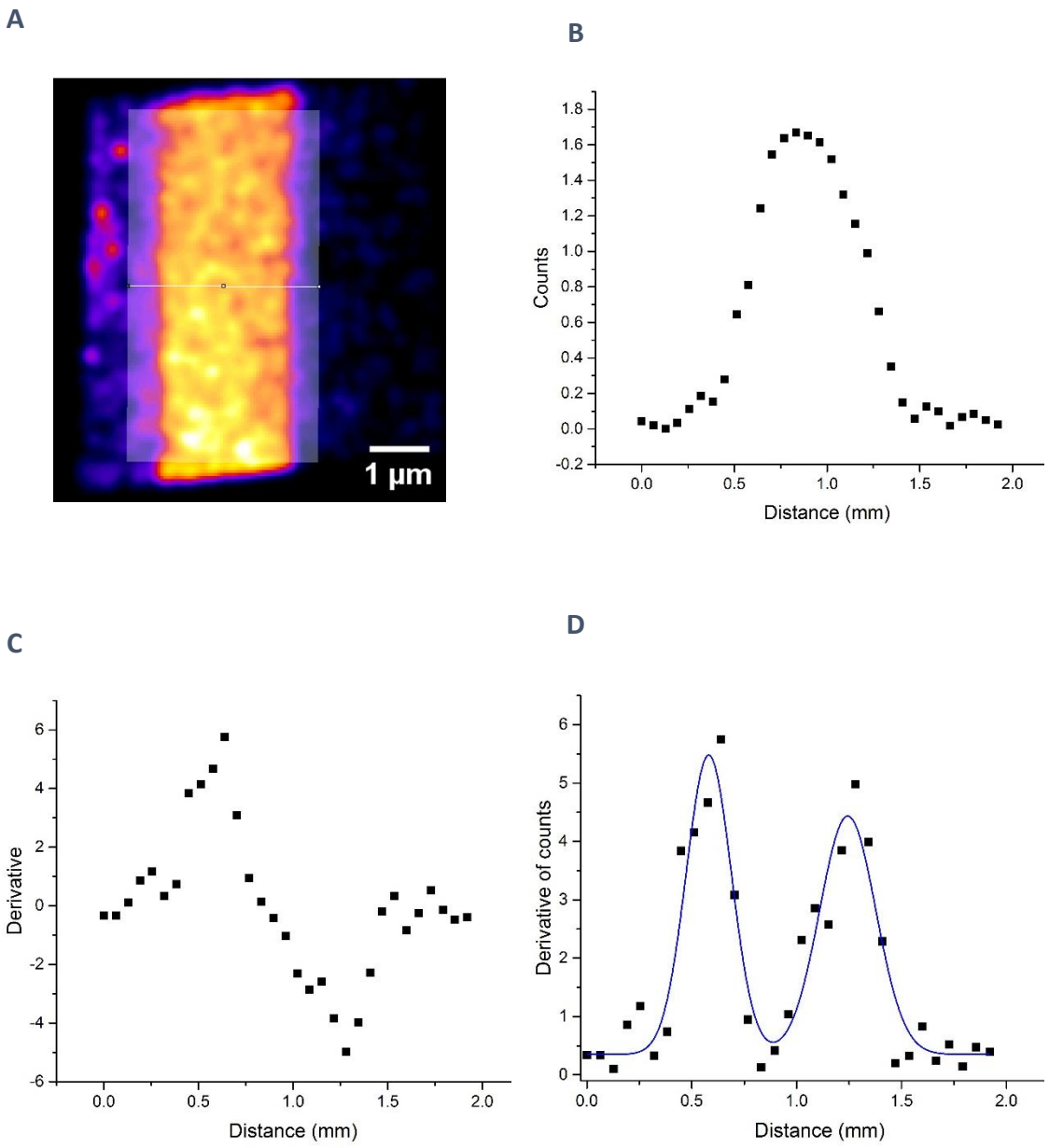

Figure 5.5: Graphs showing the intrinsic spatial resolution measurement process for the 1500 µm thick CsI:TI scintillator using 1.35 MBq ^{99m}Tc source. A) Final image of ^{99m}Tc at 200 mm distance from the 3 mm width slit. Total no. of frames was 5000. The acquisition time was 510 sec. B) Edge response function (ERF) for ^{99m}Tc source. C) Line spread function (LSF) i.e. derivative of ERF. D) Modulus of LSF with fitted Gaussians.

Table 5.2: Intrinsic spatial resolution results for 600 µm and 1500 µm thick CsI:TI scintillators.

Parameters	CsI:TI scintillator	
	600 µm	**1500 µm**
FWHM (µm)	170 ± 12	230 ± 25
FWTM (µm)	300 ± 20	468 ± 23

ii. Extrinsic spatial resolution

There was a slight difference in the method used for both thicknesses of the CsI:TI scintillator. For the thinner scintillator, a line source was used and images were acquired with scattering material only. However, for the thicker CsI:TI a point source was used instead both with and without scattering material. The difference in the method used is due to the planning of the characterisation protocol was structured after installing the thicker scintillator to the HGC, which makes it difficult to re-install the thinner scintillator to the HGC to re-acquire a new data.

According to Bhatia et al. (65), it is possible to use either a point or line source with SFOV gamma cameras. Since the pinhole collimator is used then the line source would appear as a flood image when gamma images acquired at the collimator face. So it is advisable to report the resolution at the non-magnifying point.

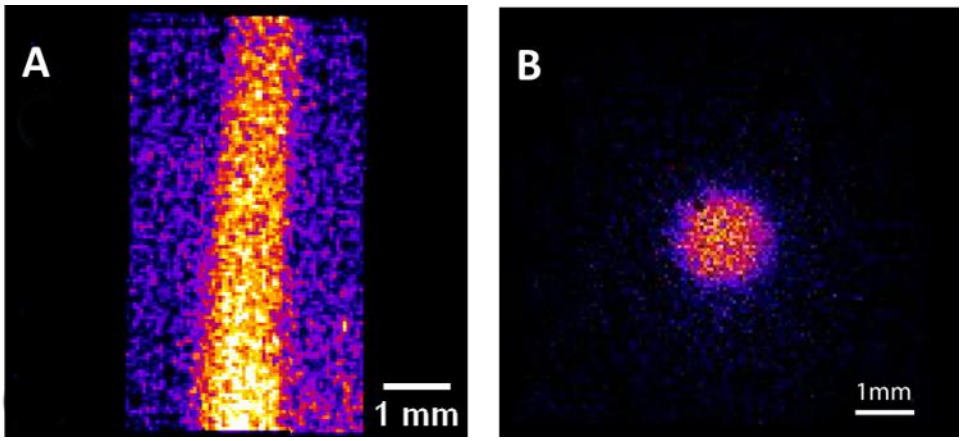

Figure 5.6: Examples of the gamma images obtained for extrinsic spatial resolution measurements using (a) a line source with the 600 µm (b) a point source with the 1500 µm CsI:TI scintillators using 1.0 mm diameter pinhole collimator. A sheet of Perspex, 20 mm thick, was placed directly between the sources and the collimator. Each image was performed with 2000 frames. The acquisition time was 204 sec.

Figure 5.6 shows examples of these images obtained with a line source using 600 µm and a point source with the 1500 µm CsI:TI scintillators. A high back ground level is noticed when using the thinner scintillator, this is due to the increase of the scattered radiation as a line source under 20 mm thickness of Perspex was used.

A 2-dimensional Gaussian curve was fitted for each measured distance using both scintillators with and without Perspex. Extrinsic spatial resolution was then defined as the FWHM of the Gaussian fitting. Figures 5.7 and 5.8 show the plot of calculated resolution measurements versus imaging distance. The error bars was propagated from the associated error in placing the source at a particular distance during camera setup. The fitted parameters of gradient *m* and intercept *c* are tabulated in (Table 5.3). The slope-intercept formula that was used to calculate the FWHM resolution value at the non-magnifying position was discussed previously in (Chapter 4, section 4.2.2).

600 µm thickness

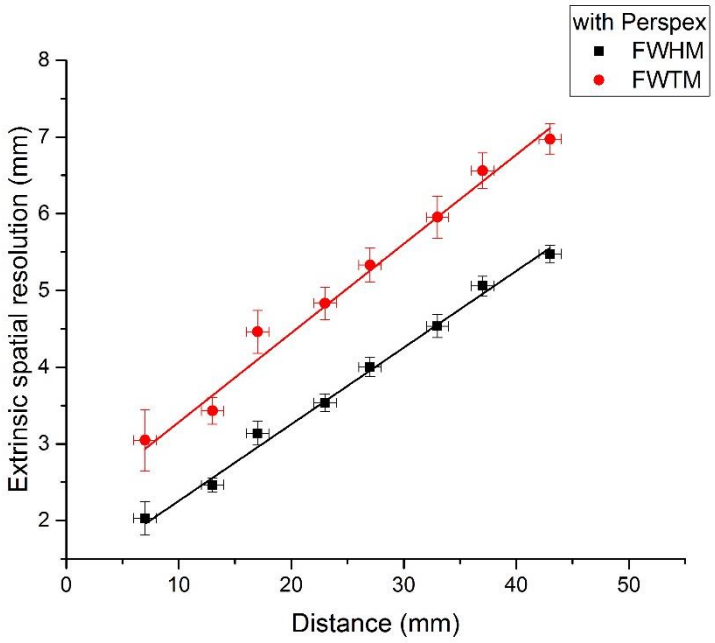

Figure 5.7: Graphs showing the extrinsic spatial resolution vs distance. FWHM (black square) and FWTM (red dots) calculated using a 1.1 mm diameter cannula filled with 30 MBq ^{99m}Tc solution with 600 µm CsI:TI scintillator using 1.0 mm diameter pinhole collimator, with Perspex. No. of frames 2000. The acquisition time was ~ 204 sec.

1500 µm thickness

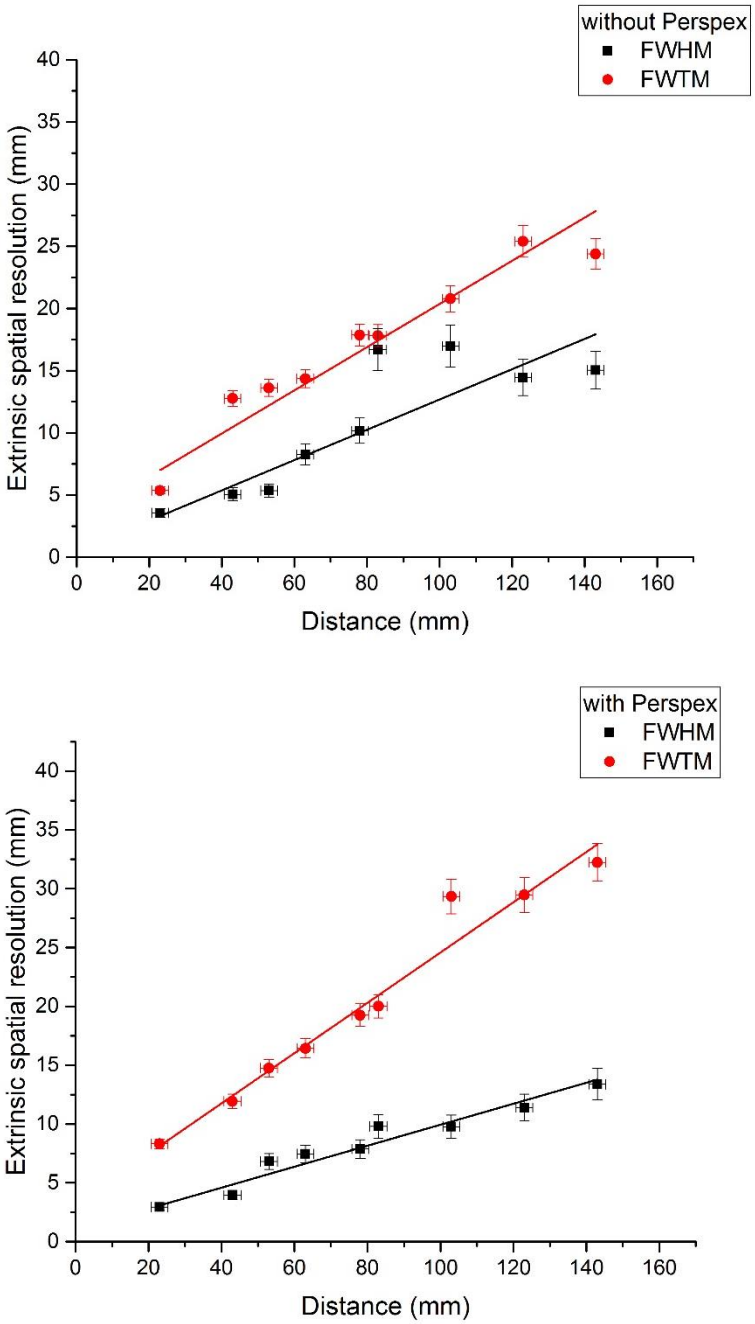

Figure 5.8: Graphs showing the extrinsic spatial resolution vs distance. FWHM (black square) and FWTM (red dots) calculated for 2 mm diameter source filled with 1.35 MBq ^{99m}Tc solution with 1500 µm CsI:TI scintillator using 1.0 mm diameter pinhole collimator. No. of frames 2000. The acquisition time was ~ 204 sec. Top: without Perspex. Bottom: with Perspex.

Table 5.3: Fitted parameters of gradient *m* and intercept *c* for the linear relationship between the extrinsic spatial resolution and the imaging distance.

CsI:TI scintillators		FWHM		R^2	FWTM		R^2
		m	*c*		*m*	*c*	
600 µm	with Perspex	0.05±0.004	1.30±0.09	0.993	0.09±0.007	2.35±0.19	0.992
1500 µm	with Perspex	0.095±0.002	1.07±0.07	0.999	0.17±0.003	1.92±0.092	0.999
	without Perspex	0.10±0.0007	0.83±0.02	0.999	0.18±0.001	1.54±0.035	0.999

Table 5.4: Extrinsic spatial resolution results for 600 µm and 1500 µm thick CsI:TI scintillators at the non-magnifying position *d* = 10 mm.

Parameters		CsI:TI scintillators	
		600 µm	**1500 µm**
FWHM (mm)	with Perspex	1.80 ± 0.13	2.02 ± 0.09
	without Perspex	NA	1.8 ± 0.03

When comparing the extrinsic spatial resolution results for both thicknesses of CsI:TI scintillators, (Table 5.4), it was noticed that the resolution is better when using the thinner scintillator (i.e. 1.80 ± 0.13 mm). In the case of the thicker CsI:TI, the resolutions degraded with increasing depths of scattering material (i.e. 2.02 ± 0.09 mm) this is expected as unscattered counts are reduced as the thickness of Perspex is increasing while the scattered counts filled the background level. When looking at extrinsic spatial resolution of CsI:TI scintillator in general, there is a close match to the theoretical geometric resolution of the 1.0 mm diameter pinhole collimator (Equation 4.6 discussed in Chapter 4).

iii. Intrinsic spatial uniformity

As discussed in Chapter 4, section 4.1.3, the coefficient of variation (CoV) is calculated to report the global changes in uniformity. The results of CoV with both 600 µm and 1500 µm thick CsI:TI scintillators are shown in (Table 5.5).

Comparing the CoV of the HGC with 600 µm and 1500 µm CsI:TI scintillators it appears that the thicker scintillator has a CoV value of (20 ± 15 %) which implies that it is more uniform compared to 600 µm CsI:TI scintillator (i.e. 25 ± 9 %).

Table 5.5: Coefficient of variation (CoV) results for both 600 µm and 1500 µm CsI:TI scintillators.

Parameters	**CsI:TI scintillators**	
	600 µm	**1500 µm**
Coefficient of variation (CoV)	25 ± 9 %	20 ± 15 %

iv. Intrinsic spatial sensitivity

To report the intrinsic spatial sensitivity in a percentage of incident counts, the solid angle formulae were applied as discussed previously in (Chapter 4, section 4.1.4). The theoretical sensitivity of the scintillator can be calculated using the photon efficiency formula (Equation 4.7) which was also discussed in Chapter 4.

A comparison of the theoretical and the experimental performance characteristics for the intrinsic spatial sensitivity of the HGC with both 600 µm and 1500 µm CsI:TI scintillators at 140.5 keV energy are shown in (Table 5.6).

There is a large difference in intrinsic sensitivity measurements, the 600 µm thick was found to have a sensitivity of (19 ± 1 %) whereas the sensitivity for the thicker scintillator was (40 ± 3 %). Both of these values are slightly less than the theoretical maximum sensitivity. This is could be due to the loss of incident radiation to the detector as during the experiment there is no optical grease between the CsI:TI scintillator and the CCD also there are some scattered radiation when the incident photons interact with the CsI:TI scintillator. According to literatures (43, 111), to achieve the best detector efficiency, optical grease is highly recommended to minimize internal reflections. The refractive index of the optical grease can also deeply affects the total amount of light collected by the gamma camera.

Table 5.6: Intrinsic spatial sensitivity results for 600 µm and 1500 µm CsI:TI scintillators at 140.5 keV.

CsI:TI scintillator	Theoretical sensitivity	Experimental sensitivity
600 µm	20.6 %	19 ± 1 %
1500 µm	43.6 %	40 ± 3 %

v. Extrinsic spatial sensitivity

Extrinsic spatial sensitivity was calculated by dividing the total recorded counts by the activity of the source to give the sensitivity in cps/MBq. Extrinsic spatial sensitivity was reported at a nominal distance of 50 mm from the 1.0 mm diameter pinhole collimator, both with and without Perspex in the case of 1500 µm thick CsI:TI scintillator. However, when the thinner scintillator was applied, the extrinsic spatial sensitivity was reported with Perspex only (Table 5.7). As discussed previously, this is due to the planning of the characterisation protocol was structured after installing the thicker scintillator to the HGC, which makes it difficult to re-install the thinner scintillator to the HGC to re-acquire a new data without using Perspex. Figures 5.9 and 5.10 show the relationship between the extrinsic spatial sensitivity and the imaging distances. The error was determined using the square root of the number of counts in the region of interest (ROI) since the number of counts registered is governed by Poisson statistics.

Table 5.7: Extrinsic spatial sensitivity results for both 600 µm and 1500 µm CsI:TI scintillators at 50 mm distance.

Parameters		CsI:TI scintillator	
		600 µm	**1500 µm**
Extrinsic spatial sensitivity	with Perspex	0.8±0.1 cps/MBq	3.3 ± 0.5 cps/MBq
	without Perspex	NA	6.6 ± 0.5 cps/MBq

600 µm thickness

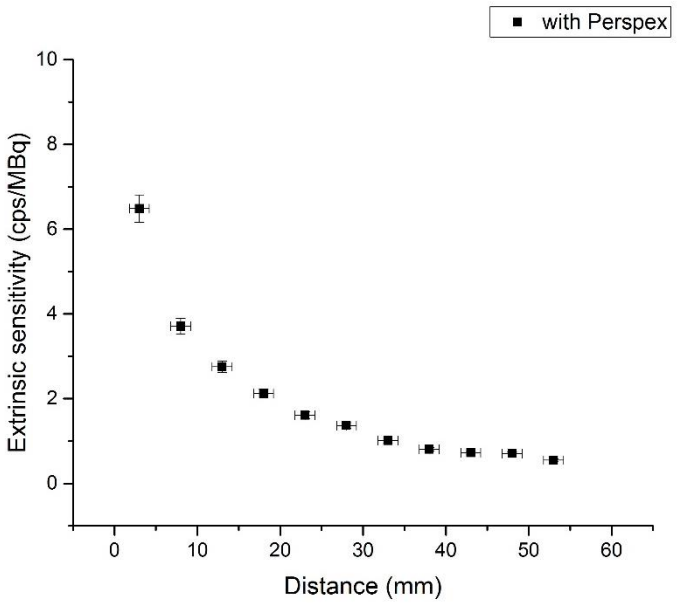

Figure 5.9: Graphs showing the relationship between the extrinsic spatial sensitivity and varying distances from the detector using 1.0 mm diameter pinhole collimator. (black squares) with Perspex calculated for 30 MBq ^{99m}Tc source using 600 µm CsI:TI scintillator.

1500 µm thickness

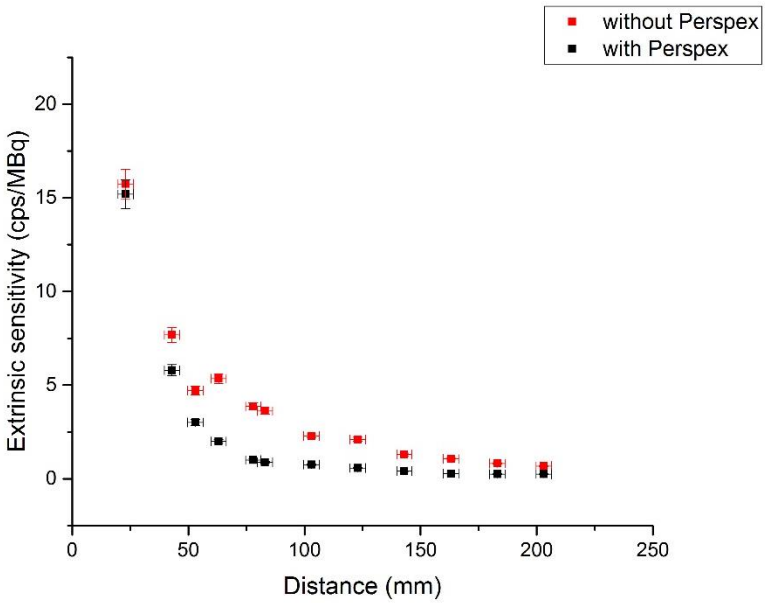

Figure 5.10: Graphs showing the relationship between the extrinsic spatial sensitivity and varying distances from the detector using 1.0 mm diameter pinhole collimator. (black squares) with Perspex (red squares) without Perspex calculated for 1.35 MBq ^{99m}Tc source with 1500 µm CsI:TI scintillator.

vi. Count rate capability

Count rate capability is expressed by the count rate response curve observing the recorded counts increasing linearly with incident count rates from a radioactive source (93). Recorded counts per second should be plotted against incident counts per second and a straight line should be fitted to the linearly proportional section of the curve for both 600 µm (Figure 5.11) and 1500 µm thick CsI:TI scintillators (Figure 5.12). The maximum incident count rate should be reported.

Comparing the count rate capability of the HGC with 600 µm and 1500 µm CsI:TI scintillators shows that the HGC has a linear count rate up to at least 1200 counts per second (cps) incident using the thinner scintillator and up to at least 3537 cps incident using the thicker CsI:TI.

600 µm thickness

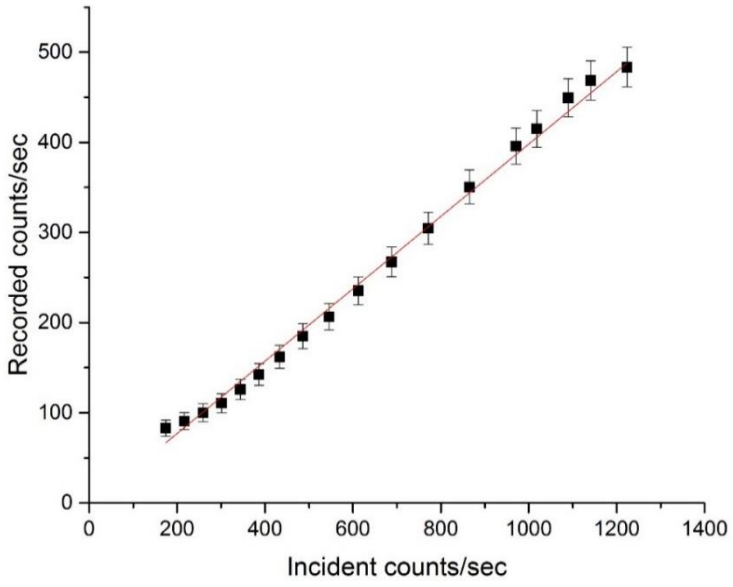

Figure 5.11: Recorded count rate capability for HGC by using 2 mm diameter ^{99m}Tc source filled with 20 MBq for the 600 µm CsI:TI scintillator placed 250 mm away from the un-collimated camera. Images were taken over the course of several days at regular intervals (i.e. every hour). No. of frames 2000. The acquisition time was ~ 204 sec.

1500 µm thickness

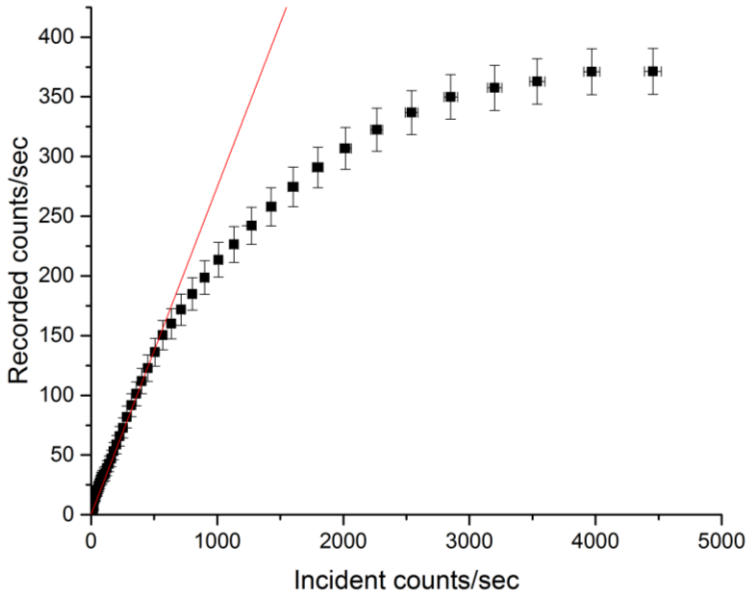

Figure 5.12: Recorded count rate capability for HGC by using 2 mm diameter ^{99m}Tc source filled with 72 MBq for the 1500 µm CsI:TI scintillator placed 250 mm away from the un-collimated camera. Images were taken over the course of several days at regular intervals (i.e. every hour). No. of frames 2000. The acquisition time was ~ 204 sec.

It has been discussed previously by Bugby et al (64) that the HGC has a limitation in count rate capability measures which it could not resolve different incident light splashes on the detector. As it is agreed that there are two factors affecting the count rate capability of the HGC. The count rate capability of the detector itself (i.e. the saturation charge level). The other factor is the appropriate counts per frame that needed in order to resolve each individual event. IPEM suggests that the count rate capability should be reported in term of the incident count rate cps unit at which there is a 20 % difference between the recorded and incident count rate.

5.2.2 GOS scintillator

To measure the performance of the HGC with the 1500 µm thick GOS scintillator, a comparison has been done between coupling the GOS scintillator to the CCD with and without using an optical grease. The optical grease used was Dow Corning 7 Release

Compound (112). It is a high performance lubricant that composed of grease like materials. It has several features; adaptable, heat-stable and compatible with plastics, rubber and metals. A thin layer of optical grease was applied between the GOS scintillator and the CCD to bind them and to optically couple them. It is well-known that optical coupling is used in order to increase the number of light photons received to the CCD (113). So, the aim in this section of the study was to figure out if optical coupling will give a better performance of the HGC.

i. Intrinsic spatial resolution

Figures 5.13 and 5.14 illustrate the full process of analysing the resultant images. Results obtained from analysing the images are tabulated in (Table 5.8).

Comparing the intrinsic spatial resolution results of the HGC using the GOS scintillator show that there is no significant difference when coupling the GOS to the CCD with (i.e. 984 μm) and without optical grease (i.e. 1090 μm). Therefore the ability of the GOS scintillator to differentiate and localise regions of interest when installed with and without optical grease are comparable. The optical grease has not improved the resolution, this might be due to the use of un-proper optical grease and/or un-proper coupling method was applied.

Table 5.8: Intrinsic spatial resolution results for the GOS scintillator.

Parameters	**GOS scintillator**	
	without optical grease	with optical grease
FWHM (μm)	1090 ± 200	984 ± 320
FWTM (μm)	1984 ± 280	1793 ± 150

Without optical grease

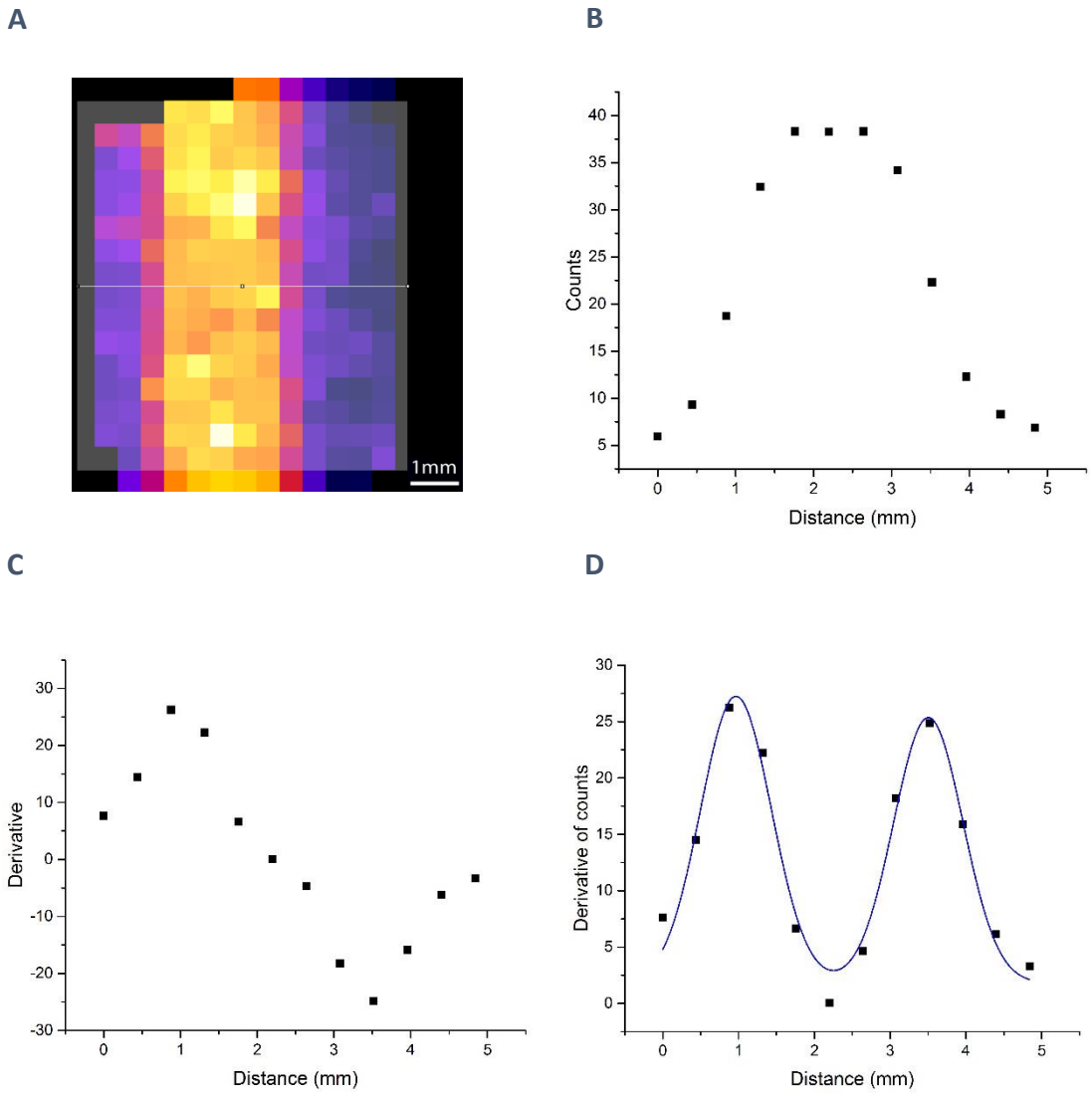

Figure 5.13: Graphs showing the intrinsic spatial resolution measurement process for the GOS scintillator without optical coupling using 14 MBq ^{99m}Tc source. A) Final image of ^{99m}Tc at 200 mm distance from the 3 mm width slit. Total no. of frames was 5000. The acquisition time was 510 sec. B) Edge response function (ERF) for ^{99m}Tc source. C) Line spread function (LSF) i.e. derivative of ERF. D) Modulus of LSF with fitted Gaussians.

With optical grease

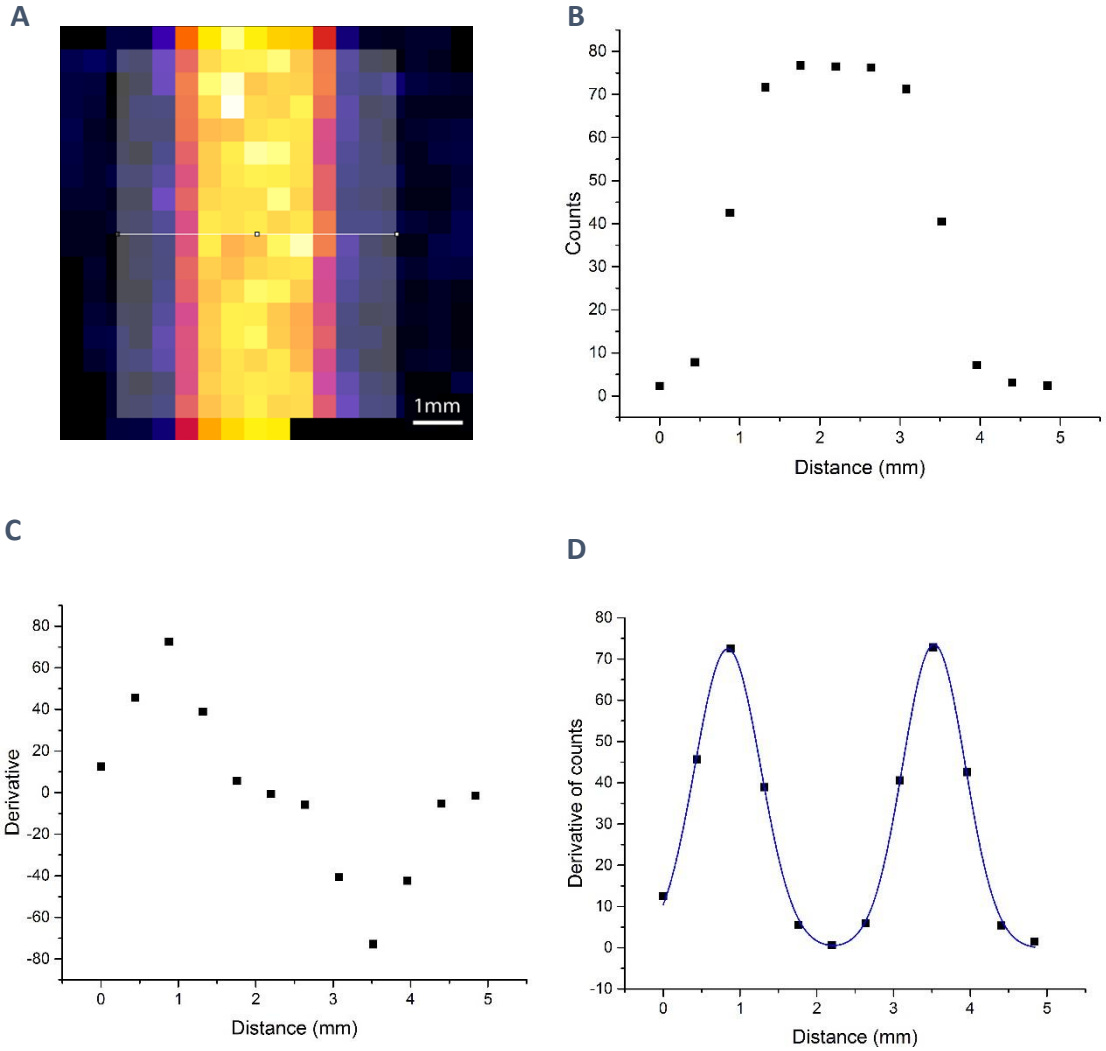

Figure 5.14: Graphs showing the intrinsic spatial resolution measurement process for the GOS scintillator with optical grease installed using 1.55 MBq ^{99m}Tc source. A) Final image of ^{99m}Tc at 200 mm distance from the 3 mm width slit. Total no. of frames was 5000. The acquisition time was 510 sec. B) Edge response function (ERF) for ^{99m}Tc source. C) Line spread function (LSF) i.e. derivative of ERF. D) Modulus of LSF with fitted Gaussians.

ii. Extrinsic spatial resolution

Figure 5.15 shows examples of the images obtained with the point source using the GOS scintillator with and without optical grease as coupling medium between the scintillator and the CCD. A 2-dimensional Gaussian curve was fitted for each measured distance using both scintillators with and without Perspex. Extrinsic spatial resolution was defined as the FWHM of the Gaussian fitting. Extrinsic spatial resolution measurements varied according to the linear relationship between imaging distance through Perspex and resolution. Figure 5.16 and Figure 5.17 show the plot of calculated resolution measurements versus imaging distance. The fitted parameters of gradient *m* and intercept *c* are tabulated in (Table 5.9) when GOS scintillator coupled to the HGC with and without optical grease and data acquired with and without Perspex in between. The results in Table 5.9 are of the order of the theoretical geometric resolution of pinhole (see Chapter 4), with slight difference due to scattered radiation, leakage through the tungsten collimator and gamma photon spreading within the crystal.

When comparing the extrinsic spatial resolution results for the GOS scintillator (Table 5.10), there was no difference noticed when coupling the GOS to the CCD with and without optical grease. This may be expected as there was no differences between them for their intrinsic spatial resolution.

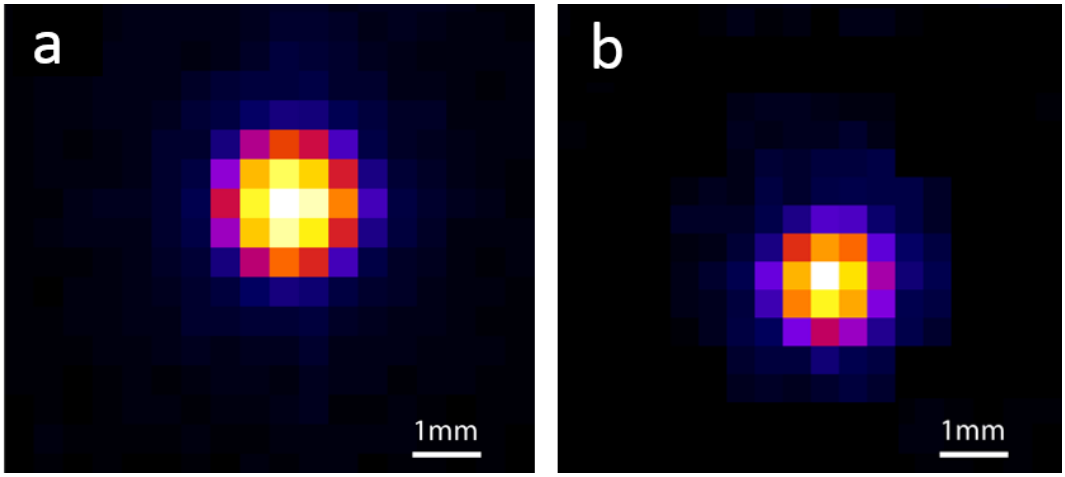

Figure 5.15: Examples of the point source images obtained for extrinsic spatial resolution measurements for the GOS scintillator (a) without optical coupling (b) with optical coupling using a 1.0 mm diameter pinhole collimator. A 20 mm of Perspex was placed directly between the point source and the collimator. Each image was acquired with 2000 frames. The acquisition time was 204 sec.

Without optical grease

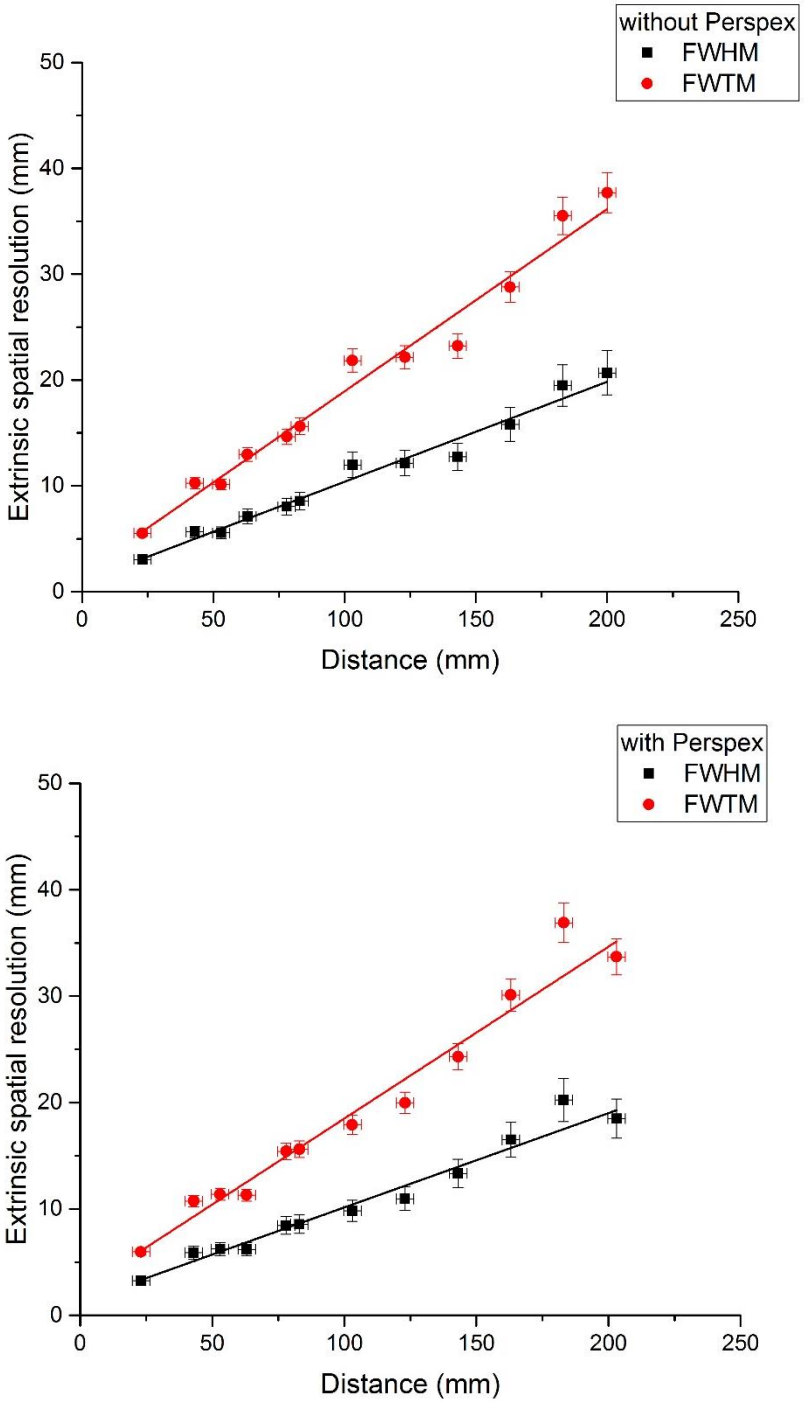

Figure 5.16: Graphs showing the extrinsic spatial resolution vs distance. FWHM (black square) and FWTM (red dots) calculated for HGC using the GOS scintillator. A 2 mm diameter ^{99m}Tc source filled with 1.70 MBq in case of no optical grease installed. A 1.0 mm diameter pinhole collimator was used. No. of frames 2000. The acquisition time was ~ 204 sec.

With optical grease

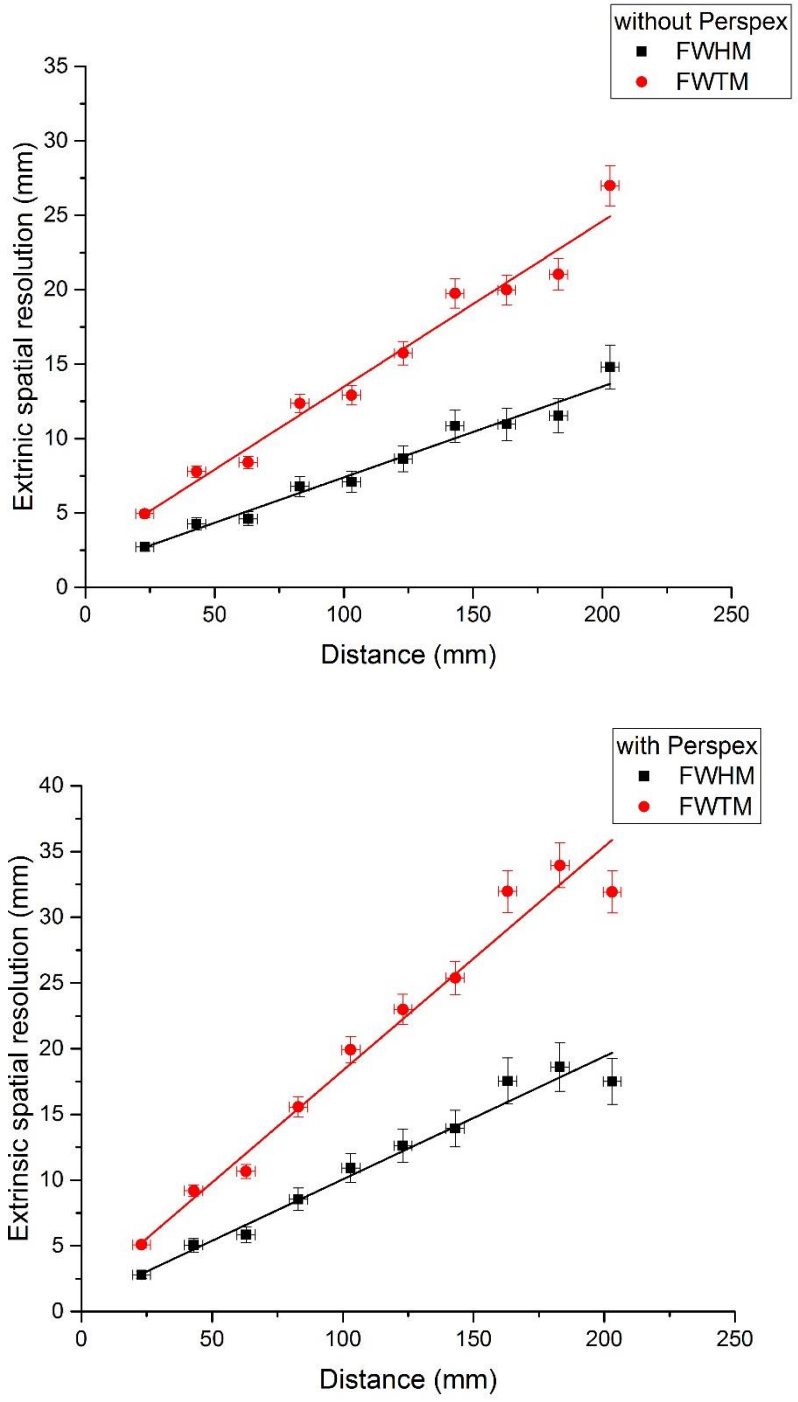

Figure 5.17: Graphs showing the extrinsic spatial resolution vs distance. FWHM (black square) and FWTM (red dots) calculated for HGC using the GOS scintillator. A 2 mm diameter ^{99m}Tc source filled with 1.55 MBq with optical grease fitted in. A 1.0 mm diameter pinhole collimator was used. No. of frames 2000. The acquisition time was ~ 204 sec.

Table 5.9: Fitted parameters of gradient *m* and intercept *c* for the linear relationship between the extrinsic spatial resolution and the imaging distance.

GOS scintillator		FWHM		R^2	FWTM		R^2
		m	*c*		*m*	*c*	
without optical grease	no Perspex	0.087±0.004	1.1±0.3	0.987	0.165±0.007	2.1±0.7	0.987
	including Perspex	0.093±0.006	1.2±0.4	0.987	0.172±0.009	2.3±0.8	0.987
with optical grease	no Perspex	0.071±0.003	1.2±0.3	0.989	0.111±0.006	2.35±0.6	0.989
	including Perspex	0.093±0.005	1.1±0.4	0.989	0.170±0.008	2.2±0.8	0.989

Table 5.10: Extrinsic spatial resolution results for the GOS scintillator both with and without optical grease installed at the non-magnifying position *d* = 10 mm.

Parameters		GOS scintillator	
		without optical grease	with optical grease
FWHM (mm)	no Perspex	1.97 ± 0.34	1.90 ± 0.33
	including Perspex	2.13 ± 0.46	2.05 ± 0.45

iii. Intrinsic spatial uniformity

The results of CoV with the GOS scintillator both with and without optical grease are shown in (Table 5.11). The CoV is comparable in the two cases, (i.e. 17 ± 9 %) without optical grease and (13 ± 4 %) with optical grease which means that is more uniform. This is may be due to the effect provided by the optical grease of evenly spreading the incident photons to the CCD.

Table 5.11: Coefficient of variation (CoV) results for the GOS scintillator both with and without optical grease installed.

Parameters	GOS scintillators	
	without optical grease	with optical grease
Coefficient of variation (COV)	17 ± 9 %	13 ± 4 %

iv. Intrinsic spatial sensitivity

A comparison of the theoretical and the experimental performance characteristics for the intrinsic spatial sensitivity of the HGC with 1500 µm thick GOS scintillator both with and without optical grease coupling at 140.5 keV energy are shown in (Table 5.12).

There is no difference in the intrinsic sensitivity measurements, in the case of no optical grease installed it was found to be 54 % whereas the sensitivity of the GOS when coupled to the CCD using optical grease was 53 %. Both of these values are less than the maximum theoretical sensitivity 69.8 %. The reduction of experimental sensitivity could be because of the scattered radiation when the incident gamma photons interact with the pixelated GOS scintillator.

Table 5.12: Intrinsic spatial sensitivity results for the GOS scintillator at 140.5 keV.

GOS scintillator	Theoretical sensitivity	Experimental sensitivity
without optical grease	69.8 %	54 ± 4 %
with optical grease		53 ± 7 %

v. Extrinsic spatial sensitivity

Extrinsic spatial sensitivity is reported at a nominal distance of 50 mm from the 1.0 mm diameter tungsten pinhole collimator, both with and without Perspex (Table 5.13). Figures 5.18 and 5.19 show the relationship between the extrinsic spatial sensitivity and the imaging distances.

For the extrinsic spatial sensitivity measurements, it was found that the GOS scintillator is more sensitive without coupling the scintillator to the CCD (i.e. 18.5 cps/MBq). However, the sensitivity of the HGC when coupling the GOS scintillator to the CCD is (16.23 cps/MBq). This difference could be due to the use of optical grease that was chosen for its vacuum compatibility properties over and above its coupling parameters. Alternatively, the coupling method itself may not have been ideal.

Table 5.13: Extrinsic spatial sensitivity results for the GOS scintillator at 50 mm distance.

Parameters		GOS scintillator	
		without optical grease	with optical grease
Extrinsic spatial sensitivity	no Perspex	18.5 ± 0.3 cps/MBq	11.23 ± 0.5 cps/MBq
	including Perspex	8.1 ± 0.3 cps/MBq	4.6 ± 0.4 cps/MBq

Without optical grease

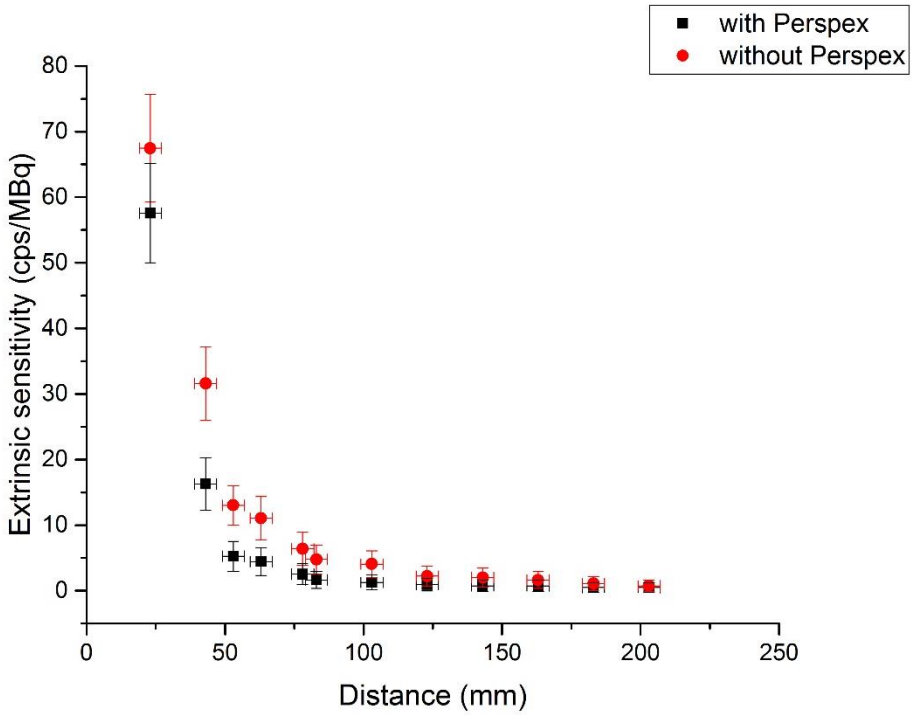

Figure 5.18: Graphs showing the relationship between the extrinsic spatial sensitivity and varying distances from the detector using 1.0 mm diameter pinhole collimator. (black squares) with Perspex (red dots) without Perspex calculated for 1.55 MBq ^{99m}Tc source with the GOS scintillator without optical grease.

With optical grease

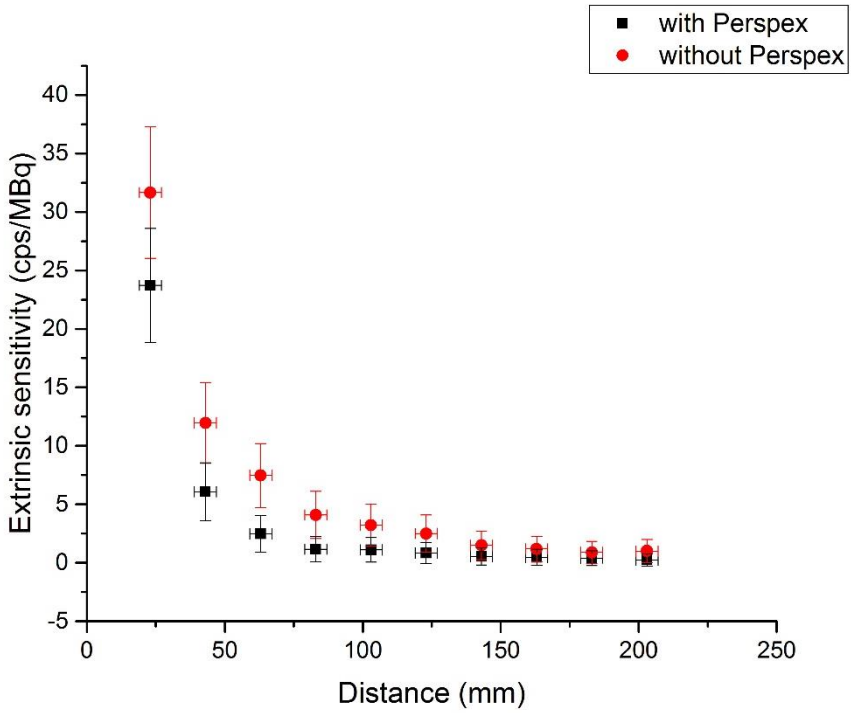

Figure 5.19: Graphs showing the relationship between the extrinsic spatial sensitivity and varying distances from the detector using 1.0 mm diameter pinhole collimator. (black squares) with Perspex (red dots) without Perspex calculated for 1.55 MBq ^{99m}Tc source with the GOS scintillator with optical grease installed.

vi. Count rate capability

Incident counts on the detector per second were calculated using solid angle formulae (Chapter 4, Equation 4.3) and plotted on a graph against recorded counts per second. The maximum recorded count rate was calculated.

A straight line was fitted to the linearly proportional section of the curve for the GOS scintillator (Figure 5.20) without optical grease (R^2 = 0.997) which indicates that the sensitivity of the HGC is linear until an incident count of at least 3170 s^{-1}. Unfortunately, in the case of using an optical grease between the GOS scintillator and the CCD, the results were not sufficient to measure the count rate capability precisely (Figure 5.21).

This is could be due to experimental error when conducting the experiment, the ^{99m}Tc source might not be positioned and stabilised vertically along with the HGC. So, that the HGC could not record acceptable range of data. The test has not been repeated as the GOS scintillator was exchanged with the $CdWO_4$ scintillator for the next performance measurements.

Without optical grease

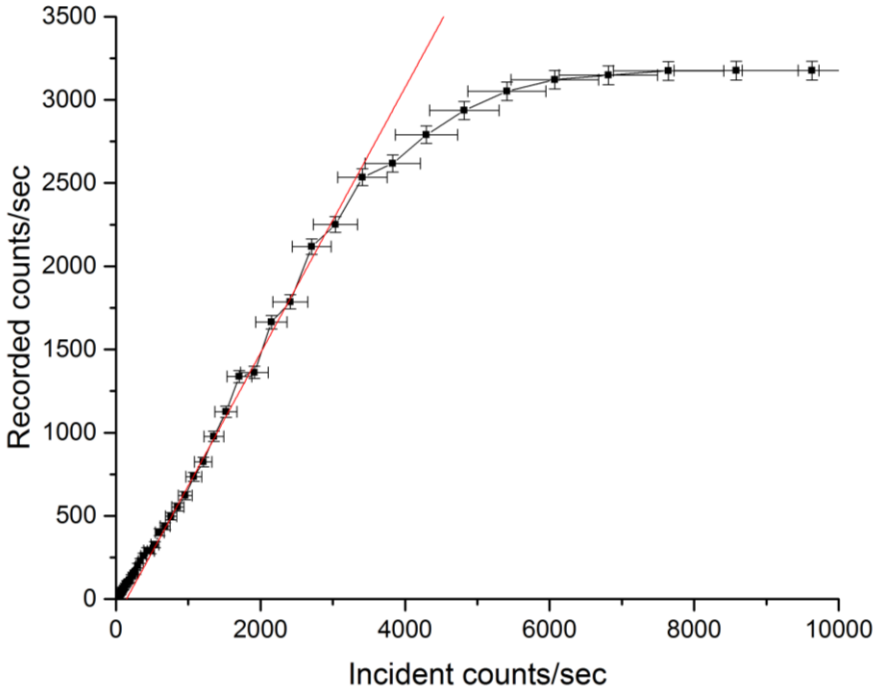

Figure 5.20: Recorded count rate capability for HGC with the GOS scintillator by using 2 mm diameter ^{99m}Tc source filled with 72.60 MBq without optical grease placed 250 mm away from the un-collimated camera. Images were taken over the course of several days at regular intervals (i.e. every hour). No. of frames 2000. The acquisition time was ~ 204 sec.

With optical grease

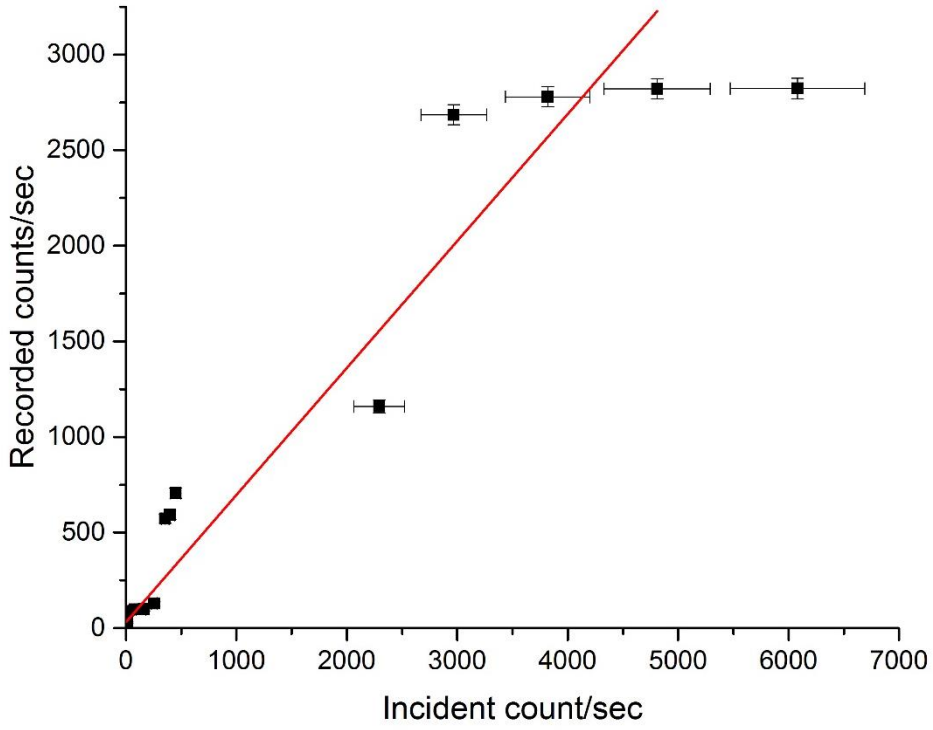

Figure 5.21: Recorded count rate capability for HGC with the GOS scintillator by using 2 mm diameter ^{99m}Tc source filled with 70.0 MBq with optical grease installed placed 250 mm away from the un-collimated camera. Images were taken over the course of several days at regular intervals (i.e. every hour). No. of frames 2000. The acquisition time was ~ 204 sec.

5.2.3 $CdWO_4$ scintillator

I. Intrinsic spatial resolution

The $CdWO_4$ scintillator was coupled directly to the CCD. Figure 5.22 shows the full process of analysing the resultant gamma image for intrinsic spatial resolution measurement. Final results calculated from analysing the image are tabulated in (Table 5.14).

Intrinsic spatial resolution of the HGC is significantly poor with the $CdWO_4$ scintillator.

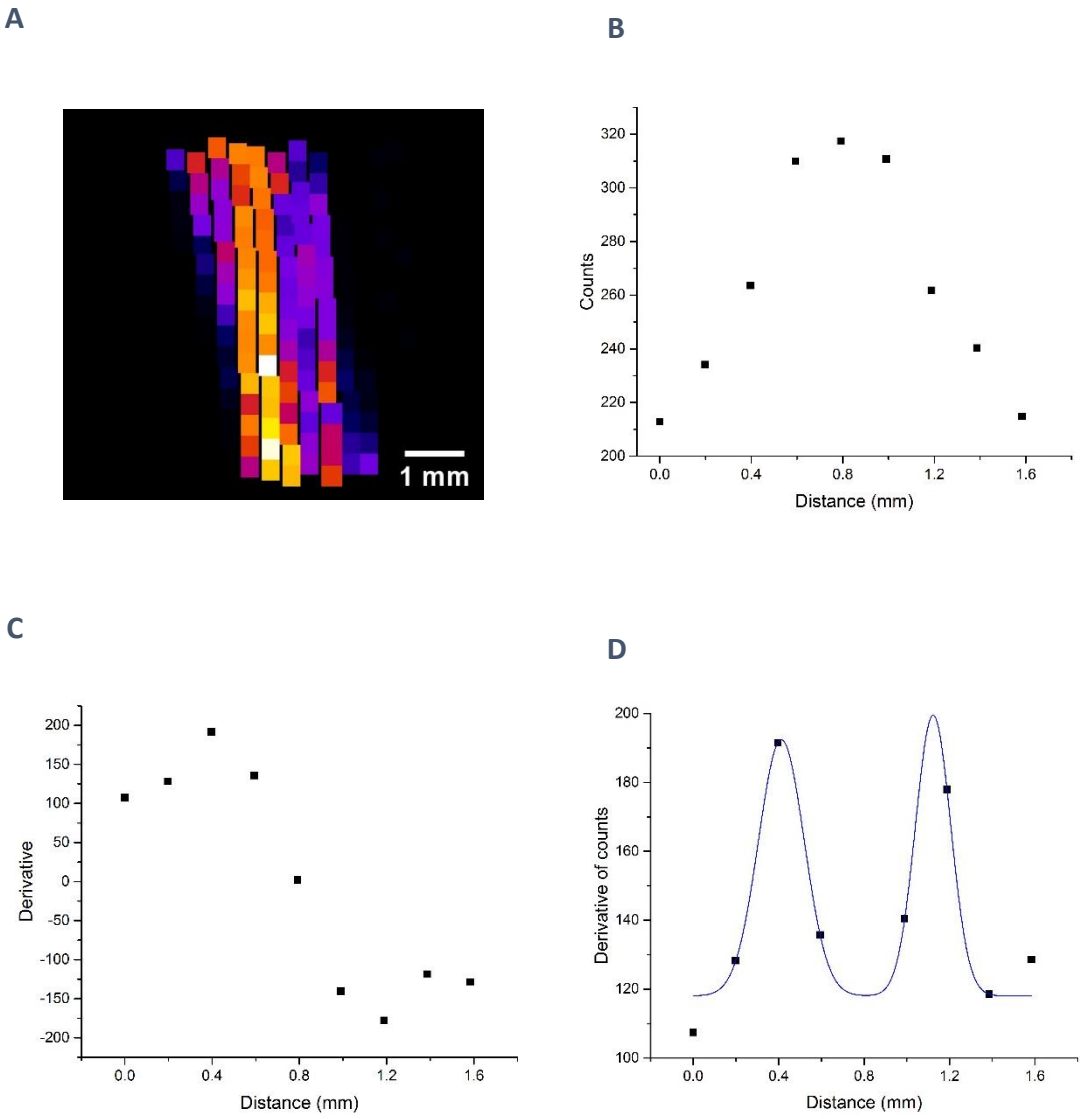

Figure 5.22: Graphs showing the intrinsic spatial resolution measurement process for the $CdWO_4$ scintillator using a 138.8 MBq ^{99m}Tc source. A) Final image of ^{99m}Tc at 200 mm distance from the 3 mm width slit. Total no. of frames was 5000. The acquisition time was 510 sec. B) Edge response function (ERF) for ^{99m}Tc source. C) Line spread function (LSF) i.e. derivative of ERF. D) Modulus of LSF with fitted Gaussians.

Table 5.14: Intrinsic spatial resolution results for $CdWO_4$ scintillator

Parameters	$CdWO_4$ scintillator
FWHM (μm)	1059 ± 305
FWTM (μm)	2091 ± 202

As the $CdWO_4$ scintillator was provided by Richard (104), it was mentioned that there were limitations in the spatial resolution measurements due to the mismatching of the crystal arrays to the requirements of the modulation transfer function (MTF) measurements, which is the parameter that determine the capability of an imaging detector in recording the transmitted signal frequencies. During manufacture of the $CdWO_4$ scintillator there were misalignment of the crystal segments that makes the array not being shifted invariantly which cause significant differences in brightness. Also, the manufacture of the crystal arrays was undertaken by hand where $CdWO_4$ crystals were mechanically cut, polished and assembled into large arrays (104, 114). All these factors explain the result obtained in Figure 5.22A. So during analysis when plotting a profile to calculate the ERF the profile was shifted and angled according to each pixel then the average profile for the entire slit image was calculated.

II. Extrinsic spatial resolution

Figure 5.23 shows example of the image obtained with the point source using the $CdWO_4$ scintillator. A 2-dimensional Gaussian curve was fitted for each measured distance both with and without Perspex. Extrinsic spatial resolution then defined as the FWHM of the Gaussian fitting.

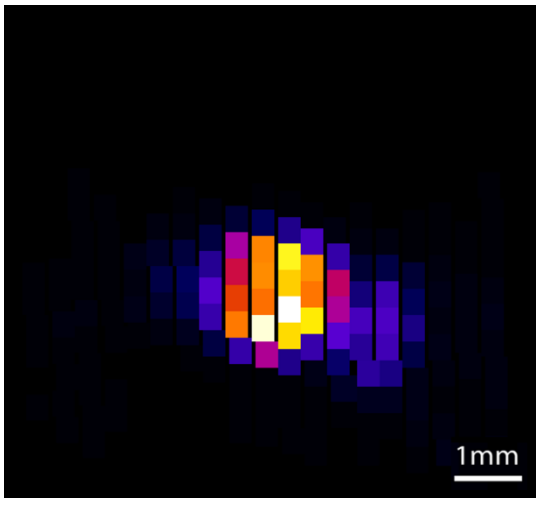

Figure 5.23: Example of a point source image obtained for extrinsic spatial resolution measurements for the $CdWO_4$ scintillator using a 1.0 mm diameter pinhole collimator. Perspex, 20 mm thick, was placed directly between the point source and the collimator. The image was acquired with 2000 frames. The acquisition time was 204 sec.

Figures 5.24 and 5.25 show the plot of calculated resolution measurements versus imaging distance.

Without Perspex

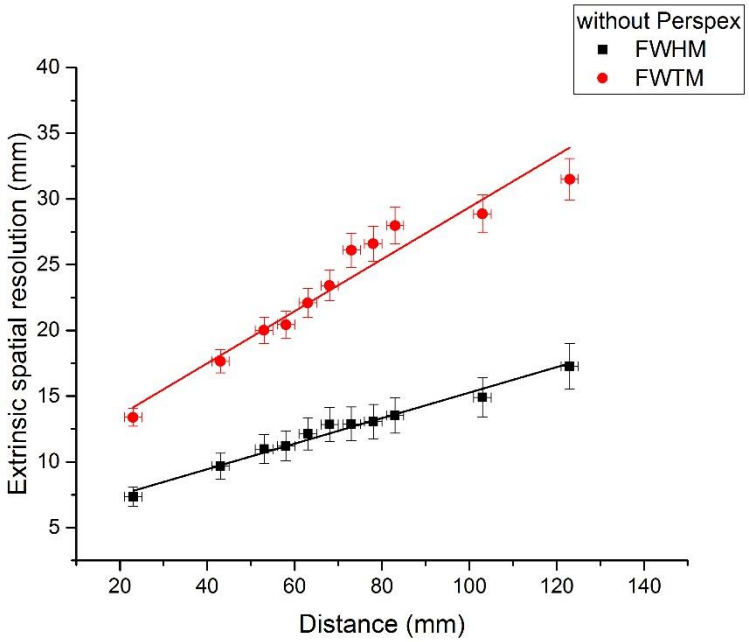

Figure 5.24: Graphs showing the extrinsic spatial resolution vs distance. FWHM (black square) and FWTM (red dots) calculated for a 2 mm diameter source filled with 110.6 MBq ^{99m}Tc solution for the $CdWO_4$ scintillator using a 1.0 mm diameter pinhole collimator without Perspex. No. of frames 2000. The acquisition time was ~ 204 sec.

The fitted parameters of gradient *m* and intercept *c* are tabulated in (Table 5.15). The results of the extrinsic spatial resolution for the $CdWO_4$ scintillator are shown in (Table 5.16).

Table 5.15: Fitted parameters of gradient *m* and intercept *c* for the linear relationship between the extrinsic spatial resolution and the imaging distance.

$CdWO_4$ scintillator	**FWHM**		**R^2**	**FWTM**		**R^2**
	m	*c*		*m*	*c*	
no Perspex	0.046±0.016	2.9±0.9	0.989	0.091±0.027	5.11±1.5	0.989
including Perspex	0.066±0.023	4.2±1.2	0.974	0.132±0.039	7.42±2.2	0.974

Table 5.16: Extrinsic spatial resolution results for the $CdWO_4$ scintillator at the non-magnifying position *d* = 10 mm.

Parameters		$CdWO_4$ scintillator
FWHM (mm)	no Perspex	3.36 ± 1.06
	including Perspex	4.86 ± 1.43

With Perspex

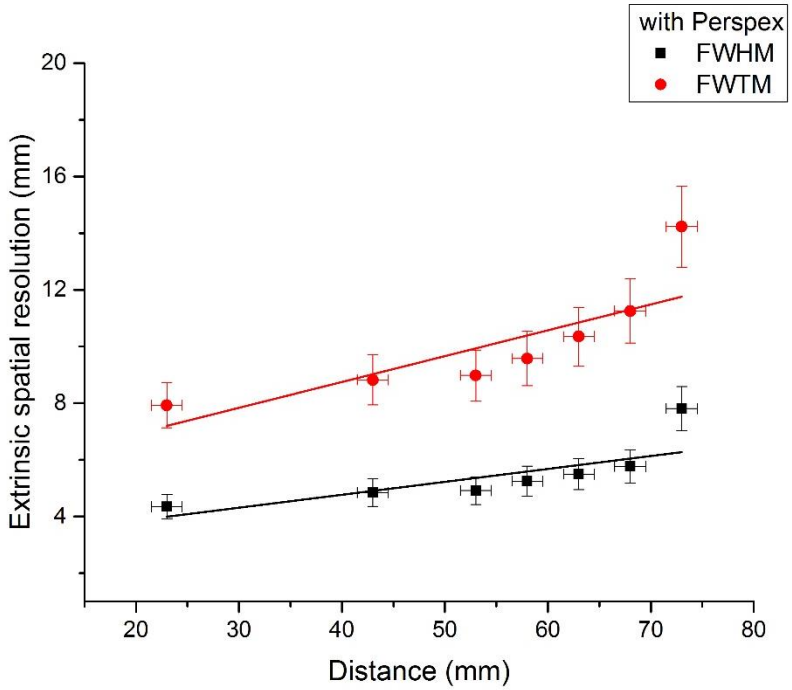

Figure 5.25: Graphs showing the extrinsic spatial resolution vs distance. FWHM (black square) and FWTM (red dots) calculated for a 2 mm diameter source filled with 110.6 MBq ^{99m}Tc solution for the $CdWO_4$ scintillator using a 1.0 mm diameter pinhole collimator with Perspex. No. of frames 2000. The acquisition time was ~ 204 sec.

Again the extrinsic spatial resolution of the HGC is significantly poor with the $CdWO_4$ scintillator.

III. Intrinsic spatial uniformity

The result of CoV with the $CdWO_4$ scintillator is shown in (Table 5.17). The CoV value is 53 % which indicates that the HGC is less uniform when using the $CdWO_4$ scintillator.

Table 5.17: Coefficient of variation (CoV) results for the $CdWO_4$ scintillator.

Parameters	$CdWO_4$ scintillator
Coefficient of variation (CoV)	53 ± 7 %

IV. Intrinsic spatial sensitivity

A comparison of the theoretical and the experimental performance characteristics for the intrinsic spatial sensitivity of the HGC with the $CdWO_4$ scintillator at 140.5 keV energy are shown in (Table 5.18).

The experimental sensitivity value does not match the theoretical efficiency value. This is may be due to inefficiencies in coupling the $CdWO_4$ scintillator to the CCD as poor coupling can lead to significant reduction in the sensitivity of the camera. Also, it is agreed by Richard (104) that as the $CdWO_4$ scintillator was manufactured and assembled by hand it is likely to have poor sensitivity. Furthermore, as the $CdWO_4$ scintillator is composed of cadmium and alternating layers of tungsten so according to hypothesise the absorption of the optical photons at the tungsten inter-segment material is the main cause of poor sensitivity (114).

Table 5.18: Intrinsic spatial sensitivity results for the $CdWO_4$ scintillator at 140.5 keV.

Parameters	$CdWO_4$ scintillator
Theoretical sensitivity	98.55 %
Experimental sensitivity	4.9 ± 12 %

V. Extrinsic spatial sensitivity

Extrinsic spatial sensitivity was reported at a nominal distance of 50 mm from the 1.0 mm diameter tungsten pinhole collimator, both with and without Perspex (Table 5.19). Figure 5.26 shows the relationship between the extrinsic spatial sensitivity and the imaging distances.

Extrinsic spatial sensitivity of the HGC is significantly lower with the $CdWO_4$ scintillator.

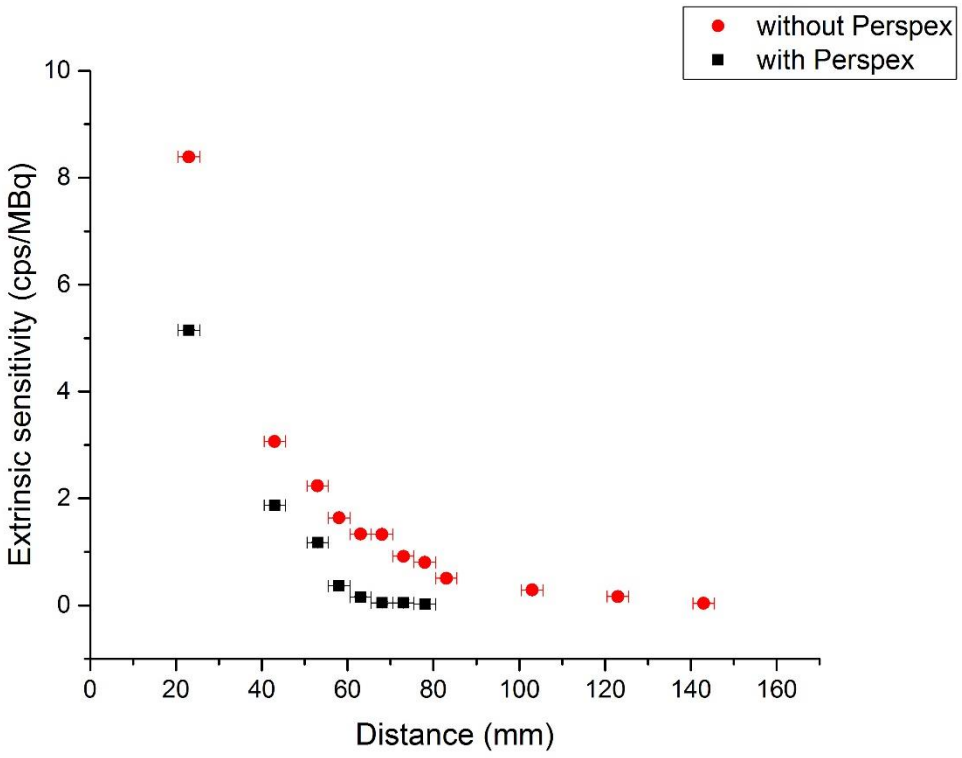

Figure 5.26: Graphs showing the relationship between the extrinsic spatial sensitivity and varying distances from the detector using 1.0 mm diameter pinhole collimator. (black squares) with Perspex (red dots) without Perspex calculated for 110.6 MBq ^{99m}Tc point source with $CdWO_4$ scintillator.

Table 5.19: Extrinsic spatial sensitivity results for the $CdWO_4$ scintillator at 50 mm distance.

Parameters		**$CdWO_4$ scintillator**
Extrinsic spatial sensitivity	no Perspex	2.36 ± 1.50 (cps/MBq)
	including Perspex	1.23 ± 1.08 (cps/MBq)

VI. Count rate capability

A straight line was fitted to the linearly proportional section of the curve for the $CdWO_4$ scintillator, Figure 5.27 (R^2 = 0.922) indicating that the sensitivity of the HGC is linear until an incident count of at least 4528 s^{-1}. This high reading might be due to the use of high amount of activity which lead to saturation level where more than one light splash overlaps. Also, this is may be related to the algorithm used for blob detection which must distinguish each light splash separately. But if more than one light splash overlap

on the same pixel, then the algorithm could not resolve these light splashes as separate and distinct events which leads to saturation.

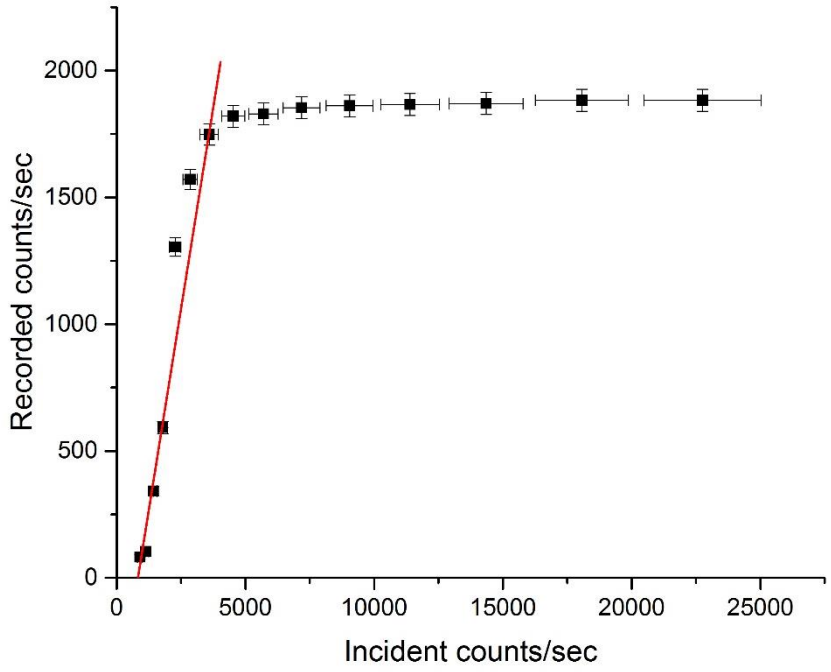

Figure 5.27: Recorded count rate capability for HGC with $CdWO_4$ scintillator by using 2 mm diameter source filled with 59.40 MBq ^{99m}Tc placed 250 mm away from the un-collimated camera. Images were taken over the course of several days at regular intervals (i.e. every hour). No. of frames 2000. The acquisition time was ~ 204 sec.

It is worth to mention that, the results of the $CdWO_4$ scintillator were not promising as the $CdWO_4$ scintillator was not constructed particularly well. According to Richards's doctoral thesis, 2015 (104) the sheets of the $CdWO_4$ scintillator were poorly aligned and had a non-uniform thicknesses. Also, there was a fault during polishing, which causes damage in some regions of the scintillator (Figure 5.3). All these factors affected the performance of the $CdWO_4$ scintillator.

It was difficult to directly compare between the performance characterisation of the $CdWO_4$ scintillator that was done by Richards's doctoral thesis, 2015 (104) and our HGC as Richard's method was completely different. Richard (104) had tested the $CdWO_4$ scintillator using X-rays from a 160 kVp 3 W tungsten anode cone beam X-ray set. Then images were acquired using a colour digital Canon 100D camera. In general, Richard's

concluded that the $CdWO_4$ scintillator prototype is non-uniform and the possible reason for that because of the absence of the inter-segment filler material. Furthermore, the lack of the alignment and the differences of thickness of the sheet make it difficult to measure the spatial resolution.

5.3 Discussion

The performance characteristics of the HGC fitted with each CsI:TI both 600 µm and 1500 µm thick, GOS both with and without optical grease installed and $CdWO_4$ scintillators have been evaluated and compared, the results are summarised in (Table 5.20).

Table 5.20: Comparison of performance characteristics for HGC with a 600 µm and 1500 µm thick CsI:TI, a 1500 µm thick GOS both with and without optical grease installed and $CdWO_4$ scintillators. This table is replicated in a larger size in Appendix A.

Scintillators			**CsI:TI**		**GOS**		**$CdWO_4$**
Parameters			600 µm	1500 µm	No optical grease	With optical grease	4350 µm
Intrinsic spatial resolution		FWHM (µm)	170±12	230±25	1090±200	984±320	1059±305
		FWTM (µm)	300±20	468±23	1984±280	1793±150	2091±202
Extrinsic spatial resolution	No Perspex	FWHM (mm)	NA	1.8±0.03	1.97±0.34	1.90±0.33	3.36±1.06
		FWTM (mm)	NA	3.3±0.05	3.75±0.77	3.45±0.66	6.02±1.76
	Including Perspex	FWHM (mm)	1.8±0.13	2.02±0.09	2.13±0.46	2.05±0.45	4.86±1.43
		FWTM (mm)	3.25±0.26	3.6±0.12	4.02±0.89	3.9±0.88	8.74±2.59
Intrinsic uniformity		CoV (%)	25±9	20±15	17±9	13±4	53±8
Intrinsic sensitivity		(%)	19±1	40±3	54±4	53±7	4.9±12
Extrinsic sensitivity	No Perspex	(cps/MBq)	NA	6.6±0.5	18.5±0.3	16.23±0.5	2.36±1.50
	Including Perspex	(cps/MBq)	0.8±0.1	3.3±0.5	8.1±0.3	6.6±0.4	1.23±1.08
Count rate capability	Maximum recorded count rate (cps)		1200±200	3537±200	3170±30	2823±50	4528±300

Comparing the intrinsic spatial resolution of the HGC with the 1500 µm thick CsI:TI and GOS scintillators shows that the CsI:TI scintillator operates with a lower intrinsic spatial resolution (i.e. 230 µm) than the GOS scintillator (i.e. 1090 µm) this being superior for

imaging purposes. Moreover, $CdWO_4$ has a poorer intrinsic spatial resolution (i.e. 1059 µm).

When comparing the extrinsic spatial resolution of both 1500 µm thick CsI:TI and GOS scintillators, we observe that there was only a slight difference in FWHM values at the non-magnifying position (i.e. 1.8 mm) for CsI:TI scintillator and (1.97 mm) for GOS scintillator. When looking at the fitting data the straight line provides a closer match to the theoretical geometric resolution of the 1 mm diameter pinhole collimator. That was related to the effect of the smaller intrinsic spatial resolution for CsI:Tl scintillator. On the other hand, the $CdWO_4$ scintillator has a FWHM value of 3.36 mm.

For intrinsic spatial uniformity, the coefficient of variation (CoV) was comparable for both CsI:TI and GOS scintillators (i.e. 20 % and 17 %) respectively. But the CoV value for the $CdWO_4$ scintillator was the worst (i.e. 53 %).

There was a significant difference in intrinsic spatial sensitivity between the two scintillators. The GOS scintillator being more sensitive (~ 54 %) than the CsI:TI scintillator (~ 40 %). Both of the experimental values are less than the theoretical sensitivity. While the $CdWO_4$ scintillator is significantly less sensitive (~ 4.9 %) comparing to the other two types of scintillator. As mentioned previously this is could be due to the $CdWO_4$ scintillator was being manufactured and assembled by hand, so it is likely expected to have poor sensitivity.

For the extrinsic spatial sensitivity measurements, it was found that at 50 mm from a 1.0 mm diameter pinhole collimator the GOS scintillator had higher sensitivity (~ 18.5 cps/MBq) than the CsI:TI scintillator (~ 6.6 cps/MBq). However, when using scattering material there is a slight large reduction in counts. Again, the $CdWO_4$ scintillator has the lowest sensitivity (~ 2.36 cps/MBq).

The maximum recorded count rate for the CsI:TI scintillator was higher (~ 3537 cps) than that recorded with the GOS scintillator (~ 3170 cps). Surprisingly the $CdWO_4$ scintillator has the highest recorded counts (~ 4528 cps).

Clearly, in this study the results indicate that the HGC has better spatial resolution when using the thinner CsI:TI scintillator. However, the thick CsI:TI scintillator can gives

gamma images that are more uniform, more sensitive and have higher count rate capability.

When coupling the 1500 µm thick GOS scintillator to the CCD with and without using an optical grease there was no significant difference.

Comparing the performance characterisation of the HGC using the 1500 µm thick CsI:TI and GOS scintillators it has found that the HGC has significantly better spatial resolution and higher count rate capability when using the CsI:TI columnar scintillator. However, the HGC is more sensitive when using the pixelated GOS scintillator.

On the other hand, the quality of the prototype $CdWO_4$ scintillator was not sufficient for measuring the performance of the HGC.

There is a trade-off between high spatial resolution and sensitivity. From the performance characteristics measured in this chapter, the GOS scintillator would consider to be the preferable choice when looking at sensitive images for clinical procedures although its pixel size limit its applicability for imaging. Also, the count rate capability of the GOS scintillator is limited due to the nature of the pixel size of the GOS crystal. Both spatial resolution and count rate capability measures could be improved by the reduction of the size of the GOS pixels, which is currently a cost effective solution.

The utility of CsI:Tl scintillator gives gamma images with superior spatial resolution so it is the better choice of scintillators when looking at precise localisation of sources is a particular concern.

5.4 Conclusion

In this study, characterisation of the HGC has been performed using two thicknesses of columnar CsI:TI scintillator (600 µm and 1500 µm), 1500 µm thick pixelated GOS scintillator and 4350 µm thick $CdWO_4$ scintillator. The protocols applied followed the modified IPEM recommendations, that include: spatial resolution (both intrinsic and extrinsic), intrinsic spatial uniformity, sensitivity (both intrinsic and extrinsic) and count rate capability.

The choice of material and its structure are key parameters when deciding which scintillator to use for particular nuclear medical imaging applications. For the current application of the HGC where spatial resolution is a priority, the CsI:TI columnar scintillator has significant advantages over the GOS pixelated scintillator.

Chapter 6

Evaluation of a semiconductor CdTe detector for medical imaging

Scintillation detectors and semiconductor detectors are the most commonly used radiation detectors in nuclear measurement systems to convert radiation energy into an electronic signal. Over the last two decades advances in semiconductor detector technology have reached the point where they are sufficiently sensitive to become an alternative to scintillators for high energy gamma ray detection for application in fields such as medical imaging.

Although the use of CdTe detectors in medical imaging systems has been limited, there have been some applications of these detectors in diagnostic X-ray mammography and small field of view (SFOV) gamma imaging (26, 115). These CdTe devices have pixel detector arrays to convert the incident photons directly into charge signals therefore offering new potential as imaging systems (27).

A fundamental phase in the management of patients with breast tumours is the assessment of the sentinel lymph nodes (SLNs) to determine if there has been tumour spread from the primary site. During breast cancer surgery the sentinel lymph nodes

(SLNs) are identified using lymphoscintigraphy. The preferred radiopharmaceutical for this procedure is ^{99m}Tc labelled nanocolloid. During the operation a gamma probe is used for measuring the radioactive uptake in SLNs, however the introduction of imaging probes based on semiconductor detectors has the potential to enhance this procedure (30).

Examples of CdTe semiconductor detection for X-ray and gamma-ray imaging indicate that the newly developed semiconductor detectors have the potential to be competitive with the existing imaging devices based on scintillators (27, 30). More details of the properties of CdTe have been discussed in (Chapter 2, section 2.6.1).

This chapter presents an evaluation of two different types of the Cadmium-Telluride (CdTe) semiconductor detectors; firstly, XRI-UNO CdTe-based detector produced by X-RAY Imatek for photon energies of interest in nuclear imaging with ^{99m}Tc and other radioactive sources (116). Secondly, the HEXITEC ASIC detector developed by Science and Technology Facilities Council (STFC), Rutherford Appleton Laboratory (RAL) (117). The measured performance characteristics include: spatial resolution (both intrinsic and extrinsic), intrinsic spatial uniformity, spatial sensitivity (both intrinsic and extrinsic), count rate capability and contrast to noise ratio.

6.1 Materials and methods

A. XRI-UNO system

The XRI-UNO system was provided by X-ray Imatek, Spain (116). Imatek has focused on the imaging applications that require operation in photon counting mode and produces the XRI series of X-ray and gamma ray cameras for medical imaging. The XRI-UNO system is a photon counting imaging device which uses the Medipix2 chip (118). The Medipix2 chip is an advanced photon counting ASIC which has a high spatial resolution, high contrast and high sensitivity to low energy X-ray photons complementary metal-oxide semiconductor (CMOS) pixel readout chip (119). It can be combined with different semiconductor sensors which convert the X-rays directly into detectable electric signals (120). The Medipix2 readout chip is bump bonded to a 1 mm thick CdTe detector. The Medipix2 measures 16.12 mm x 14.11 mm with an active area of 19.82 mm^2. It consists of 256 x 256 identical elements, each working in single photon counting mode for positive or negative input charge signals, each pixel occupies a total area of 55 µm x 55 µm. This detector normally operates at a temperature above 32℃ (116). Figure 6.1 (*top*) shows a photograph of the detector with a white square indicating the active area. A schematic is also shown in Figure 6.1 (*bottom*), which details the layout of the CdTe sensor within the detector casing.

The XRI-UNO imaging system was designed to be used for a wide range of applications such as: research on particle physics, small animal imaging, radiation monitor and computer tomography (121, 122). It was developed to be a compact imaging device used within a small to medium labs.

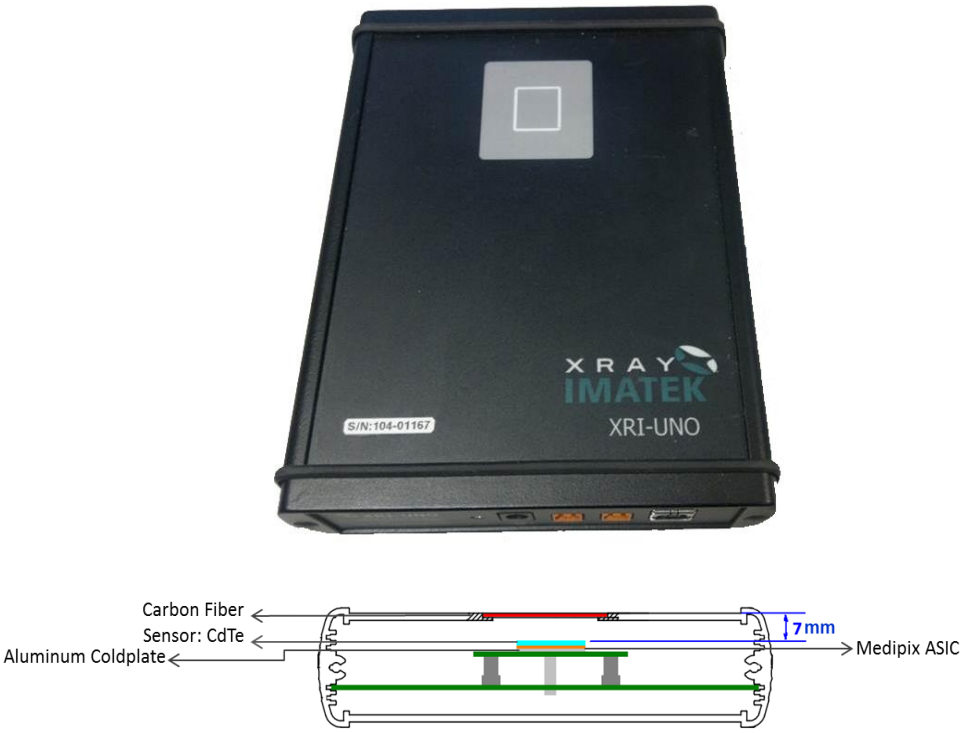

Figure 6.1: *(Top)* Image of XRI-UNO CdTe detector. The active area is the small white square in the upper part of the detector. *(Bottom)* Schematic of the XRI-UNO.

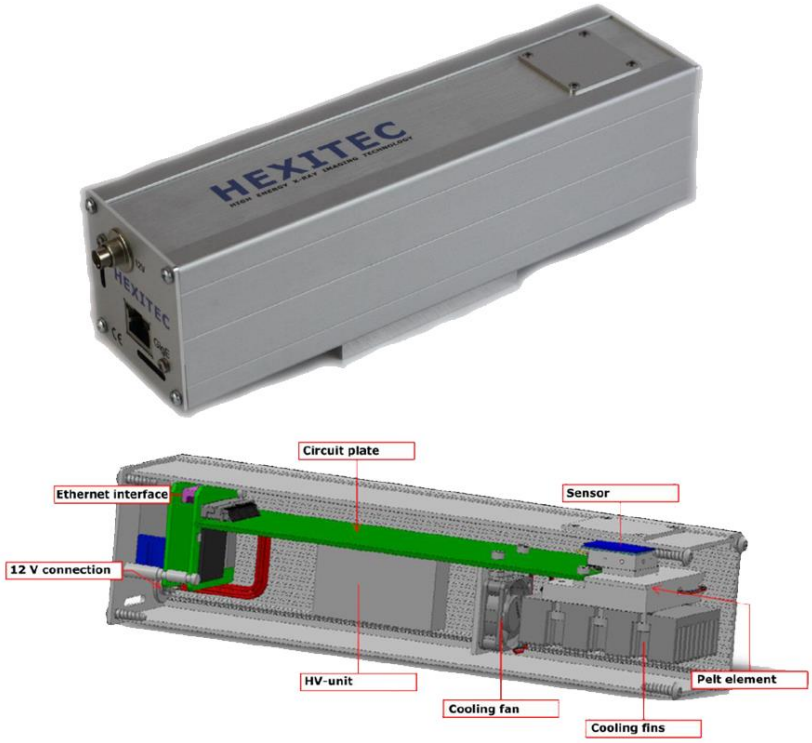

Figure 6.2: (*Top*) Image of HEXITEC detector. (*Bottom*) Design model of HEXITEC (123).

B. HEXITEC ASIC detector

The High Energy X-ray Imaging Technology (HEXITEC) has been developed by Science and Technology Facilities Council (STFC), Rutherford Appleton Laboratory (RAL) (124). This newly developed semiconductor detector consists of 1 mm thick CdTe with 80 X 80 pixels, each 250 µm square. The distance from the casing to the detector surface is 10 mm. The detector is bump bounded to the application specific integrated circuit (ASIC). The HEXITEC has been designed to be suitably used for different applications such as: synchrotron diffraction and tomography experiments also, in space science imaging. The principle concept of the HEXITEC is rely on providing a good spectroscopy for each photon that incident to the detector within a reasonable acquisition time (117, 125-129). Figure 6.2 shows a photograph of the HEXITEC detector (*top*). A schematic of HEXITEC is also shown in Figure 6.2 (*bottom*).

The physical specifications of the HEXITEC detector are compared with the XRI-UNO system as provided by the manufacturer in (Table 6.1).

Table 6.1: Comparison of the physical specifications of the XRI-UNO and HEXITEC CdTe detector (116, 130).

Physical Specification	**XRI-UNO**	**HEXITEC**
Dimension (W x L x H)	138 mm x 172 mm x 34 mm	66 mm x 56 mm x 220 mm
Weight	~ 500 g	~ 850 g
Pixel size / # Pixels	55 µm x 55 µm / 65,536 pixels	250 µm x 250 µm / 6400 pixels
Active Area	14.08 mm x 14.08 mm	20.25 mm x 21.53 mm
Power consumption	5 W	1.4 W
Bias Voltage	Down to – 500 V	Down to – 500 V
Material	1 mm thick Cadmium Telluride	1 mm thick Cadmium Telluride
Read-out Circuit	Bump-bonded CMOS	Bump-bonded ASIC

6.1.1 Imaging procedures

A. XRI-UNO system

Initial investigation

Initial experiments were performed to test the XRI-UNO CdTe system and to understand how it worked. A 0.45 mm diameter cannula tube was filled with 0.63 MBq ^{99m}Tc and several images taken. First, by using a low-resolution parallel hole collimator (i.e. 2 mm diameter hole), then with a high-resolution parallel hole collimator (i.e. 1 mm diameter hole), each is made of lead (Pb) and having a thickness of 5 mm. Finally, an image without a collimator; was taken (Figure 6.3). All images were acquired for 999 frames, which is the maximum number that can be used with the XRI-UNO CdTe system, and each frame had an acquisition time of 100 ms.

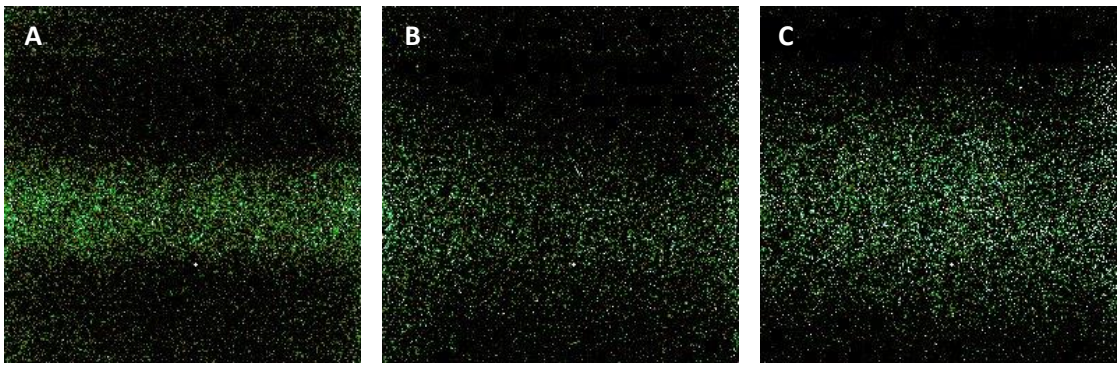

Figure 6.3: Images of a 0.45 mm diameter cannula tube, 18 mm length filled with 0.63 MBq ^{99m} Tc acquired with 999 frames. Each frame had an acquisition time of 100 ms. A) with high-resolution parallel hole (1 mm diameter hole) collimator. B) with low-resolution parallel hole (2 mm diameter hole) collimator. C) without a collimator.

All images, unless otherwise specified, were subject to the same image processing; a hot pixel mask was created by taking several background images and then the internal masking program was used to mask hot pixels. Masking hot pixels is one of the mode operations that can be used when dealing with the software. It allows the user to turn the pixel off during the acquisition, when it turns off the faulty hot and/or dead pixels will not be counting. Background images were taken each day and subtracted from each

image. Masks were re-created about every 3 hours. A number of radioactive sources were used: ^{109}Cd, ^{57}Co and ^{99m}Tc (see Table 6.2).

Table 6.2: Radioactive sources used in the experiment, their activity and principal photon energy.

Parameters investigated	Source	Activity (MBq)	Principal Energy (keV)
Spatial resolution (intrinsic and extrinsic), intrinsic spatial sensitivity and contrast to noise ratio	^{109}Cd	305	22
Intrinsic spatial uniformity	^{57}Co	2	122
Count rate capability	^{99m}Tc	229	140.5

B. HEXITEC ASIC detector

All images have been recorded using the GigE HEXITEC software. Further analysis was performed with custom-written IDL code. The IDL code was written by one of the research group team. The full pixel array of 80 x 80 pixels has been used for all images. During analysis the acquired images with .hxt files format were used. These .hxt files are pre-thresholded and measure only data from single pixel events. A dark image was acquired to create a hot pixel map. Characterisation was performed using ^{99m}Tc radioactive sources that has a photo-peak energy of 140.5 keV. The amount of activity used for each characterisation test is tabulated in (Table 6.3).

Table 6.3: ^{99m}Tc activity used for HEXITEC characterisation tests.

Parameters	Activity (MBq)
Intrinsic spatial resolution	122
Extrinsic spatial (resolution and sensitivity)	78.5
Intrinsic spatial (uniformity and sensitivity)	59.2

It is worth to mention that the data of the XRI-UNO system were acquired using three different radioactive sources (i.e. ^{109}Cd, ^{57}Co and ^{99m}Tc) while the HEXITECH detector

data were acquired using ^{99m}Tc source only. The main reason for that was because the XRI-UNO system experiment were performed at the early phase of the first year of the PhD study where the final confirmation of handling the unsealed sources within the SRC laboratory has not yet approved at that moment. However, the experiment was needed to be performed as the time was limited for having the XRI-UNO system from the owner company. For the HEXITECH data the ^{99m}Tc source was chosen as it is the widely radioactive material used in nuclear medical imaging.

6.1.2 Performance specifications

The performance characteristics evaluated were intrinsic and extrinsic spatial resolution, intrinsic spatial uniformity and sensitivity (both intrinsic and extrinsic), contrast to noise ratio and count rate capability. Protocols used for measuring the performance characteristics of HEXITECH detector have followed the protocols which have been discussed in details in Chapter 4. However, there were minor differences in the methods used for measuring the XRI-UNO performance as the experiment was implemented before setting up the protocols in Chapter 4. Again that was due to the time limitation for the availability of the XRI-UNO system. Furthermore, contrast to noise ratio (CNR) measures has been added to the evaluation of the performance characteristics of both CdTe detectors in order to evaluate the quality and the accuracy of the gamma image quantitatively.

i. Intrinsic spatial resolution

To measure the intrinsic spatial resolution, a 5 mm thick lead block with a slit of 2 mm width and 20 mm length was placed on top of the CdTe detectors. As mentioned earlier, the radioactive source used with XRI-UNO system is different from the one used with HEXITEC detector (i.e. ^{109}Cd and ^{99m}Tc respectively). This is due to the time gap between the two experiments as the performance of XRI-UNO system was done at the early phase of the PhD study while the performance of the HEXITEC detector was carried out at the final phase of the PhD study when the final approval of using the unsealed sources

at laboratory was confirmed. Then characterisation of XRI-UNO system using ^{99m}Tc could not be performed due to the unavailability of the system at that moment. Also, the experimental setup is different (i.e. the placement distance of the radioactive sources from the two detectors). This is because the evaluation of the XRI-UNO system was performed before planning the protocols for assessing the performance characterisation which is discussed in Chapter 4.

XRI-UNO system

A ^{109}Cd source (8 mm in diameter) (131) was placed at a distance of 107 mm above the surface of the lead block in order to produce a uniform flux of X-rays onto the surface to approximate parallel incident photons. Ten images were then taken, each with a total of 999 frames (with each frame having an acquisition time of 100 ms), these were summed using ImageJ software (132). A typical image is shown in (Figure 6.4A).

The resulting slit image was analysed using the edge response function (Figure 6.4), more details of this process have been discussed previously in Chapter 4. The Full Width at Half Maximum (FWHM) and the Full Width at Tenth Maximum (FWTM) were then calculated for each of the line spread function (LSF) peaks, and the average value of the two measurements is shown in (Table 6.4). Also shown Table 6.4 are the estimation of errors in the FWHM of both peaks.

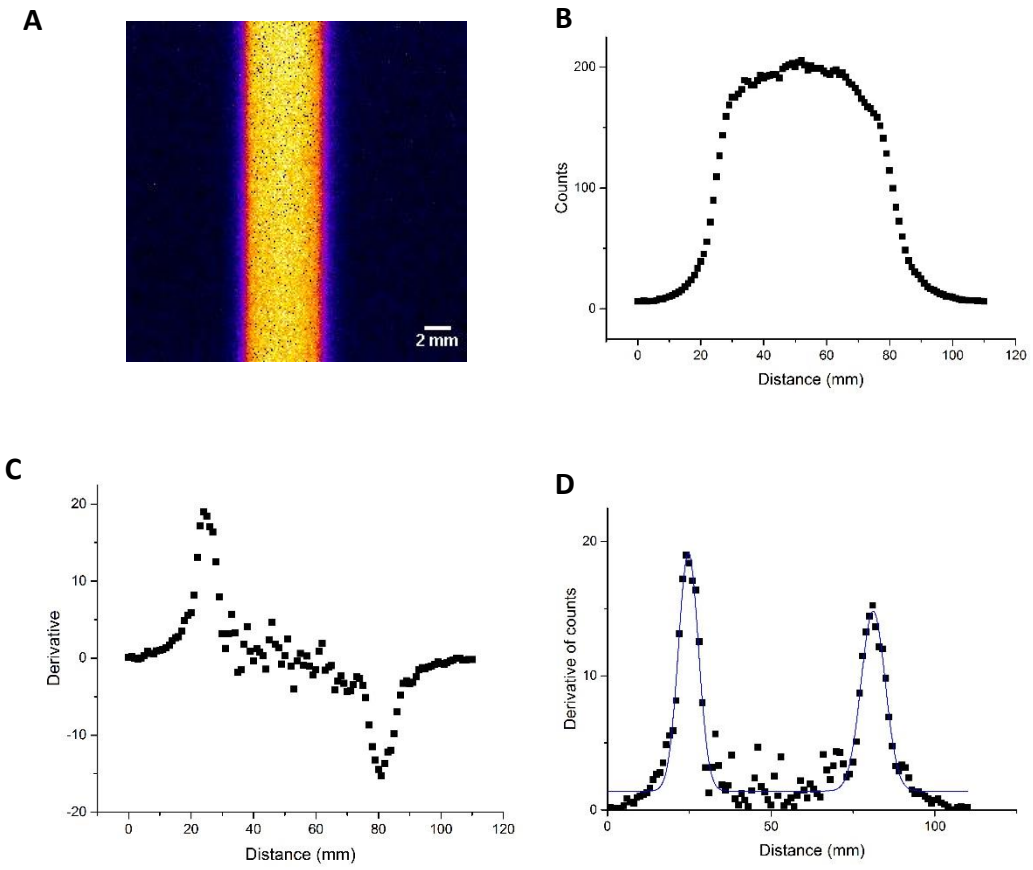

Figure 6.4: Graphs showing the intrinsic spatial resolution measurement process for the ^{109}Cd source. A) Final summed image of ^{109}Cd at 107 mm distance from the 2 mm width slit. Each sum acquired with a total of 999 frames each frame having an acquisition time of 100 ms. B) Edge response function (ERF) for ^{109}Cd source. C) Line spread function (LSF) (derivative of ERF). D) Modulus of LSF with fitted Gaussians.

HEXITEC ASIC detector

A 2 mm diameter of 122 MBq ^{99m}Tc source was placed at a distance of 300 mm above the surface of the slit. Acquisition time of the obtained slit image was 1000 s. Figure 6.5 shows the process of analysing the slit image to calculate the FWHM and FWTM. The results are tabulated in (Table 6.4).

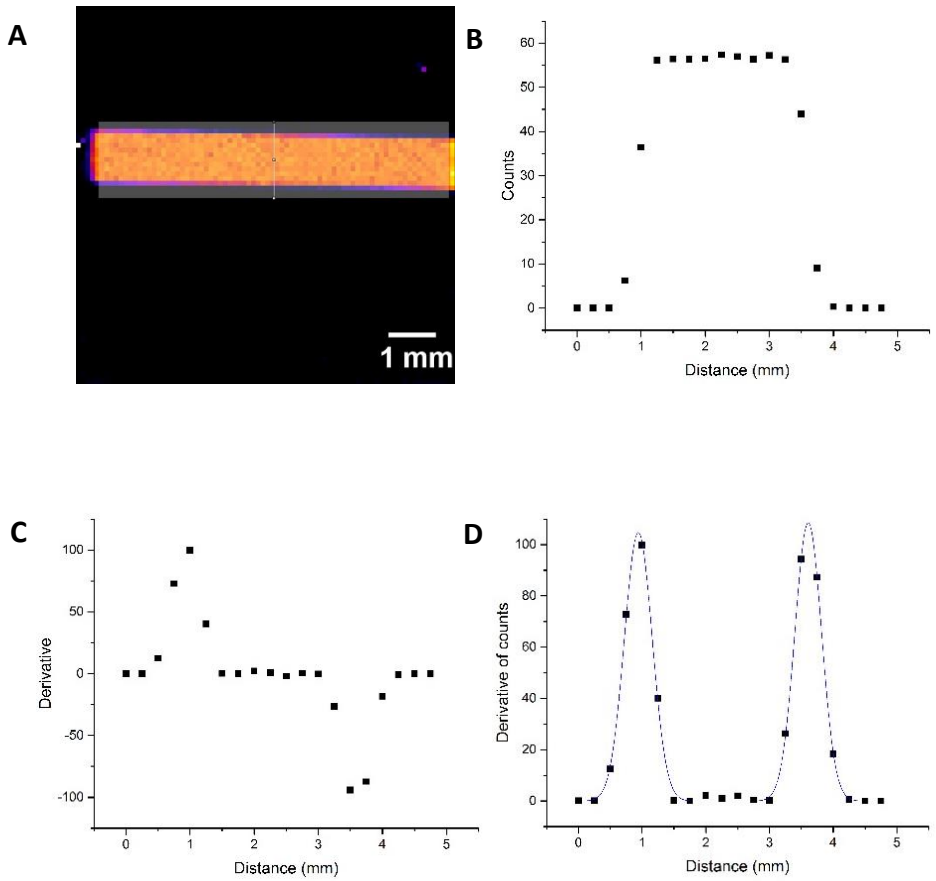

Figure 6.5: Graphs showing the intrinsic spatial resolution measurement process for the 122 MBq ^{99m}Tc source. A) Final image of ^{99m}Tc at 300 mm distance from the 3 mm width slit. Total acquisition time was 1000 s. B) Edge response function (ERF) for ^{99m}Tc source. C) Line spread function (LSF) i.e. derivative of ERF. D) Modulus of LSF with fitted Gaussians.

Table 6.4: Intrinsic spatial resolution results for XRI-UNO system using ^{109}Cd and for HEXITEC detector using ^{99m}Tc.

	XRI-UNO		**HEXITEC**	
Peak	**FWHM (µm)**	**FWTM (µm)**	**FWHM (µm)**	**FWTM (µm)**
1	497 ± 24	720 ± 31	515 ± 10	938 ± 18
2	414 ± 17	872 ± 46	495 ± 10	902 ± 18
Average	456 ± 20	796 ± 38	505 ± 10	920 ± 18

ii. Extrinsic spatial resolution

A more clinically relevant experiment was performed to investigate the spatial resolution of the CdTe detectors. This was achieved by imaging the source with a collimator and suitable scattering media in place. A pinhole collimator was used for imaging as it increases the field of view. The collimator was manufactured from tungsten, 6 mm thick and 45 mm in diameter with an acceptance angle of 60° (133). A layer of PMMA poly methyl methacrylate (Perspex) was then placed on top of the collimator. It is worth to mention that the Perspex thicknesses used with XRI-UNO system and HEXITECH detector were different. Also, the measurements of the XRI-UNO were taken with Perspex installed while the HEXITEC measurements were taken both with and without Perspex. Again this is due to the evaluation of the XRI-UNO system before setting a fixed protocols to follow and to the time limitation for having the system which makes it impossible to be re-evaluated.

XRI-UNO system

The collimator used for this test was a 0.5 mm diameter tungsten pinhole collimator that was placed on top of the detector.

A layer of PMMA poly methyl methacrylate (Perspex) with 9.5 mm thickness was then placed on top of the collimator, with the ^{109}Cd source positioned on the Perspex. A 999 frame image was taken having a ~ 10 s acquisition time. This process was repeated with more layers of Perspex (increasing up to 47.5 mm in 5 steps of 9.5 mm); increasing the source to detector distance.

The experimental setup is illustrated in (Figure 6.6). The pinhole collimator to detector distance is fixed *t*= 10 mm. The distance between the pinhole collimator to the source being imaged is varied depending on the experiment and this distance determines the demagnification on the detector.

Five images of the ^{109}Cd radioisotope source were obtained with different Perspex thicknesses. Figure 6.7 shows examples of these images. In (Figure 6.7A) the ^{109}Cd source is 17 mm away from the collimator with 9.5 mm of Perspex. And in (Figure 6.7B)

the ^{109}Cd source is 57 mm away from the collimator with 47.5 mm of Perspex. All images were processed using ImageJ in order to obtain their line profiles, which were then used to find the extrinsic spatial resolution. Figure 6.8 shows the relationship of the extrinsic spatial resolution, both FWHM and FWTM as a function of increasing Perspex thicknesses.

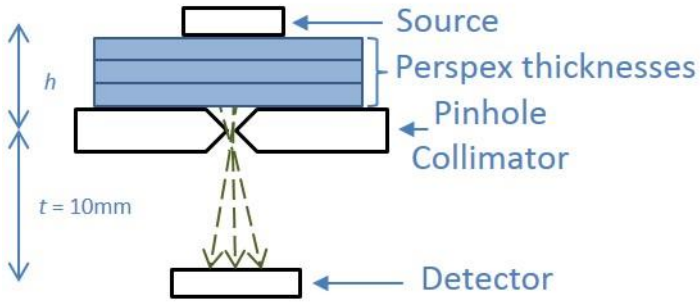

Figure 6.6: Schematic of the demagnification effect of the pinhole collimator on the XRI-UNO system.

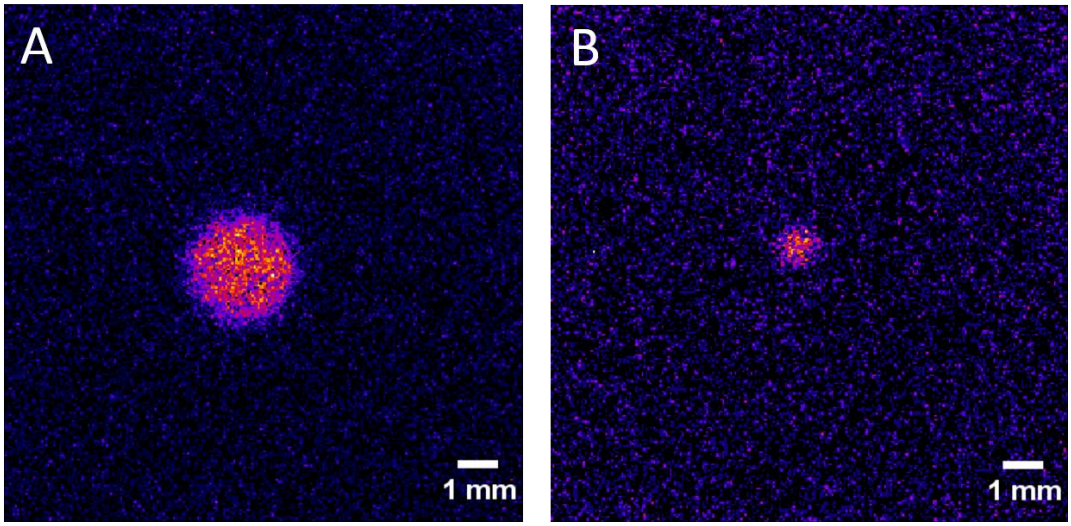

Figure 6.7: Examples of the ^{109}Cd images taken for extrinsic spatial resolution measurements, images acquired with 999 frames. Each frame had an acquisition time of 100 ms. A) ^{109}Cd source at 17 mm away from the collimator with 9.5 mm of Perspex thickness. B) ^{109}Cd source at 57 mm away from the collimator with 47.5 mm Perspex thickness.

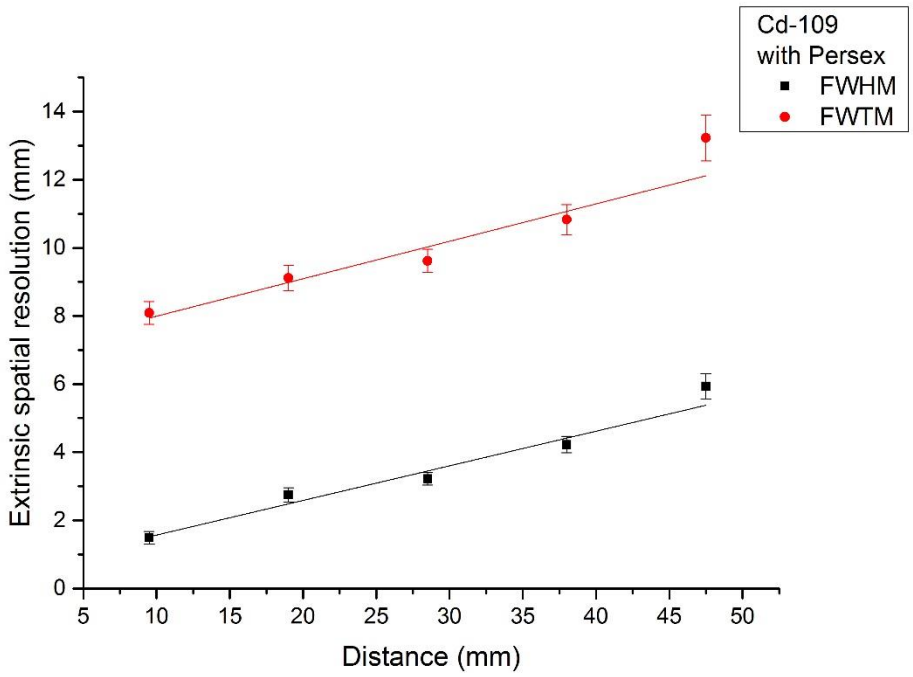

Figure 6.8: Extrinsic spatial resolution vs Perspex thickness. FWHM (black squares) and FWTM (red dots) calculated for a ^{109}Cd source with a 0.5 mm diameter pinhole collimator. Each point was calculated from an average of 999 frames, each frame having an acquisition time of 100 ms.

As discussed previously in Chapter 4, the magnification factor was calculated (64) for each source distance and then used to calculate the actual object space FWHM and FWTM values. A linear fit was found (Adj. R^2 =0.950) for the FWHM data and (Adj. R^2 =0.892) for the FWTM data. Error bars represent the accuracy of the Gaussian distribution fitting.

Using the slope-intercept formula from the line fit, as described previously in Chapter 4, the FWHM of the XRI-UNO system can be calculated for any known distance, Equation 6.1:

$$\text{FWHM} = (0.55 \pm 0.31) + (0.106 \pm 0.01)H \qquad (6.1)$$

where H is the distance from the pinhole collimator to the source. When H = 10 mm, the distance between the detector and the center of the pinhole collimator, the source is said to be at the non-magnifying position. Thus, the extrinsic spatial resolution FWHM

value at the non-magnifying position (for 0.5 mm diameter pinhole collimator) was found to be 1.61 ± 0.43 mm.

While the FWTM can be calculated from Equation 6.2:

$$FWTM = (6.90 \pm 0.50) + (0.110 \pm 0.02)H \quad (6.2)$$

Thus, the FWTM value at the non-magnifying position (for 0.5 mm diameter pinhole collimator) was found to be 8.0 $\pm$ 0.69 mm.

HEXITEC ASIC detector

A 2 mm diameter source of ^{99m}Tc was filled with 52.7 MBq. Images were acquired using a 0.5 mm diameter tungsten pinhole collimator at 10 different distances starting from 20 mm to 100 mm both with and without layers of Perspex added in between the collimator and the source ranging from 20 mm to 75 mm thicknesses. Total acquisition time for each image was 200 s. Figures 6.9 shows the relationships between the distance and the extrinsic spatial resolution both with and without Perspex. Figure 6.10 shows the FWHM for both situations together with and without Perspex. The error calculations on the extrinsic spatial resolution was propagated from the associated error in placing the source at a particular distance during camera setup.

To report the FWHM and FWTM at each distance, the magnification value should be calculated. The FWHM of the HEXITEC detector (for 0.5 mm diameter pinhole collimator) can be calculated for any known distance using slope-intercept formula from the line fit, Equation 6.3:

$$FWHM = c + (bH) \quad (6.3)$$

where H is the distance from the pinhole collimator to the source. When H = 15 mm, the distance between the detector and the centre of the pinhole collimator, the source is said to be at the non-magnifying position. b is the gradient and c is the intercept (Table 6.5) values have been tabulated as the data has been acquired with and without Perspex. Table 6.6 summarises the extrinsic spatial resolution results.

A. With Perspex

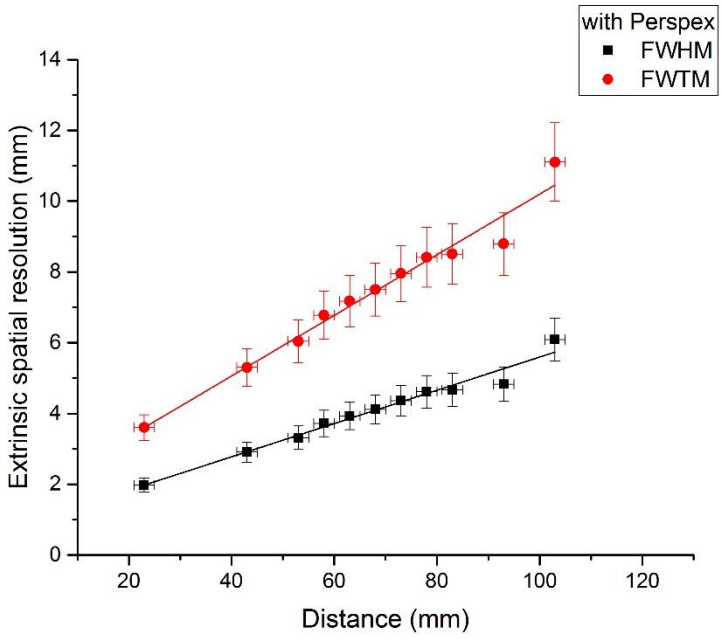

B. Without Perspex

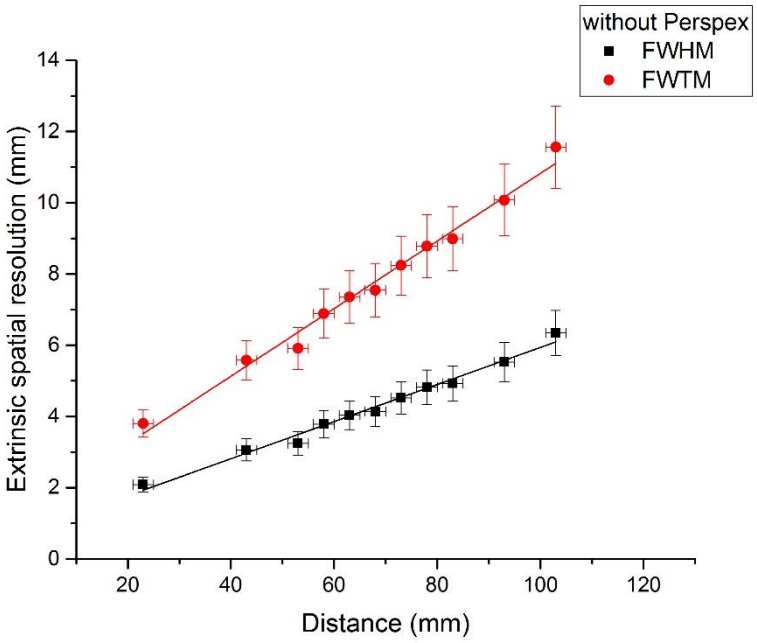

Figure 6.9: Graphs showing the extrinsic spatial resolution vs distance with Perspex ranging from 20 mm to 75 mm thicknesses (*Top*) and without Perspex (*Bottom*). FWHM (black square) and FWTM (red dots) calculated for 2 mm diameter source filled with 52.7 MBq ^{99m}Tc with 0.5 mm diameter pinhole collimator. Total acquisition time for each image was 200 s.

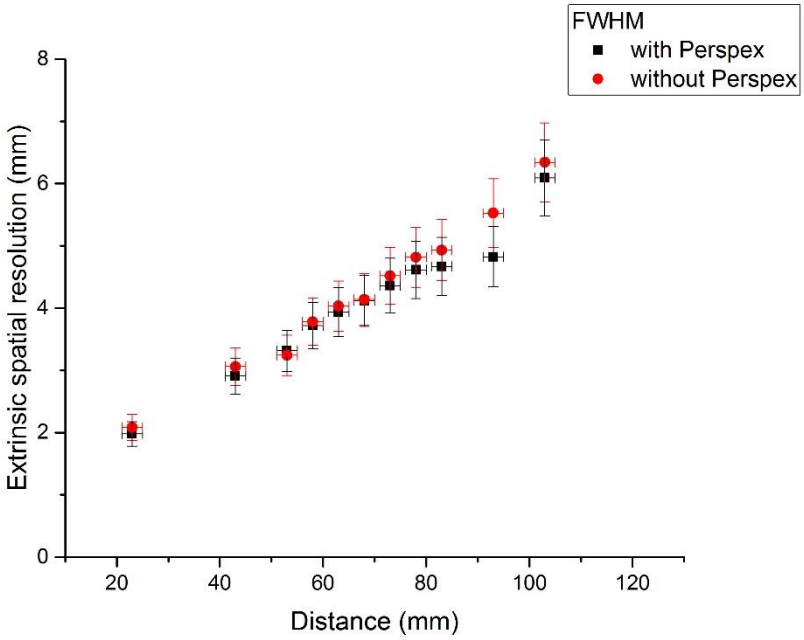

Figure 6.10: Graphs showing the extrinsic resolution vs distance with Perspex (black square) and without Perspex (red dots) calculated for 2 mm diameter point source filled with 52.7 MBq ^{99m}Tc with 0.5 mm diameter pinhole collimator. Total acquisition time for each image was 200 s.

Table 6.5: Fitted parameters of gradient *m* and intercept *c* for the linear relationship between the extrinsic spatial resolution and the imaging distance for HEXITEC detector.

Parameters		**HEXITEC**		
		m	*c*	R^2
with Perspex	FWHM	0.047±0.002	0.91±0.14	0.994
	FWTM	0.085±0.004	1.67±0.26	0.994
without Perspex	FWHM	0.050±0.002	0.82±0.12	0.991
	FWTM	0.092±0.003	1.50±0.22	0.992

Table 6.6: Extrinsic spatial resolution results at the non-magnifying position *d* = 15 mm for HEXITEC detector.

Parameters	**HEXITEC**	
	with Pespex	without Pespex
FWHM (mm)	1.62 ± 0.17	1.57 ± 0.15
FWTM (mm)	2.95 ± 0.32	2.88 ± 0.27

iii. Intrinsic spatial uniformity

Several quantitative measurements can be made for the intrinsic spatial uniformity of a detector; integral uniformity (IU) and differential uniformity (DU). For this investigation the standard measurements suggested in the IPEM report 86 (91) were used which is the coefficient of variation (CoV).

XRI-UNO system

The image used to measure the intrinsic spatial uniformity was produced by taking a flood image of a 2 MBq of ^{57}Co source (6 mm in diameter) (131) placed at a distance of 107 mm away from the detector, so as to produce a uniform illumination on to the detector.

Figure 6.11 shows a typical image produced. It should be noted that in the right upper corner there is an area of non-uniformity, so a region of interest (ROI) was chosen for the uniform region of the entire resultant image to avoid the non-uniform area. The CoV of the XRI-UNO system is 24 %.

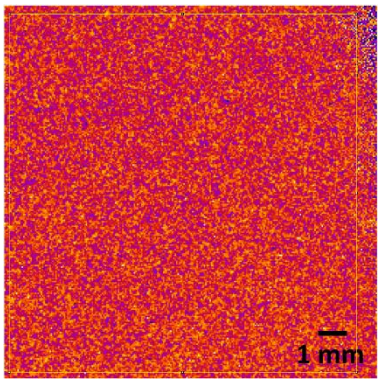

Figure 6.11: A raw flood image of a ^{57}Co source placed at 107 mm away from the detector to measure the intrinsic spatial uniformity.

HEXITEC detector

To measure the intrinsic spatial uniformity, a flood image using a 2 mm diameter source of 59.2 MBq ^{99m}Tc was produced, placed at 300 mm away from the un-collimated detector (see Figure 6.12). Total acquisition time was 2000 s. A region of interest (ROI) was chosen for the uniform region of the entire resultant image to get an accurate and precise reading of the uniformity and to avoid the two defects on the image. The CoV of the HEXITEC was calculated which is 6.4 %.

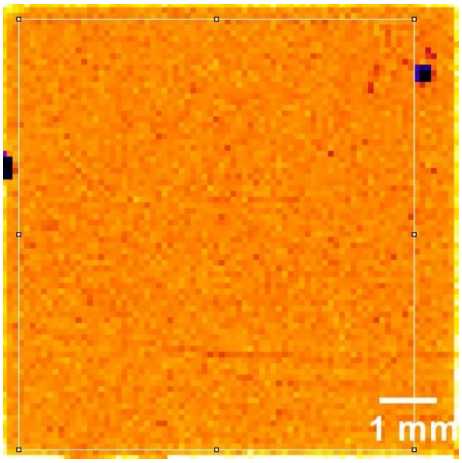

Figure 6.12: A raw flood image of a 59.2 MBq ^{99m}Tc point source, 2 mm diameter, placed at 300 mm away from the un-collimated detector to measure the intrinsic spatial uniformity. Total acquisition time was 2000 s.

iv. Intrinsic spatial sensitivity

Intrinsic spatial sensitivity is a quantitative measure of the detector's ability to measure incident photon counts. The sensitivity was calculated by dividing the total recorded counts by the incident counts on the detector. More details of calculating the incident counts using the solid angle formulae were explained in (Chapter 4, Equation 4.3). The theoretical sensitivity can be calculated using the photon efficiency formula as discussed in (Chapter 4, Equation 4.7). A comparison of the theoretical and the experimental performance characteristics for the intrinsic spatial sensitivity of the XRI-UNO system and the HEXITEC detector are shown in (Table 6.7).

XRI-UNO system

To measure the intrinsic spatial sensitivity, a ^{109}Cd source was placed at a fixed distance of 357 mm away from the surface of the detector with increasing layers of Perspex (ranging from 0 – 65 mm) on top of the detector. Each of the images were analysed and the sensitivity calculated (Figure 6.13). An exponential curve was fitted (Adj. R^2= 0.988) to the data shown in (Figure 6.13). The experimental sensitivity was found to be 99 % for the ^{109}Cd source with (22 keV energy), this is in close agreement with the theoretical sensitivity of 99.99 % calculated with the known detector parameters; thickness, mass attenuation and density. The experimental sensitivity for the ^{99m}Tc source (140.5 keV) was calculated at 31.3 %, which is in good agreement with the theoretical value of 34 %.

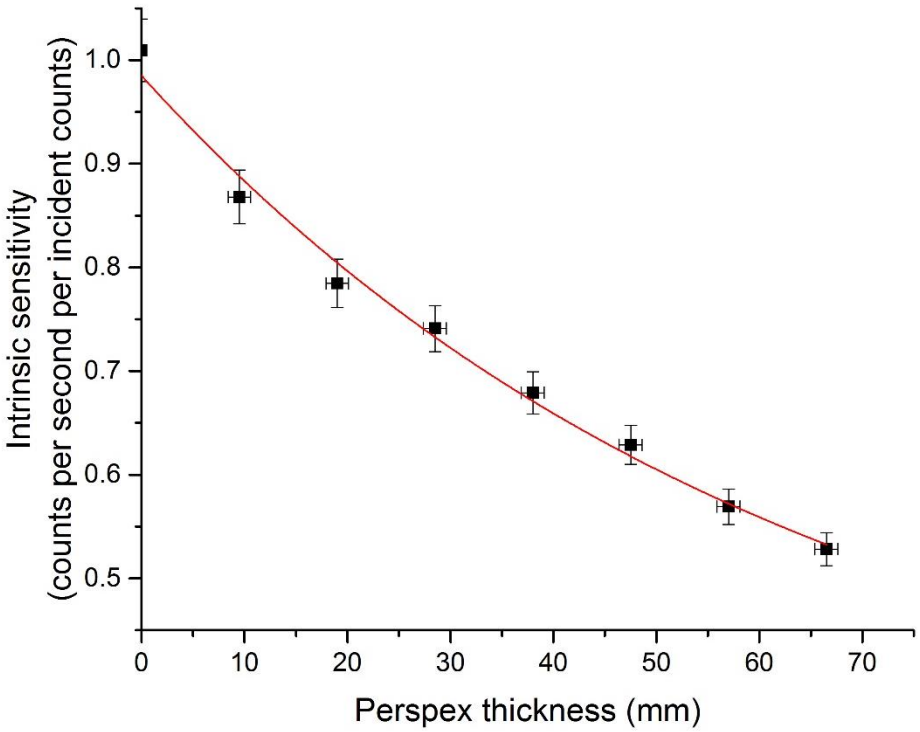

Figure 6.13: A ^{109}Cd source placed at 357 mm away from the XRI-UNO detector with increasing layers of Perspex added in between to show the relationship between the intrinsic sensitivity of the detector and the Perspex thickness.

A comparison of theoretical and experimental values is shown in Figure 6.14. Theoretical sensitivity has been calculated using (Equation 2.2, Chapter 2).

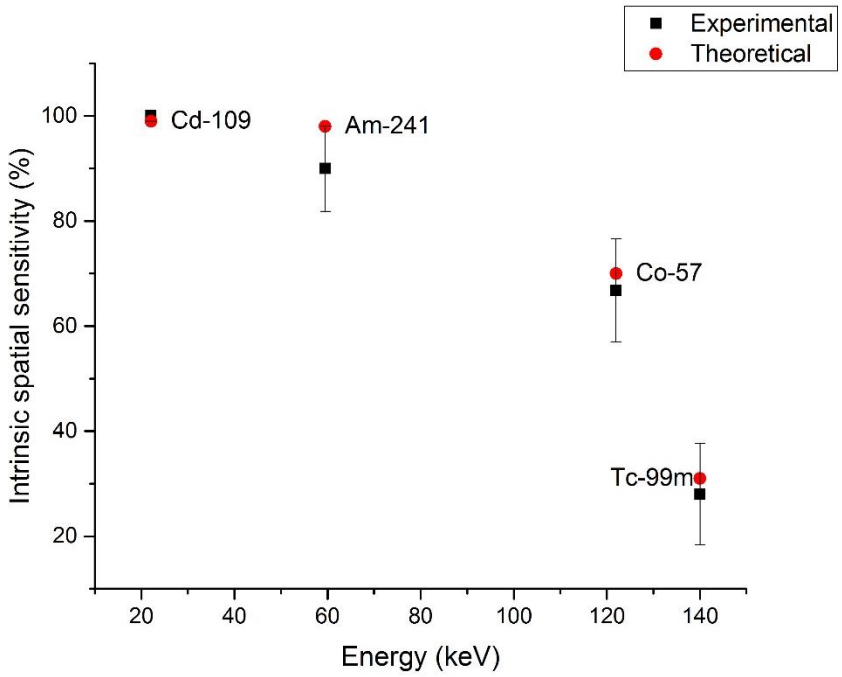

Figure 6.14: Intrinsic spatial sensitivity measurements for XRI-UNO system using ^{109}Cd (22 keV), ^{241}Am (60 keV), ^{57}Co (122 keV) and ^{99m}Tc (140.5 keV).

HEXITEC detector

Intrinsic spatial sensitivity was measured using the same flood image obtained for intrinsic spatial uniformity measurements. The theoretical sensitivity for the HEXITEC detector when using a ^{99m}Tc source was calculated i.e. 34 %. Calculation of the theoretical sensitivity was found based on the photon efficiency formula described previously in (Chapter 4, Equation 6.4). Linear attenuation coefficient of the CdTe has been derived from NIST (40). The experimental sensitivity of the HEXITEC detector using ^{99m}Tc source (140.5 keV) is 1.8 %.

Table 6.7: A comparison of the theoretical sensitivity of the CdTe detectors and the experimental intrinsic spatial sensitivity of both XRI-UNO system and HEXITEC detector.

Source	Principal energy (keV)	Theoretical sensitivity	Experimental sensitivity	
			XRI-UNO system	HEXITEC detector
^{109}Cd	22	99.99 %	100 %	60 %
^{241}Am	60	97.84 %	90 %	38.59 %
^{57}Co	122	44.44 %	66.8 %	16.62 %
^{99m}Tc	140.5	34.0 %	31.3 %	1.8 %

v. Extrinsic spatial sensitivity

XRI-UNO system

Extrinsic spatial sensitivity was measured using the same images acquired for the extrinsic spatial resolution measurements. The equation used to calculate the extrinsic spatial sensitivity has been described in (Chapter 4, section 4.1.5). Figure 6.15 shows a relationship between the extrinsic spatial sensitivity and the source distance from the detector with Perspex. The recorded result of the extrinsic spatial sensitivity at 50 mm is 1.05 cps/MBq.

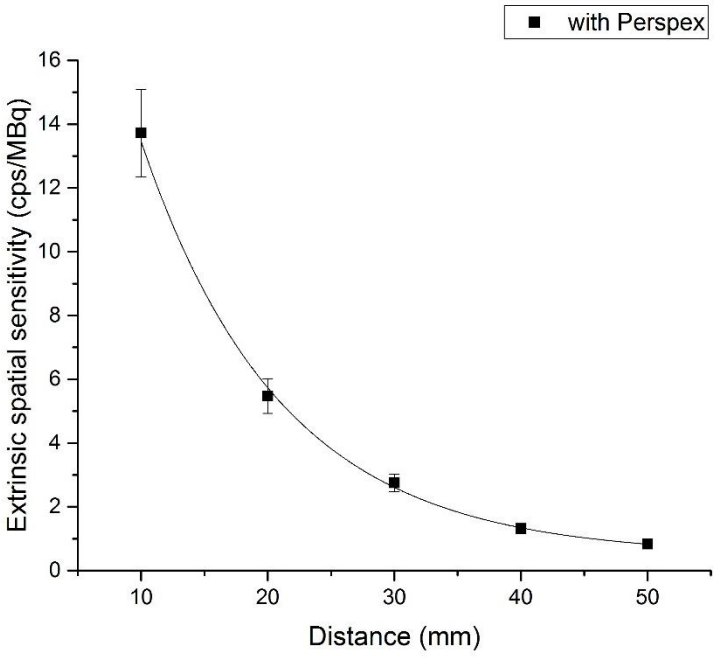

Figure 6.15: A 305 MBq ^{109}Cd source placed at different distances ranging from 10 mm to 50 mm away from the XRI-UNO system with 0.5 mm pinhole collimator with increasing layers of Perspex ranging from 10 mm to 50 mm thicknesses added in between the pinhole collimator and the ^{109}Cd source. Each point was calculated from an average of 999 frames, each frame having an acquisition time of 100 ms.

HEXITEC detector

Extrinsic spatial sensitivity was measured using the same images acquired for the extrinsic spatial resolution measurements. Layers of Perspex starting from 20 mm thickness up to 75 mm were placed between the pinhole collimator and the source. When the source to collimator distance were 80 mm and above the Perspex thickness were fixed at 75 mm as it is the maximum thickness available at the laboratory. Figures 6.16A and 6.16B shows a relationship between the extrinsic spatial sensitivity and the source distance from the detector with and without Perspex respectively. The error calculations on the extrinsic sensitivity was propagated from the associated error in placing the source at a particular distance during camera setup. Figure 6.17 shows the combined relationship with and without Perspex together. The results of the extrinsic spatial sensitivity at 50 mm are in (Table 6.8).

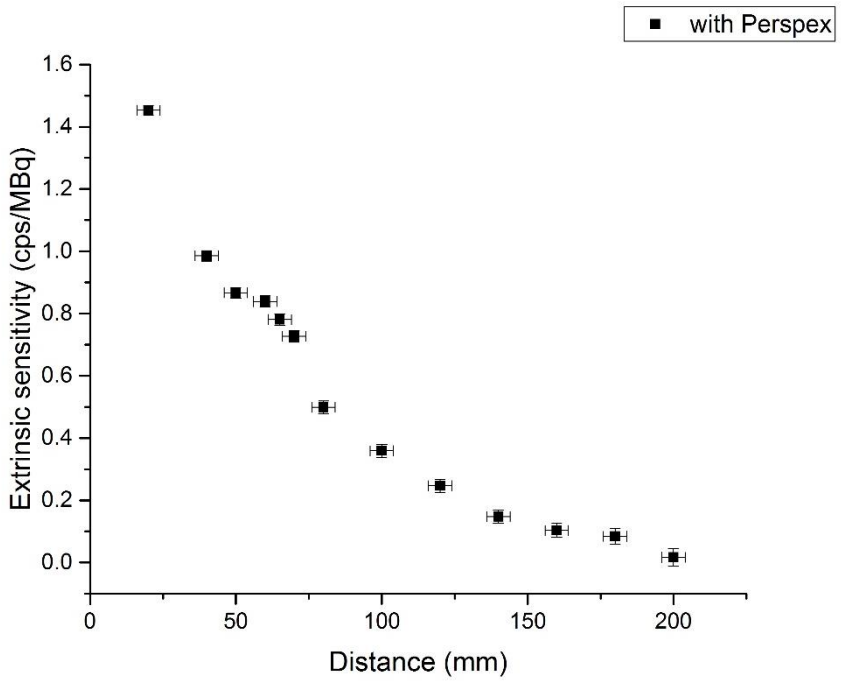

Figure 6.16A: A 78.5 MBq ^{99m}Tc source placed at different distances ranging from 2 mm to 200 mm away from the HEXITEC detector with 0.5 mm pinhole collimator with increasing layers of Perspex ranging from 20 mm to 75 mm thicknesses added in between the pinhole collimator and the ^{99m}Tc source. Total acquisition time for each image was 160 s.

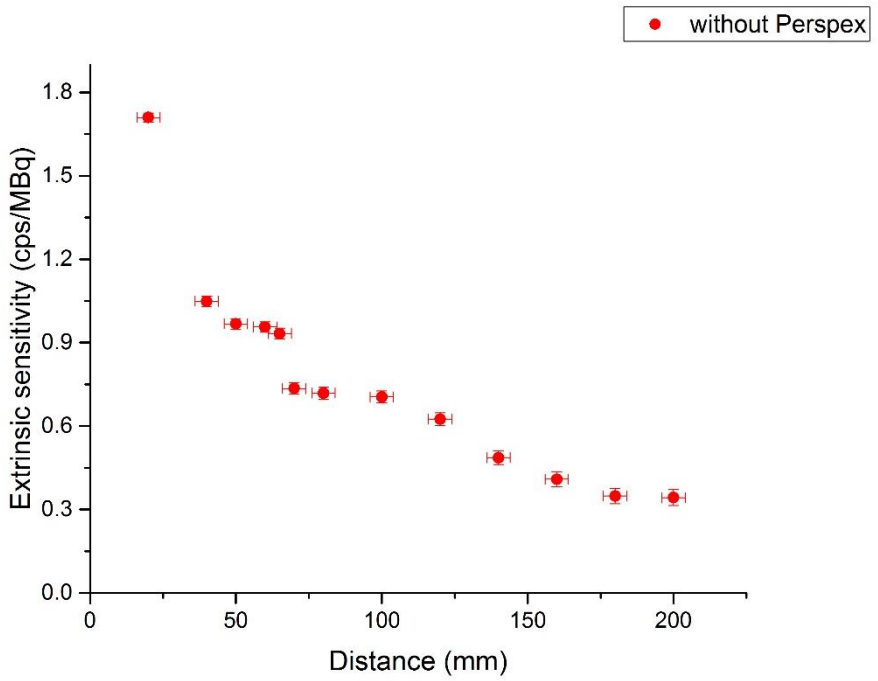

Figure 6.16B: A 78.5 MBq ^{99m}Tc source placed at different distances ranging from 2 mm to 200 mm away from the HEXITEC detector with 0.5 mm pinhole collimator without Perspex. Total acquisition time for each image was 160 s.

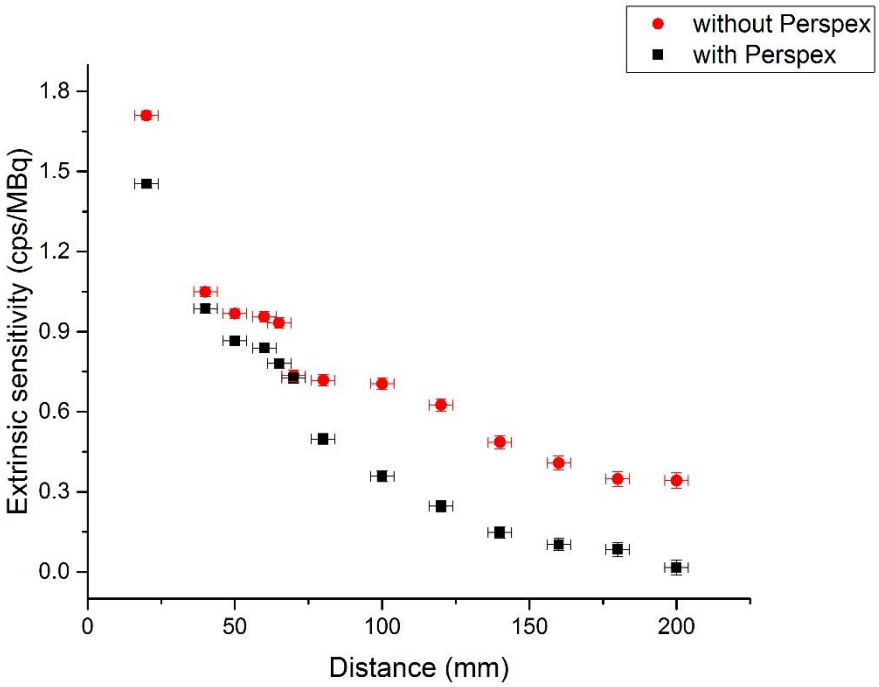

Figure 6.17: A graph showing the relationship between the distance and the extrinsic spatial sensitivity with (black squares) and without (red dots) Perspex. Total acquisition time for each image was 160 s.

Table 6.8: Extrinsic spatial sensitivity result for ^{99m}Tc.

Extrinsic sensitivity at 50mm	**(cps/MBq)**
with Perspex	0.91
without Perspex	1.02

vi. Count rate capability

The count rate capability of the detector is the ability to linearly measure counts.

XRI-UNO system

A vial of ^{99m}Tc source (10 MBq) was placed directly on top of the detector to allow for maximum saturation. In addition to ^{99m}Tc being the main radionuclide used in nuclear medicine this source was chosen due to its short half-life (6 hours). Data was taken over a period of 2 days. Incident counts were plotted against measured counts to produce a count rate capability curve (see Figure 6.18). A linear fit is calculated for the linear proportional section of the curve (Adj. R^2 = 0.999) which indicates that the XRI-UNO system behaves linearly until at least 1680 counts per second (cps) incident on the detector. The data does not go into the linear region which might be because a vial was used in the experiment rather than a point source also it was placed on top of the detector rather than at a distance from the detector. So scattered radiation detected by the detector which could affected the results.

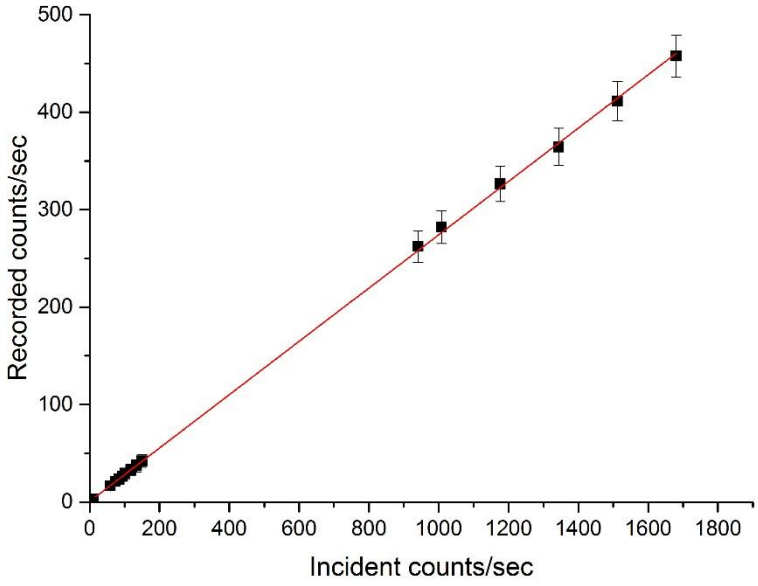

Figure 6.18: Recorded count rate capability for XRI-UNO system by using ^{99m}Tc source placed directly on top of the un-collimated detector. Images were taken over the course of 3 days.

HEXITEC detector

A 2 mm diameter source of 52.7 MBq ^{99m}Tc was placed at 300 mm distance away from the un-collimated detector. Images were taken at regular intervals (i.e. every 60 minutes). Data was taken over a period of 2 days. Each image was acquired within 200 sec. Incident counts were plotted against measured counts to produce a count rate capability curve (see Figure 6.19). It is noticed that there is a gap area between the data which is could be due to an experimental fault. As the data set have been taken within two days and due to the decay of the activity there was a sharp difference between the last point data from the first day of the experiment and the first point data from the next day. A linear fit is calculated for the linear proportional section of the curve (Adj. R^2 = 0.970) which indicates that the HEXITEC detector behaves linearly until at least 11833 counts per second (cps) incident on the detector.

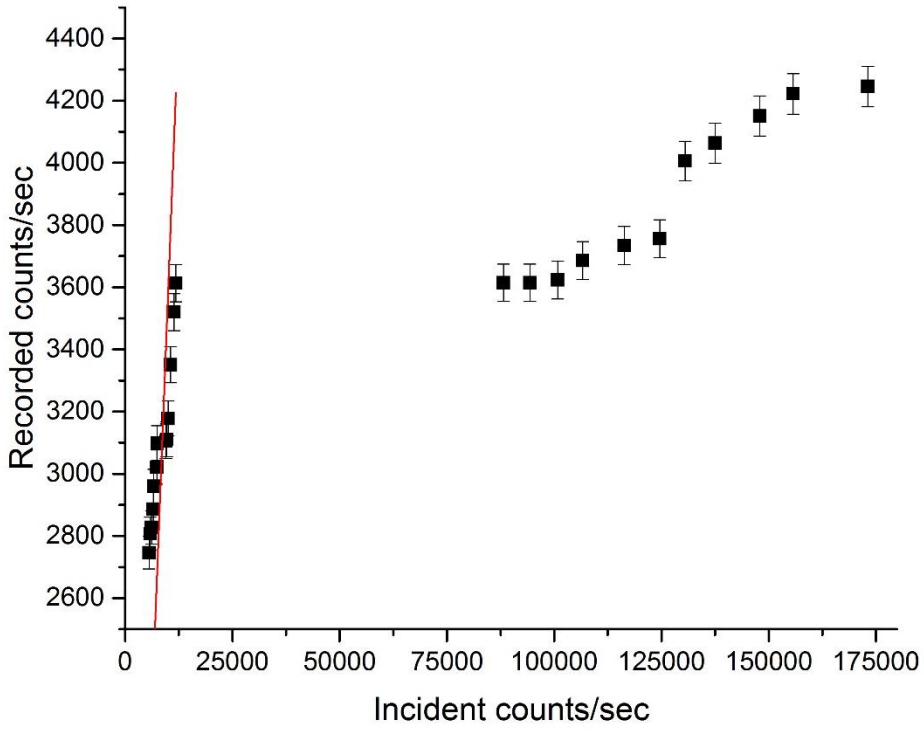

Figure 6.19: Recorded count rate capability for HEXITEC detector by using 52.7 MBq ^{99m}Tc source placed at 300 mm away from the un-collimated detector.

vii. Contrast to noise ratio

Image noise is a very important parameter in medical imaging. There are two types of image noise; random and structured noise. Random noise is the main cause of concern in nuclear medicine, and can be present everywhere in the image. Random noise can reduce the detectability of the system especially if the source being imaged has low contrast. The critical factor for detectability is the contrast to noise ratio (CNR) of the source in the image. Detectability of the source not only depends on the contrast of the source, but also on the size of the source imaged and on the background noise (134). The CNR can be calculated using the following equations (135):

$$CNR = \frac{C}{CoV} \tag{6.4}$$

$$C = \frac{(N_l - N_{bg})}{N_{bg}} \tag{6.5}$$

$$CoV = \frac{\sigma_{bg}}{N_{bg}} \tag{6.6}$$

Where *C* is the contrast that is measured with consideration of a background region. N_l is the average number of counts per pixel measured in the region of interest (ROI). N_{bg} is the average number of counts of the background, *CoV* is the coefficient of variation, σ_{bg} is the standard deviation of the background.

XRI-UNO system

To measure the CNR of the XRI-UNO system, a ^{109}Cd source was placed at fixed distance 100 mm from the collimator while the collimator to detector distance was varied from 10 mm to 40 mm. The collimator used had a 0.5 mm diameter pinhole. Images were acquired for 999 frames with each frame having an acquisition time of 100 ms. A 'ROI' was defined based on visual inspection of the image of the source and a 'noise' region of identical size was also chosen. Rose criterion (1974) (136) gives an approximation that in order to determine the detectability of the object CNR must exceed 2–5. The CNR was calculated for each image and the results are shown in (Figure 6.20).

An exponential fit was calculated (Adj. R^2 =0.995) for the CNR data and also is plotted on (Figure 6.20). It explains that the detectability of the XRI-UNO system decreases with distance.

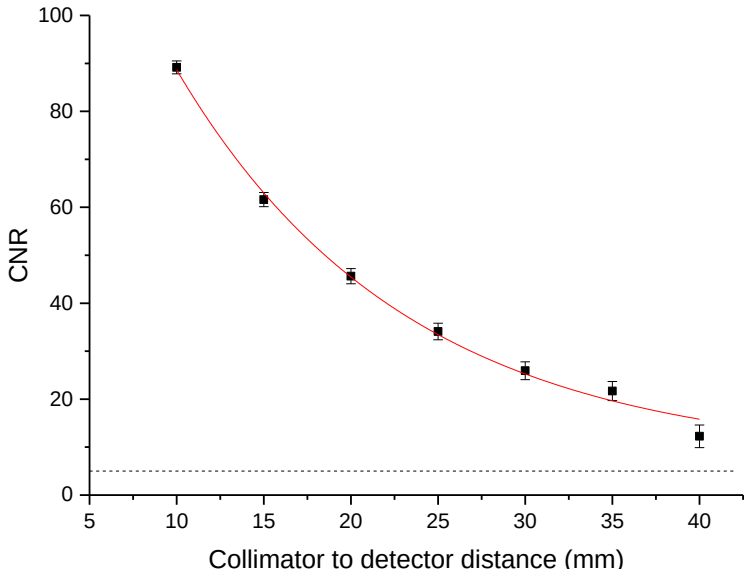

Figure 6.20: Contrast to noise ratio (CNR) of a ^{109}Cd source placed at 100 mm away from the 0.5 mm pinhole collimator. Distance from collimator to detector was varied from 10 mm to 40 mm. The dotted line at CNR = 3:5 shows a calculated threshold value based on the Rose criterion in order of the imaging object to be detectable.

HEXITEC detector

To measure the CNR of the HEXITEC detector, a 52.7 MBq of ^{99m}Tc source was placed at different distances ranging between 20 mm to 90 mm from the pinhole collimator. The collimator used had a 0.5 mm diameter pinhole. Images were acquired having an acquisition time of 200 sec. The CNR was calculated for each image and the results are shown in (Figure 6.21).

An exponential fit was calculated (Adj. R^2 =0.985) for the CNR data and also is plotted on (Figure 6.21). It demonstrates that increasing the collimator to detector distance reduces the detectability of the HEXITEC detector.

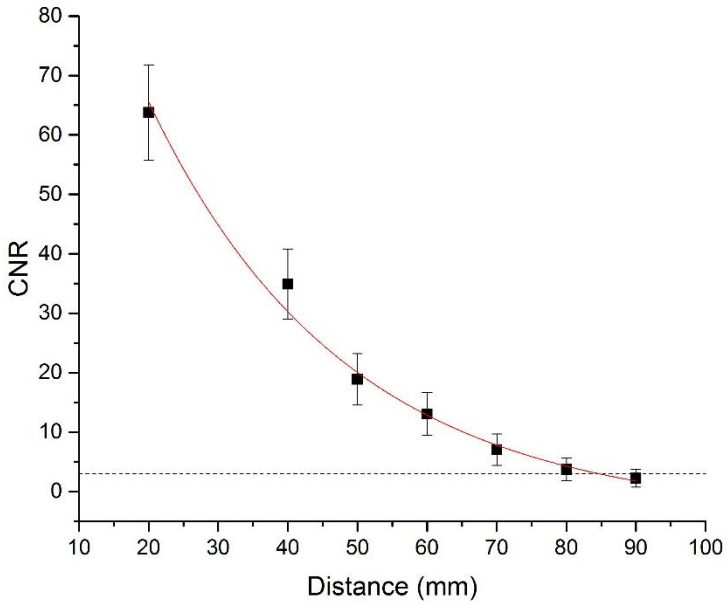

Figure 6.21: Contrast to noise ratio (CNR) of a 52.7 MBq of ^{99m}Tc source placed at varying distances from 20 mm to 90 mm from the 0.5 mm pinhole collimator. The dotted line at CNR = 3:5 shows a calculated threshold value based on the Rose criterion in order of the imaging object to be detectable.

6.2 Results and discussion

The measured performance characteristics including the spatial resolution (intrinsic and extrinsic), intrinsic spatial uniformity, spatial sensitivity (intrinsic and extrinsic), count

rate capability and contrast to noise ratio for the XRI-UNO system and the HEXITEC detector have been compared in (Table 6.9).

Firstly, it is worth to mention that there were a few differences in the methods used to perform the characterisation for both XRI-UNO system and the HEXITEC detector. A lack of indepth understanding of the XRI-UNO software, especially in the initial experiments, may have led to poor data acquisition. An example of this was the later understanding and usage of threshold equalisation, which would have improved the data by creating less variation across the image. Also, a time limitation existed as the XRI-UNO system was only available for testing for a short period of time only. For this reason, no further tests on this system could be carried out.

Table 6.9: A comparison of the performance characteristics for CdTe detectors; XRI-UNO and HEXITEC.

Parameters		XRI-UNO system	HEXITEC detector
Intrinsic spatial resolution	FWHM (µm)	456 ± 20	505 ± 10
	FWTM (µm)	796 ± 38	920 ± 18
Extrinsic spatial resolution	FWHM (mm) including Pesrpex	1.61 ± 0.34	1.62 ± 0.17
	FWTM (mm) including Pesrpex	8.0 ± 0.69	2.95 ± 0.32
Intrinsic spatial uniformity	Coefficient of variation CoV (%)	24	6.4
Intrinsic spatial sensitivity	At 140.5 keV (%)	31.3	1.8
Extrinsic spatial sensitivity	cps/MBq Including Perspex	1.05	0.91
Count rate capability	Maximum incident counts/sec	1680	11833
Contrast to noise ratio	At 40 mm collimator to detector distance	12	35

The measured intrinsic spatial resolution of the XRI-UNO system and the HEXITEC detector shows that both the CdTe detectors operate with a small intrinsic spatial resolution (i.e. 456 ± 20 µm and 505 ± 10 µm) respectively. This is expected as the XRI-UNO system and the HEXITEC detector are a direct photon counting device. However, a detector's intrinsic resolution is usually much smaller than that of the entire system and the extrinsic spatial resolution is a more clinically relevant value. In this investigation a

0.5 mm diameter pinhole collimator was used to assess the extrinsic spatial resolution of the XRI-UNO system. As stated previously by Mejia et al. (137) the pinhole's diameter can be reduced to improve the extrinsic spatial resolution but this would be at the cost of the sensitivity of the detector. The magnification factor is the ratio between the collimator to source distance and the collimator to detector distance. So with this in mind the extrinsic spatial resolution of the XRI-UNO system was determined and was found to have a value of 1.61 ± 0.34 mm at the non-magnifying point using a 0.5 mm diameter pinhole collimator.

However, for the HEXITEC detector the extrinsic spatial resolution measurements were taken with a 0.5 mm diameter pinhole collimator. Measurements were performed both with and without using scattering medium. The method performed was different from the one used with the XRI-UNO system. As the performance characteristics of the HEXITEC detector has followed the modified protocols for small field of view (SFOV) gamma cameras (106). The extrinsic spatial resolution FWHM value was measured at the non-magnifying position thus at (d = 15 mm) was found to be 1.62 ± 0.17 mm in the case of using scattering materials. This spatial resolution value closely agrees with the previously calculated one conducted for hyperspectral SPECT imaging however, they used a 1.0 mm pinhole collimator by Scuffham et al., (138) where they have stated that the HEIXTEC detector has a reasonable spatial resolution with a capability of resolving a minimum features of 2 mm.

From the measurements of intrinsic spatial uniformity, as the integral uniformity for both CdTe detectors may provide inappropriate values, the CoV was measured instead. For the XRI-UNO system it is interesting to note that in the upper right corner (Figure 6.11), there is an area of non-uniformity. This may be the result of radiation degradation, as it has been noted in literature (139), that a long period of radiation exposure damages the CdTe layer within the detector. So a ROI was chosen to avoid the non-uniform area to get an accurate and precise reading of the uniformity. The CoV for the XRI-UNO is 24 % at 122 keV. For the HEXITEC detector, a ROI has been selected as well in order to avoid the two defects on both sides of the image (Figure 6.12). The CoV of the HEXITEC is 6.4 % at 140.5 keV. Scuffham et al., (138) have calculated the average number of events per pixel for the ^{123}I source at a photo-peak of 159 keV which was

2.2 x 10^4, with a standard deviation of 0.3 x 10^4. It is difficult to compare the CoV of the two detectors as different radioactive sources were used as mentioned earlier.

After investigating the intrinsic spatial sensitivity for the XRI-UNO system, it was found that using the ^{99m}Tc source with an energy of 140.5 keV, the sensitivity was approximately 31.3 %. This is remarkably close to the 34 % theoretical efficiency calculated for the ^{99m}Tc source at 140.5 keV energy. For the HEXITEC detector, the intrinsic spatial sensitivity using the ^{99m}Tc source with an energy of 140.5 keV was approximately 1.8 %, which is much lower than the expected theoretical efficiency. It is believed that this is due to the format of the analysed image, as the HEXITEC software can record images in two formats; (.hxt files) these are pre-thresholded and contain only data from single pixel events and (.bin files) containing raw data from all pixels in all frames. Therefor the (.hxt files) format is the one used for analysis. So the difference between theoretical and experimental sensitivities could be due to the number of photons detected from single pixel events only.

For the extrinsic spatial sensitivity of the XRI-UNO system it was found that at 50 mm distance with scattering media in place the sensitivity value was 1.05 cps/MBq using the ^{109}Cd source with an energy of 22 keV. However, for the extrinsic spatial sensitivity of the HEXITEC detector it was found that at 50 mm distance with scattering media in place the sensitivity value was 0.91 cps/MBq using the ^{99m}Tc source with an energy of 140.5 keV.

The XRI-UNO system has a linear count rate up to at least 1680 counts per second (cps) incident. As seen in Figure 6.18 the incident counts/sec versus the recorded counts/sec have not reach the plateau. This is could be due to the number of the experimental data were not sufficient to calculate the linearity. Acquiring more data would not be possible as the time was restricted for having the XRI-UNO system.

However, the HEXITEC detector has a linear count rate up to at least 11833 cps incident.

For contrast to noise ratio there was a declining trend as the collimator to detector distance increases, which is thought by Strauss (140) to be mainly due to the decrease in contrast caused by increasing the distance, as fewer photons are detected by the detector. In addition, according to Dickerscheid (135) a loss in resolution will reduce the

CNR due to scatter and attenuation. The Rose criterion states that ‘‘if the CNR of a hotspot becomes smaller than 3 to 5, it becomes very difficult to observe the hotspot’’(136). In the XRI-UNO system the worst ratio detected at furthest distance measured (i.e. 40 mm collimator to detector distance) is 12. This value suggests that the XRI-UNO system has the ability to detect the source used as it was above the threshold value. For HEXITEC detector the worst ratio detected at furthest distance measured (i.e. 90 mm collimator to detector distance) is 2.

6.3 Conclusion

The performance characterisation of the XRI-UNO system has been investigated indicating that a further characterisation of the full clinical performance, including energy resolution and extrinsic spatial sensitivity should be carried out. Unfortunately, this is would not be possible as we only have the XRI-UNO system for a short period of time. The results presented in this chapter show that the XRI-UNO system has promising performance for use with lower energies less than 30 keV, but due to miss-understanding of the software at the beginning and the short period of time for having the XRI-UNO system, the performance would not be possible to repeat with higher energy radionuclides such as ^{99m}Tc, which is most commonly used in clinical nuclear imaging. However, the performance characteristics of the HEXITEC detector demonstrated in this chapter, show that the HEXITEC detector has the ability to be used in clinical nuclear medical applications. Moreover, the behaviour of this new detector make it strongly in demand in the near future in nuclear medical imaging. Sensitivity may be suitable for medical imaging at low energies but require further investigations to understand the difference between experimental and theoretical values. At 140.5 keV energy photopeak, the recorded sensitivity for the HEXITEC was 1.8 % whereas the HGC records a 40 % sensitivity. Uniformity and spatial resolution are both reasonable for medical imaging. Further characterisation such as energy resolution need to be carried out. And further analysis need to be taken into account using another image format to get more accurate readings for the actual numbers of the absorbed photons by the detector. Also, a full characterisation of the HEXITEC detector need to

be performed using the Cadmium Zinc Telluride (CZT) head and compare it with the currently used CdTe head. According to literatures (141, 142), when the CZT head is applied the expected results will have a higher spatial resolution and higher efficiency for high energy photon detection than CdTe. Furthermore, CZT has a wider band-gap than CdTe due to the presence of Zn in the lattice. This gives CZT a higher resistivity than CdTe.

Furthermore, at the time of writing measurements of high energy radiotherapy source (i.e. ^{131}I) have been taken at the Leicester Royal Infirmary (LRI) to calculate the count rate capability. Further analysis are required when the data are completed.

Chapter 7

A hybrid gamma and near infrared fluorescence imaging camera

Recently there have been important advances in optical imaging for the biomedical sciences in order to increase the ability of surgeons to detect tumour lesions and improve the assessment, resection and treatment of the abnormal tissues within human body. Optical imaging, which has superior spatial resolution and high sensitivity at the molecular level, can be used intraoperatively (143). Some limitations arises from optical imaging such as limited tissue penetration depth. Image guided near-infrared (NIR) fluorescence imaging, is now considered a powerful technique in detecting tumours which are difficult to determine using conventional imaging modalities (144). This can offer the possibility for surgeons to avoid normal tissue and only resect the cancerous cells (145). However, to achieve the greatest benefit from this technique, the development of effective fluorescence agents and a suitable imaging system are required. Besides, targeted probes, the imaging technology requires an appropriate design and specifications of the imaging system which has good sensitivity to visualise small tumours during surgery. NIR fluorescence imaging using ICG as a fluorescence contrast agent has been used clinically (146). A few examples of the clinical and surgical

procedures that could use NIR fluorescence imaging as a real-time guidance are as follows: sentinel lymph node (SLN) mapping, assessing the structure and the function of the lymphatic vessels and it can also be used in oncology imaging to identify the cancer calcification in breast tissues (147).

Nowadays the need to combine existing intraoperative imaging modalities into multimodality imaging is increasing. Dual radio-NIR fluorescence imaging is a novel technique; fluorescence contrast agents provide high spatial resolution at superficial levels. Gamma imaging, however, is superior to fluorescence imaging because of its high efficiency during non-invasive procedures to quantitatively produce high resolution images of structures through deep tissue (148). Both modalities can be used intraoperatively. The significant advantage of combining gamma imaging with NIR fluorescence imaging is the depth penetration from γ-rays with the high quality real time imaging from NIR fluorescence.

The main aim of this chapter is to describe a novel hybrid NIR-gamma small field of view camera, capable of displaying co-aligned images from both modalities, which can be fused into one image or viewed separately. This study is a preliminary investigation of the performance of the fluorescence component of this camera, including phantom studies and first images from a preclinical pilot study.

7.1 Near-Infrared (NIR) fluorescence imaging system

7.1.1 Principles of operation

Fluorescence imaging refers to the ability of a particular molecule to possess the optical properties such that absorbing light at a specific wavelength and emitting light having a longer wavelength after a short period of time (known as the fluorescence time) (149). In some fluorescence imaging light is either generated; internally by energy released from a chemical reaction which is known as bioluminescence or by an external light source. In particular NIR fluorescence imaging, has the potential to use the invisible NIR

fluorescent light within the NIR window of 700 nm to 900 nm (147). As the NIR fluorescent light has a particular bandwidth that is invisible to the human eye, special fluorescence imaging technologies are needed to image the contrast agent, which emits a signal with different spectral fluorescence characteristics after being excited. These emitted photons can be filtered with an emission filter and images can be acquired with a NIR fluorescence imaging camera.

7.1.2 Filters, light source and camera

All NIR fluorescence imaging systems have three main basic components: optical filters, a source of light and NIR fluorescence camera. A brief description of each component will be discussed below.

I. Filters

Optical filters are used in fluorescence imaging in order to transmit fluorescence emission or reflect a range of light which has a specific wavelength. There are three common types of optical filters; band-pass, long-pass and short-pass filters. Figure 7.1 illustrates the characteristics of each type of filter.

As shown in Figure 7.1, the band-pass (BP) filters are designed typically to allow the transmission of a band of the spectrum while rejecting all other unwanted wavelengths. In contrast, long-pass (LP) filters are designed to selectively transmit longer wavelengths and block out shorter wavelengths. While short-pass (SP) filters are designed to selectively transmit shorter wavelengths and block out longer wavelengths.

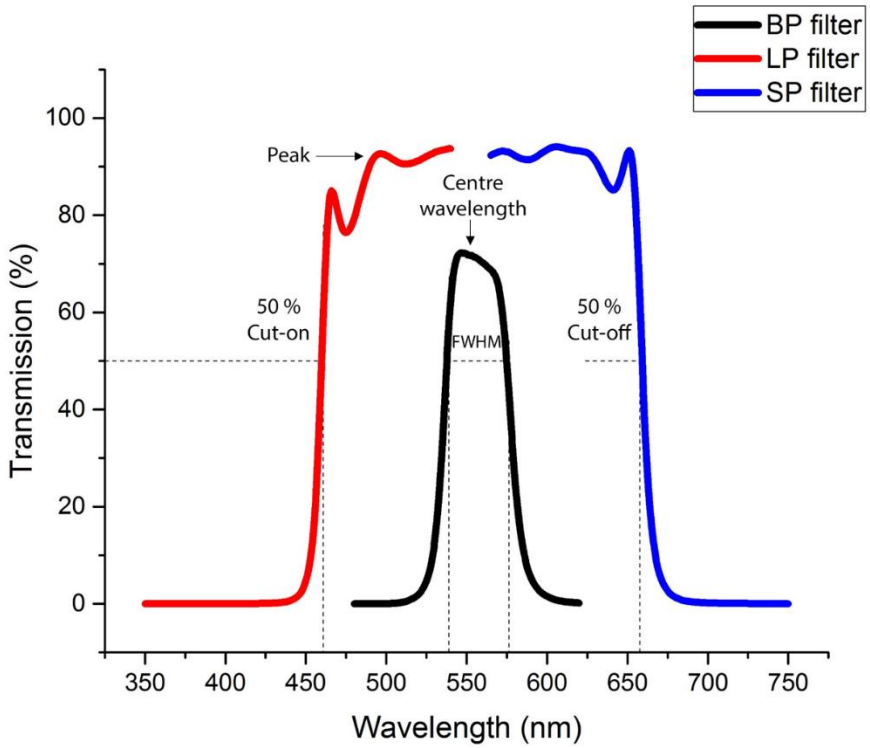

Figure 7.1: Characteristics of optical filters: long-pass LP filter (red), band-pass BP filter (black) and short-pass SP filter (blue).

II. Excitation light source

Fluorescence imaging usually requires a light to excite the fluorophore to be imaged. For NIR fluorescence imaging, the most desirable excitation light source is that the light is centered at the peak absorption wavelength of the fluorescence contrast agent used (150).

Three main technologies are available to produce light to excite the NIR fluorescence agents. Those technologies are: filtered broadband sources, light emitting diodes (LEDs) and laser diodes (147). Each of them has advantages and disadvantages which are described briefly by Gioux et al. (147, 150). The filtered broadband sources have a problem in efficiency, as the filters reject most of the light photons produced from the source. However, LEDs have a good efficiency providing an optimal power and a typical light spectrum (i.e. FWHM < 50 nm). Laser diodes can offer the best results spatially and spectrally, but they are difficult to accommodate and are high-priced at high power.

III. Fluorescence camera

The success of NIR fluorescence imaging depends on the availability of a good fluorescence imaging camera. In a previous systematic review, by Gioux et al. (147), the specification of the camera was described. In general three types of cameras have been described; silicon based CCD cameras, cameras with complementary metal oxide semiconductor (CMOS) sensors and cameras with scientific CMOS sensors.

Nowadays, most surgeons use commercially available fluorescence imaging systems. These systems have also been described in a systematic review by Gioux (147). Examples of the existing intraoperative NIR fluorescence imaging systems are: The Novadaq SPY^{TM} system (151), Fluobeam from Fluoptics (152), the Photodynamic Eye from Hamamatsu (153) and the FLARE imaging system developed by the Frangioni Laboratory (154).

The majority of the pre-clinical and clinical intraoperative studies published to date use the Pearl Impulse Small Animal Imager from (LI-COR Biosciences, Lincoln, NE) (155). The object being imaged needs to be placed inside a closed box in order to block out the ambient light. The resulting fluorescent images from the Pearl system are high quality (156). Other systems include, the Artemis imaging system which has been tested in the Centre for Translational Molecular Medicine (CTMM), Leiden, The Netherlands (156).

7.1.3 NIR fluorescent contrast agents

In order to achieve successful clinical fluorescence imaging, the use of the appropriate fluorescence contrast agent is essential. The effective fluorescence contrast agent should have a high level of brightness. The aspects that determine its suitability are; high quantum yield (QY), which is the ratio of the number of photons emitted to the number of photons absorbed, good matching between the absorption peak and the wavelength of the excitation light source and it should have a large Stoke's shift (i.e. the gap between the excitation and emission). This leads to good blocking of the excitation

light and allows the maximum collection of emission from the fluorescence source. In this thesis, two fluorescence contrast agents have been chosen for study; Indocyanine green (ICG) and IRDye 800CW. At the time of the study ICG was the only fluorescence agent approved by the U.S. Food and Drug Administration (FDA) and the European Medicines Agency (EMA) (157). However, the IRDye 800CW is undergoing clinical trials both in the U.S and Europe (158).

I. Indocyanine green (ICG)

Indocyanine green (ICG) is a fluorescent contrast agent which has been used widely in biomedical sciences. It has an emission peak at 820 nm and an absorption peak of 760 nm, Figure 7.2 illustrates the spectrum. It possesses several features that make it an ideal fluorophore source to be used in clinical applications. ICG is non-toxic and non-ionising source which is good for patient safety. It has a short life time when administered intravenously into the blood circulation and has a good signal to noise ratio (SNR). In addition it can offer deep imaging i.e. deep NIR light photon penetration at depths of greater than 1 cm.

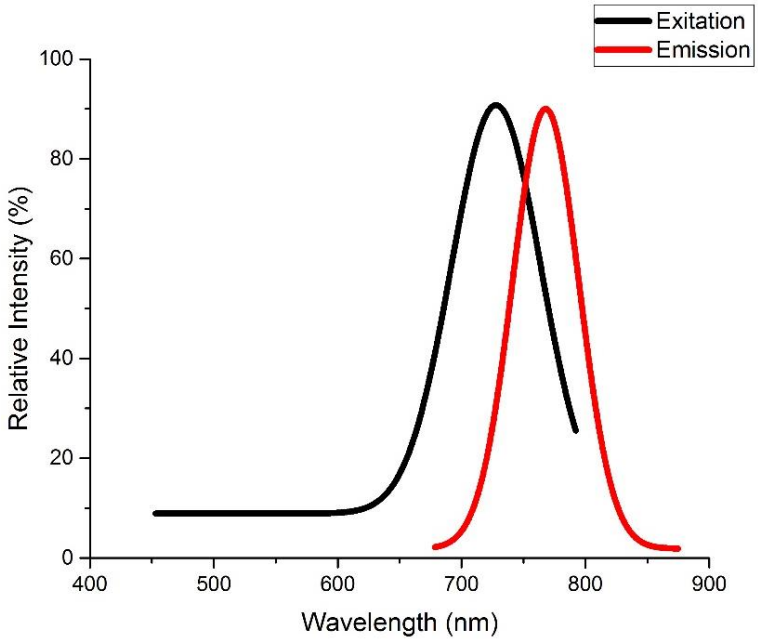

Figure 7.2: The spectrum of ICG which has an excitation maximum at 760 nm and an emission maximum at 820 nm. Data derived from AAT Bioquest (159).

II. IRDye 800CW Infrared Dye

IRDye 800CW is an infrared fluorescent dye which is made by LI-COR Bioscience. It has an emission peak at 789 nm and an absorption peak of 774 nm (160), Figure 7.3 shows a representative spectrum. It has several properties that make it the preferred choice to use during infrared fluorescence imaging. It has brighter fluorescence performance than other currently available fluorophores, with low background ratio in the near infrared wavelengths. Thus, the IRDye 800CW has a high signal to noise ratio (SNR). All these properties coupled to the availability of a good fluorescence imaging system will provide fluorescence images with enhanced sensitivity. IRDye 800CW has been tested previously and it showed that there were no significant clinical toxicities (161, 162). The FDA (Food and Drug Administration, USA) has recently approved the IRDye 800CW for clinical use (163).

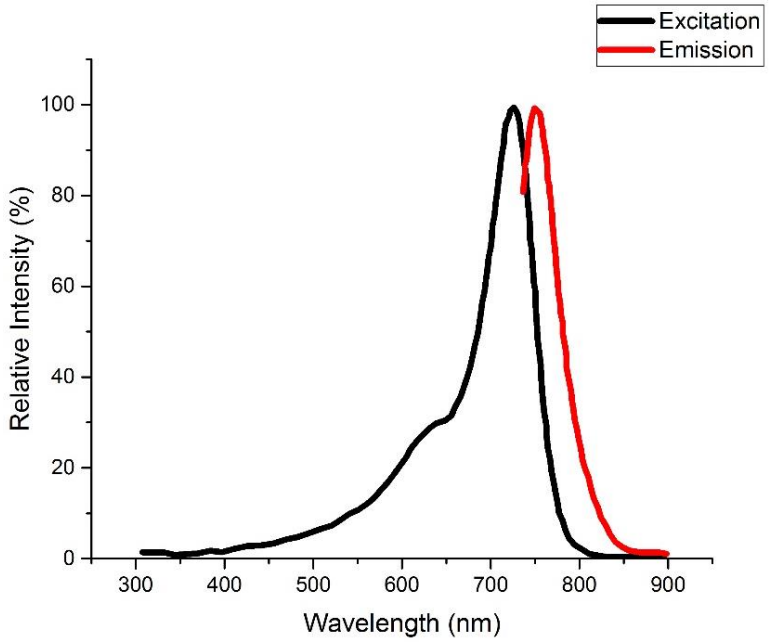

Figure 7.3: The spectrum of IRDye 800CW which has an excitation maximum at 774 nm and an emission maximum at 789 nm. Data derived from AAT Bioquest (159).

7.2 Materials and methods

7.2.1 Fluorescence imaging camera

I. NIR CP camera

A Near-Infrared NIR CP camera obtained from (IDS, Imaging Development System) has been tested (164). The NIR CP camera is a complementary metal oxide semiconductor (CMOS) mono sensor. It measures 29.0 mm x 29.0 mm x 29.0 mm and weighs 52 g and it offers 1.31 mega-pixel sensor and it has pixel size of 5.3 µm. The resolution of the acquired image is 1280 x 1024 pixel at a rate of 60 fps. A manual focused lens is mounted to the camera which has 6 mm focal length. The CP camera is connected directly to a laptop through a USB cable. Figure 7.4 shows a photograph of the NIR CP camera.

Figure 7.4: A photograph of Near-Infrared (NIR) CP camera with a mounted lens.

II. XS camera

An XS camera obtained from (IDS, Imaging Development System) has been tested as well. An XS camera is a complementary metal oxide semiconductor (CMOS) colour sensor. It is small and measures 26.5 mm x 23.0 mm x 21.5 mm and weighs only 12 g. It offers a 5.04 mega-pixel sensor and has a pixel size of 1.4 µm. The resolution of the

acquired image is 2592 x 1944 pixel at a rate of 15 fps. The XS camera is also connected directly to the laptop through a USB cable. The original XS camera was modified at the SRC laboratory by removing the IR-blocking filter over the sensor to allow the fitting of an optical NIR filter to enable its use as an NIR fluorescence camera. Figure 7.5 shows a photograph of the XS camera.

Figure 7.5: A photograph of the modified XS camera

7.2.2 LED 740 nm ring

A commercially available compact infrared LED ring with a wavelength of 740 nm (30 nm FWHM) provided by (Edmund Optics) has been used in the investigations. The LED ring measures 70.8 mm in diameter and 17 mm height. It provides the high-power illumination that is required in fluorescence imaging. Figure 7.6 shows a photograph of the LED ring. Figure 7.7 shows the spectral output of the light emitted (peaking at 740 nm), data were derived from the luminous efficacy tables (165).

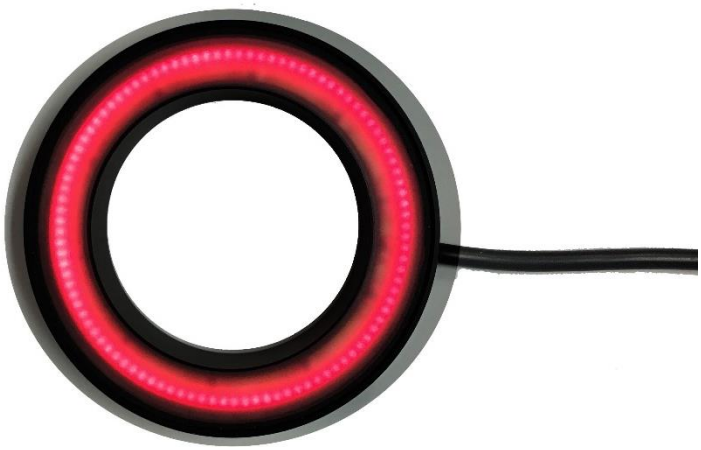

Figure 7.6: A photograph of 740 nm (30 nm FWHM) LED ring.

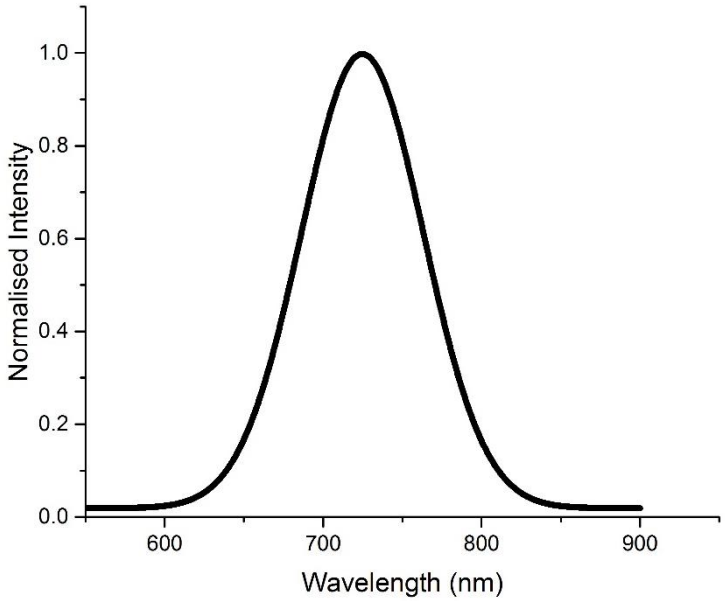

Figure 7.7: Graph showing the typical spectral intensity distribution for the light emitted from the LED ring peaking at 740 nm.

7.2.3 Filters

Two types of optical filters manufactured by PIXELTEQ have been used in this study; band-pass and long-pass filters, which are suitable for both the CP and the XS cameras. The specifications of filters used are a 850nm (100nm FWHM) band-pass (BP) filter and an 800nm long-pass (LP) filter. The circular filter used for the CP camera was 18 mm in diameter. Whereas, the dimensions of the square filter used for the XS camera were 8 mm x 8 mm. Both of them are 1.1 mm thick (166). Figures 7.8 and 7.9 show the transmission graph of both 850nm (100nm FWHM) BP and 800nm LP filters respectively, data were derived from Andover Corporation (167).

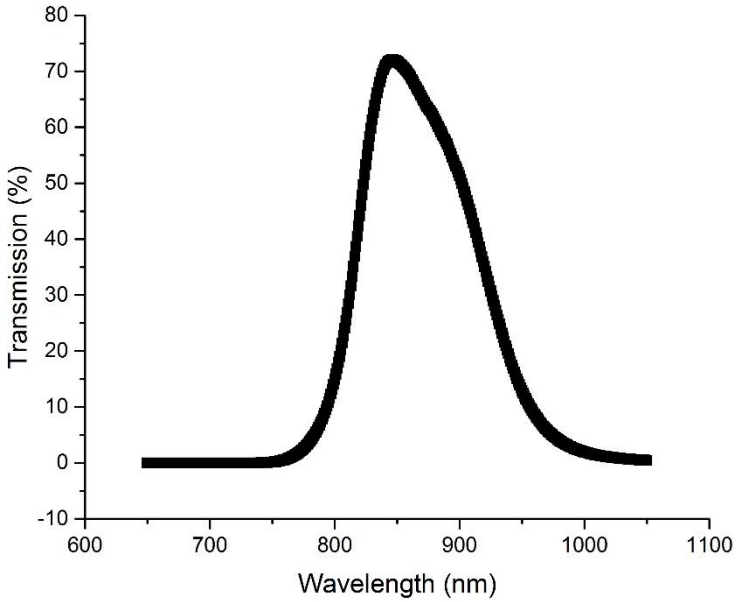

Figure 7.8: Transmission graph of the 850nm (100nm FWHM) BP filter.

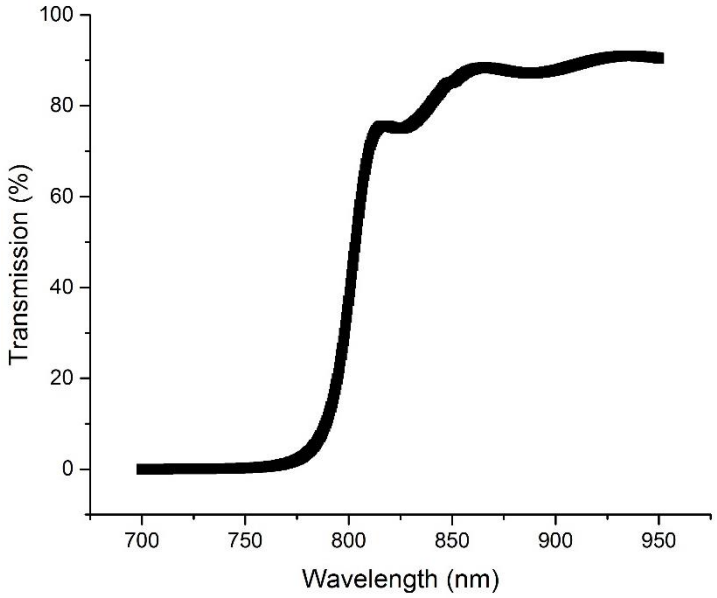

Figure 7.9: Transmission graph of the 800nm LP filter.

7.2.4 Initial investigation

Initial experiments were performed to test the fluorescence system. An ICG fluorescence source was prepared in three different concentrations to determine the best concentration that can be used to fluoresce, (see Figure 7.10). Due to lack of a measurement balance with sufficient sensitivity, we could not measure the exact volume of the ICG fluorescence powder. A smear of the ICG powder was taken with a needle and then diluted with 1 ml of water, (see Figure 7.10A). Then a 0.5 ml of the mixture was taken and diluted with 0.5 ml of water, (see Figure 7.10B). Finally a 0.5 ml of the second prepared mixture was taken and diluted with 0.5 ml of water, (see Figure 7.10C).

A **B** **C**

Figure 7.10: Optical image of ICG fluorescence mixture (A) high ICG concentration (B) middle ICG concentration (C) low ICG concentration.

Figure 7.11 shows the resultant fluorescence image using the XS camera. It is clear by visual inspection that the highest concentration of ICG mixture, (Figure 7.11A) does not fluoresce. While, the lowest concentration of ICG mixture, (Figure 7.11C) would fluoresce at a very low level. The most suitable concentration of ICG mixture is shown

in (Figure 7.11B). It is worth mentioning that, for the high ICG concentration it is clear that the ICG is quenching. Quenching of the fluorescence contrast agent depends on its concentration, when the concentration is too high the fluorescence source will exhibit fluorescence quenching. Once a quenching level is reached, the fluorescence intensity will decrease (168).

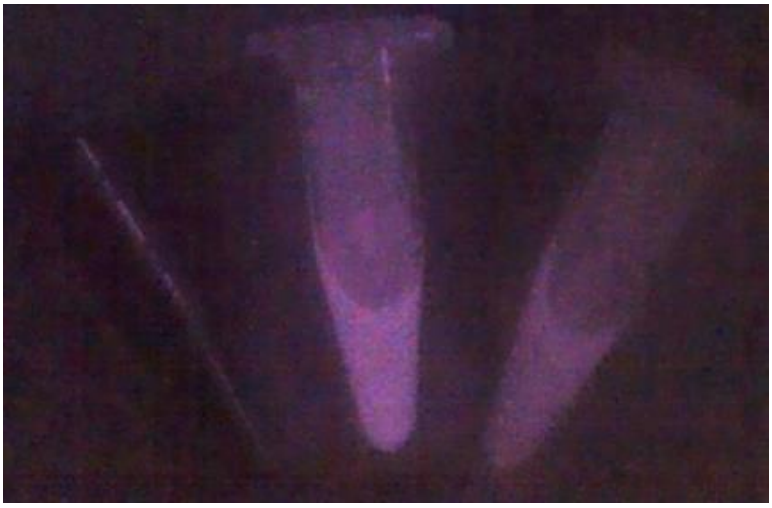

A **B** **C**

Figure 7.11: Fluorescent image of ICG mixtures using XS camera (A) high ICG concentration (B) middle ICG concentration (C) low ICG concentration.

After finding the most suitable ICG concentration level, the hot spot phantom which has four holes 1, 2, 3 and 4 mm diameter drilled in a 12 mm thick piece of Perspex, was filled with the ideal ICG mixture, (see Figure 7.12). Images have been recorded using XS camera at two different distances; 140 mm away from the camera, (Figure 7.12A) and 230 mm away from the camera, (Figure 7.12B).

The resultant images from the initial investigation show that the fluorescence system has an excellent level of spatial resolution, (see Figure 7.13). This led us to investigate the fluorescence system in more depth using different experimental techniques.

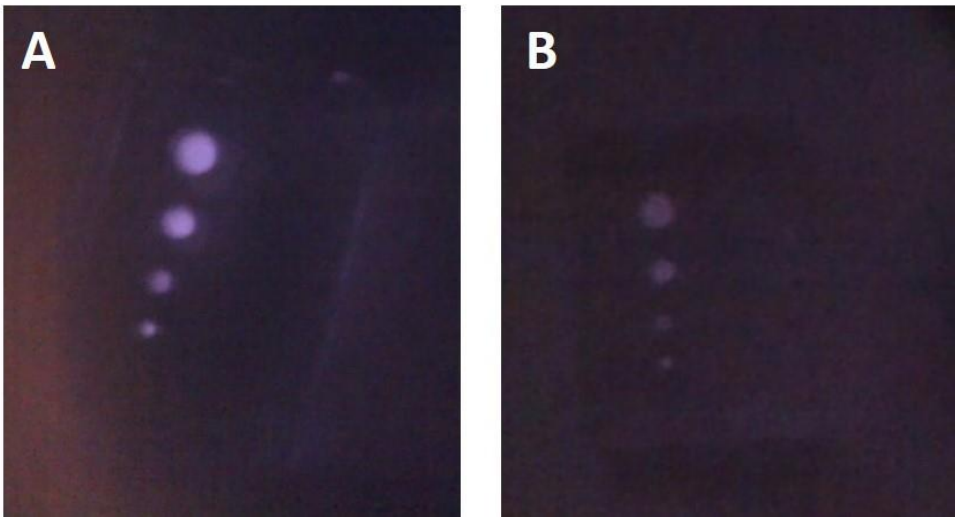

Figure 7.12: Fluorescence image using XS camera of the hot spot phantom filled with ICG fluorescence source. (A) At 140 mm distance from the camera. (B) At 230 mm distance from the camera.

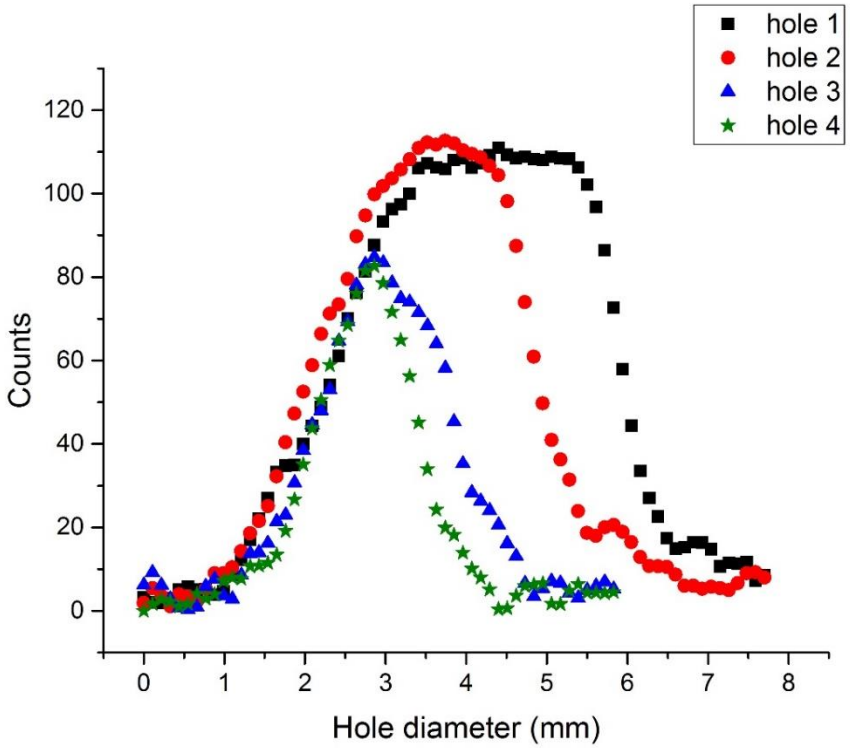

Figure 7.13: The horizontal line profile across the fluorescence image of the hot spot phantom filled with ICG fluorescence source placed at 140 mm distance from the XS camera. (Black square) profile of the 4 mm diameter hole. (Red circle) profile of the 3 mm diameter hole. (Blue triangle) profile of the 2 mm diameter hole. (Green stars) profile of the 1 mm diameter hole.

7.2.5 Quantitative performance of the fluorescence imaging

The first study of the quantitative performance of the fluorescence system was performed with both NIR CP and XS cameras. Both ICG and IRDye 800CW fluorescence sources were prepared by filling the phantom which has a hole of 6 mm depth, 10 mm diameter drilled in a 8 mm thick of Perspex. As mentioned before, the exact concentrations of both sources could not be measured precisely. Fluorescence images were taken with both 850nm BP and 800nm LP filters using the CP camera (Figure 7.14) and the XS camera (Figure 7.15). The fluorescence sources were 65 mm away from the camera face.

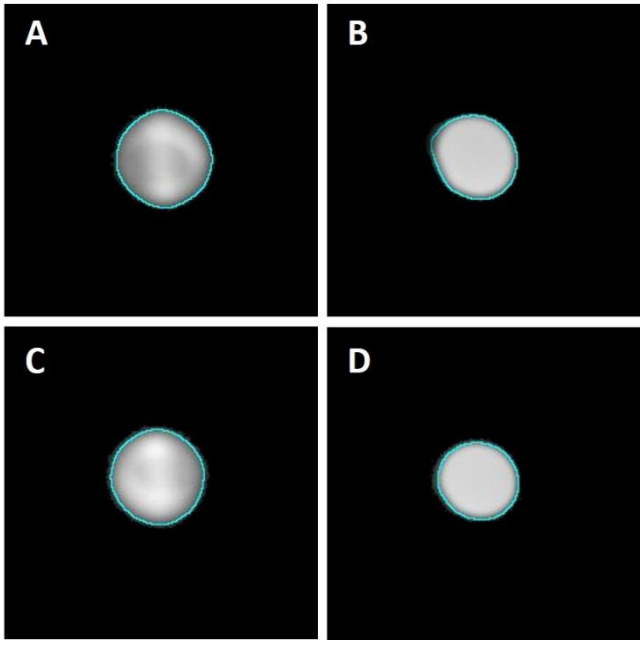

Figure 7.14: Fluorescence images performed using the CP camera. A) For ICG source with 850 nm BP filter. B) For IRDye 800CW source with 850 nm BP filter. C) For ICG source with 800 nm LP filter. D) For IRDye 800CW source with 800 nm LP filter. In all cases the source to camera distance was 65 mm.

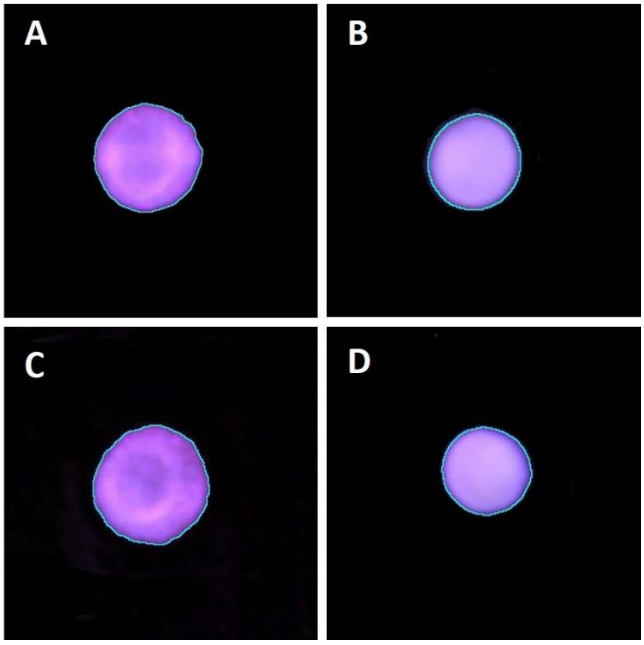

Figure 7.15: Fluorescence images performed using the XS camera. A) For ICG source with 850 nm BP filter. B) For IRDye 800CW source with 850 nm BP filter. C) For ICG source with 800 nm LP filter. D) For IRDye 800CW source with 800 nm LP filter. In all cases the source to camera distance was 65 mm.

A region of interest (ROI) has been drawn around the resultant fluorescence images (Figures 7.14 and 7.15). The contrast to noise ratio (CNR) was calculated for both ICG and IRCW800 fluorescence sources using both the CP and the XS cameras with the BP and the LP filters. A full explanation of the CNR calculations and equations were discussed previously in Chapter 6.

A column graph has been plotted to show the contrast to noise ratio (CNR) of ICG and IRCW800 fluorescence sources using the CP camera (Figure 7.16) and XS camera (Figure 7.17) with both the 850nm BP filter and 800nm LP filter.

As shown in Figure 7.16, the CNR of the CP camera is higher when using the 850nm BP filter with both ICG and IR800CW fluorescence sources. This is expected as the emission peaks of ICG and IRCW800 are 820nm and 789nm respectively, which are within the range of the wavelength of the BP filter used (i.e. between 750 nm and 950 nm as the BP filter has a FWHM of 100 nm). Also, this is because the spectrum wavelength of the LED ring is 740 nm (30 nm FWHM), which means that it is more suitable to be used with

the 850nm BP filter rather than the 800nm LP filter. From the results, it is better to use the 850nm BP filter with CP camera to get images with higher CNR.

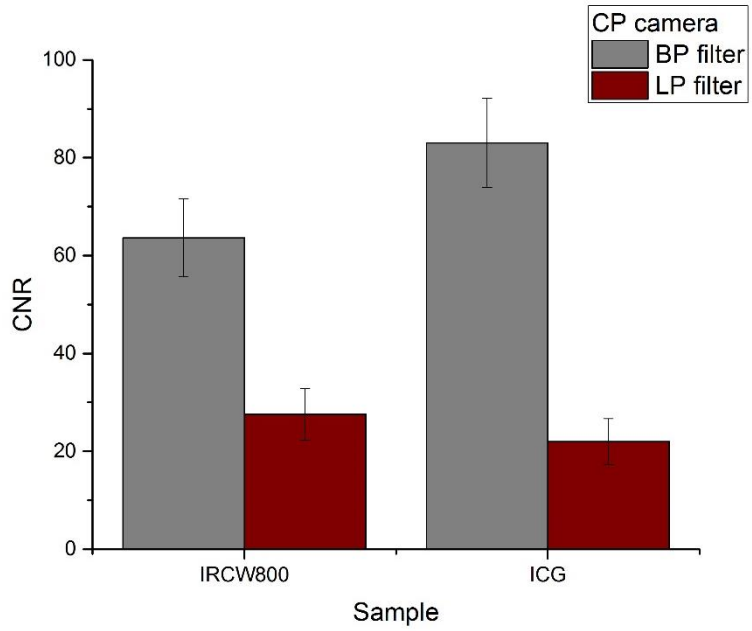

Figure 7.16: Contrast to noise ratio (CNR) graph of the ICG and IRCW800 fluorescence contrast agents using CP camera with 850nm BP filter (grey) and 800nm LP filter (red).

However, the CNR from the XS camera (Figure 7.17) is essentially the same when using either the 850nm BP or the 800nm LP filters with both ICG and IR800CW fluorescence sources. The reason for that is because the XS camera is mainly designed as an optical camera and it has been modified in the laboratory in order to be used as a NIR fluorescence camera. Also, the spectrum wavelength of the LED ring (i.e. 740 nm (30 nm FWHM)) has an effect on the results. As the wavelength of the LED within the range spectrum of the 850nm BP filter. So when the fluorescence contrast agents excited by the LED ring and the camera fitted with 800nm LP filter not all the background noise can be rejected. This is due to the maximum wavelength the LED can excite is 770 nm. From this it is advised to use the 850nm BP filter with the XS camera.

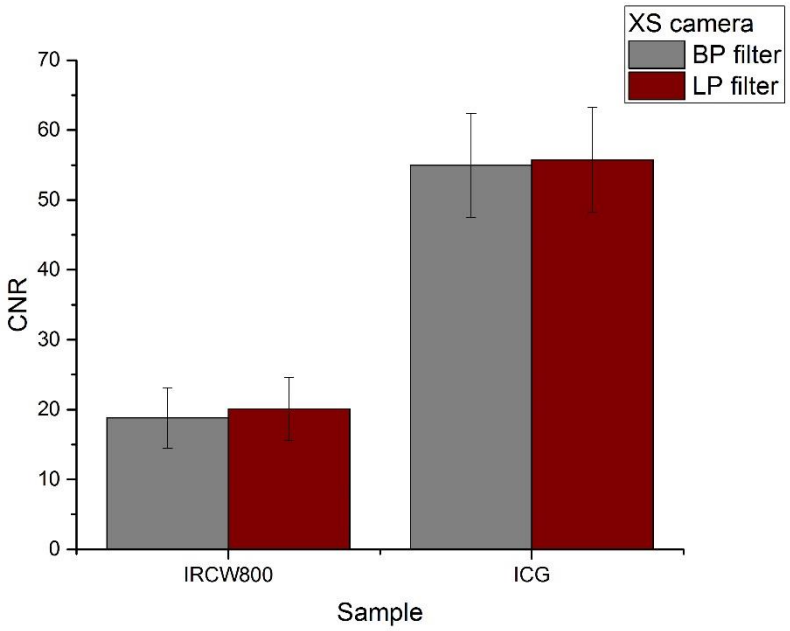

Figure 7.17: Contrast to noise ratio (CNR) graph of the ICG and IRCW800 fluorescence contrast agents using XS camera with 850nm BP filter (grey) and 800nm LP filter (red).

7.2.6 Performance of the fluorescence imaging using 96-well plate

Plastic 96-well plates were used in the experiment. Two plates (clear and black) were obtained from Thermo Fisher Scientific. Both of them were made from polystyrene with a flat bottom. They have 96 wells with each well having a volume of 360 µL and a working volume of 280 µm. Each well measures 6.4 mm in diameter and 11.2 mm depth with 9 mm well to well spacing. The wells are completely chimney for 360° - this means the well geometry is designed to keep each well separated from each other with a gap to reduce and/or to prevent cross contamination.

The performance of the fluorescence imaging was quantified in this study for the fluorophore ICG using a concentration series from 3 mM to 1 fM in a clear 96-well plate with water as the solute. Images were taken at a distance of 90 mm, with an integration time of 60 sec, in a darkened room. Figure 7.18 illustrates the experimental setup. A schematic of the filled plastic 96-well plate is shown in Figure 7.19. The first left well in

the first row of the plate was the most concentrated one (i.e. the stock solution) with 3 mM of ICG mixture. After that, each following well was diluted by adding 1 ml of water to the earlier well. The last (right well) was filled with 1 fM ICG mixture. The fourth row of the plate was filled only with water as a control.

Figure 7.18: Experimental setup of the performance of the fluorescence imaging using clear plastic 96-well plate filled with ICG fluorescence source using a concentration series from 3 mM to 1 fM. The XS camera was fitted to the HGC system and the LED ring was mounted on the HGC face. The plate was placed at 90 mm distance from the HGC surface. The same experimental setup was used with the black 96-well plate.

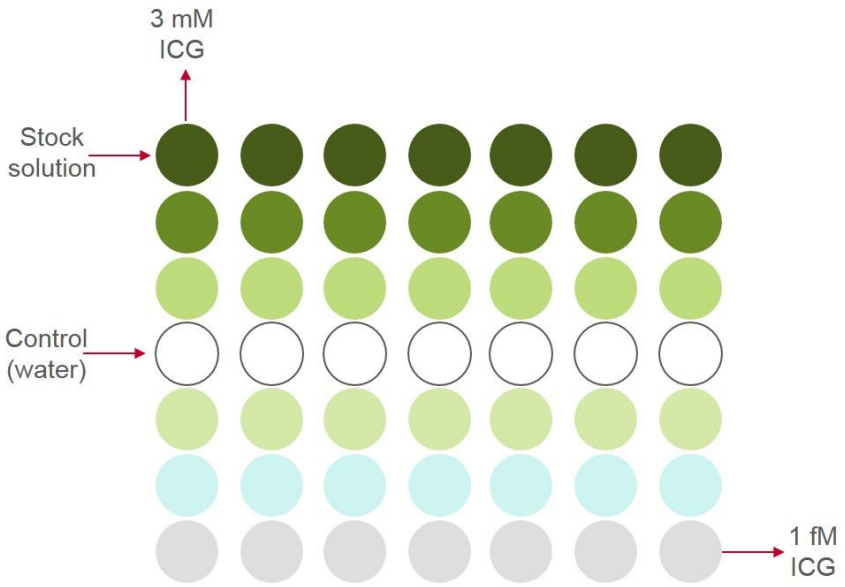

Figure 7.19: Schematic diagram of the filled plastic 96-well plate with ICG fluorescence source. The first (left well) was filled with 3 mM ICG mixture. Then each time 1 ml of the previous concentration was taken and 1 ml water was added and used to fill the next well. The last (right well) was filled with 1 fM ICG mixture. The fourth row was filled with water as a control.

I. Clear 96-well plate

Two fluorescence images have been recorded using the XS camera with two different filters. Figure 7.20 shows a fluorescence image obtained using an 850nm BP filter. While Figure 7.21 shows a fluorescence image recorded using an 800nm LP filter.

The resultant images show that the fluorescence imaging system could not be quantified successfully using a clear plastic 96-well plate. Even the ICG fluorescence source on each well fluoresce, but the reflection of the LED ring that seen on the surface of the plate make the quantification very difficult.

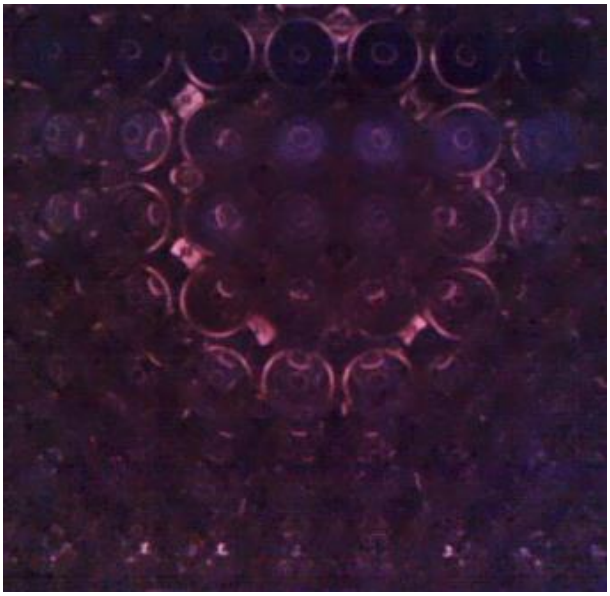

Figure 7.20: Fluorescence image of the clear 96-well plate obtained from the XS camera using ICG fluorescence source with 850nm BP filter. Images were taken at a distance of 90 mm, with an integration time of 60 sec.

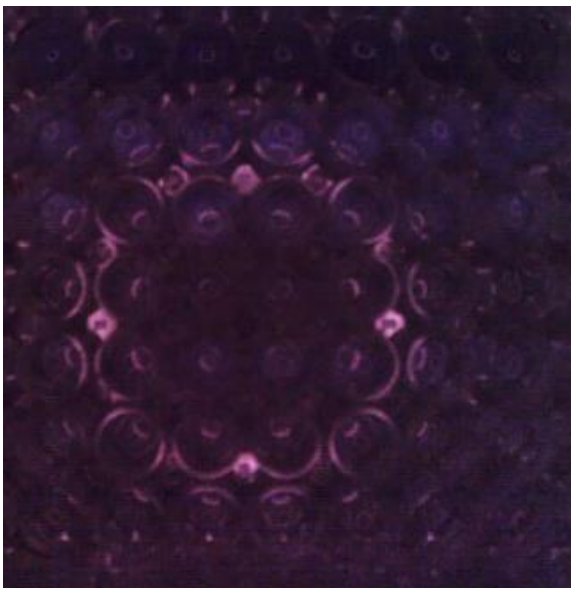

Figure 7.21: Fluorescence image of the clear 96-well plate recorded from the XS camera using ICG fluorescence source with 800nm LP filter. Images were taken at a distance of 90 mm, with an integration time of 60 sec.

II. Black 96-well plate

A second trial was performed using a black 96-well plate aiming to avoid the LED ring reflection. The same experimental setup has been used using ICG with a concentration series from 3 mM to 1 fM in a black 96-well plate with water as the solute. Images were taken at a distance of 90 mm, with an integration time of 60 sec, in a darkened room.

Again two fluorescence images have been taken using the XS camera with two different filters. Figure 7.22 shows a fluorescence image recorded using an 850nm BP filter. While Figure 7.23 shows a fluorescence image obtained using an 800nm LP filter.

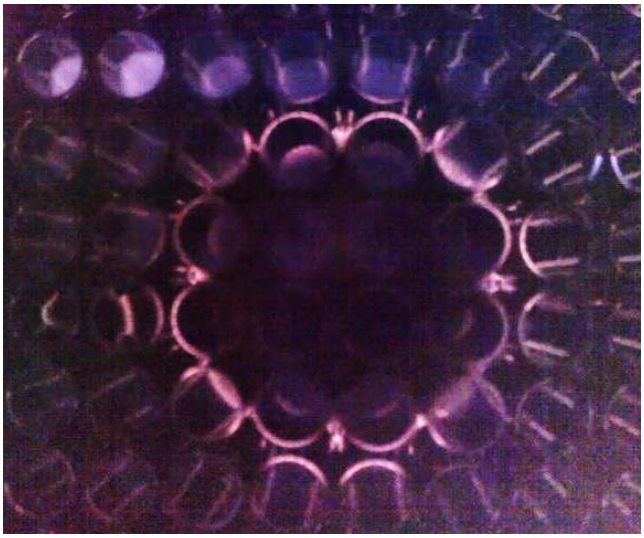

Figure 7.22: Fluorescence image of the black 96-well plate recorded from the XS camera using ICG fluorescence source with 850nm BP filter. Images were taken at a distance of 90 mm, with an integration time of 60 sec.

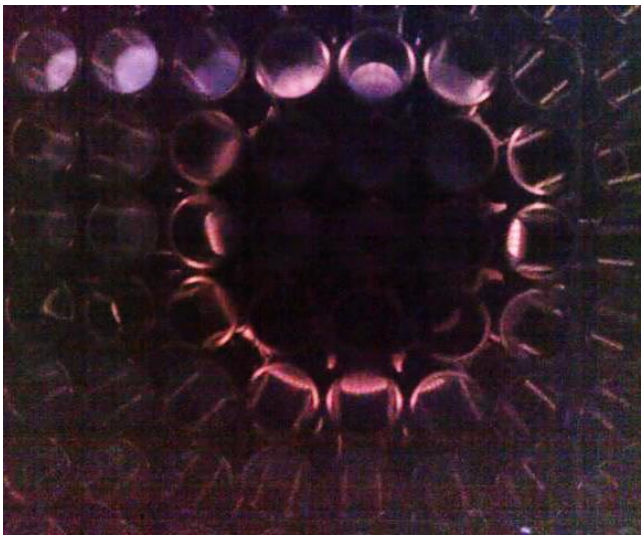

Figure 7.23: Fluorescence image of the black 96-well plate recorded from the XS camera using ICG fluorescence source with 800nm LP filter. Images were taken at a distance of 90 mm, with an integration time of 60 sec.

The resultant images show that the fluorescence imaging system again could not be quantified successfully using the black 96-well plate. The reflection of the LED ring from the surface of the plate interfered with the image of the ICG fluorescence source making quantification extremely difficult. A possible way to avoid the reflection is to use a diffuser in front of the LED ring. This will be taken into account in the future work. Also, a sufficiently accurate electronic scale should be used in the future to measure the exact amount of the ICG powder precisely. Furthermore, the availability in the future of laboratory materials such as pipette and tips would improve the accuracy of the volume used for the fluorescence source.

7.3 Dual radio-NIR fluorescent tracers

The main disadvantages of using NIR fluorescence tracer alone in clinical applications is that the detection of the targeted tissue is limited to ~ 5 – 8 mm depth. However, using a dual radio-NIR fluorescence tracer would increase the probability of detecting deeper abnormal tissue at 25 mm. As the ability of light penetrating a tissue is limited to a certain depth, due to higher absorption and scattering of light by overlying tissues compared to that of γ-rays (32). Figure 7.24 illustrates the difference in using NIR fluorescence imaging alone and using the dual radio-NIR fluorescence imaging.

7.4 Dual radio-NIR fluorescent camera

Our Hybrid Gamma Camera (HGC) (69) has been adapted to be used as a novel hand-held hybrid NIR-gamma small field of view camera. A modified XS camera replaced the optical camera to allow imaging in the infrared. The fluorescence camera was fitted with an 850 nm (100 nm FWHM) bandpass filter and aligned to provide the same field of view as the HGC. Also, an off-the-shelf LED ring with a spectrum extending to the necessary excitation wavelength which is 740 nm (30 nm FWHM) was fixed to the front of the camera (see Figure 7.25).

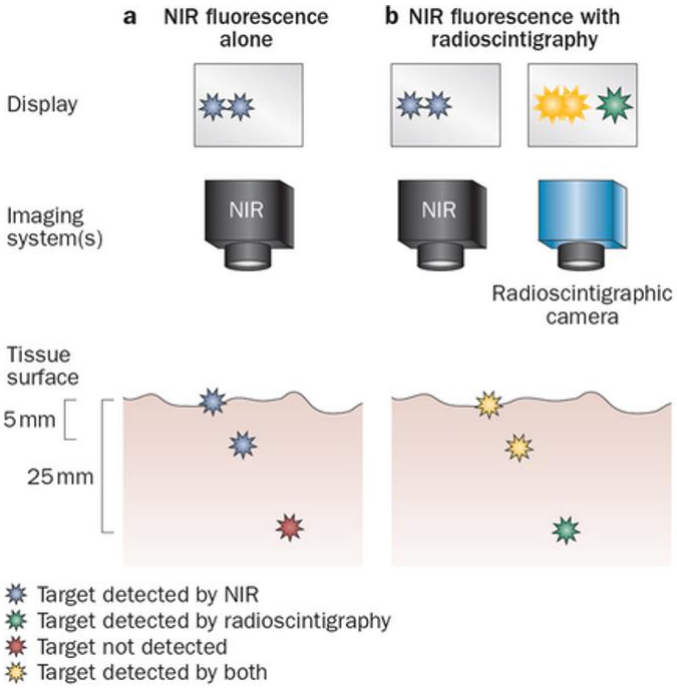

Figure 7.24: Comparison of NIR fluorescence imaging alone and dual radio-NIR fluorescence imaging. Image adapted from Image-guided cancer surgery using near-infrared fluorescence by Vahrmeijer et al., 2013 (169).

Figure 7.25: Photograph of the novel hand-held hybrid NIR-gamma camera.

7.5 Dual radio-NIR fluorescent imaging

The performance of the fluorescence component of the dual radio-NIR fluorescent camera was quantified in this study for the fluorophores ICG and IRDye800CW including phantom studies and first images from a preclinical pilot study (69).

7.5.1 In vitro

Preliminary in vitro tests were conducted to demonstrate the capability of the dual radio-NIR fluorescent camera to be used for fluorescence imaging. A dual radio-NIR fluorescent tracer was used which was ^{111}In-CW800. The ^{111}In radio tracer has gamma emission energies of 254 keV and 171 keV and the emission wavelength of the CW800 NIR fluorescent tracer is 794 nm. The dual radio-NIR fluorescent tracer ^{111}In-CW800 was placed in an Eppendorf container and then positioned in front of the dual radio-NIR fluorescent camera. Experiments were undertaken in a laboratory with the overhead lights turned off. In this test, the Artemis Fluorescence Imaging System (Quest Medical Imaging, Netherlands) was used as an external excitation light source. Both gamma and fluorescent images were obtained. The dual radio-NIR fluorescent camera was placed at 80 mm distance from the source with an integration time of 60 sec. Figure 7.26 shows the images obtained from the in vitro test.

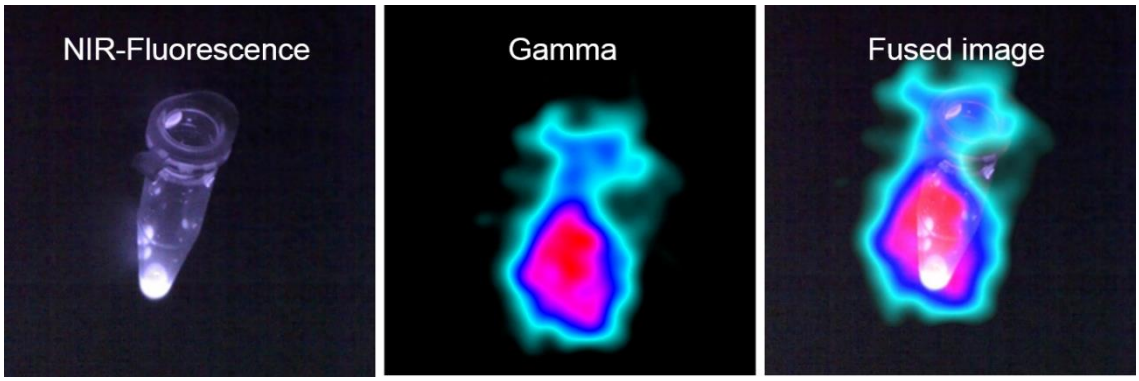

Figure 7.26: (A) Fluorescence image showing NIR-fluorescence source in a small Eppendorf. (B) Gamma image of ^{111}In radio tracer. (C) The fused fluorescence and gamma image.

7.5.2 In vivo

Pre-clinical imaging using the dual radio-NIR fluorescent camera was undertaken at Leiden University Medical Centre (LUMC), Leiden, The Netherlands. This study was a part of an existing trail with ethical approval. A targeted hybrid tracer (cRGD-CW800-TCO + TCO-DOTA-^{111}In) was injected into a mouse with HT29 colorectal cancer xenografts. After sacrifice, a number of tissue samples were excised and imaged with the dual radio-NIR fluorescent camera and the Pearl Impulse Small Animal Imaging System (LI-COR, USA). In this study, the Artemis Fluorescence Imaging System (Quest Medical Imaging, Netherlands) was used as an external excitation light source for the dual radio-NIR fluorescent camera images, (see Figure 7.27). These images have been used for a qualitative comparison between the dual radio-NIR fluorescent camera and a commercially available fluorescence imaging system.

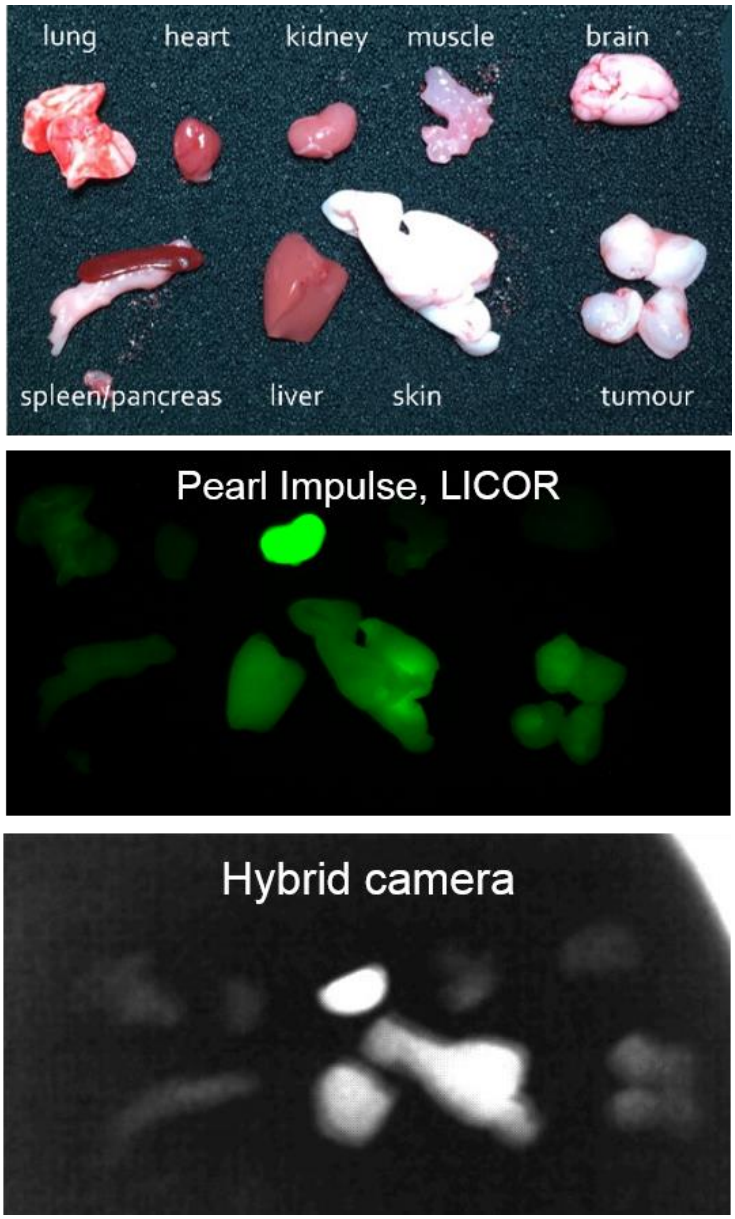

Figure 7.27: (A) Optical image of the excised tissue samples from the mouse with HT29 colorectal cancer xenografts. (B) Fluorescence image recorded by Pearl Impulse Small Animal Imaging System. (C) Fluorescence image obtained by the dual radio-NIR fluorescent camera.

7.6 Results and discussion

7.6.1 In vitro imaging

Figure 7.26 illustrates the resultant images from the in vitro test using the dual radio-NIR fluorescent camera. Figure 7.26A shows the NIR fluorescent image, Figure 7.26B is the gamma image only and Figure 7.26C is the fused fluorescence and gamma image. It is clear from Figure 7.26C, that there was good alignment between the NIR fluorophore from the CW800 fluorescence tracer and the gamma rays emitted from the ^{111}In radio tracer. This indicates the feasibility of the hybrid imaging concept that offers a new imaging technology for clinical applications.

7.6.2 In vivo imaging

Figure 7.27 shows the resultant images from the in vivo test using the Pearl Impulse Small Animal Imaging System (Figure 7.27B) and the dual radio-NIR fluorescent camera (Figure 7.27C). The fluorescence image obtained from the Pearl Impulse Small Animal Imaging System and the fluorescence image obtained from the dual radio-NIR fluorescent camera were analysed and the contrast to noise ratio (CNR) was calculated, see Figure 7.28. A ROIs were drawn by hand based on the fluorescence images for each organ, then both the mean μ values and the standard deviation σ values were measured to calculate the CNR.

The graph in Figure 7.28 illustrates that the Pearl Impulse Small Animal Imaging system has better imaging sensitivity with contrast to noise ratios (CNRs) an order of magnitude higher than the dual radio-NIR fluorescent camera. This is to be expected as the Pearl Impulse images within a light-tight box and can be considered the gold standard for fluorescence imaging. Furthermore, the CNRs of the dual radio-NIR fluorescent camera follow the same trend as the Pearl system. This means that the dual radio-NIR fluorescent camera has a good imaging sensitivity although the effect of a high noise level from the background.

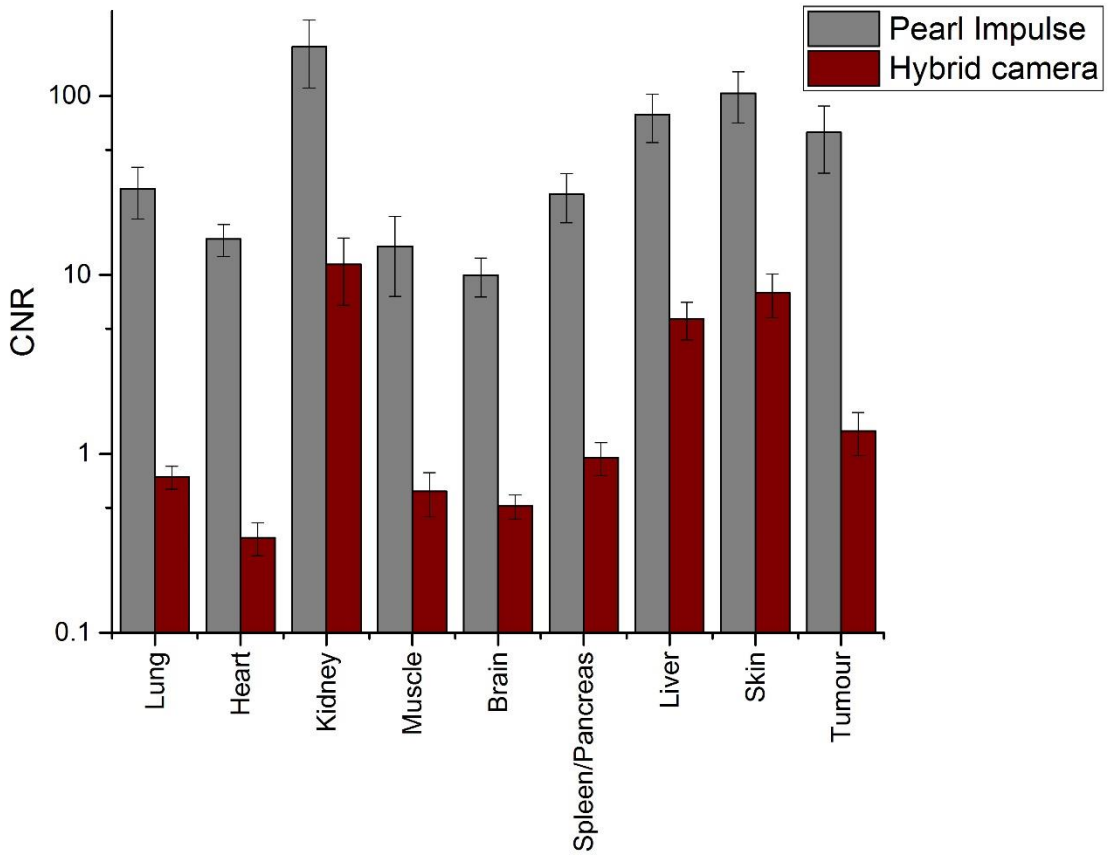

Figure 7.28: Contrast to noise ratio (CNR) graph of the removed mouse organ using Pearl Impulse Small Animal Imaging System (grey) and the dual radio-NIR fluorescent camera (red).

7.7 Conclusion

The initial investigation of the fluorescence imaging system along with the first quantitative performance measurements using the fluorescence system with both NIR CP and XS cameras have been successfully carried out. The results show that the fluorescence system has excellent levels of spatial resolution. These initial results encourage us to carry out further in depth experimental tests.

The dual radio-NIR fluorescent camera has been shown to successfully image the dual NIR-gamma tracer. The sensitivity of the camera to NIR-fluorescence is less than that

seen with a commercially available camera (i.e. Pearl Impulse Small Animal Imaging System). The ability to simultaneously image gamma and NIR-fluorescence in a portable system is believed to be unique. With further development, this camera could be used intraoperatively, offering the benefits of high resolution surface NIR fluorescence imaging and the depth penetration of gamma imaging in a single imaging system.

Chapter 8

Summary, conclusion and future work

8.1 Summary and conclusion

The key to the successful development of diagnostic nuclear medicine procedures is that they must improve the diagnosis efficacy of diseases. In this thesis the development of SFOV gamma cameras has been discussed. In particular, this work investigated the transition of the Hybrid Gamma Camera (HGC) from laboratory towards clinical applications.

The available quantitative tests for assessing the performance characteristics of medical gamma cameras are mainly designed and applicable for standard LFOV gamma cameras. To fully understand the specification of the SFOV hybrid gamma camera, IPEM protocols have been modified and evaluated to test the performance of the HGC.

The fundamental design of the HGC has been described, it is a scintillator-based gamma camera, that utilises an BI-EMCCD coupled to a columnar CsI:TI scintillator. Either a 0.5 mm or 1.0 mm diameter pinhole collimator can be fitted to the camera. The hybrid

system, composed of a gamma camera co-aligned with an optical camera was shown to offer superior spatial resolution, compared to a standard gamma camera.

The capability of the HGC was assessed quantitatively by phantom studies. Various anthropomorphic bespoke phantoms were designed and constructed at both the SRC laboratory and at the University of Nottingham. The manufactured phantoms simulated different small organs in the human body which are frequently diagnosed in the nuclear medicine department.

The current stage of development of the HGC is the introduction of the system into clinical applications. A clinical trial was undertaken at Queen's Medical Centre, Nottingham University Hospitals NHS Trust aiming to investigate the suitability of the hybrid system for use with clinical patients.

In this thesis, the characterisation of the HGC has been performed using two thicknesses of columnar CsI:TI (i.e. 600 µm and 1500 µm) scintillator. The protocols applied followed the IPEM standards include: spatial resolution (both intrinsic and extrinsic), intrinsic spatial uniformity, intrinsic spatial sensitivity and count rate capability. A comparison between two scintillator thicknesses has been made for small field of view gamma camera imaging, to investigate the effects of scintillator thickness on the listed characteristics. The results indicate that the HGC has better spatial resolution when using the thinner 600 µm thick CsI:TI scintillator. However, the thicker CsI:TI scintillator (i.e. 1500 µm) can give gamma images that are more uniform, more sensitive and have higher count rate capability.

Also, the performance characterisation of the HGC has been investigated using 1500 µm thick pixelated GOS scintillator and a transparent inorganic $CdWO_4$ scintillator. In the case of GOS scintillator it was fitted to the HGC twice; with and without optical grease. The $CdWO_4$ scintillator was coupled to the HGC without optical grease. When coupling the 1500 µm thick GOS scintillator to the CCD with and without using optical grease there was no significant difference in the results. While the $CdWO_4$ scintillator results were problematic and could not be compared to the other scintillators. This is due to the prototype $CdWO_4$ scintillator not being of sufficient quality for measuring the performance of the HGC.

Clearly, when comparing the performance of the HGC using both 1500 µm thick CsI:TI and GOS scintillators the results indicate that the HGC has significantly better spatial resolution and higher count rate capability when using the CsI:TI columnar scintillator. However, the HGC is more sensitive when using the pixelated GOS scintillator.

One of the valuable key parameters in developing hybrid gamma cameras for diagnostic nuclear medicine procedures is choosing the suitable scintillator with a specific structure. For the current diagnostic nuclear medical application of the HGC where spatial resolution is a priority, the columnar CsI:TI scintillator has significant advantages over the pixelated GOS scintillator.

Overall, the measured characteristics of the HGC applied to determine the suitability of the hybrid system during surgical theatre settings. The results indicate that it may have advantages for use in a range of healthcare applications such as small organ imaging and surgical investigation.

The second topic discussed in this thesis is the comparison of the performance of CdTe semiconductor detectors; the XRI-UNO system and HEXITEC detector to investigate their usefulness and suitability for nuclear medical imaging. The comparison was partially successful although it was difficult to make a full comparison between the XRI-UNO CdTe detector and the HGC in such areas as energy resolution due to the limitations of the XRI-UNO. Also, a time limitation existed as the detector was available for short period of time only.

Comparing the XRI-UNO CdTe detector to that of the HGC showed that the XRI-UNO CdTe detector is superior in areas such as intrinsic resolution and count rate capability than the HGC. However, the HGC is better in areas such as sensitivity, system spatial resolution and uniformity.

Furthermore, the HGC system is more sensitive than the HEXITEC detector. While the uniformity and spatial resolution of the HEXITEC detector are both reasonable for medical imaging uses. Further characterisation in areas such as energy resolution need to be performed and then compared to the HGC system.

A novel hand-held hybrid NIR-gamma small field of view camera has been described. The components of the imaging system: optical filters, LED excitation light and NIR cameras have been tested. Initial experimental investigations have been carried out to understand the most suitable way of preparing the fluorescence sources for both ICG and the IRDye 800CW. Furthermore, both in vitro and vivo tests have been performed that showed that the dual radio-NIR fluorescence imaging system is capable of producing both gamma, NIR and combined gamma-NIR images. The initial pre-clinical images demonstrated proof of principle that the system could be adapted for fluorescence imaging.

8.2 Future work

This area of research has several opportunities to be considered and improved to make the system a genuine diagnostic medical tool. As the work done in this thesis had tested different areas, the suggested future work has been classified into four categories: HGC system, HEXITEC detector, dual radio-NIR fluorescence imaging modality and small animal imaging.

8.2.1 HGC system: further development

I. Depth estimation

In order to develop the HGC system, its concept can be extended to a multimodal detector design offering both stereoscopic images and depth estimation of radioactive sources within human body. Estimation of the depth of the abnormal tissues could help the surgeon to locate the exact location of the tumour offering better and accurate diagnosis and then a treatment plan for tumour resection. Preliminary tests have been conducted by Lees et al. (60, 69) reporting that the depth estimation is geometrically possible when using a two separated HGC systems. In this case development of the HGC to fulfil the depth estimation requires designing of new compact camera head capable to include multiple detectors.

II. Clinical applications

Further work in clinical studies need to be carried out to gather more clinical cases to increase the number of patient images. Thus, physicians can have clinical based evidence for the suitability of the HGC system in small organ imaging. At the time of writing, a contemporary clinical trial is on-going (HRA reference number: 17/YH/0041) at both Queen's Medical Centre, Nottingham University Hospitals NHS Trust and Nottingham City Hospital to assess the clinical performance of the HGC system in an extended range of nuclear medical procedures. A wide range of different clinical investigations has been assessed so far, these include renal scintigraphy, localisation of sentinel lymph node in patients with melanoma and ectopic parathyroid adenoma imaging, in addition to thyroid imaging and lymphoscintigraphy scan. Also, further patient imaging studies should be conducted using different radioactive materials other than ^{99m}Tc for example; ^{125}I, ^{131}I, ^{111}In and ^{75}Se.

Furthermore, further collaborations with the surgeons need to be undertaken. In order to introduce the hybrid camera into a real surgical scenarios specifically in breast cancer surgery for sentinel lymph node biopsy.

8.2.2 HEXITEC detectors

The HEXITEC software can record images in two formats; (.hxt files) these are pre-thresholded and measure only data from single pixel events. In contrast, (.bin files) record raw data from all pixels in all frames. The performance characteristics in this thesis were measured using the (.hxt files) which were sufficient to obtain the results. Further work is need to investigate charge spreading using the (.bin files) format.

Also, a full performance characterisation of the HEXITEC detector need to be obtained using the Cadmium Zinc Telluride (CZT) detector to compare it with the currently used CdTe detector.

At the time of writing, the HEXITEC detector is being tested in parallel with the HGC in a collaboration with Leicester Royal Infirmary (LRI) to investigate the suitability of the HEXITEC detector for medical imaging at high energies. Count rate capability (CRC) measurements are under inspection using the ^{131}Iodine (^{131}I) radioactive capsule source. ^{131}I is the radioactive material used for thyroid treatment in the nuclear medicine department. It has a gamma energy of 364 keV with a half-life of 8 days. Once the CRC measurements are complete, further plan with the HEXITEC detector and the HGC is to measure both the extrinsic spatial resolution and extrinsic spatial sensitivity of the detector using ^{131}I solution. The main reason for testing the ^{131}I is that because once the patients are administered with a set activity of ^{131}I, the individual assessments of different uptake is usually done by LFOV gamma cameras. However, some hospitals are facing difficulties in performing dosimetry assessment. This could be due to lack of the availability of LFOV gamma system, or the high cost of imaging every patient. So, the aim of this work is to investigate the capability of the SFOV hybrid gamma camera in measuring the uptake of dosimetry instead of LFOV gamma cameras.

8.2.3 Fluorescence development

Improvement of the HGC system to be a novel dual radio-NIR fluorescence imaging camera is still on going. Further laboratory simulations need to be carried out in addition to the pre-clinical studies. At the time of writing, a new LED ring with a typical peak wavelength of 780 nm (100 nm FWHM) has been designed and built at SRC laboratory. The new LED ring was designed to avoid the reflection faced during the experiment of the performance of the fluorescence imaging using 96-well plate. Also, the availability of a suitable diffuser infront of the LED ring could decrease the reflection. A number of laboratory materials such as pipette and tips have been sourced, the use of those materials allows calculation of accurate concentrations of the fluorescence sources. Also, a new NIR camera should be identified to replace the modified XS camera to get better image resolution. Furthermore, as the currently available clinical use of hybrid gamma-NIR fluorescence has so far been limited to the use of ICG as the fluorescence source due to its licence status, further indepth investigations need to be undertaken

using the IRDye 800CW as it has recently been licensed for use in clinical trials by FDA, USA and EMA, Europe.

8.2.4 Small animal imaging

A three dimensional (3D)-printed mouse phantom was designed and manufactured at SRC, University of Leicester. The phantom was developed to simulate the anatomy of the mouse to test the performance of the dual system in pre-clinical imaging. A mouse skeleton phantom was designed and developed at SRC too. The skeleton phantom was manufactured to simulate the anatomy of the typical mouse skeleton to acquire gamma image for bone scan. Future work need to use these mouse phantoms to investigate the ability of the system to produce gamma, NIR and combined gamma-NIR images.

Appendix A

Comparison of performance characteristics for HGC using CsI:TI, GOS and CdWO4 scintillators

In this appendix, Table 5.20 – which compares the performance characteristics for HGC with a 600 μm and 1500 μm thick CsI:TI, a 1500 μm thick GOS and $CdWO_4$ scintillators – is reproduced at a larger size.

Scintillators			CsI:Tl		GOS		$CdWO_4$
Parameters			600 µm	1500 µm	No optical grease	With optical grease	
Intrinsic spatial resolution		FWHM (µm)	170±12	230±25	1090±200	984±320	1059±305
		FWTM (µm)	300±20	468±23	1984±280	1793±150	2091±202
Extrinsic spatial resolution	No Perspex	FWHM (mm)	NA	1.8±0.03	1.97±0.34	1.90±0.33	3.36±1.06
		FWTM (mm)	NA	3.3±0.05	3.75±0.77	3.45±0.66	6.02±1.76
	Including Perspex	FWHM (mm)	1.8±0.13	2.02±0.09	2.13±0.46	2.05±0.45	4.86±1.43
		FWTM (mm)	3.25±0.26	3.6±0.12	4.02±0.89	3.9±0.88	8.74±2.59
Intrinsic uniformity		CoV (%)	25±9	20±15	17±9	13±4	53±8
Intrinsic sensitivity		(%)	19±1	40±3	54±4	53±7	4.9±12
Extrinsic sensitivity	No Perspex	(cps/MBq)	NA	6.6±0.5	18.5±0.3	16.23±0.5	2.36±1.50
	Including Perspex	(cps/MBq)	0.8±0.1	3.3±0.5	8.1±0.3	6.6±0.4	1.23±1.08
Count rate capability	Maximum recorded count rate (cps)		1200±200	3537±200	3170±30	2823±50	4528±300

Bibliography

1. Maher K ea. Basic Physics of Nuclear Medicine. Germany: Wikibooks; 2006.
2. Jacene HG, S. Patel, H. Wahl, R. Ziessman, H. Advantages of Hybrid SPECT/CT vs SPECT Alone. The Open Medical Imaging Journal. 2008;2:67-9.
3. Morton DL, Wen D, Wong JH, et al. Technical details of intraoperative lymphatic mapping for early stage melanoma. Archives of Surgery. 1992;127(4):392-9.
4. Giuliano AE, Jones RC, Brennan M, Statman R. Sentinel lymphadenectomy in breast cancer. Journal of Clinical Oncology. 1997;15(6):2345-50.
5. Rietbergen D, Berg N, Leeuwen F, Olmos R. Hybrid techniques for intraoperative sentinel lymph node imaging : early experiences and future prospects. Imaging Med. 2013;5(2):147-59.
6. Marinelli. LD, B G. The concentration of P32 in some superficial tissues of living patients. Radiology. 1942;39:454-63.
7. Low-Beer BVA, Bell HG, McCorkle HJ, Stone RS. Measurement of Radioactive Phosphorus in Breast Tumors in Situ; a Possible Diagnostic Procedure. Radiology. 1946;47(5):492-3.
8. Selverstone B, Sweet WH, Robinson CV. The Clinical Use of Radioactive Phosphorus in the Surgery of Brain Tumors. Annals of Surgery. 1949;130(4):643-50.
9. Harris. CC, Bigelow. RR, Francis. JE, Kelley. GG, PR B. A CsI(Tl) crystal surgical scintillation probe. Nucleanics. 1956;14:102-8.
10. Sarikaya I, Sarikaya A, Reba RC. Gamma probes and their use in tumor detection in colorectal cancer. International seminars in surgical oncology : ISSO. 2008;5:25.
11. Hurwitz SR, Ashburn WL, Green JP, Halpern SE. Clinical Applications of a “Portable” Scintillation Camera. Journal of Nuclear Medicine. 1973;14(8):585-7.
12. Nuclear Medicine. Southern Scientific Limited; 2016.
13. Formiconi AR, Di Martino F, Volterrani D, Passeri A. Study of high energy multihole collimators. IEEE Transactions on Nuclear Science. 2002;49(1):25-30.
14. Jaszczak RJ, Li J, Wang H, Zalutsky MR, Coleman RE. Pinhole collimation for ultra-high-resolution, small field of view SPECT. Physics in medicine and biology. 1994;39(3):425-37.
15. Barber HB, Barrett HH, Wild WJ, Woolfenden JM. Development of Small in-Vivo Imaging Probes for Tumor Detection. IEEE Transactions on Nuclear Science. 1984;31(1):599-604.
16. Hung NM, Joung J, Lee K, Kim Y. Development of correction schemes for a small field of view gamma camera. Biomedical Engineering Letters. 2013;2(4):215-22.
17. Goertzen AL, Thiessen JD, McIntosh B, Simpson MJ, Schellenberg J, editors. Characterization of a handheld gamma camera for intraoperative use for sentinel lymph node biopsy. 2013 IEEE Nuclear Science Symposium and Medical Imaging Conference (2013 NSS/MIC); 2013 27 Oct.-2 Nov. 2013.
18. Mathelin C, Salvador S, Huss D, Guyonnet JL. Precise Localization of Sentinel Lymph Nodes and Estimation of Their Depth Using a Prototype Intraoperative Mini-Camera in Patients with Breast Cancer. Journal of Nuclear Medicine. 2007;48(4):623-9.

19. Lees JE, Bugby SL, Bhatia BS, Jambi LK, Alqahtani MS, McKnight WR, et al. A small field of view camera for hybrid gamma and optical imaging. Journal of Instrumentation. 2014;9(12):C12020-C.
20. Aarsvod JN, Greene CM, Mintzer RA, Grant SF, Styblo TM, Alazraki NP, et al. Intraoperative gamma imaging of axillary sentinel lymph nodes in breast cancer patients. Physica Medica. 2006;21:76-9.
21. Tsuchimochi M, Hayama K. Intraoperative gamma cameras for radioguided surgery: technical characteristics, performance parameters, and clinical applications. Physica medica : PM : an international journal devoted to the applications of physics to medicine and biology : official journal of the Italian Association of Biomedical Physics. 2013;29(2):126-38.
22. Olcott P, Pratx G, Johnson D, Mittra E, Niederkohr R, Levin CS. Clinical evaluation of a novel intraoperative handheld gamma camera for sentinel lymph node biopsy. Physica medica : PM : an international journal devoted to the applications of physics to medicine and biology : official journal of the Italian Association of Biomedical Physics. 2014;30(3):340-5.
23. Perkins AC, Ng AH, Lees JE. Small field of view gamma cameras and intraoperative applications. Gamma cameras for interventional and intraoperative imaging. 1 ed: CRC Press; 2016.
24. Johansen, Anton G, Jackson, Peter. Radioisotope Gauges for Industrial Process Measurements. Chichester, UK: John Wiley & Sons, Incorporated; 2004.
25. Knoll GF. Radiation Detection and Measurement. 3rd ed. The University of Michigan: Wiley; 2000. 802 p.
26. Eisen Y, Shor A, Mardor I. CdTe and CdZnTe xray and gamma ray detectors for imaging systems. Transaction on Nuclear Science. 2004;51(3):1191-8.
27. Yin S, Tumer T, Maeding D, Mainprize J, Mawdsley G, Yaffe M, et al. Direct conversion CdZnTe and CdTe detectors for digital mammography. IEEE Transactions on Nuclear Science. 2002;49(1):176-81.
28. Kalender WA, Beister M, Boone JM, Kolditz D, Vollmar SV, Weigel MC. High-resolution spiral CT of the breast at very low dose: concept and feasibility considerations. European radiology. 2012;22(1):1-8.
29. Kalender WA, Kolditz D, Steiding C, Ruth V, Luck F, Rossler AC, et al. Technical feasibility proof for high-resolution low-dose photon-counting CT of the breast. European radiology. 2017;27(3):1081-6.
30. Russo P, Curion AS, Mettivier G, Esposito M, Aurilio M, Caracò C, et al. Evaluation of a CdTe semiconductor based compact gamma camera for sentinel lymph node imaging. Medical Physics. 2011;38(3):1547.
31. Acharya G, Mitra AK, Cholkar K. Chapter 10 - Nanosystems for Diagnostic Imaging, Biodetectors, and Biosensors. Emerging Nanotechnologies for Diagnostics, Drug Delivery and Medical Devices. Boston: Elsevier; 2017. p. 217-48.
32. Jacques SL. Corrigendum: Optical properties of biological tissues: a review. Physics in medicine and biology. 2013;58(14):5007-8.
33. Ralf B. Schulz, Semmler W. Fundamentals of Optical Imaging. Handbook of Experimental Pharmacology. 2008.
34. Prout D, Silverman R, Chatziioannou A, editors. Detector concept for OPET, a combined PET and optical imaging system. 2003 IEEE Nuclear Science Symposium Conference Record (IEEE Cat No03CH37515); 2003 19-25 Oct. 2003.

35. Prout D, Silverman R, Chatziioannou A, editors. Readout of the optical PET, (OPET) detector. 2003 IEEE Nuclear Science Symposium Conference Record (IEEE Cat No03CH37515); 2003 19-25 Oct. 2003.
36. Li C, Wang G, Qi J, Cherry SR. Three-Dimensional Fluorescence Optical Tomography in Small Animal Imaging using Simultaneous Positron Emission Tomography Priors. Optics letters. 2009;34(19):2933-5.
37. Li C, Yang Y, Mitchell GS, Cherry SR. Simultaneous PET and Multispectral 3-Dimensional Fluorescence Optical Tomography Imaging System. Journal of nuclear medicine : official publication, Society of Nuclear Medicine. 2011;52(8):1268-75.
38. Wang G, Li C, Cherry SR, Qi J, editors. Statistical image reconstruction for hybrid fluorescence optical tomography and positron emission tomography. 2011 IEEE International Symposium on Biomedical Imaging: From Nano to Macro; 2011 30 March-2 April 2011.
39. Hendee WR, Ritenour ER. Medical Imaging Physics. 4 ed. New York: John Wiley & Sons; 2003.
40. M.J. Berger, J.H. Hubbell, S.M. Seltzer, J. Chang, J.S. Coursey, R. Sukumar, et al. XCOM: Photon cross section database: NIST Standard reference database; 1998. http://www.physics.nist.gov/PhysRefData/Xcom/html/xcom1.html].
41. Martin JE. Interactions of Radiation with Matter. Physics for Radiation Protection: Wiley; 2013.
42. Cherry SR, Sorenson JA, Phelps ME. Interaction of Radiation with Matter. 2012:63-85.
43. Cherry SR, Sorenson JA, Phelps ME. Radiation Detectors. 2012:87-106.
44. Lilley J. Nuclear Physics: Principles and Applications: Wiley; 2001. 412 p.
45. Gobian S. CsI(Tl) and (Na) data sheet. Saint Gobian Ceramics & Plastics. 2007.
46. Blahuta S, Viana B, Bessière A, Mattmann E, LaCourse B. Luminescence quenching processes in Gd2O2S:Pr3+,Ce3+ scintillating ceramics. Optical Materials. 2011;33(10):1514-8.
47. Gridin S, Belsky A, Moszynski M, Syntfeld-Kazuch A, Shiran N, Gektin A. Scintillation properties of CsI:In single crystals. Nuclear Instruments and Methods in Physics Research Section A: Accelerators, Spectrometers, Detectors and Associated Equipment. 2014;761:13-8.
48. Bugby SL, Lees JE, Ng AH, Alqahtani MS, Perkins AC. Investigation of an SFOV hybrid gamma camera for thyroid imaging. Physica medica : PM : an international journal devoted to the applications of physics to medicine and biology : official journal of the Italian Association of Biomedical Physics. 2016;32(1):290-6.
49. Siman W, Kappadath SC. Performance characteristics of a new pixelated portable gamma camera. Med Phys. 2012;39(6):3435-44.
50. Stuart R. Miller, Valeriy Gaysinskiy, Irina Shestakova, Nagarkar VV. Recent advances in columnar CsI(Tl) scintillator screens. Proce SPIE 5923. 2005.
51. Exelis. IDL reference guide. Exelis Visual Information Solutions; 2010.
52. Han L, Miller BW, Barber HB, Nagarkar VV, Furenlid LR. A New Columnar CsI(Tl) Scintillator for iQID detectors. Proceedings of SPIE--the International Society for Optical Engineering. 2014;9214:92140D.
53. GresKovish CD, S. Ceramic Scintillators. Annual Reviews of Materials Science. 1997;27:69-88.

54. Lawson RS. The Gamma Camera: A Comprehensive Guide. York: IPEM Institute of Physics and Engineering in Medicine; 2013.
55. Felber P. Charge-Coupled Devices. Illinois Institute of Technology. 2002.
56. Lesser M. Charge coupled device (CCD) image sensors. 2014:78-97.
57. Eisen Y, Shor A, Gilath C, Tsabarim M, Chouraqui P, Hellman C, et al. A gamma camera based on CdTe detectors. Nuclear Inst and Methods in Physics Research. 1996;380(1):474 - 8.
58. Darambara DG. Detector design for small field of view nuclear cameras. Gamma cameras for interventional and intraoperative imaging: CRC Press; 2016.
59. Darambara DG, Todd-Pokropek A. Solid state detectors in nuclear medicine. The quarterly journal of nuclear medicine : official publication of the Italian Association of Nuclear Medicine (AIMN) [and] the International Association of Radiopharmacology (IAR). 2002;46(1):3-7.
60. Lees JE, Bassford DJ, Blake OE, Blackshaw PE, Perkins AC. A Hybrid Camera for simultaneous imaging of gamma and optical photons. Journal of Instrumentation. 2012;7(06):P06009-P.
61. CCD97-00. Back illuminated 2-phase IMO series peltier pack electron multiplying CCD sensor. e2v technologies limited. 2011.
62. Lees JE, Bassford DJ, Blake OE, Blackshaw PE, Perkins AC. A high resolution Small Field Of View (SFOV) gamma camera: a columnar scintillator coated CCD imager for medical applications. Journal of Instrumentation. 2011;6(12):C12033-C.
63. Bugby SL. Development of a hybrid portable medical gamma camera: University of Leicester; 2015.
64. Bugby SL, Lees JE, Bhatia BS, Perkins AC. Characterisation of a high resolution small field of view portable gamma camera. Physica medica : PM : an international journal devoted to the applications of physics to medicine and biology : official journal of the Italian Association of Biomedical Physics. 2014;30(3):331-9.
65. Bhatia BS, Bugby SL, Lees JE, Perkins AC. A scheme for assessing the performance characteristics of small field-of-view gamma cameras. Physica medica : PM : an international journal devoted to the applications of physics to medicine and biology : official journal of the Italian Association of Biomedical Physics. 2015;31(1):98-103.
66. Ng AH, Clay D, Blackshaw PE, Bugby SL, Morgan PS, Lees JE, et al. Assessment of the performance of small field of view gamma cameras for sentinel node imaging. Nuclear medicine communications. 2015;36(11):1134-42.
67. Alqahtani MS, Lees JE, Bugby SL, Jambi LK, Perkins AC. Lymphoscintigraphic imaging study for quantitative evaluation of a small field of view (SFOV) gamma camera. Journal of Instrumentation. 2015;10(07):P07011-P.
68. Alqahtani MS, Lees JE, Bugby SL, Jambi LK, Perkins AC. Quantitative investigation of a novel small field of view hybrid gamma camera (HGC) capability for sentinel lymph node detection. The British Journal of Radiology. 2016(89):20160435.
69. Lees JE, Bugby SL, Alqahtani MS, Jambi LK, Dawood NS, McKnight WR, et al. A Multimodality Hybrid Gamma-Optical Camera for Intraoperative Imaging. Sensors. 2017;17(3).
70. Alqahtani MS, Lees JE, Bugby SL, Samara-Ratna P, Ng AH, Perkins AC. Design and implementation of a prototype head and neck phantom for the performance evaluation of gamma imaging systems. EJNMMI Phys. 2017;4(1):19.

71. Ng AH, Blackshaw PE, Alqahtani MS, Jambi LK, Bugby SL, Lees JE, et al. A novel compact small field of view hybrid gamma camera: first clinical results. Nuclear medicine communications. 2017;38(9).
72. L.A. Amanat, T.E. Hilditch, KWOK CS. Lacrimal scintigraphy II Its role in the diagnosis of epiphora. British Journal of Opthalmology. 1983;67:720-8.
73. James DJM. Lacrimal Scintigraphy. In: Society BNM, editor. 2013.
74. Lees JE, Fraser GW, Keay A, Bassford D, Ott R, Ryder W. The high resolution gamma imager (HRGI): a CCD based camera for medical imaging. Nuclear Instruments and Methods in Physics Research Section A: Accelerators, Spectrometers, Detectors and Associated Equipment. 2003;513(1-2):23-6.
75. Lees JE, Bassford D, Fraser GW, Monk D, Early M, Ott RJ, et al. Investigation of scintillator coated CCDs for medical imaging. IEEE Transactions on Nuclear Science. 2006;53(1):9-13.
76. Rova A, Celler A, Hamarneh G. Development of NEMA-based software for gamma camera quality control. J Digit Imaging. 2008;21(2):243-55.
77. NEMA. Performance Measurements of Scintillatin Gamma Cameras. National Electrical Manufacturers Association. 2001(NU 1-2001).
78. Demirkaya O, Almazrou R. Performance Test Data Analysis of Scintillation Cameras. IEEE Transactions on Nuclear Science. 2007;54(5).
79. Gerd Muehllehner, Wake RH, Sano R. Standards for Performance Measurements in Scintillation Cameras. J Nucl Med. 1981;22:72-7.
80. Mettler FA, Guiberteau MJ. Instrumentation and Quality Control. 2012:23-69.
81. Cecchin D, Poggiali D, Riccardi L, Turco P, Bui F, De Marchi S. Analytical and experimental FWHM of a gamma camera: theoretical and practical issues. PeerJ. 2015;3:e722.
82. Cherry SR, Sorenson JA, Phelps ME. The Gamma Camera. 2012:209-31.
83. John Vesel, Petrillo M. Improved Gamma Camera Performance using Event Positioning Method Based on Distance Dependent Weighting. IEEE Transactions on Nuclear Science Conference Record. 2005;5:2445-8.
84. Gerralt A. De Vree, Albert H. Westra, IAn Moody, Frans van der Have, Kees M. Ligtvoet, Beekman FJ. Photon-counting gamma camera based on an electron-multiplying CCD. IEEE Transactions on Nuclear Science. 2005;52(3):580-8.
85. Lees JE, Bassford DJ, Blackshaw PE, Perkins AC. Design and use of mini-phantoms for high resolution planar gamma cameras. Appl Radiat Isot. 2010;68(12):2448-51.
86. Brendan Vastenhouw, Beekman F. Submillimeter total-body murine imaging with U-SPECT-I. Journal of Nuclear Medicine. 2007;48(3):487-93.
87. Smith SW. Special Imaging Techniques. The Scientis and Engineer's Guide to Digital Signal Processing: Newnes; 2002.
88. Ferreira CC, Ximenes RE, Garcia CAB, Vieira JW, Maia AF. Total mass attenuation coefficient evaluation of ten materials commonly used to simulate human tissue. Journal of Physics: Conference Series. 2010;249:012029.
89. Saha G. Performance Parameters of Gamma Cameras. Physics and Radiobiology of Nuclear Medicine: Springer New York; 2006. p. 118-38.
90. Hine GJ, Brownell GL. Radiation Dosimetry: Elsevier; 2013.
91. IPEM. Quality control of gamma camera system. York: Institute of Physics and Engineering in Medicine, 2003 Contract No.: 86.

92. Zanzonico P. Routine quality control of clinical nuclear medicine instrumentation: a brief review. J Nucl Med. 2008;49(7):1114-31.
93. Silosky MS. Characterisation of the count rate performance and evaluation of the effects of high count rates on modern gamma cameras. UT GSBS Dissertation and Theses. 2012:304.
94. OriginLabCorporation. OriginLab [cited 2014 November]. Available from: http://www.originlab.com/doc/.
95. Cherry SR, Sorenson JA, Pheleps ME. Physics in Nuclear Medicine. 3rd ed: Saunders; 2003.
96. Paix D. Pinhole imaging of gamma rays. Physics in Medicine & Biology. 1967;12(4):489.
97. Roberto Accorsi, Metzler S. Analytic Determiniation of the Resolution-Equivalent Effective Diameter of a Pinhole Collimator. IEEE Transactions on Medical Imaging. 2004;23(6):750-63.
98. Metzler SD, Accorsi R. Resolution- versus sensitivity-effective diameter in pinhole collimation: experimental verification. Physics in medicine and biology. 2005;50(21):5005-17.
99. Alsótőrőkvész u. Nucline cardio-C data sheet. Hungary: Mediso Medical Imaging Systems; 2004.
100. IAEA. Guided Inraoperative Scintigraphic Tumour Trgeting (GOSTT) Implementing Advanced Hybrid Molecular Imaging and Non-imaging Probes for Advanced Cancer Manegement. IAEA Human Health Series. 2014(29).
101. Hall DJ, Holland A, Soman M. The influence of electron multiplication and internal X-ray fluorescence on the performance of a scintillator-based gamma camera. Nuclear Instruments and Methods in Physics Research Section A: Accelerators, Spectrometers, Detectors and Associated Equipment. 2012;678:64-77.
102. X-Ray Scintillator Technical Information. Hammamatsu Photonics, Electron Tube Division. 2010.
103. GOS pixellated scintillator. Toshiba Materials Co Ltd, Toshiba Corporation, Yokohama works, 8, Shinsugita-cho, Isogo-ku, Yokohama City.
104. Richards S. Laser Micromachining of Cadmium Tungstate Scintillator for High Energy X-Ray Imaging [PhD Thesis]: University of Surrey; 2015.
105. David J. Hall, Andrew Holland, Smith DR. The use of automatic scale selection to improve the spatial and spectral resolution of a scintillator-coupled EMCCD. Nuclear Inst and Methods in Physics Research. 2009;A(604):207-10.
106. Bugby SL, Jambi LK, Lees JE. A comparison of CsI:Tl and GOS in a scintillator-CCD detector for nuclear medicine imaging. Journal of Instrumentation. 2016;11(09):P09009-P.
107. Capintec I. CRC-55t R-PET Chamber Manual. 2015(9250-0137).
108. Acton PD, Choi SR, Plossl K, Kung HF. Quanitification of dopamine transporters in the mouse brain using ultra-high resolution single-photon emission tomography. European journal of nuclear medicine and molecular imaging. 2002;29.
109. FP D. Design and performance of a multi-pinhole collimation device for small animal imaging with clinical SPECT and SPECT-CT scanners. Physics in medicine and biology. 2008;53.

110. Quian J, Bradley EL, Majewski S, Popov V, Saha MS, MF S. A small-animal imaging system capable of multipinhole circular/helical SPECT and parallel-hole SPECT. Nucl Instrum Methods Phys Res A. 2008;594:102-10.
111. Wilkinson F. CHAPTER 13 - Scintillators. In: Wernick MN, Aarsvold JN, editors. Emission Tomography. San Diego: Academic Press; 2004. p. 229-54.
112. DowCorning. Dow Coring 7 Release Compound. In: Corporation DC, editor. 2013.
113. Beekman FJ, de Vree GA. Photon-counting versus an integrating CCD-based gamma camera: important consequences for spatial resolution. Physics in medicine and biology. 2005;50(12):N109-19.
114. Richards S, Baker MA, Wilson MD, Lohstroh A, Seller P. Femtosecond laser ablation of cadmium tungstate for scintillator arrays. Optics and Lasers in Engineering. 2016;83:116-25.
115. Tsuchimochi M, Sakahara H, Hayama K, Funaki M, Ohno R, Shirahata T, et al. A prototype small CdTe gamma camera for radioguided surgery and other imaging applications. European journal of nuclear medicine and molecular imaging. 2003;30(12):1605-14.
116. Imatek X-R. XRI-UNO/CdTe Manual. In: Eureka E, editor. Barcelon, Spain2012.
117. Jones L, Seller P, Wilson M, Hardie A. HEXITEC ASIC—a pixellated readout chip for CZT detectors. Nuclear Instruments and Methods in Physics Research Section A: Accelerators, Spectrometers, Detectors and Associated Equipment. 2009;604(1-2):34-7.
118. The XRI series UNO & QUATRO. Barcelona, Spain: X-ray Imatek.
119. Iwanczyk JS, Nygard E, Meirav O, Arenson J, Barber WC, Hartsough NE, et al. Photon Counting Energy Dispersive Detector Arrays for X-ray Imaging. IEEE Trans Nucl Sci. 2009;56(3):535-42.
120. Niederlohner D, Nachtrab F, Michel T, Anton G, editors. Using the Medipix2 detector for photon counting computed tomography. IEEE Nuclear Science Symposium Conference Record, 2005; 2005 23-29 Oct. 2005.
121. Dammer J, Frallicciardi PM, Jakubek J, Jakubek M, Pospisil S, Prenerova E, et al. Real-time in-vivo μ-imaging with Medipix2. Nuclear Instruments and Methods in Physics Research Section A: Accelerators, Spectrometers, Detectors and Associated Equipment. 2009;607(1):205-7.
122. Whiting BR, Hoeschen C, Park SE, Kim JG, Hegazy MAA, Cho MH, et al. A flat-field correction method for photon-counting-detector-based micro-CT. 2014;9033:90335N.
123. STFC. Hard X-ray imaging detector. Science and Technology Facilities Council 2015.
124. Wilson MD, Cernik R, Chen H, Hansson C, Iniewski K, Jones LL, et al. Small pixel CZT detector for hard X-ray spectroscopy. Nuclear Instruments and Methods in Physics Research Section A: Accelerators, Spectrometers, Detectors and Associated Equipment. 2011;652(1):158-61.
125. Wilson MD, Seller P, Veale MC, Sellin PJ. Investigation of the small pixel effect in CdZnTe detectors. 2007:1255-9.
126. Wilson MD, Seller P, Hansson C, Cernik R, Marchal J, Xin Z-J, et al. X-ray performance of pixilated CdZnTe detectors. 2008:239-45.
127. Seller P, Bell S, Cernik RJ, Christodoulou C, Egan CK, Gaskin JA, et al. Pixellated Cd(Zn)Te high-energy X-ray instrument. Journal of instrumentation : an IOP and SISSA journal. 2011;6(12).

128. Veale MC, Bell SJ, Jones LL, Seller P, Wilson MD, Allwork C, et al. An ASIC for the Study of Charge Sharing Effects in Small Pixel CdZnTe X-Ray Detectors. IEEE Transactions on Nuclear Science. 2011;58(5):2357-62.
129. Wilson MD, Dummott L, Duarte DD, Green FH, Pani S, Schneider A, et al. A 10 cm × 10 cm CdTe Spectroscopic Imaging Detector based on the HEXITEC ASIC. Journal of Instrumentation. 2015;10(10):P10011-P.
130. Holland AD, Beletic J, Baumgartner WH, Christe SD, Ryan DF, Inglis AR, et al. The HEXITEC hard x-ray pixelated CdTe imager for fast solar observations. 2016;9915:99151D.
131. Eckert&Ziegler. Industrial radiation sources. In: Products EZI, editor. Valencia, USA2008.
132. Abramoff MD, Magalhaes PJ, Ram SJ. Image Processing with ImageJ. Biophotonics International. 2004;11(7):36-42.
133. Ultimate Metals. 46 Larkshall Road, E4 7HZ Chingford London, UK.
134. Cherry SR, Sorenson JA, Phelps ME. Image Quality in Nuclear Medicine. Physics in Nuclear Medicine: Elsevier/Saunders; 2012. p. 233-51.
135. Dickerscheid D, Lavalaye J, Romijn L, Habraken J. CNR analysis and optimisation of breast specific gamma imaging acquisition protocol. EJNMMI research. 2013;3(1):1-9.
136. Rose A. The Visual Process. Vision Human and Electronic. Optical Physics and Engineering. New York - London: Plenum Press; 1974.
137. Mejia J, Galvis-Alonso OY, Castro AAd, Braga J, Leite JP, Simões MV. A clinical gamma camera-based pinhole collimated system for high resolution small animal SPECT imaging. Brazilian Journal of Medical and Biological Research. 2010;43(12):1160-6.
138. Scuffham JW, Wilson MD, Seller P, Veale MC, Sellin PJ, Jacques SDM, et al. A CdTe detector for hyperspectral SPECT imaging. Journal of Instrumentation. 2012;7(08):P08027-P.
139. Cavallini A, Fraboni B, Dusi W, Auricchio N, Chirco P, Zanarini M, et al. Radiation effects on II–VI compound-based detectors. Nuclear Inst and Methods in Physics Research. 2002;476(3):770-8.
140. Strauss LJ, Rae WI. Image quality dependence on image processing software in computed radiography. South African Journal of Radiology. 2012;16(2):44-8.
141. Limousin O. New trends in CdTe and CdZnTe detectors for X- and gamma-ray applications. Nuclear Instruments and Methods in Physics Research Section A: Accelerators, Spectrometers, Detectors and Associated Equipment. 2003;504(1-3):24-37.
142. Sordo SD, Abbene L, Caroli E, Mancini AM, Zappettini A, Ubertini P. Progress in the Development of CdTe and CdZnTe Semiconductor Radiation Detectors for Astrophysical and Medical Applications. Sensors. 2009;9(5):3491-526.
143. Weissleder R, Pittet MJ. Imaging in the era of molecular oncology. Nature. 2008;452:580.
144. Nguyen QT, Tsien RY. Fluorescence-guided surgery with live molecular navigation — a new cutting edge. Nature Reviews Cancer. 2013;13:653.
145. van Dam GM, Themelis G, Crane LMA, Harlaar NJ, Pleijhuis RG, Kelder W, et al. Intraoperative tumor-specific fluorescence imaging in ovarian cancer by folate receptor-α targeting: first in-human results. Nature Medicine. 2011;17:1315.

146. Marshall MV, Rasmussen JC, Tan IC, Aldrich MB, Adams KE, Wang X, et al. Near-Infrared Fluorescence Imaging in Humans with Indocyanine Green: A Review and Update. Open surgical oncology journal. 2010;2(2):12-25.
147. Sylvian Gioux, Hak Soo Choi, Frangioni JV. Image-Guided Surgery using Invisible Near-Infrared Light: Fundamentals of Clinical Translation. Mol Imaging. 2010;9(5):237-55.
148. An FF, Chan M, Kommidi H, Ting R. Dual PET and Near-Infrared Fluorescence Imaging Probes as Tools for Imaging in Oncology. AJR Am J Roentgenol. 2016;207(2):266-73.
149. Ntziachristos V, Bremer C, Weissleder R. Fluorescence imaging with near-infrared light: new technological advances that enable in vivo molecular imaging. European radiology. 2003;13(1):195-208.
150. Sylvian Gioux, Vida Kianzad, Razvan Ciocan, Sunil Gupta, Rafiou Oketokoun, Frangioni J. High-power, computer-controlled, light-emitting diode-based light sources for fluorescence imaging and image-guided surgery. Mol Imaging. 2009;8(3):156-65.
151. Gurtner GC, Jones GE, Neligan PC, Newman MI, Phillips BT, Sacks JM, et al. Intraoperative laser angiography using the SPY system: review of the literature and recommendations for use. Annals of Surgical Innovation and Research. 2013;7:1.
152. De Leeuw F, Breuskin I, Abbaci M, Casiraghi O, Mirghani H, Ben Lakhdar A, et al. Intraoperative Near-infrared Imaging for Parathyroid Gland Identification by Auto-fluorescence: A Feasibility Study. World Journal of Surgery. 2016;40(9):2131-8.
153. Furukawa N, Oi H, Yoshida S, Shigetomi H, Kanayama S, Kobayashi H. The usefulness of photodynamic eye for sentinel lymph node identification in patients with cervical cancer. Tumori Journal. 2015;96(6):936-40.
154. Troyan SL, Kianzad V, Gibbs-Strauss SL, Gioux S, Matsui A, Oketokoun R, et al. The FLARE™ Intraoperative Near-Infrared Fluorescence Imaging System: A First-in-Human Clinical Trial in Breast Cancer Sentinel Lymph Node Mapping. Annals of surgical oncology. 2009;16(10):2943-52.
155. LI-COR B. Pearl Impulse Small Animal Imaging System. In: Inc L-C, editor. 2011.
156. van Driel PB, van de Giessen M, Boonstra MC, Snoeks TJ, Keereweer S, Oliveira S, et al. Characterization and evaluation of the artemis camera for fluorescence-guided cancer surgery. Molecular imaging and biology : MIB : the official publication of the Academy of Molecular Imaging. 2015;17(3):413-23.
157. Schaafsma BE, Mieog JSD, Hutteman M, van der Vorst JR, Kuppen PJK, Löwik C, et al. The clinical use of indocyanine green as a near-infrared fluorescent contrast agent for image-guided oncologic surgery. Journal of surgical oncology. 2011;104(3):323-32.
158. Rosenthal EL, Warram JM, de Boer E, Chung TK, Korb ML, Brandwein-Gensler M, et al. Safety and Tumor Specificity of Cetuximab-IRDye800 for Surgical Navigation in Head and Neck Cancer. Clinical cancer research : an official journal of the American Association for Cancer Research. 2015;21(16):3658-66.
159. Bioquest A. Spectrum Viewer [cited 2017 Nov]. Available from: https://www.aatbio.com/spectrum/.
160. Bugby SL, Lees JE, Perkins AC. Hybrid intraoperative imaging techniques in radioguided surgery: present clinical applications and future outlook. Clinical and Translational Imaging. 2017.
161. Zinn KR, Korb M, Samuel S, Warram JM, Dion D, Killingsworth C, et al. IND-directed safety and biodistribution study of intravenously injected cetuximab-IRDye800

in cynomolgus macaques. Molecular imaging and biology : MIB : the official publication of the Academy of Molecular Imaging. 2015;17(1):49-57.
162. Marshall MV, Draney D, Sevick-Muraca EM, Olive DM. Single-dose intravenous toxicity study of IRDye 800CW in Sprague-Dawley rats. Molecular imaging and biology : MIB : the official publication of the Academy of Molecular Imaging. 2010;12(6):583-94.
163. Alford R, Simpson HM, Duberman J, Hill GC, Ogawa M, Regino C, et al. Toxicity of Organic Fluorophores Used in Molecular Imaging: Literature Review. Molecular Imaging. 2009;8(6):7290.2009.00031.
164. IDSimaging. UI-3240CP-NIR-GL. In: Systems IID, editor. Germany.
165. Orna MV. Light and Color in Nature and Art, by Samuel J. Williamson and Herman Z. Cummins, John Wiley and Sons, New York, 1983, 488 pp. Price: $30.95. Color Research & Application. 1985;10(2):123-4.
166. PIXELTEQ. Optical Filter Shop Florida, USA: PIXELTEQ; 2015.
167. AndoverCorp. Optical Coating and Filters: Quality you can trust. In: Corporation A, editor. US2016.
168. Williams ATR. An Introduction to Fluorescence Spectroscopy: Perkin-Elmer; 1981.
169. Vahrmeijer AL, Hutteman M, van der Vorst JR, van de Velde CJ, Frangioni JV. Image-guided cancer surgery using near-infrared fluorescence. Nature reviews Clinical oncology. 2013;10(9):507-18.